Prediction of bending wave transmission across coupled plates affected by spatial filtering and non-diffuse vibration fields

Thesis submitted in accordance with the requirements of the University of Liverpool for the degree of Doctor of Philosophy

by

David John Wilson

School of Architecture, University of Liverpool

January 2014

Abstract

This thesis concerns models based on Statistical Energy Analysis (SEA) to predict bending wave vibration in heavyweight buildings from structure-borne sound sources such as machinery. These sources tend to inject most power in the low- and mid-frequency ranges where the walls and floors have low mode counts and low modal overlap for which calculated Coupling Loss Factors (CLFs) from semi-infinite plate theory can be in error. For machinery it is necessary to predict vibration on walls/floors that are remote from the source room. In this situation, propagation across successive structural junctions causes spatial filtering of the wave field and the assumption of a diffuse field in each plate subsystem breaks down. The predictive approach described in the European Standard EN12354 uses SEA path analysis which assumes that transmission is dominated by first-order paths. However the feasibility of extending the concept of path analysis to walls and floors of rooms that are distant from the source room(i.e. not adjacent) is unknown. These issues are addressed in the thesis.The feasibility of SEA path analysis was assessed by quantifying the total contribution to receiver subsystem energy from paths containing specified numbers of CLFs. For receiving subsystems which are attached directly to the source subsystem, the EN12354 approach was found to underestimate the energy levels. For rooms remote from the source room, path analysis was found to significantly underestimate the vibration of the walls/floors which form the receiver room. Alternative approaches to improve predictions in large heavyweight buildings were assessed through comparison with Monte-Carlo Finite Element Method (MCFEM) models which were validated on a small heavyweight building. Matrix SEA was used with CLFs calculated for L-, T- and X-junctions using analytical models for rectangular plates to try and incorporate modal features. For isolated junctions, there was good agreement with MCFEM but in large buildings. However, it was unable to predict the peaks and troughs in the vibration response to one-third octave band accuracy although it can estimate the envelope response for plates that are directly connected to the source plate. In general, matrix SEA using finite plate theory CLFs does not improve the prediction in one-third octave bands when the statistical mode count is less than unity. Ray tracing was therefore investigated which showed that the angular distribution of power incident on the plate edges differed significantly from a diffuse field. Computationally efficient ray tracing was then developed for inclusion in Advanced SEA (ASEA) models to account for indirect coupling between plate subsystems. ASEA gave significant improvements over matrix SEA when there were large numbers of structural junctions between the source and receiving plates.

Acknowledgements

I would like to thank my supervisor Dr Carl Hopkins for his help and guidance over the past three years. I would also like to thank Dr Gary Seiffert and Prof Barry Gibbs for helping to create such an excellent environment in which to carry out my research.

I would like to thank Dr Gary Seiffert, Matt Robinson and Christoph Hoeller for their help with the experimental work carried out in this thesis.

I would like to thank all my colleagues at the ARU. In particular, Nuno Ferriera for many useful conversations over the past three years and Jianfei Yin (Ken) for his help and advice on ASEA and ABAQUS.

Last but not least I would like to thank my family and my girlfriend Amanda for their support whilst I was studying at Liverpool.

I gratefully acknowledge the funding provided by the UK Engineering and Physical Sciences Research Council.

Contents

List of Symbols and constants

a, $\ddot{\varepsilon}$ – Out of plane acceleration

$c_{\mathrm{g},i}$ – Bending wave group velocity of subsystem *i*

$c_{\mathrm{L},i}$ – Quasi-longitudinal wave velocity of subsystem *i*

d – Distance

e_i – Modal energy in subsystem *i*

$f_{11(\mathrm{B})}$ – Fundamental frequency of bending wave mode

$f_{11(\mathrm{L})}$ – Fundamental frequency of quasi-longitudinal wave mode

$f_{11(\mathrm{T})}$ – Fundamental frequency of torsional wave mode

h – Plate thickness

k_B^i – Bending wavenumber in subsystem *i*

$k_{\mathrm{x},i}$ – Bending wavenumber along x direction in plate *i*

$k_{\mathrm{x},i}^{\mathrm{N}}$ – Nearfield bending wavenumber along x direction in plate *i*

$k_{y,i}$ – Bending wavenumber along y direction

m – Mass

n_i – Modal density of subsystem *i*

t – Time

t_{ij} – Power transmission coefficient between plate *i* and *j*

B – Plate bending stiffness

$D_{\mathrm{E},ij}^n$– Level difference between subsystem *i* and *j* for ensemble member *n*

$D_{\mathrm{E},ij}$– Ensemble average level difference between subsystem *i* and *j*

E – Young's Modulus

E_i – Total energy in subsystem *i*

$E_{\mathrm{k},i}$– Kinetic energy in subsystem *i*

$E_{\frac{1}{3}\text{oct},i}$– One-third octave band average energy in subsystem *i*

E_{ij} – Energy in subsystem *i* when power is input to subsystem *j*.

$\boldsymbol{F}_i$- Complex driving force applied at node *i*

$I_{\text{inc},i}$ – Intensity/energy flux of the incident wave in plate *i*

$I_{\text{tran},j}$ – Intensity/energy flux of the transmitted wave in plate *j*

L_{ij} – Junction length between subsystems *i* and *j*

M_i – Modal overlap factor of subsystem *i*

M_y– Moment around y-axis

M_x – Moment around x-axis

N_{ensbl}– Total number of ensemble members

S_i – Surface area of subsystem *i*

Y_{dp}– Driving point mobility

$\overline{Y_{dp}}$ – Spatially averaged driving point mobility

α_R- Rayleigh damping coefficient alpha

β_R- Rayleigh damping coefficient beta

ϵ – Energy density

ρ_s – Plate surface density

ρ – Plate mass density

ϕ_y– Angular rotation around y-axis

ϕ_x – Angular rotation around x-axis

π_{ij} – Net power flow between subsystems *i* and *j*

π_i – Input power to subsystem *i*

π_{diss} – Dissipated power

ε – Out of plane displacement

σ – Standard deviation

v, $\dot{\varepsilon}$ – Out of plane velocity

η_{ij} – Coupling loss factor between subsystems *i* and *j*

η_i – Internal loss factor of subsystem *i*

η_{ii} – Total loss factor of subsystem *i*

λ_B – Bending wavelength

ω – Angular frequency

ω^k – Angular frequency at sample *k*

$\omega_{n,m}$– Eigenfrequency *n,m* in angular units

ν – Poisson's ratio

$\psi_{n,m}$– Mode shape associated with the Eigenfrequency $\omega_{n,m}$

List of Figures

List of Tables

Chapter 1 Introduction

1.1 Statement of the problem

Exposure to sound and vibration usually needs to be minimised for reasons of health and safety and/or human comfort. For this reason there are requirements in building, aeronautic, automotive and marine structures that set limits for the sound pressure level or vibration level. In general it is most cost effective to consider this at the design stage; hence the accurate prediction of sound transmission is relevant to many engineering industries. In this work the focus is on structure-bore sound in heavyweight buildings (i.e. concrete/masonry) although many of the methods apply to other engineering structures.

In buildings, common sources of structure-borne sound are household appliances such as boilers, dishwashers or washing machines, sanitary installations or other service machinery. A significant proportion of the structure-borne sound power from these devices tends to be in the low- and mid-frequency ranges and is broadband noise, although sometimes there are tonal components. Structure-borne sound can be transmitted across the walls and floors of the building and cause disturbance in neighbouring dwellings.

This thesis focuses on the prediction of bending wave transmission across coupled plates that form heavyweight buildings by consideration of the effects of spatial filtering and non-diffuse vibration fields. There is a need to predict vibration levels on the walls and floors in one-third octave bands due to excitation from building machinery or household appliances (e.g. white goods). For this reason, the frequency range of interest is 50 to 1000Hz which is the range in which most structure-borne sound sources in buildings inject significant power. The thesis considers situations where the source is located in a room adjoining the receiver room as well as the case where source and receiver rooms are separated by several structural junctions.

The complexity in the prediction partly arises from the fact that in heavyweight buildings the sound transmission is rarely dominated by a single path, and even the inclusion of first-order paths (such as used in EN12354) is not always sufficient[1-3]. It also occurs due to the fact that walls and floors in typical heavyweight building structures tend to have low modal overlap factors and low mode counts in one-third octave bands between 50 and 1000Hz. However, there is significant uncertainty in the response of building structures due to

workmanship and variation in wall/floor properties that a purely deterministic approach is unlikely to be appropriate.

1.2 Aims of the research

The main objective in this thesis is to to model bending wave transmission in heavyweight buildings undergoing mechanical excitation where there is spatial filtering and the vibration fields are non-diffuse. Heavyweight buildings provide the case studies to test theories based on Statistical Energy Analysis (SEA).

SEA can either be solved using a matrix formulation which accounts for all possible transmission paths or using path analysis to quantify the strength of individual transmission paths. This thesis will investigate the feasibility of using path analysis in large buildings for sound transmission between walls/floors in non-adjacent rooms. There are known to be issues using Coupling Loss Factors (CLF) calculated from semi-infinite plate theory when plates have low modal overlap and low mode counts hence the thesis will investigate alternative approaches to calculate the CLFs. This will include analytical modes based on a global mode approach for isolated junctions as well as a combination of Finite Element Methods (FEM) and Experimental SEA (ESEA). A Monte-Carlo approach to Finite Element Methods (MCFEM) will be validated against measurements on a small heavyweight room construction and subsequently used to assess the SEA, ESEA and ASEA models.

In order to develop models based upon the principles of SEA it is convenient to use Rain on the Roof (ROTR) excitation. However, in practical situations the mechanical excitation is usually applied at a specific location within on the wall or floor rather than over the entire surface. To investigate the practical implications of this approach further the vibration levels of the walls and floors of heavyweight building in response to a simulated white goods appliance using MCFEM and the results are compared to case when ROTR excitation is applied.

SEA assumes that a diffuse field is present in all subsystems. In systems of coupled plates the junction lines between the plates filter the wavefields in a process known as spatial filtering. In this thesis a ray tracing method is developed which is computationally efficient for large

building structures. This ray tracing approach is used for two purposes. Firstly, to assess the effect of spatial filtering across junctions of rectangular plates in large buildings. Secondly the ray tracing method is incorporated into an Advanced SEA (ASEA) calculation to determine the indirect coupling between plates.

1.3 Outline of the thesis

The outline structure of the thesis is that chapters 2 and 3 describe the relevant theory, Chapter 4 describes the experimental work to validate MCFEM and chapters 5, 6, 7 and 8 contain the results from SEA, ASEA, ESEA and MCFEM.

Chapter 2 contains the theory for SEA, ASEA, ESEA and MCFEM.

Chapter 3 describes the theory used to calculate the structure-borne sound transmission across L, X and T junction configurations using finite and semi-infinite plate theory.

Chapter 4 describes the experimental work carried out to validate the MCFEM approach that is used for the numerical experiments in chapters 5 to 8.

Chapter 5 contains analysis of the EN12354 models and compares these against wave theory SEA for two types of building structure. The SEA models are also compared against MCFEM models of the building structures.

Chapter 6 contains analysis of the L, T and X junctions using ESEA. The CLFs resulting from the ESEA on the isolated junctions are incorporated into SEA models of building structures and the results compared against MCFEM.. The results are discussed in relation to a five-plate structure containing L and T junctions.

Chapter 7 investigates the effects of spatial filtering in building structures. The ASEA model is compared against MCFEM for two types of heavyweight building structure.

Chapter 8 contains the conclusions and suggestions for future work.

1.4 Literature review

Statistical Energy Analysis (SEA) [4] is a well-established method for predicting structure-borne sound transmission in buildings. Gibbs and Gilford [5] used an SEA approach to predict the bending wave transmission through quarter scale T-and X-junctions found in building structures. The predicted results agreed well with measurement. Craik [6, 7] applied SEA to building structures and predicted the spatial average vibration levels of walls and floors in a heavyweight building to within 4dB of the measured values (on average). The SEA models only included bending wave transmission at structural joints which was listed as a possible reason for the larger errors in the higher frequency octave bands. The measurements appear to have been confined to walls and floors which lie in the section plane of the building.

Later work [8-10] showed that transverse shear and quasi-longitudinal waves play an important role in the transmission of structure-borne sound. Wave conversion between bending and in-plane vibration at junctions is of particular importance when the receiver plate separated from the source plate by many structural junctions [11, 12]. Craik compared the Energy Level Difference (ELD) between various walls and floors of a heavyweight structure in the 125Hz, 500Hz and 2000Hz one-third octave bands using SEA models with and without in-plane subsystems. The effect of including the in-plane subsystems on the ELD was largest for plates which where furthest from the source plate in the 2000Hz one third octave band. The results were also compared to measurements and acceptable results were obtained for receiver plates which were close to the source plate. However, it is unlikely that any resonant local in-plane modes were present in the heavyweight plates in the octave bands below 500Hz which potentially invalidates the comparison between SEA models assuming in-plane waves and the measured data at the lower frequencies. To further investigate issues with in-plane waves in heavyweight buildings, Hopkins [13-15] used two FEM models of T- and L-junctions: one with the junction line free and the other with the junction line pinned. The free boundary condition allowed in-plane and bending wave transmission at the junction line whereas the pinned boundary condition only allowed the transmission of bending waves. The vibration level difference from FEM was compared to results from measurements on a physical model. Below the lowest thin plate bending wave limit of any plate in the junction (800Hz) both models adequately predicted the vibration level difference across the T junction. Above 800Hz only the free junction line model adequately predicted the vibration

level difference across the T-junction. This indicates that in-plane waves are more important at frequencies above the lowest thin plate bending limit of any plate in the structure when dealing with a single junction. From the aforementioned research it can be concluded that models considering only bending wave transmission for heavyweight buildings excited by typical domestic machinery should be sufficient, even where several structural junctions exist between the source and the receiving plate. For structure borne sound transmission between coupled plates, SEA generally provides a close estimate of the mean response when the one-third octave band statistical mode count is greater than five and the modal overlap factor is greater than unity [3, 16]. In heavyweight building structures these criteria are not usually met in the frequency range 50 to 1000Hz and SEA tends to underestimate the ELD between source and receiver plates [17, 18].

Wester and Mace [19] investigated the use of SEA on two edge coupled rectangular plates using a wave approach and defined two parameters which quantify the strength of the coupling between the two plates. An expression for the ensemble average CLF between the two plates was derived which accounted for the strength of the coupling between the plates and the finite width of the plate. Compared to this expression the standard theory based on diffuse fields and semi-infinite plates [20] generally overpredicts the CLF between the two plates for most systems of practical interest. The method was used by Park *et al* [21, 22] to investigate the CLF between two rectangular plates of various thickness. The ensemble average CLF appeared to provide a good estimate of the mean value of the effective CLF calculated for a single ensemble member. A similar wave approach has been used to investigate the transmission coefficient between two finite coupled rectangular plates[23]. It was found that the transmission coefficient between the two finite plates was overestimated by semi-infinite plate theory. For use in large heavy-weight buildings it may be possible is to extend the approach used by Wester and Mace to obtain expressions for the ensemble average CLFs in T and X junctions. Using these CLFs in an SEA model of large scale buildings may improve the SEA predictions in the region of low mode count and low modal overlap.

The European Standard EN12354-2 [24] outlines an approach to estimate impact sound insulation in heavyweight building structures. The method was proposed by Gerretsen [25] and can be described as first-order SEA path analysis where the power balance equations are written for each subsystem. It is assumed that the power flows from source to receiver and cannot return to any given subsystem. In this thesis these paths will be referred to ‘forward paths’.

Magrans [26] has shown that by rearranging the SEA power balance equations the inversion of the energy matrix can be written as a sum of contributions from an infinite number of paths. However the inverse matrix contains path terms which may return to any subsystem any number of times. Hence assuming all forward paths have been identified, the inverse matrix approach will give a similar solution to EN12354 when the power returning to any subsystem is negligible.

Guasch *et al* [27, 28] applied graph theory to SEA models to develop efficient methods to rank order the strongest transmission paths between any two subsystems in an SEA model.

The approach in EN12354 was validated by Gerretsen with X-and T-junctions of different constructions [25] and good agreement was observed between measured and predicted levels. However for heavyweight buildings, it has been subsequently shown [1, 2, 29] that each individual flanking path is often weaker than the direct path but there are so many flanking paths that collectively the higher-order paths can significantly reduce the sound insulation between two adjacent rooms.

FEM [30] is the most commonly used numerical tool to model the vibration transmission between complex structures or plates which have low modal overlap and low statistical mode counts. Simmons[31] investigated FEM modelling of rectangular Perspex plate arranged in an 'H' structure configuration. It was concluded that FEM was unable to accurately predict the narrow band point response of the structure but was able to predict the band and spatial average response to a sufficient accuracy. Simmons determined Coupling Loss Factors(CLFs) using the spatial and band average output from the FEM. It was suggested that by varying uncertainties such as boundary conditions or plate dimensions an ensemble of CLFs could be generated for the structure for use in SEA; however, this is an unusual and impractical definition of an SEA ensemble. Craik and Steel [32] used FEM and ESEA to investigate the maximum and minimum CLF between two plates for the purpose of validating previous work by Craik[17]. It was shown that the CLF between two rectangular plates varied proportionally to the spatial-average driving point mobility of the receiving subsystem.

Hopkins [33, 34] used ESEA to extend the use of SEA to plate systems with low modal overlap and statistical mode count. The focus was on rectangular plates arranged in L-and T-junctions. The length of the plates in the direction perpendicular to the junction line was randomly chosen from a normal distribution to generate an ensemble of 'similar' junctions. ESEA was then performed on each ensemble member to generate a set of CLFs between each

of the subsystems in the junction. It was found that the probability distribution of the linear CLFs were right skewed when the modal overlap was less than one, however the distribution could be reasonably well approximated by a lognormal distribution which enabled the mean value and confidence limits to be determined for the CLF. With knowledge of the mean and the lower and upper confidence limits of the isolated plate junctions an approach called the SEA permutations method was developed. The SEA power balance equations for a built up structure (consisting of the isolated plate junctions) were inverted once using the mean value of the CLFs and then for all permutations of the lower and upper value of CLF between all subsystems in the built up structure. This enabled estimates of the mean value of the vibration level difference with lower of upper confidence limits between any two subsystems in the built up structure. The method was applied to a seven plate structure which represented rectangular masonry walls forming two rooms that was compared directly to the output generated from an ensemble of FEM models of the structure. In general good agreement was found between the mean value predicted by the SEA permutations method and the FEM prediction. However the SEA permutations method overestimated the vibration level difference for some cases where the receiver plate was not directly attached to the source plate. The SEA permutations method tended to overestimate the upper and lower confidence intervals of the vibration level difference and it was concluded that more numerical experiments were required to investigate the limitations of the approach. One possible reason for the differences between the FE and SEA permutations method predictions might be that in the case of the SEA permutations method all seven plates could be assigned values of length independently from the remaining plates. However only three lengths(one length for the width of the room and one length for each room breadth) could be assigned in the FEM model without distorting the 90° corners of the structure. To avoid this issue in this thesis, use is made of the significant variation in the quasi-longitudinal wave velocity of the plates that is found in building structures [35]. This can be used to generate an ESEA ensemble instead of plate dimensions. Another potential issue is that the *in-situ* Total Loss Factor (TLF) is assigned to the plates in the junction. For a large building this would require a significant number of junctions to be modelled using FEM which may be a more time consuming process than directly modelling the entire structure with FEM.

An alternative approach to SEA has been developed which is referred to as Energy Flow Methods (EFM) [36-38]. Provided that the forces acting on a structure are uncorrelated the

mean square velocity at a point in the structure, and hence the kinetic energy in each plate, can be written as a sum of the mean square velocities in response to each load applied separately. For the case of ROTR excitation this allows the formation of an Energy Influence Coefficient (EIC) matrix [39, 40]. This gives the spatial and band averaged energy in each subsystem in response to a known input power. The EIC matrix can be determined from knowledge of the global eigenfrequencies and eigenfunctions of the built up structure. The EIC matrix is closely related to the inverse of the SEA energy matrix [40] and hence using the EIC matrix directly avoids inversion errors.

The main advantage of the energy flow method developed by Mace and Shorter [38] is that the plate energy and input power do not need to be computed at discrete frequency points since use is made of the definition of ROTR to derive analytical expressions for the band-average response values. This saves a great deal of computational expense.

To determine the response statistics knowledge of the statistical distribution of the material properties and structural dimensions is required in order to define an ensemble of similar structures for which a set of EICs matrices can be determined. Multiplying the input power vector by each EIC matrix in turn allows a mean value of the energy in each subsystem to be determined with confidence limits. For typical heavyweight building structures with a mesh size that is accurate up to 1000Hz the total number of degrees of freedom is extremely large and computing the required integrals on the global mode shapes, as outlined by Shorter[38], for each of the deterministic analyses would be computationally expensive.

The ESEA ensemble and the EFM approaches developed by Hopkins and Mace respectively rely on the fact that all the uncertainties can be described statistically. In building structures this may not always be the case and there is a need to determine confidence limits for the mean response predicted by wave theory SEA. Lyon [4] developed a method to determine the response variance in an SEA model which was based on the assumption that the spacing between eigenfrequencies in a given subsystem are described by Poisson statistics. Craik [17] found that for building acoustics this method tends to overestimate the variance by a considerable margin and proposed an empirical formulae relating the CLF to the spatial and band-average point mobility of the receiver plate. More recent work by Langley *et al* [41-44] shows that the eigenfrequency spacing is more likely to follow statistics based on the Gaussian orthogonal ensemble (GOE) rather than Poisson statistics with the exception of systems with a high degree of symmetry (e.g. a simply supported plate). A method was developed to predict the variance based on GOE statistics which showed reasonable

agreement with numerical and physical experiments provided the assumptions of SEA were valid and that GOE statistics were applicable. For the systems investigated, at lower frequencies both these assumptions were invalid.

In building acoustics the case of most interest often concerns sound transmission between two adjacent dwellings. However for structure-borne sound sources such as machinery, it is also important to be able to assess transmission to a receiver room that is more distant from the source. Hence it is important to be able to predict the vibration levels of the walls and floors that form this receiving room in order to accurately predict the SPL. For coupled plates where the receiver plate is connected to the source plate across several junctions, Langley [45] described a process referred to as 'spatial filtering' where the angular distribution of the wave field is increasing filtered by the transmission coefficient at each junction line. Hence even when there is a diffuse field on the source plate the filtering action of the structural junctions can lead to a non-diffuse field on the other coupled plates. This invalidates the SEA assumption of a diffuse field in all subsystems. To account for spatial filtering Langley developed Wave Intensity Analysis (WIA)[46]. WIA applies the power balance equation in each angular band for the transmitted and reflected waves at each junction line to generate a set of coupled linear equations which can be solved by using a set of shape functions to represent the energy density within each plate. The approach has been validated for a range of engineering structures [47] with a significant improvement over SEA in cases where many structural junctions exist between source and receiver plate. However the structures investigated to date have been 'in-line' plates which are simply supported along the edges perpendicular to the junction lines. This is not because WIA is restricted to these systems but the 'exact' numerical solution sought to validate WIA was obtained using the dynamic stiffness method which requires two opposite edges of the plate to be simply supported. The main obstacle to applying WIA to building structures is that it is not clear whether the method could be adapted to include plates with 'cut-outs' such as walls which contain windows or doorways.

Heron [48] proposed an alternative method to WIA which he called Advanced SEA (ASEA). This method uses a ray theory approach to track the energy flow across each subsystem and combines this with SEA to account for any residual power once the ray tracing procedure has stopped. Heron applied ASEA to a series of rods of varying thickness connected in a line. Only longitudinal wave transmission was allowed and the predicted vibration level differences were compared to SEA and an exact analytical solution. It was found that ASEA performed well for the distant subsystems whereas SEA performed poorly. The system of

rods validated the ASEA approach however it was not a typical engineering structure since the rods were several tens of meters in length. Heron also outlined a method for applying ASEA to systems of plates; however at the time it was noted that this could be computationally expensive. Recently Yin and Hopkins [49] adopted this procedure for ASEA for plates to predict the vibration level difference from a homogeneous plate attached to a periodic ribbed plate. ASEA results were compared with FEM, SEA and physical experiments results for the vibration level difference between the source plate and each bay of the ribbed plate structure. There was good agreement between FEM, ASEA and the experimental results with most results lying within 10dB of each other whereas SEA over-predicted the level difference by as much as 40dB in the last bay of the ribbed plate. In his thesis[50], Yin also investigated other structures including one in which another plate was attached to the L-junction between the homogeneous and ribbed plate so as to provide flanking transmission to the bays of the ribbed plate. Good agreement was found between ASEA and FEM for all the plate structures that were investigated.

Whilst there are indications in the literature that non-diffuse vibration fields and spatial filtering can be included in the models such as ASEA or WIA, there is no evidence of these being adapted to model more than a few coupled plates. This is addressed in this thesis.

Chapter 2 Theory – Statistical energy analysis and finite element methods for structure-borne sound propagation

2.1 Introduction

This chapter describes the approaches used in this thesis to predict the vibration levels as spatial, ensemble and frequency-averaged values for heavyweight floors and walls in buildings. The first approach is primarily statistical, and is based around SEA. This will include Matrix SEA, SEA Path Analysis, Experimental SEA and Advanced SEA. The second approach is deterministic and is used to establish a baseline against which the statistical methods can be compared by using a Monte-Carlo approach to Finite Element Methods (MCFEM).

2.2 Statistical Energy Analysis (SEA)

Statistical Energy Analysis is a framework of analysis which is commonly used to investigate transmission between structural components such as plates and beams and enclosed air volumes. It is assumed that the systems under investigation are drawn from statistical populations with known distributions and the primary variable used in the analysis is the total energy of the individual components, hence the name SEA [4]. The output from SEA gives spatial, ensemble and frequency-averaged values for the response of each subsystem.

Numerical simulations carried out on systems of coupled plates [51] indicate that SEA is most accurate when the statistical mode count per band is greater than five for each plate and the geometric mean of the modal overlap factors for the source and receiver plates is greater than one. For heavyweight structures investigated in this thesis these conditions are not met below 1000Hz and alternative methods have been investigated with the aim of improving the prediction in this frequency region.

2.2.1 Overview of Statistical Energy Analysis

SEA originates from the observation that the net power flow between two linearly coupled oscillators is proportional to the difference between the uncoupled energies of the oscillators[52]. The flow is always from the oscillator with the higher energy to the oscillator with lower energy provided that statistically independent broad band excitation is applied and

that the oscillators are weakly coupled [52]. This results in the power flow proportionality equation

$$\pi_{12} = K_1[E_1 - K_2 E_2] \tag{2.1}$$

In SEA multi-modal subsystems such as rooms, beams and plates are treated as stores of modal energy. The power flow proportionality in eq.2.1 can be extended to coupling between multi-modal subsystems with $K_1 = \omega\eta_{12}$ and $K_2 = n_2/n_1$ where η_{ij} is the coupling loss factor (CLF) from plates *i* to *j*, n_j is the modal density of subsystem '*j'* and ω is the angular centre frequency of the band. This step is valid provided a number of criteria are satisfied, these are [4]

1) The coupling between modes in separate subsystems is 'weak'
2) The eigenfrequencies of a subsystem are equally probable over a given frequency interval
3) Equipartion of modal energy in each subsystem and incoherent modal response

For multi-modal systems eq.2.1 gives the net power flow from subsystem 1 to subsystem 2 as

$$\pi_{12} = \omega[\eta_{12}E_1 - \eta_{21}E_2] \tag{2.2}$$

where the CLFs are related through the consistency relationship

$$\eta_{21} = \frac{n_2}{n_1}\eta_{12} \tag{2.3}$$

The power flow between plate *i* and plate *j* is defined as $\omega\eta_{ij}E_i$which is analogous to the power dissipated in a subsystem *i* due to internal damping $\omega\eta_i E_i$, where η_i is the internal loss factor (ILF) of subsystem *i.*

The standard procedure to determine the CLF between plates uses the angular average power flow transmission coefficient.

$$\eta_{ij} = \frac{c_{\mathrm{g},i}L_{ij}}{\omega\pi S_i}\int_0^{\frac{\pi}{2}} \tau_{ij}\,(\theta)\cos(\theta)\mathrm{d}\theta \tag{2.4}$$

where $c_{\mathrm{g,i}}$ is the bending wave velocity at angular frequency ω, L_{ij} is the length of the junction, S_i is the area of plate subsystem *j*, τ_{ij} is the junction transmission coefficient. The CLF η_{ji} can be determined from eq.2.3. The modal density of plate subsystem *i* is given by.

$$n_i(f) = \frac{k_B^i\, S_i}{c_{\mathrm{g},i}} = \frac{\sqrt{3}\, S_i}{h c_{\mathrm{L},i}} \tag{2.5}$$

2.2.2 Power balance equations

Under steady state conditions a power balance equation can be written for each subsystem in which the sum of the power flowing into the subsystem must equal the sum of the power flowing out of the subsystem including dissipative losses. Application of eqs. 2.2 and 2.3 to the power balance equations on each subsystem leads to a set of simultaneous equations which relate the total energy in each subsystem to the total external power input injected into the system. For a system consisting of *N* subsystems this gives:

$$\begin{bmatrix} \eta_1 + \sum_{j=2}^{N} \eta_{1j} & -\eta_{21} & -\eta_{31} & \cdots & -\eta_{N1} \\ -\eta_{12} & \eta_2 + \sum_{j=1,\neq 2}^{N} \eta_{2j} & -\eta_{32} & \cdots & -\eta_{N2} \\ -\eta_{13} & -\eta_{23} & \eta_3 + \sum_{j=1,\neq 3}^{N} \eta_{3j} & \cdots & -\eta_{N3} \\ \vdots & \vdots & \vdots & \ddots & \vdots \\ -\eta_{1N} & -\eta_{2N} & -\eta_{3N} & \cdots & \eta_N + \sum_{j=1,\neq N}^{N} \eta_{1j} \end{bmatrix} \begin{bmatrix} E_1 \\ E_2 \\ E_3 \\ \vdots \\ E_N \end{bmatrix} = \frac{1}{\omega} \begin{bmatrix} \pi_{\mathrm{in},1} \\ \pi_{\mathrm{in},2} \\ \pi_{\mathrm{in},3} \\ \vdots \\ \pi_{\mathrm{in},N} \end{bmatrix} \quad (2.6)$$

In the standard SEA procedure both sides of equation (2.6) are multiplied by the inverse loss factor matrix to give the subsystem energies in terms of the input powers. The total loss factor (TLF) for subsystem j is denoted by η_{jj} and these form the diagonal elements of the loss factor matrix. The off diagonal elements are the coupling loss factors denoted by η_{ji}.

2.2.3 Transmission Path analysis

Equation 2.6 can be written in the following form,

$$\left[\begin{bmatrix} 1 & 0 & 0 & \cdots & 0 \\ 0 & 1 & 0 & \cdots & 0 \\ 0 & 0 & 1 & \cdots & 0 \\ \vdots & \vdots & \vdots & \ddots & \vdots \\ 0 & 0 & 0 & \cdots & 1 \end{bmatrix} - \begin{bmatrix} 0 & \frac{\eta_{21}}{\eta_{11}} & \frac{\eta_{31}}{\eta_{11}} & \cdots & \frac{\eta_{N1}}{\eta_{11}} \\ \frac{\eta_{12}}{\eta_{22}} & 0 & \frac{\eta_{32}}{\eta_{22}} & \cdots & \frac{\eta_{N2}}{\eta_{22}} \\ \frac{\eta_{13}}{\eta_{33}} & \frac{\eta_{23}}{\eta_{33}} & 0 & \cdots & \frac{\eta_{N3}}{\eta_{33}} \\ \vdots & \vdots & \vdots & \ddots & \vdots \\ \frac{\eta_{1N}}{\eta_{NN}} & \frac{\eta_{2N}}{\eta_{NN}} & \frac{\eta_{3N}}{\eta_{NN}} & \cdots & 0 \end{bmatrix} \right] \begin{bmatrix} E_1 \\ E_2 \\ E_3 \\ \vdots \\ E_N \end{bmatrix} = \frac{1}{\omega} \begin{bmatrix} \pi_{\mathrm{in},1}/\eta_{11} \\ \pi_{\mathrm{in},2}/\eta_{22} \\ \pi_{\mathrm{in},3}/\eta_{33} \\ \vdots \\ \pi_{\mathrm{in},N}/\eta_{NN} \end{bmatrix} \quad (2.7)$$

and by taking the inverse matrix, the subsystem energies are given by

$$\begin{bmatrix} E_1 \\ E_2 \\ E_3 \\ \vdots \\ E_N \end{bmatrix} = \left[\begin{bmatrix} 1 & 0 & 0 & \cdots & 0 \\ 0 & 1 & 0 & \cdots & 0 \\ 0 & 0 & 1 & \cdots & 0 \\ \vdots & \vdots & \vdots & \ddots & \vdots \\ 0 & 0 & 0 & \cdots & 1 \end{bmatrix} - \begin{bmatrix} 0 & \frac{\eta_{21}}{\eta_{11}} & \frac{\eta_{31}}{\eta_{11}} & \cdots & \frac{\eta_{N1}}{\eta_{11}} \\ \frac{\eta_{12}}{\eta_{22}} & 0 & \frac{\eta_{32}}{\eta_{22}} & \cdots & \frac{\eta_{N2}}{\eta_{22}} \\ \frac{\eta_{13}}{\eta_{33}} & \frac{\eta_{23}}{\eta_{33}} & 0 & \cdots & \frac{\eta_{N3}}{\eta_{33}} \\ \vdots & \vdots & \vdots & \ddots & \vdots \\ \frac{\eta_{1N}}{\eta_{NN}} & \frac{\eta_{2N}}{\eta_{NN}} & \frac{\eta_{3N}}{\eta_{NN}} & \cdots & 0 \end{bmatrix} \right]^{-1} \begin{bmatrix} \pi_{\mathrm{in},1}/\omega\eta_{11} \\ \pi_{\mathrm{in},2}/\omega\eta_{22} \\ \pi_{\mathrm{in},3}/\omega\eta_{33} \\ \vdots \\ \pi_{\mathrm{in},N}/\omega\eta_{NN} \end{bmatrix} \quad (2.8)$$

Magrans [26] has shown if that if all the off-diagonal terms in eq.2.7 are less than 1 then the inverse matrix in eq.2.8 can be expanded in a power series to give the subsystem energies as an infinite sum.

$$\begin{bmatrix} E_1 \\ E_2 \\ E_3 \\ \vdots \\ E_N \end{bmatrix} = \left[\begin{bmatrix} 1 & 0 & 0 & \cdots & 0 \\ 0 & 1 & 0 & \cdots & 0 \\ 0 & 0 & 1 & \cdots & 0 \\ \vdots & \vdots & \vdots & \ddots & \vdots \\ 0 & 0 & 0 & \cdots & 1 \end{bmatrix} + \sum_{n=1}^{\infty} \begin{bmatrix} 0 & \frac{\eta_{21}}{\eta_{11}} & \frac{\eta_{31}}{\eta_{11}} & \cdots & \frac{\eta_{N1}}{\eta_{11}} \\ \frac{\eta_{12}}{\eta_{22}} & 0 & \frac{\eta_{32}}{\eta_{22}} & \cdots & \frac{\eta_{N2}}{\eta_{22}} \\ \frac{\eta_{13}}{\eta_{33}} & \frac{\eta_{23}}{\eta_{33}} & 0 & \cdots & \frac{\eta_{N3}}{\eta_{33}} \\ \vdots & \vdots & \vdots & \ddots & \vdots \\ \frac{\eta_{1N}}{\eta_{NN}} & \frac{\eta_{2N}}{\eta_{NN}} & \frac{\eta_{3N}}{\eta_{NN}} & \cdots & 0 \end{bmatrix}^n \right] \begin{bmatrix} \pi_{\mathrm{in},1}/\omega\eta_{11} \\ \pi_{\mathrm{in},2}/\omega\eta_{22} \\ \pi_{\mathrm{in},3}/\omega\eta_{33} \\ \vdots \\ \pi_{\mathrm{in},N}/\omega\eta_{NN} \end{bmatrix} \quad (2.9)$$

The energy in the receiver can be considered as the combination of an infinite number of 'path contributions'[3, 7] with each path contribution consisting of different products of the off-diagonal elements of eq.2.8 . For example, the energy contribution to subsystem 3 along path 1-2-3 when power $\pi_{\mathrm{in},1}$ is input to subsystem 1 only is

$$E_{1-2-3} = \frac{\eta_{12}}{\eta_{22}} \frac{\eta_{23}}{\eta_{33}} \frac{\pi_{in,1}}{\omega\eta_{11}} \quad (2.10)$$

Assuming no energy returns to the source subsystem

$$E_s \approx \frac{\pi_{in,s}}{\omega\eta_{ss}} \quad (2.11)$$

Then the level difference between along the path 1-2-3 is given

$$\frac{E_{1-2-3}}{E_1} = \frac{\eta_{12}}{\eta_{22}} \frac{\eta_{23}}{\eta_{33}} \quad (2.12)$$

In this way all the paths can be assessed and ranked in order of their 'importance' i.e. ranked in order of the percentage contribution to the receiver subsystem energy.

Path analysis is sometimes used as a stand-alone predictive method to allow quick estimation of the performance of structural elements *in-situ* [53]. For this method to be of practical worth the majority of the receiver subsystem energy must have been transmitted from the

source via a relatively small number of easy identifiable paths otherwise a significant percentage of the receiver subsystem energy will be left unaccounted for [54].

2.2.4 Experimental SEA (ESEA)

In some cases the CLFs cannot be easily be predicted using the angular average transmission coefficient. For example, the structural connection between subsystems may be too complex to determine a transmission coefficient [31] or the subsystems may have a low statistical mode count and modal overlap factor. In such cases taking an angular average over all angles of incidence is no longer strictly appropriate [34] and it may be better to estimate the CLF between subsystems experimentally using ESEA.

Lyon [55] has described a form of ESEA to determine the CLFs of a built-up structure by application of the SEA power balance equations with power injected into each subsystem in turn. This results in an energy matrix which can be inverted to obtain the CLFs of the structure.

$$\begin{bmatrix} \eta_{11} & -\eta_{21} & -\eta_{31} & \cdots & -\eta_{N1} \\ -\eta_{12} & \eta_{22} & -\eta_{32} & \cdots & -\eta_{N2} \\ -\eta_{13} & -\eta_{23} & \eta_{33} & \cdots & -\eta_{N3} \\ \vdots & \vdots & \vdots & \ddots & \vdots \\ -\eta_{1N} & -\eta_{2N} & -\eta_{3N} & \cdots & \eta_{NN} \end{bmatrix} = \begin{bmatrix} \frac{\pi_{\mathrm{in},1}}{\omega} & 0 & 0 & \cdots & 0 \\ 0 & \frac{\pi_{\mathrm{in},2}}{\omega} & 0 & \cdots & 0 \\ 0 & 0 & \frac{\pi_{\mathrm{in},3}}{\omega} & \cdots & 0 \\ \vdots & \vdots & \vdots & \ddots & \vdots \\ 0 & 0 & 0 & \cdots & \frac{\pi_{\mathrm{in},N}}{\omega} \end{bmatrix} \begin{bmatrix} E_{11} & E_{12} & E_{13} & \cdots & E_{1N} \\ E_{21} & E_{22} & E_{23} & \cdots & E_{2N} \\ E_{31} & E_{32} & E_{23} & \cdots & E_{3N} \\ \vdots & \vdots & \vdots & \ddots & \vdots \\ E_{N1} & E_{N2} & E_{N3} & \cdots & E_{NN} \end{bmatrix}^{-1} \tag{2.13}$$

where E_{ij} is the energy in subsystem *i* when power is input to subsystem *j*.

Large errors in the CLFs can occur when the matrix containing the subsystem energies is ill-conditioned (i.e. when the off-diagonal terms become comparable to the terms on diagonal) [3].

An improved method to determine the CLFs has been proposed by Lalor [56]. The internal loss factors are removed from eq.2.13 to give the set of equations which can be inverted to give the CLFs only. The resulting equations may be written in block matrix form as

$$\begin{bmatrix}\boldsymbol{\eta_1}\\ \boldsymbol{\eta_2}\\ \boldsymbol{\eta_3}\\ \vdots\\ \boldsymbol{\eta_N}\end{bmatrix}=\begin{bmatrix}[\boldsymbol{E_1}] & 0 & 0 & \cdots & 0\\ 0 & [\boldsymbol{E_2}] & 0 & \cdots & 0\\ 0 & 0 & [\boldsymbol{E_3}] & \cdots & 0\\ \vdots & \vdots & \vdots & \ddots & \vdots\\ 0 & 0 & 0 & \cdots & [\boldsymbol{E_N}]\end{bmatrix}^{-1}\begin{bmatrix}\boldsymbol{\pi_1}\\ \boldsymbol{\pi_2}\\ \boldsymbol{\pi_3}\\ \vdots\\ \boldsymbol{\pi_N}\end{bmatrix} \tag{2.14}$$

The elements of the above block matrices are given by

$$\boldsymbol{\eta_j}=\begin{bmatrix}\eta_{1j}\\ \eta_{2j}\\ \eta_{3j}\\ \vdots\\ \eta_{Nj}\end{bmatrix} \tag{2.15}$$

$$[\boldsymbol{E_j}]=\begin{bmatrix}\left(\frac{E_{11}}{E_{j1}}-\frac{E_{1j}}{E_{jj}}\right) & \left(\frac{E_{21}}{E_{j1}}-\frac{E_{2j}}{E_{jj}}\right) & \left(\frac{E_{31}}{E_{j1}}-\frac{E_{3j}}{E_{jj}}\right) & \cdots & \left(\frac{E_{N1}}{E_{j1}}-\frac{E_{Nj}}{E_{jj}}\right)\\ \left(\frac{E_{12}}{E_{j2}}-\frac{E_{1j}}{E_{jj}}\right) & \left(\frac{E_{22}}{E_{j2}}-\frac{E_{2j}}{E_{jj}}\right) & \left(\frac{E_{32}}{E_{j2}}-\frac{E_{3j}}{E_{jj}}\right) & \cdots & \left(\frac{E_{N2}}{E_{j2}}-\frac{E_{Nj}}{E_{jj}}\right)\\ \left(\frac{E_{13}}{E_{j3}}-\frac{E_{1j}}{E_{jj}}\right) & \left(\frac{E_{23}}{E_{j3}}-\frac{E_{2j}}{E_{jj}}\right) & \left(\frac{E_{33}}{E_{j3}}-\frac{E_{3j}}{E_{jj}}\right) & \cdots & \left(\frac{E_{N3}}{E_{j3}}-\frac{E_{Nj}}{E_{jj}}\right)\\ \vdots & \vdots & \vdots & \ddots & \vdots\\ \left(\frac{E_{1N}}{E_{jN}}-\frac{E_{1j}}{E_{jj}}\right) & \left(\frac{E_{2N}}{E_{jN}}-\frac{E_{2j}}{E_{jj}}\right) & \left(\frac{E_{3N}}{E_{jN}}-\frac{E_{3j}}{E_{jj}}\right) & \cdots & \left(\frac{E_{N3}}{E_{jN}}-\frac{E_{Nj}}{E_{jj}}\right)\end{bmatrix} \tag{2.16}$$

$$\boldsymbol{\pi_j}=\begin{bmatrix}\frac{\pi_{\mathrm{in},j}}{\omega E_{jj}}\\ \frac{\pi_{\mathrm{in},j}}{\omega E_{jj}}\\ \frac{\pi_{\mathrm{in},j}}{\omega E_{jj}}\\ \vdots\\ \frac{\pi_{\mathrm{in},j}}{\omega E_{jj}}\end{bmatrix} \tag{2.17}$$

Since the block matrix is diagonal it can be solved for each element individually. For example $\boldsymbol{\eta_1}=[\boldsymbol{E_1}]^{-1}\boldsymbol{\pi_1}$ gives the coupling loss factors in vector $\boldsymbol{\eta_1}$.

This reduces the size of the energy matrix from *N*x*N* to (*N-1)*x*(N-1)* and in some cases may improve the conditioning of the matrix. The internal loss factors can be determined separately by considering the power balance for the whole system for each case of source subsystem.

$$\begin{bmatrix}\eta_1\\ \eta_2\\ \eta_3\\ \vdots\\ \eta_N\end{bmatrix}=\frac{1}{\omega}\begin{bmatrix}E_{11} & E_{12} & E_{13} & \cdots & E_{1N}\\ E_{21} & E_{22} & E_{23} & \cdots & E_{2N}\\ E_{31} & E_{32} & E_{23} & \cdots & E_{3N}\\ \vdots & \vdots & \vdots & \ddots & \vdots\\ E_{N1} & E_{N2} & E_{N3} & \cdots & E_{NN}\end{bmatrix}^{-1}\begin{bmatrix}\pi_{\mathrm{in},1}/\eta_{11}\\ \pi_{\mathrm{in},2}/\eta_{22}\\ \pi_{\mathrm{in},3}/\eta_{33}\\ \vdots\\ \pi_{\mathrm{in},N}/\eta_{NN}\end{bmatrix} \tag{2.18}$$

One possible outcome from the matrix inversion is that CLFs can occur between plates which are not connected together. In the standard SEA power balance equations this coupling is not included. These 'non-adjacent' coupling loss factors can be forced to zero by rearranging the rows and columns of the block matrix eq.2.16 so that the non-adjacent CLFs are located in the last block. The remaining CLFs between directly coupled subsystems are determined from the remaining system of equations which do not include any terms from the block of non-adjacent CLFs, an example applied to a three subsystem model is found in reference [50] and the application to a five subsystem model can be found in Chapter 6.

When the transmission between source subsystem i and receiver subsystem j is dominated by a single direct path the energy in the receiver subsystem given by eq. 2.16 can be approximated by[3]:

$$E_{ji} \approx \frac{\eta_{ij}}{\eta_{jj}} \frac{\pi_{\text{in},i}}{\omega \eta_{ii}} \tag{2.19}$$

Assuming that the total contribution to the source subsystem energy from the numerous transmission paths in eq.2.9 is small in comparison to the initial contribution from the power input the total energy in the source subsystem can be approximated by $E_{ii} \approx \frac{\pi_{in,i}}{\omega \eta_{ii}}$

The coupling loss factor can be approximated by

$$\eta_{ij} \approx \frac{E_{ji}}{E_{ii}} \eta_{jj} = \frac{1}{\omega} \frac{E_{ji}}{E_{ii}} \frac{\pi_{\text{in},j}}{E_{jj}} \tag{2.20}$$

where the following approximation has been made $\eta_{jj} \approx \frac{\pi_{\text{in},j}}{\omega E_{jj}}$.

2.3 Advanced Statistical Energy Analysis (ASEA) using ray tracing

2.3.1 Introduction

From a wave theory perspective the SEA assumption that there is equipartion of modal energy in each subsystem requires the wave field on each subsystem to be diffuse. This may be appropriate on the source plate when there are a high number of modes per band and the modal overlap is large. However, as Langley [45] has pointed out, the angular dependence of the transmission coefficients at plate junctions leads to spatial filtering of wave field in subsystems remote from the source. Langley proposed a new modelling approach, Wave Intensity Analysis (WIA) to account for this spatial filtering [45][47].

Heron [48] proposed an alternative approach that he called Advanced Statistical Energy Analysis(ASEA) which was able to account for spatial filtering as well as power lost across

the subsystems. Although Heron outline the procedure to apply SEA to plates he focused on rods because he noted that implementation 'could well turn out to be computationally expensive'. Hence Section 2.3.4 introduces an approach to avoid this problem. ASEA has the advantage that it is easier to implement and understand from a physical perspective and it uses a ray tracing procedure which can easily be adapted to plates with cut-outs' such as windows and doorways. Yin [49] has investigated the use of ASEA on periodic ribbed plates and linear arrays of L-junctions as well as other small scale structures. In this thesis the technique is extended to systems consisting of a large number of plates in a box-like arrangement that resemble building structures.

2.3.2 Formulation of ASEA equations

Following Heron's approach the SEA power balance equations can be written in terms of the modal energy, $e_j = E_j / n_j$

$$\begin{bmatrix} M_{11} & 0 & 0 & \cdots & 0 \\ 0 & M_{22} & 0 & \cdots & 0 \\ 0 & 0 & M_{33} & \cdots & 0 \\ \vdots & \vdots & \vdots & \ddots & \vdots \\ 0 & 0 & 0 & \cdots & M_{NN} \end{bmatrix} \begin{bmatrix} e_1 \\ e_2 \\ e_3 \\ \vdots \\ e_N \end{bmatrix} + \begin{bmatrix} A_{11} & A_{12} & A_{13} & \cdots & A_{1N} \\ A_{21} & A_{22} & A_{23} & \cdots & A_{2N} \\ A_{31} & A_{32} & A_{33} & \cdots & A_{3N} \\ \vdots & \vdots & \vdots & \ddots & \vdots \\ A_{N1} & A_{N2} & A_{N3} & \cdots & A_{NN} \end{bmatrix} \begin{bmatrix} e_1 \\ e_2 \\ e_3 \\ \vdots \\ e_N \end{bmatrix} = \begin{bmatrix} \pi_{\text{in},1} \\ \pi_{\text{in},2} \\ \pi_{\text{in},3} \\ \vdots \\ \pi_{\text{in},N} \end{bmatrix} \quad (2.21)$$

where the matrix M contains the modal overlap factors of each subsystem based on the internal damping.

$$M = \begin{bmatrix} \omega n_1 \eta_1 & 0 & 0 & \cdots & 0 \\ 0 & \omega n_2 \eta_2 & 0 & \cdots & 0 \\ 0 & 0 & \omega n_3 \eta_3 & \cdots & 0 \\ \vdots & \vdots & \vdots & \ddots & \vdots \\ 0 & 0 & 0 & \cdots & \omega n_N \eta_N \end{bmatrix} \quad (2.22)$$

and the matrix A contains equivalent terms for the coupling loss factors

$$A = \begin{bmatrix} \sum_{j=2}^{N} \omega n_1 \eta_{1j} & -\omega n_2 \eta_{21} & -\omega n_3 \eta_{31} & \cdots & -\omega n_N \eta_{N1} \\ -\omega n_1 \eta_{12} & \sum_{j=1,\neq 2}^{N} \omega n_2 \eta_{2j} & -\omega n_3 \eta_{32} & \cdots & -\omega n_N \eta_{N2} \\ -\omega n_1 \eta_{13} & -\omega n_2 \eta_{23} & \sum_{j=1,\neq 3}^{N} \omega n_3 \eta_{3j} & \cdots & -\omega n_N \eta_{N3} \\ \vdots & \vdots & \vdots & \ddots & \vdots \\ -\omega n_1 \eta_{1N} & -\omega n_2 \eta_{2N} & -\omega n_3 \eta_{3N} & \cdots & \sum_{j=1,\neq N}^{N} \omega n_N \eta_{Nj} \end{bmatrix} \quad (2.23)$$

The diagonal elements of A include the sum of the CLFs.

The off-diagonal elements of *A* represent the power transmitted from subsystem *j* to subsystem *i* per unit modal energy in *j*.

In ASEA the input power in each subsystem is divided into free power *P* and fixed power *Q*, both of which are per unit modal energy. Similarly, the modal energy is divided into contributions from free (available) modal energy, *e* and from fixed (unavailable) modal energy, *d*. The latter is referred to as modal energy although it actually refers to energy dissipated as the waves propagate across the subsystem; hence it doesn't involve the subsystem modes. The free (available) modal energy corresponds to the stored modal energy in a subsystem that is considered in classical SEA.

The modal energies are related to the input power through the equations:

$$[A][e] + [M][e] = [P] \tag{2.24}$$

$$[B][e] + [M][d] = [Q] \tag{2.25}$$

where the matrix *B* contains the free power to fixed power transfers (per unit modal energy) , *Q* is the fixed power input, *P* is the free power input, and the elements of *A* contain the free power to free power transfers(per unit modal energy).

Equation 2.24 is exactly the same as eq.2.6 which means that in the absence of free to fixed power transfers (eq. 2.25) the ASEA equations are the same as the standard SEA equation.

The total modal energy in each subsystem comprises of free modal energy and fixed modal energy and can be calculated by combining eqs.2.24 and 2.25 to give

$$[e] + [d] = [M]^{-1}([Q] + [R]) \tag{2.26}$$

where the matrix R is given by

$$R = ([M] - [B])([M] + [A])^{-1}[P] \tag{2.27}$$

When rain-on-the-roof excitation is applied to the structure the fixed power input *Q* is zero [48] and the power balance equations may be written in the form:

$$([M] + [A])([M] - [B])^{-1}[M]([e] + [d]) = [P] \tag{2.28}$$

This is an SEA-like relationship between the total modal energy in each subsystem and the power input; hence.

$$[A_{sea}]([e] + [d]) = [P] \tag{2.29}$$

where the advanced SEA matrix $A_{sea}$is defined as

$$[A_{sea}] = (M + A)(M - B)^{-1}M \tag{2.30}$$

The elements of *A* and *B* are determined using an iterative ray tracing algorithm to calculate the power exchanges between subsystems as proposed by Heron[48]. The ASEA solution will converge on a final value when all the most significant power exchanges between subsystems have been accounted for. This will occur at a finite iteration number which is here defined as ASEA *N*. All ASEA iterations between zero and N are labelled ASEA*0* to ASEA *N* to indicate the number of times power has been traced across the source subsystem.

The A and B matrices are inserted into eq.2.30 to give the ASEA matrix which is then inverted to give the total modal energies of each subsystem in response to a known rain-on-the-roof power input vector [*P*] using eq. 2.29.

2.3.3 ASEA in systems of connected plates

ASEA can be implemented using the computational procedure outlined schematically in Figure 2.1. The ASEA computation firstly requires the formation of an ASEA model which is similar to the formation of an SEA model. The built-up structure is sub-divided into subsystems that are characterised by general plate properties such as thickness, density, junction length and quasi-longitudinal wave velocity. However, the ASEA model must also use a global coordinate system in order to describe the relative position of the plates so as to enable ray tracing around the structure.

The ASEA calculation can then be described in a series of five steps (see Figure 2.2) in which the power flow is tracked around the structure. The free and fixed powers added to A and B matrices respectively at each stage are indicated in Figure 2.2. The ASEA calculation requires that these steps are repeated for each angle of incidence, on each section of the perimeter of every subsystem in the structure.

In other work on ASEA [49,50] the power flow has been tracked using a ray tracing procedure in which the initial subsystem perimeter was divided into infinitesimal sections. However, applying this process to large building structures would result in large computation times. For example, for an isolated L-junction comprised of two plates, the number of rays doubles each time the rays intersect the junction line, and for an isolated T-junction the

number of rays will treble. An alternative method which shall be referred to as ‘beam tracing’ is introduced in this thesis to reduce the calculation time by reducing the number of rays at the start of the ASEA procedure. Rather than divide the perimeter into sections dL and carry out a numerical integration of over the perimeter of the source plate as was described in reference[50] it is more efficient to divide the source plate into its constituent edges and use a beam tracing approach to determine these integrals. Hence the tracing of individual rays at each segment dL along a single edge of the source plate is replaced by a pair of rays at each end of the edge which defines a ‘beam’ of rays (see Figure 2.1).

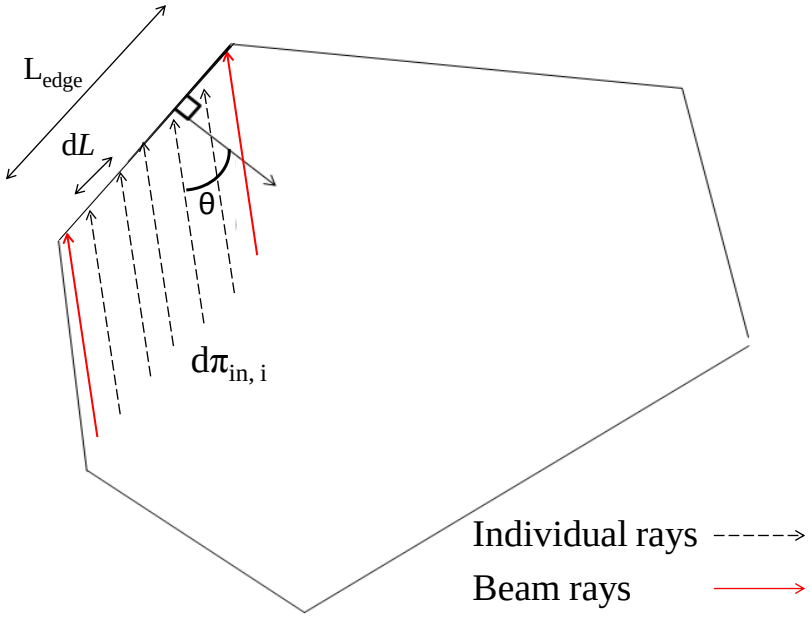

Figure 2.1. Replacement of individual rays with a single ‘beam’

However there will still be an exponential growth in the number of beams with increasing ASEA iteration number. This occurs because transmitted and reflected beams are generated each time a beam ‘illuminates’ a junction. The ASEA solution converges when the number of ASEA iterations approaches the total number of subsystems in the model, hence, for structures that contain many subsystems there is a need to reduce the growth in the number of beams with ASEA iteration number otherwise the total number of beams will rapidly become unmanageable. This is achieved in Step 5 of the calculation procedure in which beams that are incident on a junction line with the same angle of incidence are combined into a single beam.

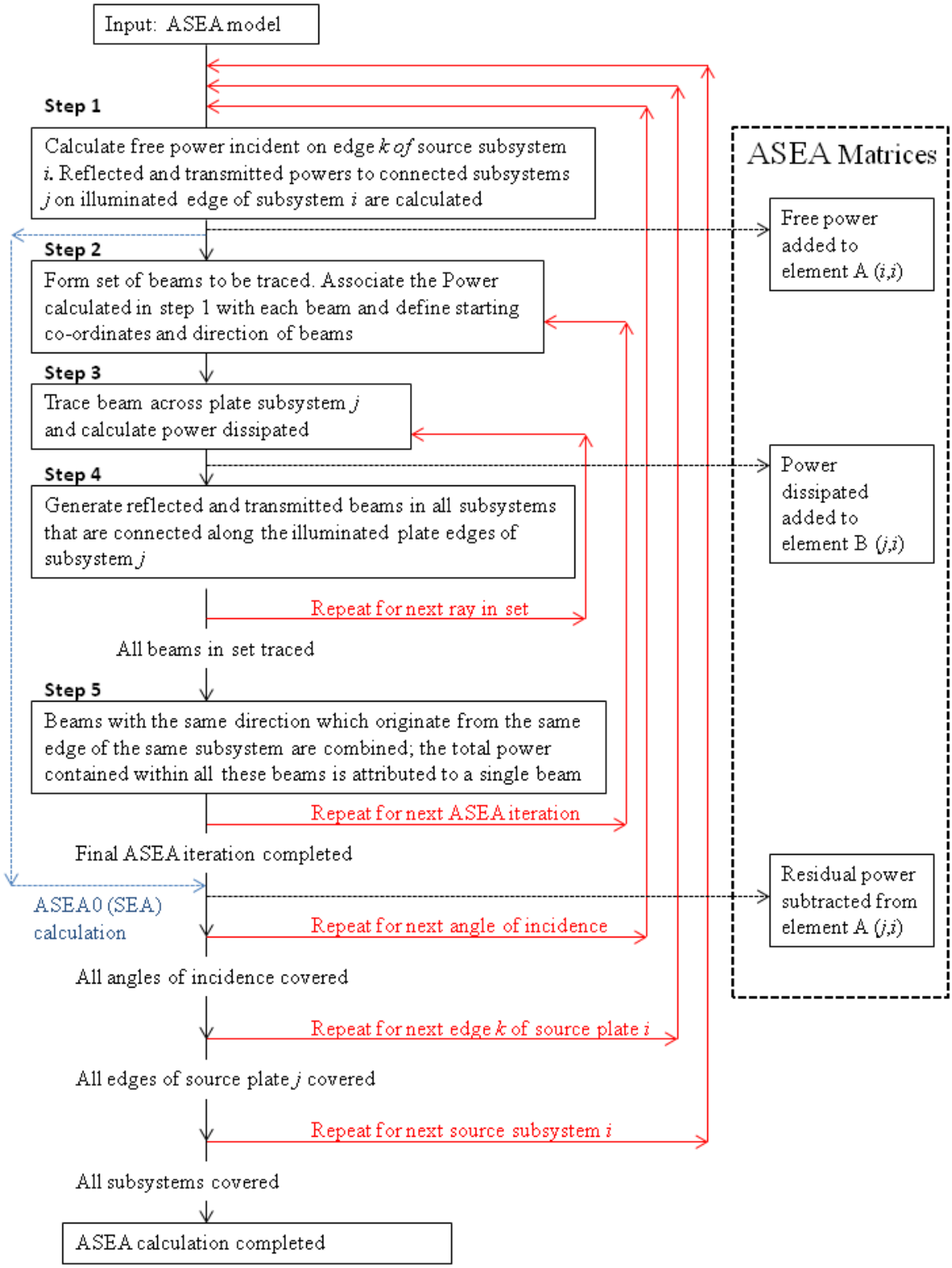

Figure 2.2. Schematic diagram of the ASEA calculation.

In this section the construction of an ASEA model will be described as well as details of the calculation Steps 1 to 5 shown in figure 2.2.

The ASEA model consists of a set of subsystems, for each subsystem the physical properties and plate dimensions are catalogued and a coordinate system is defined to position the plate subsystem relative to the other subsystems in the model through a global coordinate system (see Figure 2.3).

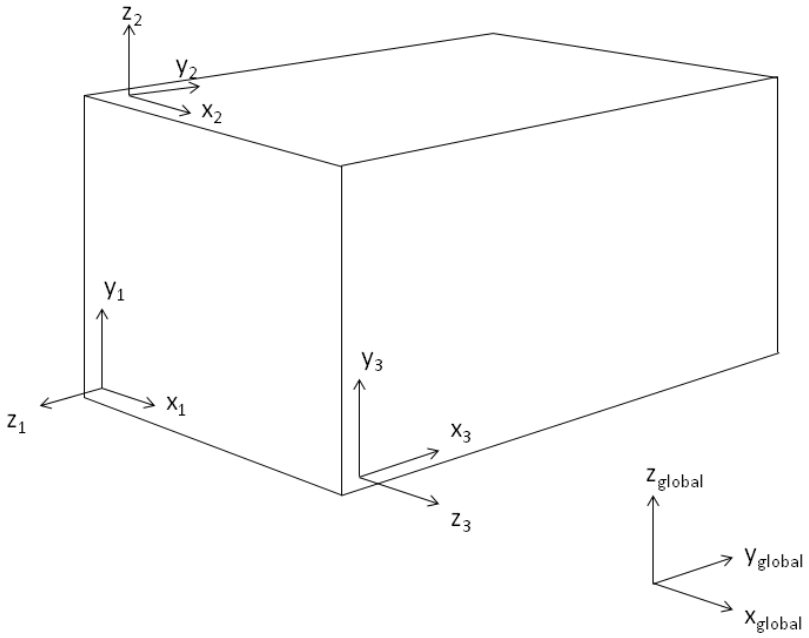

Figure 2.3. An example of the global and local coordinate systems

Transformation matrices which describe rotations and translations between the global and local (i.e. subsystem) coordinates systems are used to track the beams as they are transmitted from one subsystem to another. This process is made easier if a third set of coordinates called ‘edge coordinates’ are defined in which the x-axis lies along the direction of the junction line. Transformation from the subsystem to the edge coordinates simplifies the application of Snell’s law for the transmission of beams between plates since when using these coordinates the x-component of the transmitted beam can be set equal to the x-coordinate of the incident beam. The component of the transmitted beam perpendicular to the junction line can then be calculated using eq 2.31

$$k_y = \sqrt{(k_B)^2 \ - (k_x)^2} \tag{2.31}$$

Once the ASEA model has been developed the main calculation procedure can commence. This is outlined as follows:

Step 1. **The initial free power input at angle θ to the segment L normal is added to the element**

Assuming a diffuse field on plate subsystem i due to the initial free power input the power incident on a section of the plate perimeter L per unit modal energy e_i within a narrow angular range $\mathrm{d}\theta$ is given by

$$\frac{\mathrm{d}\pi_{in,i}}{e_i} = \frac{k_B^i L}{2\pi} cos\theta \mathrm{d}\theta \qquad 2.32)$$

This initial power is added to element A_{ii}. The transmitted and reflected power can then be calculated by multiplying eq. 2.32 by the appropriate intensity coefficient (see section 3.2.2). Note that SEA or ASEA0 does not use steps 2 to 5.

Step 2. **Generate a set of initial beams associated with each of the transmitted or reflected powers calculated in step 1 or from the previous ASEA iteration**

The 'set' of beams is a two dimensional indexed array containing information required to trace the beams.

Step 3. **Trace the beam across the subsystems**

When a beam travels across a subsystem, different sections of the beam can 'illuminate' different edges and they will generally travel different distances before reaching the perimeter of the plate. The calculation procedure is now explained using an example. Consider an assembly of rectangular plates shown in Figure 2.3. The two rays comprising the beam travel from points a and c of one edge and intersect the perimeter again at points f and d respectively. The ray travelling from a to f intersects edge 1 and the ray travelling from c to d intersects edge 2. Point e is the intersection point between the lines representing edge 1 and edge 2. Point b is the intersection point between the line representing edge 3 and a line with the same slope as the ray that passes through the point e. When all points have been determined the beam is divided into two sections. The fraction of the

initial power π_{start} entering each section is determined by the ratio $\frac{L_1}{L_1+L_2}$. The fraction of power lost in each section is given by

$$D = \frac{\exp\left(-\frac{\omega\eta_i}{c_{\text{g,i}}} d_{\min}\right) - \exp\left(-\frac{\omega\eta_i}{c_{\text{g,i}}} d_{\max}\right)}{\frac{\omega\eta_i}{c_{\text{g,i}}} d_{\max} - \frac{\omega\eta_i}{c_{\text{g,i}}} d_{\min}} \tag{2.33}$$

where $d_{\min}$is the minimum distance and $d_{\max}$is the maximum distance between the initial edge and the intersected edge in each section. The fraction of power lost in each section is added to element B_{ji}. The remaining power is available for further tracking.

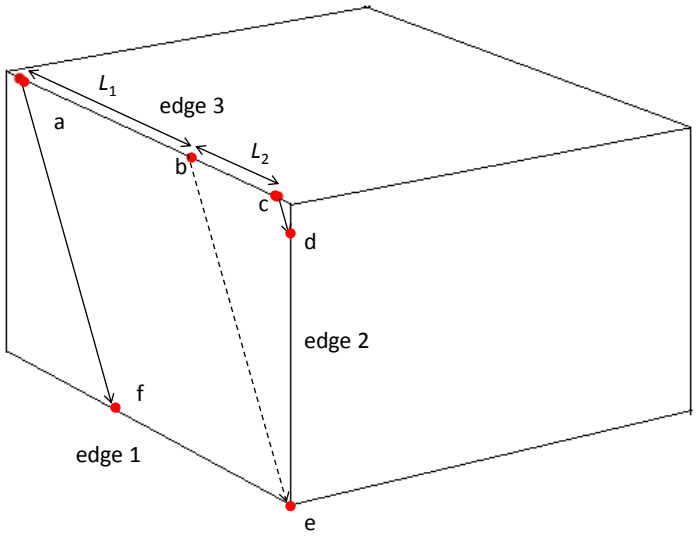

Figure 2.3. Assembly of three rectangular plate subsystems showing sections of the beam

Step 4. **Generate transmitted and reflected beams along illuminated edges of subsystem *j***

The power incident on each of the plate edges is calculated and the transmitted and reflected powers can be found by applying the appropriate intensity transmission (or reflection) coefficient.

The ASEA procedure returns to Step 3 until all beams in the set have been traced.

Step 5. **Combine all outward going beams created in Step 4 that originate from the same edge of the same subsystems with the same heading into a single beam**

The issue of an exponentially increasing number of rays is addressed by combining beams within the same subsystem that emanate from the same edge with the same heading into a single beam. That is, the total sum of all the power exchanges into a subsystem, leaving a common boundary with the same heading is taken before returning to Step 2 for the next ASEA iteration. When processing the final ASEA iteration the power of the outgoing rays in subsystem *j* that is generated in Step 4 is treated as 'residual power' and added to element A_{ji}.

The initial coordinates of the resulting beam are an average value of the initial coordinates of each pair of rays in the set of beams that are weighted by the initial power of the beam. For example, consider the beam shown in Figure 2.3 the initial coordinates of the two rays are [0,a] and [0,c]. This results in a set of *N* beams each emanating from the same edge as these rays with the same heading, the average coordinates of each ray, $[0, \bar{a}]$ and $[0, \bar{c}]$, in the beam are given by:

$$[0, \bar{a}] = \frac{1}{\sum_{k=1}^{N} \pi_{\text{start},k}} \sum_{k=1}^{N} \pi_{\text{start},k}[0, a_k] \tag{2.34}$$

$$[0, \bar{c}] = \frac{1}{\sum_{k=1}^{N} \pi_{\text{start},k}} \sum_{k=1}^{N} \pi_{\text{start},k}[0, c_k] \tag{2.35}$$

When the subsystems represent rectangular plates this considerably reduces the total number of beams with high ASEA iteration numbers because it combines all the beams in each subsystem which repeat the same pattern of reflections into a single equivalent beam.

When the final ASEA iteration number has been completed Steps 1 to 5 are repeated for the next angle of incidence. Once all angles of incidence have been covered the process is repeated for all angles of incidence on the next edge of the subsystem perimeter. This process

is repeated on the next subsystem for all angles of incidence, on all edges comprising the perimeter of the subsystem, until all subsystems in the model have been covered.

2.4 Finite Element Methods (FEM)

2.4.1 Introduction

FEM is a numerical method that is commonly used structural dynamics. It is particularly useful when dealing with complex structures where analytical methods are difficult to apply. The technique relies on discretization of the structure into a set of elements connected at nodal points which forms an element mesh over the structure. The response within each element is approximated by a shape function which is used to relate the force and moments at the nodes of the element to the displacement and rotations[57, 58].

In discretized form the equation of motion of the structure may be written

$$[M]\{\ddot{\boldsymbol{\varepsilon}}\} + [C]\{\dot{\boldsymbol{\varepsilon}}\} + [K]\{\boldsymbol{\varepsilon}\} = \{F\} \tag{2.36}$$

where $\boldsymbol{\varepsilon}$ is the vector containing the degrees of freedom at the nodes, M is the mass matrix, K is the stiffness matrix, C is the damping matrix and F is the vector of forces applied at the mesh nodes.

There are two methods for solving equation 2.36 for the case of the steady state harmonic excitation [57, 59]. The first is to solve the response of the system directly in terms of the degrees of freedom which is called the direct method. The second determines the modes of the free system and calculates the response in terms of the modal coordinates.

These methods both give a single deterministic solution for the exact boundary conditions and physical properties assigned to structure. An accurate solution requires at least 6 nodes per free bending wavelength[3] . Due to finite computational resources this restricts the analysis to relatively small structures where the bending wavelength is small compared to the structure.

2.4.2 Monte-Carlo FEM (MCFEM)

In the building structures investigated the walls are made from a different material than the floors and the ground level floors have a frequency-dependent loss factor to account for the high radiation losses into the earth. In this case the most suitable method to solve eqn.2.36 is the direct method[59] which was done using ABAQUS v6.10 software on the high performance cluster at the University of Liverpool.

In the frequency region of interest the plates in the structure are well described by STRI3 elements which are three node triangular elements that use thin plate theory[58]. The element size was set so that at least 10 nodes were assigned per free bending wavelength (at 1000Hz) in all plates. The boundary nodes between plates were constrained to having only rotational degrees of freedom with translational displacement set to zero. This allows the transmission of bending waves only at the plate junctions[33].

Each plate can be assigned a critical damping ratio approximated using Rayleigh damping. In terms of the Rayleigh coefficients α_R and β_R the critical damping ratio is:

$$\gamma = \frac{\alpha_R}{2\omega} + \frac{\beta_R \omega}{2} \tag{2.37}$$

The critical damping is simply related to the loss factor[3]; hence curve fitting is used to determine the Rayleigh coefficients for each third octave band.

To approximate the SEA condition of equipartion of modal energy and incoherent modal response statistically-independent point forces with unit magnitude and random phase are applied in a direction normal to the surface to the unconstrained nodes of the source plate. This type of excitation is commonly referred to as rain-on-the-roof (ROTR).

The total power input is obtained by summing the real part of the product of the complex force applied in the transverse direction $\boldsymbol{F}_n$, and transverse velocity $\boldsymbol{v}_n$ at node n for each unconstrained node in the source subsystem.

$$\pi_{\text{in}} = \frac{1}{2}\sum_{n=1}^{N} Re\{\boldsymbol{F}_n \boldsymbol{v}_n^*\} = \frac{1}{2}\sum_{n=1}^{N} \text{Im}\{\boldsymbol{F}_n\}\text{Re}\{\boldsymbol{\varepsilon}_n\} - \text{Re}\{\boldsymbol{F}_n\}\,\text{Im}\{\boldsymbol{\varepsilon}_n\} \tag{2.38}$$

where N is the total number of unconstrained nodes in the source subsystem and $\boldsymbol{\varepsilon}_n$ is the transverse displacement at node n.

The primary variable of interest is the total energy in each plate subsystem, $E_j$which is related to the out-of-plane nodal displacement through the equation

$$E_j(\omega) = 2E_{\text{k},j} = \omega^2 \left[\frac{1}{2}\sum_{n=1}^{N} m_n |\varepsilon_n|^2\right] \tag{2.39}$$

where the sum is taken over all unconstrained nodes in subsystem' *j'*, m_n is the mass associated with node *n*, ε_n is the out-of-plane displacement of node *n*. $E_{k,j}$ is the kinetic energy of the plate subsystem.

The total power dissipated in the structure is given by a sum over the power dissipated in each plate subsystem.

$$\pi_{\text{diss}} = \sum_{j=1}^{N_s} \omega \eta_j E_j \tag{2.40}$$

Conservation of power is used to test the error of the FEM mesh. The mesh error is defined as

$$\text{mesh error } = \frac{\pi_{\text{in}} - \pi_{\text{diss}}}{\pi_{\text{in}}} \times 100 \tag{2.41}$$

To address the issue of uncertainty in the SEA ensemble the Young's modulus of the plates in the structure is randomly selected from a Normal distribution. Solving for the case of a particular set of ROTR excitation applied to a particular plate in the structure gives a set of subsystem energies and input powers. Repeating the process a number of times using a different set of Young's modulus and ROTR forces generates an ensemble of subsystem energies. The subsystem energies and input powers must be averaged between the upper and lower limits of one-third octave bands to provide a baseline against which other methods are compared. For *D* samples equally spaced in frequency the one-third octave band energies are given by:

$$E_{\frac{1}{3}\text{oct},j} = \sum_{k=1}^{D} E_j(\omega^k) \tag{2.42}$$

where $E_j(\omega^k)$ is the energy in subsystem '*j'* at a sample frequency ω^k.

The level difference between source subsystem *i* and receiver subsystem *j* for a single ensemble member *n* is defined as:

$$D_{\text{E},ij}^n = 10 \lg \left(\frac{E_{\frac{1}{3}\text{oct},i}}{E_{\frac{1}{3}\text{oct},j}} \right) \tag{2.43}$$

The ensemble average level difference is defined as an arithmetical average of the dB values from the ensemble results:

$$D_{\mathrm{E},ij} = \frac{1}{N_{\mathrm{ensbl}}} \sum_{n=1}^{N_{\mathrm{ensbl}}} D_{\mathrm{E},ij}^{n} \tag{2.44}$$

where N_{ensbl} is the total number of ensemble members.

The 95% confidence limits associated with this energy level difference is

$$CL_{95\%} = \left(\frac{\sigma^2}{N_{\mathrm{ensbl}}}\right)^{1/2} t_{0.975,\nu} \tag{2.45}$$

where σ is the standard deviation of $D_{\mathrm{E},ij}^{n}$ for the ensemble.

2.5 Conclusions

This chapter introduced SEA, ASEA and FEM that will be used to model sound transmission through heavyweight building structures in this thesis.

The framework of Statistical Energy Analysis was introduced from which it was shown how Experimental SEA can be derived. A form of ESEA will be used in Chapter 3 to determine CLFs between finite plates in L, T and X junction configurations. ESEA will be used in conjunction with FEM in Chapter 6 to investigate non-adjacent CLFs between subsystems in a five-plate structure.

ASEA was introduced as a potential solution to deal with spatial filtering, non-diffuse vibration fields and propagation losses as waves travel across subsystems. This requires ray tracing, hence an efficient ray tracing procedure was proposed to allow simulations of large buildings. ASEA will be used in Chapters 7 to investigate the effects of spatial filtering and non-diffuse vibration fields in heavyweight building.

An overview was given of Finite Element Methods and the Monte-Carlo approach that will be used extensively in Chapters 5, 6 7 and 8 as a form of numerical experiment for comparison with predictions using SEA and ASEA.

Chapter 3 Theory – Vibration transmission across plate junctions

3.1 Introduction

All plates considered in this thesis are assumed to be isotropic and homogeneous (i.e. contain no inclusions or stiffeners) and only 'thin plate' bending wave theory is considered in that the effects of rotatory inertia and shear deformation are not included. The later features become important when the free bending wavelength is within an order of magnitude of the thickness of the plate[20, 60]. An indication of the upper limit for the use of pure bending wave theory is given by Cremer *et al*. [20]

$$\lambda_B = 6h$$

In the audio frequency range, typical heavyweight walls and floors support three wave types, bending, transverse shear and quasi-longitudinal waves. Transverse shear and quasi-longitudinal waves are collectively known as in-plane waves as the wave motion is predominantly in the plane of the plate. In terms of sound radiation, the most important of these are bending waves [3] since these waves determine the out-of-plane response of the plate. However, in large built-up structures there is conversion between in-plane and bending waves at plate junctions which plays a significant role in the transmission process[9]. For the heavyweight building structures investigated in this thesis many of the component plates do not support in-plane modes in the frequency range of interest; hence the contribution from theses waves to the structure-borne sound transmission is not considered. The problem then reduces to focus on the transmission of bending waves across plate junctions.

The methods used to determine the structural coupling can be categorised as wave and modal approaches. Wave approaches typically treat the coupled plates as semi-infinite with the aim of calculating the ratio of the transmitted power to the incident power per unit length of junction for an obliquely incident propagating wave.

Modal approaches seek to calculate the coupling loss factor of the junction through the calculation of the standing wave patterns or mode shapes of the plates. Two modal methods are investigated here, the first method is called the receptance method[61, 62] and is based on the local modes of the plate 'substructures'. The second is based on the global modes of the junction and was developed by Guyader *et al* [18, 36]. The calculation of the global modes

allows Energy Influence Coefficients (EIC's) to be determined using ideal ROTR loading conditions on the source plate. The EIC matrix can be inverted to give the CLF matrix.

3.1.1 Bending waves on a thin homogeneous plate

Bending waves on a thin isotropic plate are governed by the equation

$$B\nabla^4\varepsilon(x,y,t) + \rho h\frac{\partial^2}{\partial t^2}\varepsilon(x,y,t) = 0 \tag{3.1}$$

where h is the plate thickness, ρ is the mass density of the plate and ε is the displacement in the positive z direction. B is the bending stiffness per unit width given by

$$B = \frac{Eh^3}{12(1-\nu^2)} \tag{3.2}$$

where E is the Young's modulus and ν is the Poisson's ratio.

The fourth order differential operator is defined

$$\nabla^4 = \frac{\partial^4}{\partial x^4} + \frac{\partial^4}{\partial y^4} + 2\frac{\partial^2}{\partial y^2}\frac{\partial^2}{\partial x^2} \tag{3.3}$$

Assuming a harmonic time dependence $\sim\exp(j\omega t)$ gives

$$B\nabla^4\varepsilon(x,y) - \rho h\omega^2\varepsilon(x,y) = 0 \tag{3.4}$$

Substituting the trial function $\exp(k_b.r)$ gives a solution to this equation which is valid provided that the following equation is satisfied.

$$k_b^4 = \frac{\rho h}{B}\omega^2 \tag{3.5}$$

In the notation used here the wave field at a point r is given by

$$\exp(jk_b.r) = A\exp(jk_x'x)\exp\left(jk_y y\right) \tag{3.6}$$

where k_y is real and A is a constant.

Substituting this into the bending wave Eq.3.1 gives

$$\left((k_x')^2 + k_y^2\right)^2 - \frac{\rho h}{B}\omega^2 = 0 \tag{3.7}$$

Solving for $k_x^{'}$ yields four possible solutions. The first two solutions are imaginary and are given by eq.3.8a

$$k_x^N = \pm j\sqrt{\omega\sqrt{\frac{\rho h_p}{B}} + k_y^2} \tag{3.8a}$$

These represent forward and backward propagating evanescent (or near-field) waves with the wavenumber in the x-direction $k_{\mathrm{N},x}$. The second two solutions are given by equation eq.3.8b

$$k_x = \pm\sqrt{\omega\sqrt{\frac{\rho h_p}{B}} - k_y^2} \tag{3.8b}$$

The wavenumbers can represent either

1) evanescent waves or

2) forward and backward propagating travelling waves depending on whether the term under the square root is negative or positive respectively.

In general the out-of-plane displacement will be a combination of all the possible wave types:

$$\begin{aligned}\varepsilon(x,y) = \{&A\exp(-jk_x x) + B\exp(jk_x x) + C\exp(-k_x^N x) \\ &+ D\exp(k_x^N x)\}\exp(jk_y y)\end{aligned} \tag{3.9}$$

The angular rotation of the plate cross section around the *y*-axis is defined as

$$\phi_y = \frac{\partial \varepsilon}{\partial x} \tag{3.10}$$

with a similar expression for the angular rotation around the *x*-axis

$$\phi_x = \frac{\partial \varepsilon}{\partial y} \tag{3 11}$$

The moment around the *x*-or *y*-axis is related to the transverse displacement by [20]

$$M_x = B_p\left(\frac{\partial^2 \varepsilon}{\partial y^2} + \nu\frac{\partial^2 \varepsilon}{\partial x^2}\right), M_y = B_p\left(\frac{\partial^2 \varepsilon}{\partial x^2} + \nu\frac{\partial^2 \varepsilon}{\partial y^2}\right) \tag{3. 12}$$

3.1.2 Boundary conditions

For pure bending wave transmission the boundary condition at the interface between plates is ideally the pinned condition. This ensures the displacement/velocity is zero in the three translation coordinate directions along the junction line to allow the propagation of bending waves and prevent the transmission of in-plane waves. The continuity condition requires that the gradient of the displacement is continuous across the interface between the plates. This requires that the trace wavelength along the junction line is the same in all plates and that the angular rotation (when referenced to a common system of coordinates) is equal in all plates.

The co-ordinate systems of the plates is chosen to be consistent with the sign convention commonly used in the literature [7, 20, 36, 63]. In this convention the system of coordinates are set up to ensure that a positive shear force (or moment) acting on the junction beam is countered by another shear force (or moment) directly opposite the junction beam with opposite sign. In the case of the pinned boundary the junction beam is completely rigid and has zero mass, its introduction here is solely for the purpose of orientating the plates in the junction. Positive displacement ε is defined in the positive z–direction and a positive angular rotation ϕ is defined as an anti-clockwise rotation from the x-or y-axis as shown in Figures 3.1. The origin of the coordinate system in each plate is centred on the junction beam although Figure 3.1 show a displaced set of coordinates for ease of interpretation.

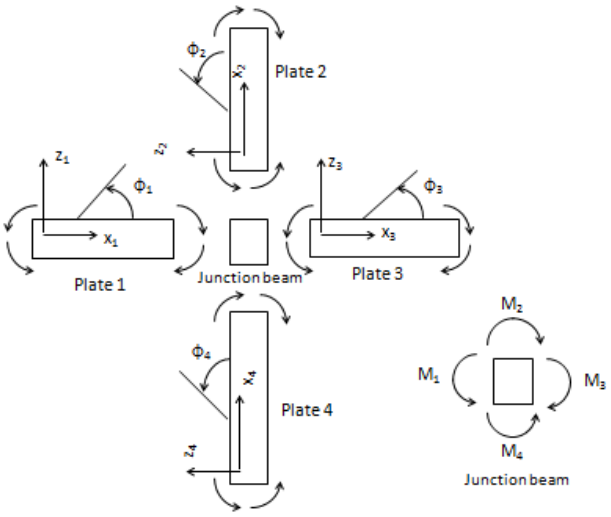

Figure 3.1. Moments acting on the junction beam, showing the common sign convention for plates in the junction.

Using this system of coordinates the boundary conditions at the junction interface can be summarised as:

Zero displacement on the junction boundary

$$\varepsilon_1 = \varepsilon_2 = \varepsilon_3 = \varepsilon_4 = 0 \tag{3.13}$$

Resultant moment acting on the junction beam is zero

$$M_1 - M_2 - M_3 + M_4 = 0 \tag{3.14}$$

The condition that the displacement is zero along the length of the junction line means the first (and hence the second) order derivative with respect to y is zero at the junction. The moment acting on the junction beam from plate i is then given by:

$$M_y^i = B_i\left(\frac{\partial^2 \varepsilon_i}{\partial x_i^2} + \nu\frac{\partial^2 \varepsilon_i}{\partial y_i^2}\right) = B_i\left(\frac{\partial^2 \varepsilon_i}{\partial x_i^2}\right) \tag{3.15}$$

The rotational displacement must be continuous across the plate boundary

$$\frac{\partial \varepsilon_1}{\partial x_1} = \frac{\partial \varepsilon_2}{\partial x_2} = \frac{\partial \varepsilon_3}{\partial x_3} = \frac{\partial \varepsilon_4}{\partial x_4} \tag{3.16}$$

Snell's Law for elastic waves requires that the trace wavelength along the junction line is the same in all plates. In the system of coordinates defined here this is equivalent to equating the y component of the wavenumber in each plate.

$$k_{y,1} = k_{y,2} = k_{y,3} = k_{y,4} \tag{3.17}$$

In finite plates, boundary conditions must be applied not only along the junction line between plates but the remaining external edges of the plates as well. For plates in structures where only bending wave transmission is considered the pinned boundary condition is the most appropriate choice for these external edges [33]. This results in a similar set of conditions as for the interface (eq.3. 13 – eq.3.16) however in the absence of any other plates connected along the external edge the resultant moment reduces to the moment generated by a single plate and the restriction on the rotational displacement (eq.3.16) is not required.

3.2 Semi-infinite plates

3.2.1 Transmission between semi-infinite plates

In the case of semi-infinite plates the junction line extends from minus infinity to infinity along the y axis and is located at x=0. The only wave incident on the boundary is a single propagating wave with unit amplitude, the unknown values are the transmitted near field and propagating waves in each plate. The procedure used here outlines that given by Craik[7] and Cremer *et al* [20].

For plate 1 with the incident wave the out-of-plane displacement is given by

$$\varepsilon_1 = \left\{\exp\left(-jk_{x,1}x_1\right) + T_1 \exp\left(jk_{x,1}x_1\right) + T_{\mathrm{N},1} \exp\left(k_{x,1}^N x_1\right)\right\} \exp\left(jk_{y,1}y_1\right) \qquad (3.18)$$

Using the condition that the wavenumber along the junction boundary is the same in all plates (eq.3.17), expressions for the out-of-plane displacement in the remaining plates are obtained.

For plate 2

$$\varepsilon_2 = \left\{T_2 \exp\left(-jk_{x,2}x_2\right) + T_{\mathrm{N},2} \exp\left(-k_{x,2}^N x_2\right)\right\} \exp\left(jk_{y,1}y_1\right) \qquad (3.19)$$

For plate 3

$$\varepsilon_3 = \left\{T_3 \exp\left(-jk_{x,3}x_3\right) + T_{\mathrm{N},3} \exp\left(-k_{x,3}^N x_3\right)\right\} \exp\left(jk_{y,1}y_1\right) \qquad (3.20)$$

For plate 4

$$\varepsilon_4 = \left\{T_4 \exp\left(jk_{x,4}x_2\right) + T_{\mathrm{N},4} \exp\left(k_{x,4}^N x_4\right)\right\} \exp\left(jk_{y,1}y_1\right) \qquad (3.21)$$

In the above equations the near field wave number in the x direction $k_{\mathrm{N},j}$ is given by eq.3.8a and the travelling wave $k_{x,j}$ is given by eq.3.8b.

The condition that the trace wavenumber $k_{y,j}$ is the same in all the plates gives the travelling wavenumber in plate *j*, $k_{x,j}$ as:

$$k_{x,j} = \pm\sqrt{\omega\sqrt{\frac{\rho_j h_j}{B_j}} - k_{y,1}^2} = \pm\sqrt{k_{b,j}^2 - k_{y,1}^2} \tag{3.22}$$

There is a cut-off value for the travelling wavenumber when $k_{y,1}^2$ is greater than the square of the bending wavenumber $k_{b,j}$ in the receiving plate. In this case $k_{x,j}$becomes imaginary and represents the decay constant of a nearfield wave originating from the junction boundary. In this case substitution of $-k_{\mathrm{x,j}}$ into eqs.3.19 to 3.21 will give the correct solution as the wave field must approach zero as the distance from the boundary approaches infinity.

Applying the boundary conditions, eq.3.13 to 3.17, gives a matrix expression which can be solved to give the amplitude transmission coefficients for each plate [7].

$$\begin{bmatrix} -k_{x,1}^N + jk_{x,1} & -k_{x,2}^N + jk_{x,2} & 0 & 0 \\ -k_{x,1}^N + jk_{x,1} & 0 & -k_{x,3}^N + jk_{x,3} & 0 \\ -k_{x,1}^N + jk_{x,1} & 0 & 0 & k_{x,4}^N - jk_{x,4} \\ B_1 k_{b,1}^2 & -B_2 k_{b,2}^2 & -B_3 k_{b,3}^2 & -B_4 k_{b,4}^2 \end{bmatrix} \begin{bmatrix} T_1 \\ T_2 \\ T_3 \\ T_4 \end{bmatrix} = \begin{bmatrix} k_{x,1}^N + jk_{x,1} \\ k_{x,1}^N + jk_{x,1} \\ k_{x,1}^N + jk_{x,1} \\ -B_1 k_{b,1}^2 \end{bmatrix} \tag{3.23}$$

In cases where $k_{y,1}^2 > k_{b,j}^2$, $-k_{x,j}$ is substituted for $k_{x,j}$ into eq.3.23. The standard notation used in the literature[7] is to substitute $k_{x,1} = k_{b,1}\cos\theta_1$into the above. The transmission coefficients are then given as a function of the angle of incidence from the junction normal, θ_1.

In buildings the most common intersections between walls and floors occur in X, T or L junction configuration. An equivalent matrix can be generated for the T (or L) junction by removing the 3rd row and 4th column (or the 2nd row, 3rd row and 3rd column and 4th column in addition for the L junction) from equation (3.23). Further simplifications are possible when pairs of in-line plates have the same properties (for example when plates 1 and 3 or plates 2 and 4 have identical properties) results for the amplitude transmission coefficients in this specific case are given by Craik[7].

3.2.2 Power transmission coefficients between semi-infinite plates

Of particular interest in SEA and ASEA are the power transmission coefficients which relate the total transmitted power to the incident power per unit length of junction. This coefficient is related to the amplitude transmission coefficient through the structural intensity. The structural intensity is a vector quantity which points in the direction of wave propagation (see Figure 3.2).

The magnitude of the structural intensity is related to the energy density ϵ through the group velocity

$$I = c_{\mathrm{g}}\epsilon = c_{\mathrm{g}}\rho h\omega^2\langle\epsilon^2\rangle \tag{3.24}$$

The units of the structural intensity are in Wm^{-1} wheras the energy density has units of Jm^{-2}.

Substituting the contribution to the total out of plate displacement from the incident wave into the eq.3.24 gives the intensity of the incident wave in plate *i*.

$$I_{\mathrm{inc,i}} = c_{\mathrm{g},i}\rho_i h_i\omega^2 \tag{3.25}$$

Similarly by substituting the out of plate displacement in the receiver plate *j* into Eq.3.24 and ignoring the contribution from the near-field wave gives the intensity of the transmitted wave in plate *j* .

$$I_{\mathrm{tran},j} = c_{\mathrm{g},j}\rho_j h_j\omega^2\left|T_j\right|^2 \tag{3.26}$$

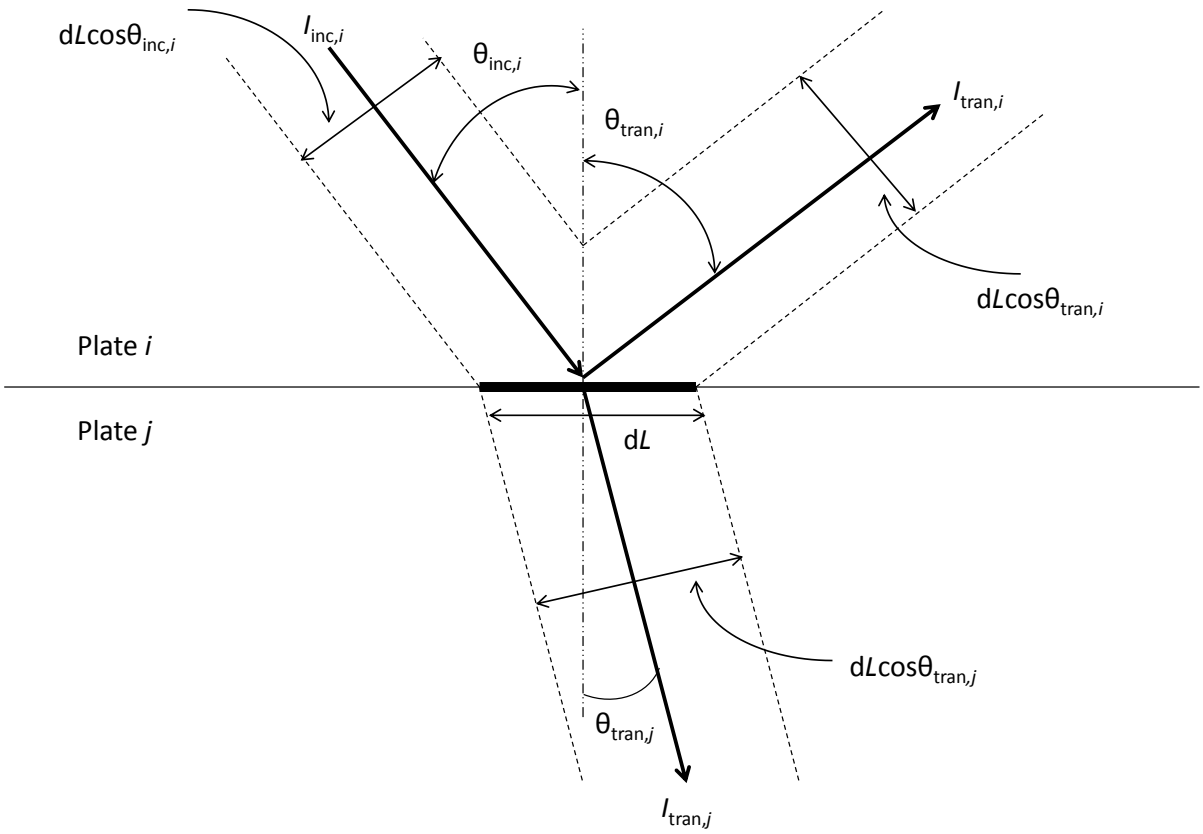

Figure 3.2. A sketch showing the relation between the transmitted power, reflected power and incident power to the structural intensity in plate *i* and plate *j*.

The total power incident onto a section of the junction line dL is obtained by projecting the intensity vector $\boldsymbol{I}$ onto the junction line. The power balance across the junction boundary ensures that the incident power or energy flux incident onto the boundary equals the energy flux flowing out of the boundary (see Figure 3.2.2.1). For the X junction described in Section 3.2.1 the power balance relation gives:

$$I_{\mathrm{inc},i} dL \cos\theta_{\mathrm{inc},i} = \sum_{j=2}^{4} I_{\mathrm{tran},j} dL \cos\theta_{\mathrm{tran},j} + I_{\mathrm{tran},i} dL \cos\theta_{\mathrm{tran},i} \tag{3.27}$$

Where $\theta_{\mathrm{tran},j}$is related to the angle of incidence in plate i, $\theta_{\mathrm{inc},i}$, through Snell's Law and $\theta_{\mathrm{tran},i}$ is related to $\theta_{\mathrm{inc},i}$ through the law of specular reflection.

Dividing through by the LHS gives:

$$1 = \sum_{j=2}^{4} \frac{I_{\text{tran},j} dL \cos\theta_{\text{tran},j}}{I_{\text{inc},i} dL \cos\theta_{\text{inc},i}} + \frac{I_{\text{tran},i} dL \cos\theta_{\text{tran},i}}{I_{\text{inc},i} dL \cos\theta_{\text{inc},i}} \tag{3.28}$$

Substituting for $I_{tran,j}$ and $I_{tran,i}$ into Eq.3.28 gives the following relation

$$1 = \sum_{j=2}^{4} \frac{c_{g,j}\rho_j h_j}{c_{g,i}\rho_i h_i} \frac{cos\theta_{t,j}}{cos\theta_i} |T_j|^2 + |T_i|^2 \tag{3.29}$$

The power transmission coefficient [20]or transmittance [64] is defined as the ratio of the transmitted energy flux to the incident energy flux and is related to the amplitude transmission coefficients by

$$t_{ij}(\theta_{inc,i}) = \frac{I_{\text{tran},j} \cos\theta_{\text{tran},j}}{I_{\text{inc},i} \cos\theta_{\text{inc},i}} = \frac{c_{\text{g},j}\rho_j h_j}{c_{\text{g},i}\rho_i h_i} \frac{\cos\theta_{\text{tran},j}}{\cos\theta_{\text{inc},i}} |T_j|^2 \tag{3.30}$$

3.3 Finite plates – Global mode approach

3.3.1 Determination of global Eigenvalues and eigenfunctions

The global mode of the junction is here defined as a solution to the bending wave equation (eq.3.1) which satisfies all the external and internal boundary conditions (eqs.3.13 to eq.3.16). The method used here to determine the global modes of an isolated junction is identical to the method developed by Guyader *et al* [18, 36] however the notation and derivation used is different in order to bring the analysis more in line with the other methods used in this thesis.

The orientation of the plates is the same as shown in figure 3.1.The junction beam is located at x =0 in the local coordinates of plates 2 and 3 and is located at position $x=L_{x,j}$ in the local coordinates of plates 1 and 4 with the y-axis in the same direction in all plates.

The pinned boundary condition on the edges y=0 and $y=L_{\text{y}}$ leads to a solution for the out-of-plane displacement in plate j which has the form [65]

$$\varepsilon_j(x_j, y) = \sum_{n=1}^{\infty} \varepsilon_j(x_j) \sin(k_{y,n} y) \tag{3.31}$$

where the wavenumber in the y-direction is restricted to integer multiples of π/L_y

$$k_{y,n} = \frac{n\pi}{L_y}\ , n = 1,2,3\ \ldots \tag{3.3.1.2}$$

Substituting the solution (eq.3.31) back into the bending wave equation for plate *j* (eq.3.4) multiplying by $\sin(k_{y,m}y)$ and integrating over the length of the plate, L_y, gives the equation:

$$\frac{\partial^4}{\partial x^4}\varepsilon_j(x_j) + (k_{y,m})^4\varepsilon_j(x_j) - 2(k_{y,m})^2\frac{\partial^2}{\partial x^2}\varepsilon_j(x_j) - \frac{\rho h}{B_p}\omega^2\varepsilon_j(x_j) = 0 \tag{3.33}$$

The solution is obtained by substituting the trial function $\exp(k_x x)$ into the Eq.3.33 which gives a solution for $\varepsilon_j(x_j)$ that is identical to Eq.3.9. The out of plane displacement in plate *j* is given by

$$\begin{aligned}\varepsilon_j(x_j, y) = \{&A_j \exp(-jk_{x,j}x_j) + H_j \exp(jk_{x,j}x_j) + C_j \exp(-k_{x,j}^N x) \\ &+ D_j \exp(k_{x,j}^N x)\}\sin(k_{y,m}y)\end{aligned} \tag{3.34}$$

where the wavenumbers $k_{x,j}^N$ and $k_{x,j}$ are given by eqs.3.35a and 3.35b respectively :

$$k_{x,j}^N = \pm\sqrt{\omega\sqrt{\frac{\rho_j h_j}{B_j}} + k_{y,m}^2} \tag{3.35a}$$

$$k_{x,j} = \pm\sqrt{\omega\sqrt{\frac{\rho_j h_j}{B_j}} - k_{y,m}^2} \tag{3.35b}$$

The condition that the trace wavelength along the junction line is the same in all plates means that the wavenumber in the y-direction is common to all plates. In some cases there will be a cut-off-point at which the travelling wavenumber $k_{x,j}$ becomes imaginary and only near-field waves are present in the plate because the wavenumber $k_{y,m}$ in equation 3.1.1.5b is greater than the bending wavenumber in that plate $k_{b,j}$.

The displacement in plate j given by eqn.3 4 may be written in the form [36]:

Case 1: In eq. 3.35b. $k_{y,m}^2 \leq \omega\sqrt{\frac{\rho_j h_j}{B_j}}$

$$\varepsilon_j(x_j, y) = \alpha_j\{E_j \sinh\left(k_{\mathrm{x},j}^N(x_j - F_j)\right) + \sin\left(k_{x,j}(x_j - G_j)\right)\}\sin\left(k_y y\right) \tag{3.36a}$$

Case 2: In eq. 3.35b. $k_{y,m}^2 > \omega\sqrt{\frac{\rho_j h_j}{B_j}}$

$$\varepsilon_j(x_j, y) = \alpha_j\{E_j \sinh\left(k_{\mathrm{x},j}^N(x_j - F_j)\right) + \sinh\left(k_{\mathrm{x},j}^{''}(x_j - G_j)\right)\}\sin\left(k_y y\right) \tag{3.36b}$$

where G_j and $F_j$are constants and $k_{\mathrm{x},j}^{''}$ in eq.3.36b is given by eq.3.37.

$$k_{\mathrm{x},j}^{''} = \pm\sqrt{k_{y,m}^2 - \omega\sqrt{\frac{\rho_j h_j}{B_j}}} \tag{3.37}$$

The requirement that the out of plane displacement is zero at the edges x=0 and x=$L_{x,j}$ (eq.3.1) in each plate, along with the condition that the moment is zero on the external edge ($x = L_{x,j}$ for plates 2 and 3, $x = 0$ for plates 1 and 4 in Figure 3.1) allows three of the four coefficients to be determined.

	Case 1	Case 2
E_1	$-\sin\left(k_{\mathrm{x},1}L_{x,1}\right) / \sin\mathrm{h}\left(k_{\mathrm{x},1}^N L_{x,1}\right)$	$-\sin\left(k_{x,1}L_{x,1}\right) / \sin\mathrm{h}\left(k_{\mathrm{N},x}^1 L_{x,1}\right)$
F_1	0	0
G_1	0	0
E_2	$-\sin\left(k_{\mathrm{x},2}L_{x,2}\right) / \sin\mathrm{h}\left(k_{\mathrm{x},2}^N L_{x,2}\right)$	$-\sinh\left(k_{\mathrm{x},2}^{''}L_{x,2}\right) / \sin\mathrm{h}\left(k_{\mathrm{N},x}^3 L_{x,2}\right)$
F_2	$L_{x,2}$	$L_{x,2}$
G_2	$L_{x,2}$	$L_{x,2}$
E_3	$-\sin\left(k_{\mathrm{x},3}L_{x,3}\right) / \sin\mathrm{h}\left(k_{\mathrm{x},3}^N L_{x,3}\right)$	$-\sin\mathrm{h}\left(k_{\mathrm{x},3}^{''}L_{x3}\right) / \sin\mathrm{h}\left(k_{\mathrm{N},x}^3 L_{x3}\right)$
F_3	$L_{x,3}$	$L_{x,3}$
G_3	$L_{x,3}$	$L_{x,3}$
E_4	$-\sin\left(k_{x,4}L_{x,4}\right) / \sin\mathrm{h}\left(k_{\mathrm{x},4}^N L_{x,4}\right)$	$-\sinh\left(k_{\mathrm{x},4}^{''}L_{x,4}\right) / \sin\mathrm{h}\left(k_{\mathrm{N},x}^4 L_{x,4}\right)$
F_4	0	0
G_4	0	0

Application of the interface conditions (eq.3.3) and (eq.3.4) on the interface leads to a set of simultaneous equations which can be written in matrix form as

$$\begin{bmatrix} X_{1,1} & X_{1,2} & 0 & 0 \\ X_{2,1} & 0 & X_{2,3} & 0 \\ X_{3,1} & 0 & 0 & X_{3,4} \\ X_{41} & X_{42} & X_{43} & X_{44} \end{bmatrix} \begin{bmatrix} \alpha_1 \\ \alpha_2 \\ \alpha_3 \\ \alpha_4 \end{bmatrix} = \begin{bmatrix} 0 \\ 0 \\ 0 \\ 0 \end{bmatrix} \tag{3.38}$$

The elements of the matrix (eq.3.38) for the case of real $k_{\mathrm{x,j}}$ (case 1) are

$$X_{1,1} = -k^1_{\mathrm{N},x} \sin\left(k_{x,1}L_{x,1}\right) \coth\left(k^N_{\mathrm{x},1}L_{x,1}\right) + k_{x,1} \cos\left(k_{x,1}L_{x,1}\right) \tag{3.39a}$$
$$X_{1,2} = k^2_{\mathrm{N},x} \sin\left(k_{x,2}L_{x,2}\right) \coth\left(k^N_{\mathrm{x},2}L_{x,2}\right) - k_{x,2} \cos\left(k_{x,2}L_{x,2}\right) \tag{3.39b}$$
$$X_{2,1} = -k^1_{\mathrm{N},x} \sin\left(k_{x,1}L_{x,1}\right) \coth\left(k^N_{\mathrm{x},1}L_{x,1}\right) + k_{x,1} \cos\left(k_{x,1}L_{x,1}\right) \tag{3.39c}$$
$$X_{2,3} = k^3_{\mathrm{N},x} \sin\left(k_{x,3}L_{x,3}\right) \coth\left(k^N_{\mathrm{x},3}L_{x,3}\right) - k_{x,3} \cos\left(k_{x,3}L_{x,3}\right) \tag{3.39d}$$
$$X_{3,1} = -k^1_{\mathrm{N},x} \sin\left(k_{x,1}L_{x,1}\right) \coth\left(k^N_{\mathrm{x},1}L_{x,1}\right) + k_{x,1} \cos\left(k_{x,1}L_{x,1}\right) \tag{3.39e}$$
$$X_{3,4} = k^4_{\mathrm{N},x} \sin\left(k_{x,4}L_{x,4}\right) \coth\left(k^N_{\mathrm{x},4}L_{x,3}\right) - k_{x,4} \cos\left(k_{x,4}L_{x,3}\right) \tag{3.39f}$$

$$X_{41} = B_1 \left[\left(k^N_{\mathrm{x},1}\right)^2 + \left(k_{x,1}\right)^2\right] \sin\left(k_{x,1}L_{x,1}\right) \tag{3.39g}$$
$$X_{42} = B_2 \left[\left(k^N_{\mathrm{x},2}\right)^2 + \left(k_{x,2}\right)^2\right] \sin\left(k_{x,2}L_{x,2}\right) \tag{3.39h}$$
$$X_{43} = B_3 \left[\left(k^N_{\mathrm{x},3}\right)^2 + \left(k_{x,3}\right)^2\right] \sin\left(k_{x,3}L_{x,3}\right) \tag{3.39i}$$
$$X_{44} = B_4 \left[\left(k^N_{\mathrm{x},4}\right)^2 + \left(k_{x,4}\right)^2\right] \sin\left(k_{x,4}L_{x,4}\right) \tag{3.39j}$$

The elements of the matrix (eq.3.38) for the case of imaginary $k_{\mathrm{x,j}}$ (case 2) are

$$X_{1,1} = k^1_{N,x} \sin\left(k_{x,1}L_{x,1}\right) \coth\left(k^1_{N,x}L_{x,1}\right) - k_{x,1} \cos\left(k_{x,1}L_{x,1}\right) \tag{3.40a}$$
$$X_{1,2} = -k^2_{N,x} \sin\left(k_{x,2}L_{x,2}\right) \coth\left(k^2_{N,x}L_{x,2}\right) + k''_{\mathrm{x},2} \cos \mathrm{h}\left(k''_{\mathrm{x},2}L_{x,2}\right) \tag{3.40b}$$
$$X_{2,1} = k^1_{N,x} \sin\left(k_{x,1}L_{x,1}\right) \coth\left(k^1_{N,x}L_{x,1}\right) - k_{x,1} \cos\left(k_{x,1}L_{x,1}\right) \tag{3. 40c}$$
$$X_{2,3} = -k^3_{N,x} \sin\left(k_{x,3}L_{x,3}\right) \coth\left(k^3_{N,x}L_{x,3}\right) + k''_{\mathrm{x},3} \cos \mathrm{h}\left(k''_{\mathrm{x},3}L_{x,3}\right) \tag{3. 40d}$$
$$X_{3,1} = k^1_{N,x} \sin\left(k_{x,1}L_{x,1}\right) \coth\left(k^1_{N,x}L_{x,1}\right) - k_{x,1} \cos\left(k_{x,1}L_{x,1}\right) \tag{3.40e}$$
$$X_{3,4} = -k^4_{N,x} \sin\left(k_{x,4}L_{x,4}\right) \coth\left(k^4_{N,x}L_{x,3}\right) + k''_{\mathrm{x},4} \cos \mathrm{h}\left(k''_{\mathrm{x},4}L_{x,3}\right) \tag{3.40f}$$

$$X_{4,1} = B_1 \left[k^N_{\mathrm{x},1} + \left(k_{x,1}\right)^2\right] \sin\left(k_{x,1}L_{x,1}\right) \tag{3.40g}$$
$$X_{4,2} = B_2 \left[k^N_{\mathrm{x},2} - \left(k''_{\mathrm{x},2}\right)^2\right] \sinh\left(k''_{\mathrm{x},2}L_{x,2}\right) \tag{3.40h}$$
$$X_{4,3} = B_3 \left[k^N_{\mathrm{x},3} - \left(k''_{\mathrm{x},3}\right)^2\right] \sinh\left(k''_{\mathrm{x},3}L_{x,3}\right) \tag{3.40i}$$
$$X_{4,4} = B_4 \left[k^N_{\mathrm{x},4} - \left(k''_{\mathrm{x},4}\right)^2\right] \sinh\left(k''_{\mathrm{x},4}L_{x,4}\right) \tag{3.40j}$$

For non-trivial solutions the determinant of the matrix in eq.3.9 is zero at the eigenfrequencies $\omega_{n,m}$ of the structure. For a given value of $k_{y,m}$ the eigenfrequencies are found numerically by varying ω in small increments to determine the roots of the determinant equation over a finite range of frequencies. The roots can be determined accurately using the

Regula-Falsi method [18] or using another root finding algorithm such as the 'fzero' function in Matlab.

The coefficients α_j are obtained by setting $\alpha_1 = 1$ the remaining coefficients are then given through the continuity of the rotational displacement across the boundary (eq.3.4). In terms of the matrix elements in eq.3.8 these are

$$\alpha_2 = -\frac{X_{1,1}}{X_{1,2}} \tag{3.41a}$$

$$\alpha_3 = -\frac{X_{2,1}}{X_{2,3}} \tag{3.41b}$$

$$\alpha_4 = -\frac{X_{3,1}}{X_{3,4}} \tag{3.41c}$$

This procedure gives the global mode shape $\psi_{n,m}$ associated with the eigenfrequency $\omega_{n,m}$ (Note that the labels *n* and *m* are not necessarily integer values but are used here only as labels). The mode shapes must be mass normalised so that the integral of the product of the surface density and the mode shape squared over the surface of the whole structure equals unity.

$$\iint \psi_{n,m}(x,y)\rho_s(x,y)\psi_{n,m}(x,y)\,\mathrm{d}S = 1 \tag{3.42}$$

They are also orthogonal so that the integral over the surface of whole the structure any two different modes is zero

$$\iint \psi_{n,m}(x,y)\rho_s(x,y)\psi_{k,l}(x,y)\,\mathrm{d}S = 0 \; if \; n \neq k \; or \; m \neq l \tag{3.43}$$

3.3.2 Determining the coupling loss factors from the global modes

The response at any position (x_r, y_r) on the structure due to harmonic excitation at a position (x_s, y_s) is given by a weighted sum over the product of the modal response at the source and receiver positions.

$$\begin{aligned}\varepsilon(\omega, x_s, y_s, x_r, y_r) &= \sum_{n=1}^{\infty}\sum_{m=1}^{\infty} \frac{\psi_{n,m}(x_s,y_s)\psi_{n,m}(x_r,y_r)}{(1+i\eta_{n,m})\omega_{n,m}^2 - \omega^2}\boldsymbol{F} \\ &= \sum_{n=1}^{\infty}\sum_{m=1}^{\infty} \alpha_{n,m}\psi_{n,m}(x_s,y_s)\psi_{n,m}(x_r,y_r)\,\boldsymbol{F}\end{aligned} \tag{3.44}$$

where $\boldsymbol{F}$ is a complex force and $\eta_{n,m}$is the modal loss factor

In terms of the out of plane displacement the time averaged kinetic energy ϵ at point (x_r, y_r) is given by

$$\epsilon(x_r, y_r) = \frac{1}{4}\omega^2 |F|^2 \rho_s(x_r, y_r) \left(\sum_{n=1}^{\infty}\sum_{m=1}^{\infty}\sum_{k=1}^{\infty}\sum_{l=1}^{\infty} \mathrm{Re}\{\alpha_{n,m}\alpha_{l,k}^*\}\psi_{n,m}(x_s, y_s)\psi_{n,m}(x_r, y_r)\psi_{k,l}(x_s, y_s)\psi_{k,l}(x_r, y_r) \right) \quad (3.45)$$

The total kinetic energy of the plate *j* is obtained by integrating the kinetic energy given by eq.3.45 over the surface area of the plate *j*. Rain-on-the roof forces are defined as spatially delta-correlated broad band excitation distributed over the surface area of the source plate *i* whose magnitude $|F|^2$ is proportional to the local mass density[38]. The mean-square force term in eq. 3.45 can be replaced by[40]

$$|F|^2 = 2S_f(\omega)\rho_s\delta\omega \quad (3.46)$$

Since the forces are spatially delta correlated the total energy density at any point in the structure is given by the sum over the contributions from each point force independently.

The contribution to the kinetic energy in the plate *j* from excitation in a spectral band $\delta\omega$ is

$$\delta E_{\mathrm{k},j} = \frac{1}{2}\omega^2 S_f(\omega)\delta\omega \left(\sum_{n=1}^{\infty}\sum_{m=1}^{\infty}\sum_{k=1}^{\infty}\sum_{l=1}^{\infty} \mathrm{Re}\{\alpha_{nm}\alpha_{lk}^*\}\beta_{nm,kl}^{(i)}\beta_{nm,kl}^{(j)} \right) \quad (3.47)$$

where $S_f(\omega)$ is spectral density and the constants $\beta_{nm,kl}^{(i)}$ and $\beta_{nm,kl}^{(j)}$ are

$$\beta_{nm,kl}^{(i)} = \iint \psi_{n,m}(x_s, y_s)\rho_s(x_s, y_s)\psi_{k,l}(x_s, y_s)\, dx_i dy_i \quad (3.48)$$

$$\beta_{nm,kl}^{(j)} = \iint \psi_{k,l}(x_r, y_r)\rho_s(x_r, y_r)\psi_{k,l}(x_r, y_r)\, dx_j dy_j \quad (3.49)$$

where the integrals in eq 3.48 and eq.3.49 are taken over the surface of the source plate i and the receiver plate j respectively.

The band-average kinetic energy is given by integrating Eq. 3.47 between the upper (ω_u) and lower limits (ω_l) of the frequency band of interest.

$$E_{\frac{1}{3}\mathrm{oct,k},j} = \frac{1}{\Omega}\int_{\omega_l}^{\omega_u} \delta E_{\mathrm{k},j}\, \mathrm{d}\omega \quad (3.50)$$

where Ω is the bandwidth $\omega_u - \omega_l$

If the spectral density is constant across the frequency band of interest the only frequency dependent term in eq.3.47 is $\mathrm{Re}\{\alpha_{nm}\alpha_{lk}^*\}$. A closed form expression for this integral is given by Mace and Shorter [38] and also Yap and Woodhouse[16].

$$\int_{\omega_l}^{\omega_u} \mathrm{Re}\{\alpha_{nm}\alpha_{lk}^{*}\}\,\omega^2 \mathrm{d}\omega = \Gamma_{nm,kl}$$
$$= \frac{\sqrt{-z_{nm}}}{z_{kl}-z_{nm}} \arctan\left(\frac{\Omega\sqrt{-z_{nm}}}{\omega_u\omega_l - z_{nm}}\right) + \frac{\sqrt{-z_{kl}}}{z_{nm}-z_{kl}} \arctan\left(\frac{\Omega\sqrt{-z_{kl}}}{\omega_u\omega_l - z_{kl}}\right) \quad (3.51)$$

where $z_{nm} = \omega_{nm}^2(1 - i\eta_{nm})$ and $z_{kl} = \omega_{kl}^2(1 - i\eta_{kl})$.

The total energy in the plate j is approximately equal to twice the kinetic energy $E_{\frac{1}{3}\mathrm{oct},j} = 2E_{\frac{1}{3}\mathrm{oct,k},j}$

The total power input one-third octave band to the source plate is given by

$$\pi_{\mathrm{in},i} = S_f\left(\sum_{n=1}^{\infty}\sum_{m=1}^{\infty} \Gamma_{nm,nm}\beta_{nm,nm}^{(i)}\right) \quad (3.52)$$

This enables an energy influence coefficient to be defined [18, 38, 40] as the energy in plate 'j' when power is injected into plate 'i'. The elements of the energy influence coefficients A_{ji} are given by:

$$A_{ji} = \frac{E_{\frac{1}{3}\mathrm{oct},j}}{\pi_{\mathrm{in},i}} = \frac{1}{2}\left(\sum_{n=1}^{\infty}\sum_{m=1}^{\infty}\sum_{k=1}^{\infty}\sum_{l=1}^{\infty} \Gamma_{nm,kl}\beta_{nm,kl}^{(i)}\beta_{nm,kl}^{(j)}\right) / \left(\sum_{n=1}^{\infty}\sum_{m=1}^{\infty} \eta_{nm}\omega_{nm}\Gamma_{nm,nm}\beta_{nm,nm}^{(i)}\right) \quad (3.53)$$

The energy influence coefficients are related to the coupling loss factors through

$$\eta_{ij}(\omega) = -\frac{1}{\omega}[A^{-1}]_{ji} \quad (3.54)$$

Alternatively some of the methods discussed in section 2.2.5 can be used to determine the coupling loss factors from the energy influence coefficients.

3.4 Conclusions

Two different methods have been described to calculate coupling loss factors between simply supported plates for bending wave transmission across the junction.

For semi-infinite plates, wave theory has been used to determine transmission coefficients which relate the amplitude of the outward propagating transmitted wave in each plate to the incident wave. However in finite plates both inward and outward propagating waves are present on the junction and this can cause fluctuations in the transmission coefficient between plates when the outward and inward propagating waves combine coherently [45].

For finite plates, the CLF can account for the fluctuations in the power flow between the coupled plates caused by interference but some assumptions must be made about the boundary conditions on the remaining edges of the plates in the junction. Such assumptions may or may not be valid when the plates are coupled *in-situ*. The global mode method in Section 3.3.3 gives a solution for the CLF in which an ideal set of ROTR forces is applied to the structure. The advantage of this approach over a MCFEM approach (Section 2.4) is that it is much quicker and easier to implement. This is an important factor to consider when deciding how to calculate the CLFs for SEA models of large buildings. Hence the aim in Chapter 5 is to assess the CLF's calculated using these different approaches with large buildings.

Chapter 4 Validation of the Monte-Carlo FEM (MCFEM) approach using a heavyweight building structure

4.1 Introduction

This chapter focuses on the validation of the MCFEM approach for predicting structure-borne sound transmission on a heavyweight building structures through comparison with measurements. For these laboratory experiments, one side of a small transmission suite (the north room shown in figure 4.1) is used which is located in the Acoustics Research Unit (ARU) at the University of Liverpool.

Measurements were carried on the walls and floors to determine their physical properties for input into the FEM models. The quasi-longitudinal phase speed and thickness of all the walls and floors of the transmission suite were measured directly. Using this data the density of the walls and floors was estimated by comparing measurements of the spatial and frequency-averaged driving-point mobility to the driving-point mobility of an infinite plate.

Measurements of the energy level differences between source and receiving plate subsystems were obtained for two cases for comparison with MCFEM; in the first case excitation was applied to one of the walls of the north room and in the second case excitation was applied to the upper floor.

4.2 Test construction

The building layout is shown schematically in Figure 4.1 and a photograph is shown in Figure 4.2. The building consists of heavyweight concrete floors and brickwork walls which are plastered on the inner side. The two rooms are decoupled by a fibreglass filling and the lower floor is decoupled from the laboratory floor via a resilient layer. This has been confirmed by previous experimental work [66] in which the TLF's of the plates compared well with the theoretical values for the isolated building.

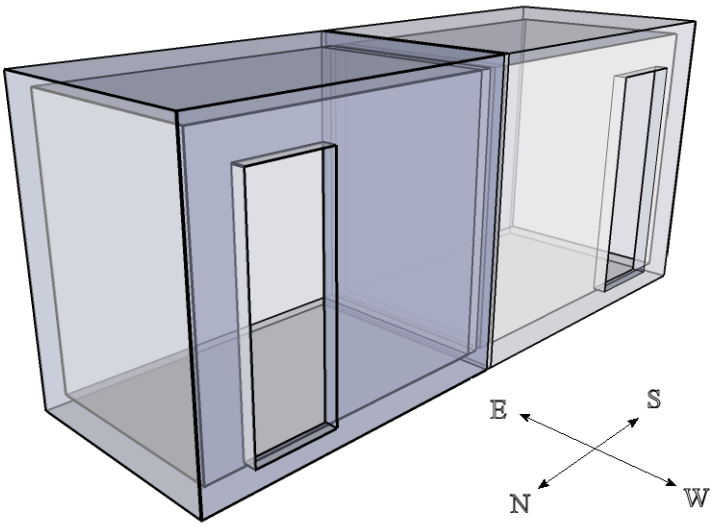

Figure 4.1. Schematic diagram of the ARU transmission suite. The highlighted area shows the north room on which measurements were conducted. The walls were labelled according to the compass located in the bottom right hand corner.

Figure 4.2. Photograph showing test construction in the same orientation as shown in Figure 4.1.

The room contains some features that could potentially affect sound transmission. These are the small rectangular window and the doorway in the western wall(see Figure 4.2), a 1x1m area on the south wall which has been filled in with dense aggregate block, 1cm thick bonded screed on the upper concrete floor and a safety railing on the upper floor.

Measured values of plate width, height and thickness are shown in Table 4.1. The plate dimensions were taken from the inside surfaces of the room northern room shown in Figure

4.1 to make the model consistent with the SEA model which uses inner dimensions to calculate coupling loss factors from the plates to the room.

	Width(m)	Height(m)	h(m)
Lower Floor	2.86	1.82	0.13
Upper Floor	2.86	1.82	0.12
North Wall	2.48	1.82	0.10
East Wall	2.86	2.48	0.10
South Wall	2.48	1.82	0.10
West Wall	2.86	2.48	0.10

Table 4.1. Measured internal dimensions of the plates that form the north room of the ARU transmission suite.

4.3 Measurement Methods

4.3.1 Measurement of quasi-longitudinal phase velocity

To measure the quasi-longitudinal phase velocity of the walls and floors an impulse was generated on the edge of the plate and the time was measured for the pulse to reach an accelerometer placed a distance, *d,* from the point of impact. The force transducer and single accelerometer approach was taken instead of the more common two accelerometer method [3] in order to maximise the distance between the excitation position and the accelerometer and hence reduce the error in the measured time to within acceptable limits.

To excite in-plane waves a B&K Type 8202 force hammer with plastic tip was struck on the side of the plate as shown in Figure.4.3. In order to detect the in-plane vibration the main axis of sensitivity of the accelerometer was parallel to the surface of the plate. The time signal recording was triggered by the impact of the force hammer and the time-of-flight, Δt, was determined from the time taken for the rising slope of the impulse to reach the accelerometer output. The quasi-longitudinal phase velocity of the plate is given by:

$$c_{\mathrm{L}} = \frac{d}{\Delta t} \tag{4.1}$$

The measurement was repeated at two locations on each plate with four repeat measurements made at each location. A schematic of the equipment used for the experiments is shown in Figure 4.4.

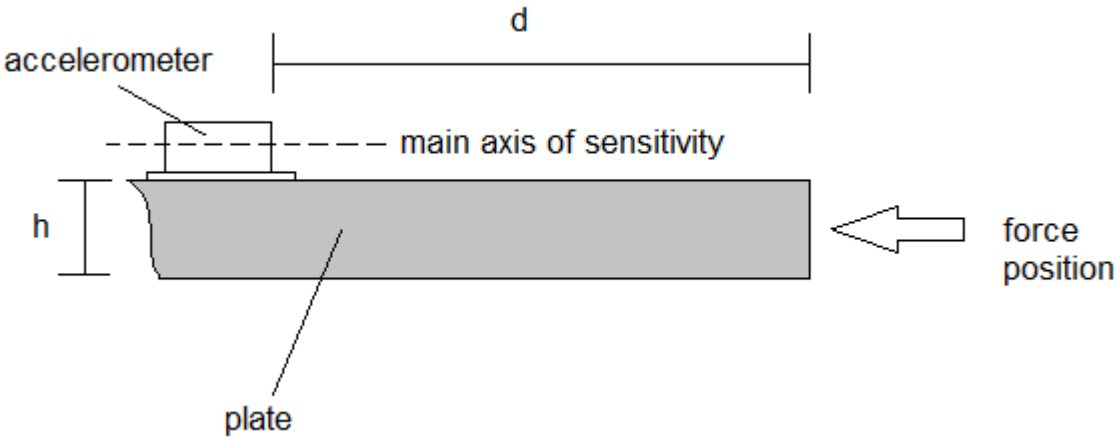

Figure 4.3. Schematic diagram of the measurement setup for measuring quasi-longitudinal phase velocity.

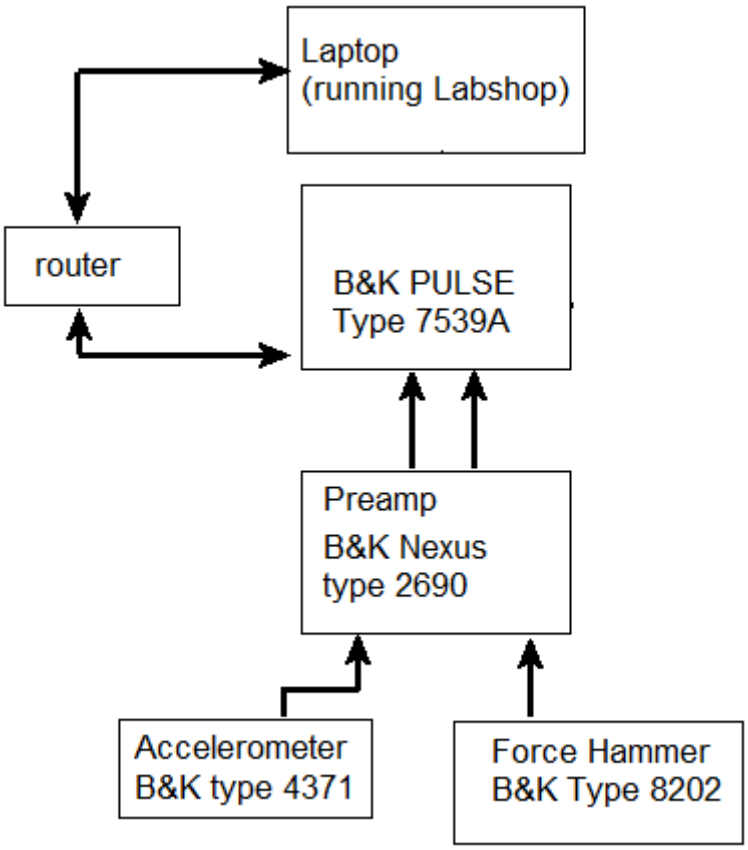

Figure 4.4. Equipment used to measure quasi-longitudinal phase velocity and driving-point mobility.

4.3.2 Measurement of driving point mobility

The definition of the driving point mobility, Y_{dp}, is the transverse velocity spectrum divided by the input force spectrum measured at the excitation point on the plate.

$$Y_{\mathrm{dp}} = v(\omega)/F(\omega) \tag{4.2}$$

In practice this is not possible with a separate accelerometer and force hammer, the best approximation to this is obtained by reducing the distance *d* as much as possible as shown in Figure 4.5. The distance should be chosen such that at the highest frequency of the relation $kd \ll 1$.

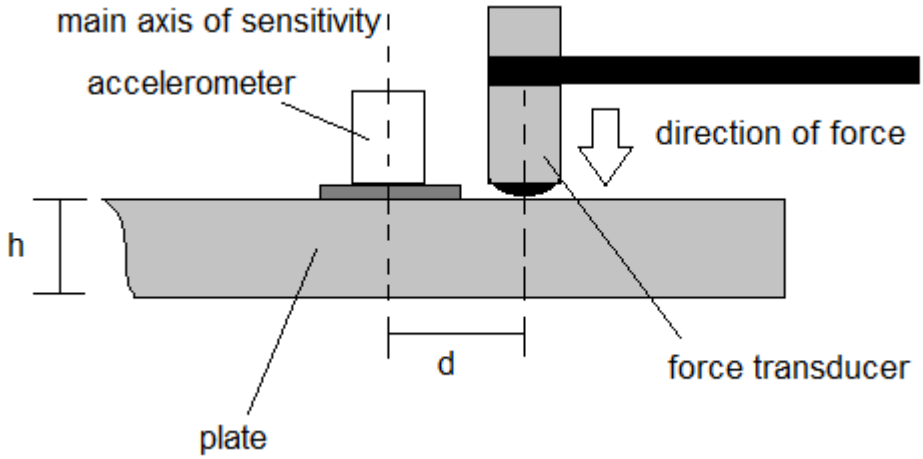

Figure 4.5. Measurement setup for the driving point mobility

The time signal of the plate response was measured using a B&K type 4371 accelerometer with the main axis of sensitivity directed out of the plane of the plate, the force impulse was applied and measured using a B&K Type 8202 force hammer with plastic tip which gives a flat force spectrum up to 1500Hz. Both pieces of equipment were calibrated in accordance with ISO 7626 -2 [67].The mobility measurement was processed using narrow band FFT analysis using the same equipment as previously shown in Figure 4.4. The frequency response function *H1* was output which gives the cross-spectrum normalised to the input auto-spectrum. This minimises the error in the result when noise is present in the output (accelerometer) signal [68].

Note that all mobility data shown in decibels is calculated using 10lg(Y_{dp} / 1m/Ns).

4.3.3 Evaluating the density from the spatial-average driving-point mobility

To estimate the density, driving point mobilities were measured at three different points on the plate. Positions were chosen that were at least 50cm from the edge of the plate to

minimise the effect of near-field components from the junction lines. The average of four measurements was taken at each position. The infinite plate driving point mobility was estimated by fitting a horizontal straight line through the spatial-average of the measured data in the frequency region 700 – 1000Hz (see Figure 4.6). The higher frequency region was chosen since the higher modal overlap factor reduces the modal fluctuations; hence the assumption that the plate can be treated as extending infinitely is a better approximation in the higher frequency region. The density of the plate was estimated from the equation for the infinite plate driving point mobility [20] using.

$$Re\{\overline{Y_{dp}}\} = \frac{1}{2.3\rho h^2 c_{\mathrm{L}}} \tag{4.3}$$

Rearranging this equation gives the density of the plate as

$$\rho = \frac{1}{2.3 Re\{\overline{Y_{dp}}\} h^2 c_{\mathrm{L}}} \tag{4.4}$$

The quasi-longitudinal phase velocity c_{L} was measured as described in section 4.3.1 and the plate thickness *h* was measured directly.

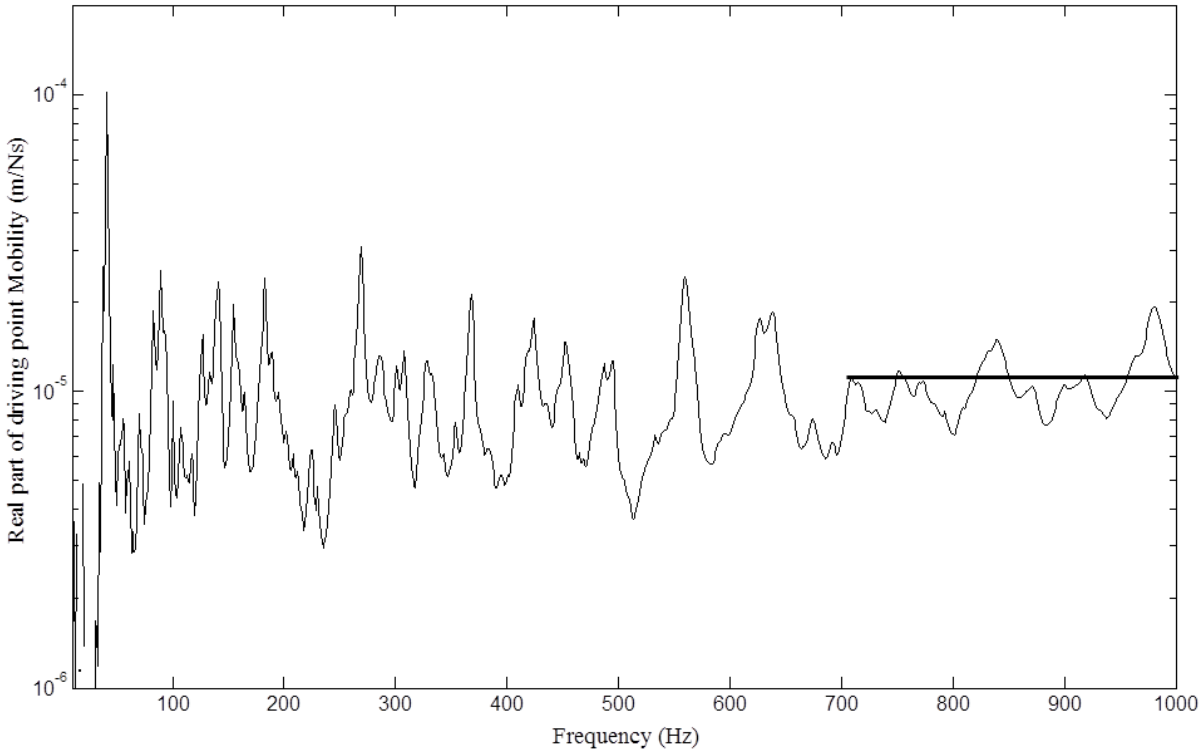

Figure 4.6. Straight line fitted to the real part of the spatial average driving-point mobility in the region 700 -1000Hz.

4.3.4 Measuring steady state energy level differences (ELD's)

The aim of the ELD measurements was to provide a measured data for comparison with bending wave transmission models using MCFEM and SEA-like models. This required measurement of the spatial and temporal average mean-square velocity levels in one-third octave bands on the source and receiver plates in response to statistically independent excitation.

In order to excite bending waves on the source plate a shaker was mounted so the force was perpendicular to the surface of the plate. The shaker positions were at least 0.5m from the plate edges and 1m from each other. For a particular source position the bending wave vibration on the source and receiver plates is measured at a set of random positions by accelerometers arranged so that the main axis of sensitivity is directed out of the plane of the plate. To avoid the effects of near-fields the positions of the accelerometers are selected so that they are at least 1m from the excitation point and 0.25m from the edge of the plate [3]. A minimum distance of 0.5m between accelerometers was also chosen to avoid correlation between the sampling points. Due to the small dimensions of the plates only two source positions and eight measurement points on each plate were possible.

The equipment used for the measurements is shown in Figure 4.7. The output signal from the accelerometers was passed through a bank of one-third octave band filters in the B&K PULSE before time averaging the result to give the one-third-octave band average velocity levels. White noise was sent to the shaker via a graphic equaliser to ensure that there was less than 5dB difference between adjacent one-third-octave bands in the measured response for a given source position and receiver position. This was done to avoid the skirts of each one-third octave band filter from affecting the measurement in adjacent bands and also to try to satisfy the SEA requirement that power is injected into all modes equally.

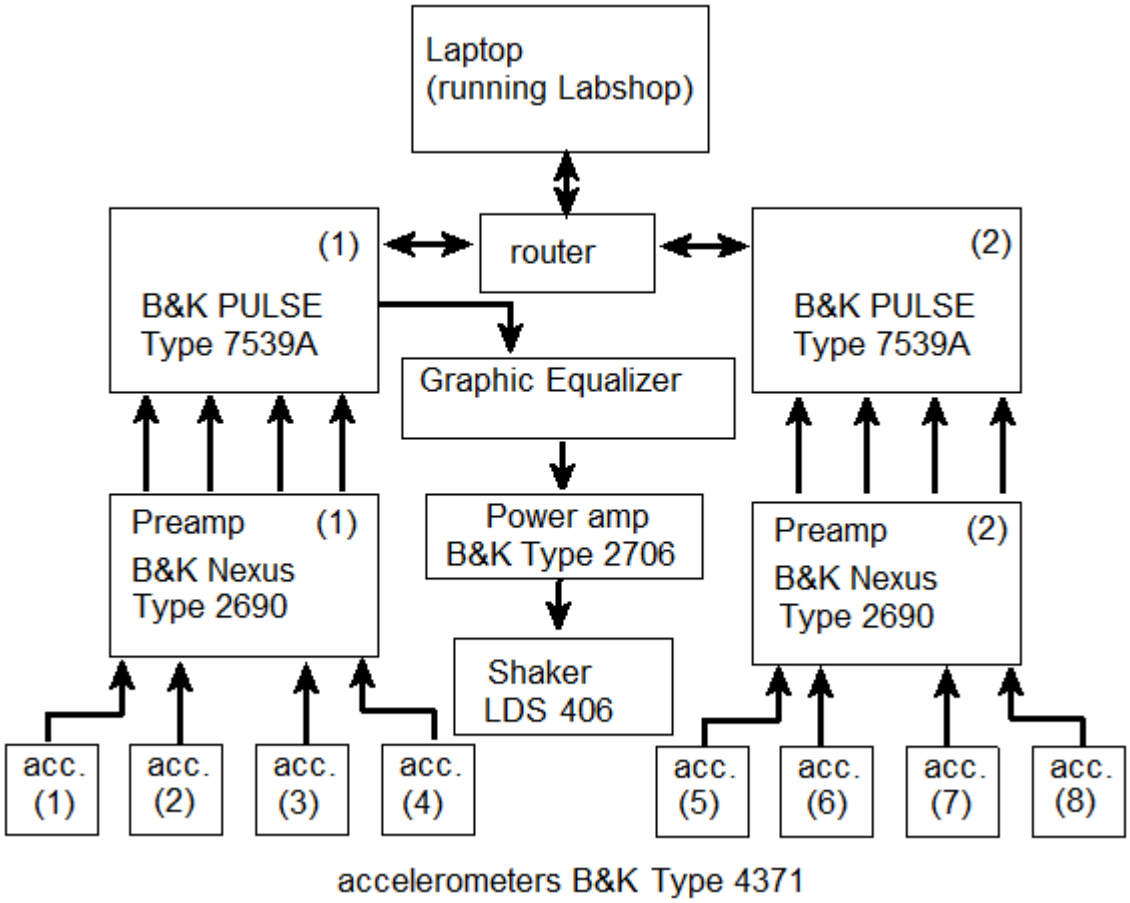

Figure 4.7. Schematic diagram of the equipment used to measure energy level differences

A total of eight accelerometer positions on the source and receiver plate were chosen. The measurements at each accelerometer position were combined to give the spatial and temporal average square velocity in one-third-octave band along with the associated standard deviation on each plate for each source position.

The one-third octave band energy in each plate is related to the spatial and temporal average square velocity through the equation

$$E_T = m < v^2 > \tag{4.5}$$

where *m* is the total mass of the plate.

The ELD can be calculated for each source position j along with a combined standard deviation, $\sigma_{\mathrm{Source}j}$, given by:

$$\sigma_{\mathrm{Source}j} = \left(\frac{\sigma_S^2}{8} + \frac{\sigma_R^2}{8}\right)^{1/2} \tag{4.6}$$

where σ_S is the standard deviation of the measured energies on the source plate and σ_R is the standard deviation of the measured energies on the receiver plate.

The ELD is calculated by linearly averaging the ELD's obtained for each source position. The 95% confidence limits can be obtained by combing the effective standard deviation and effective number of degrees of freedom from the Student-t distribution[66].

4.4 MCFEM model

4.4.1 Modelling considerations

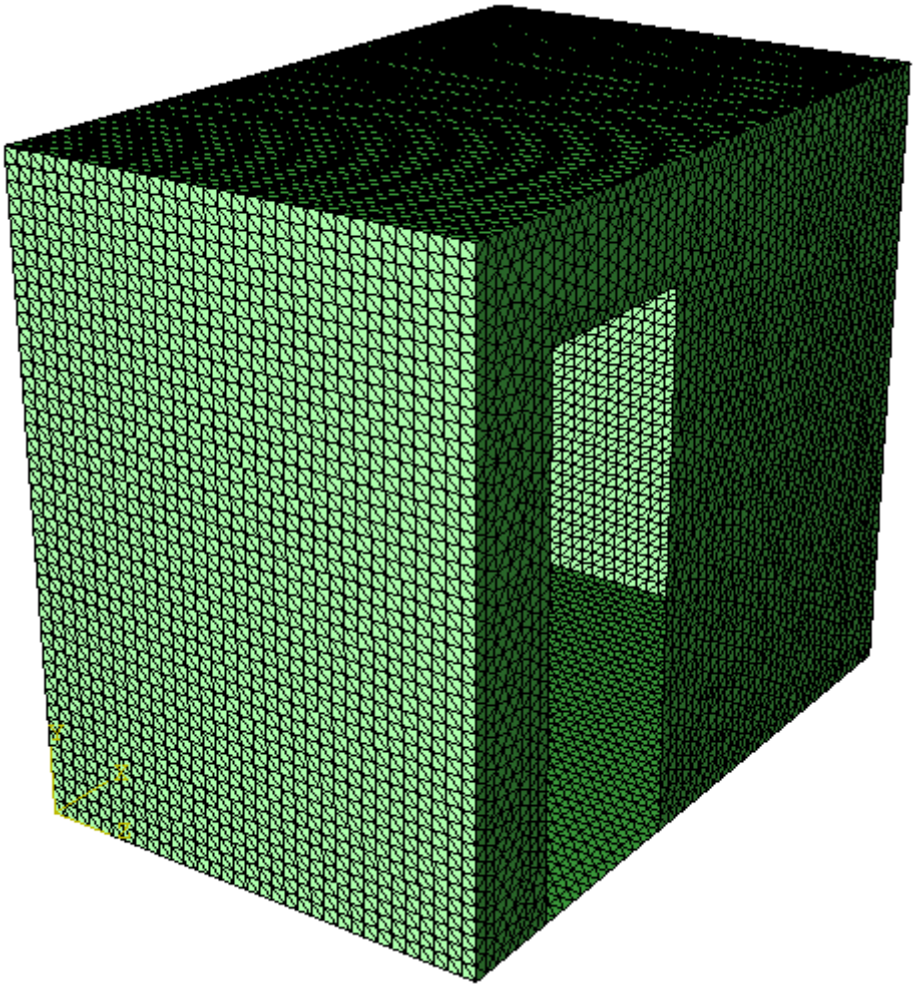

Figure 4.8 Finite element mesh of the north room of the ARU transmission suite.

The FEM model of the building does not include all of the features of the building. The small window on the western wall has dimensions much smaller than the free bending wavelength of the wall and was much smaller than any of the junction lengths; as a result this was not included in the FEM model. The screed on the upper floor is much thinner than the thickness of the floor and it is not expected to alter the vibrational properties of the floor. Hence the

upper floor is modelled as a homogeneous plate. The railing on top of the building potentially provides an unwanted flanking path between the two sides of the transmission suite, however due to the strength of the plate coupling it was assumed that this path is negligible and the frame was not included in the FEM models.

Two features that might affect structure-borne sound transmission are the door aperture in the western wall [14] and the filled-in aperture on the south wall. The filled aperture was modelled by treating the south wall as a homogeneous plate with effective density and quasi-longitudinal phase velocity both of which were determined experimentally (see sections 4.3.3 and 4.3.1). The doorway was treated as a hole in the western wall. However the heavy door frame surrounding the doorway meant that it was not known whether the boundary condition around the doorway was clamped or free. Therefore the driving-point mobility from the FEM model with clamped or free boundary conditions was compared to the measured value at a point on the western wall. From Figure 4.9 it is seen that in the region of the fundamental mode there is better agreement between FEM and the measurement when the doorway edge was modelled with free boundaries.

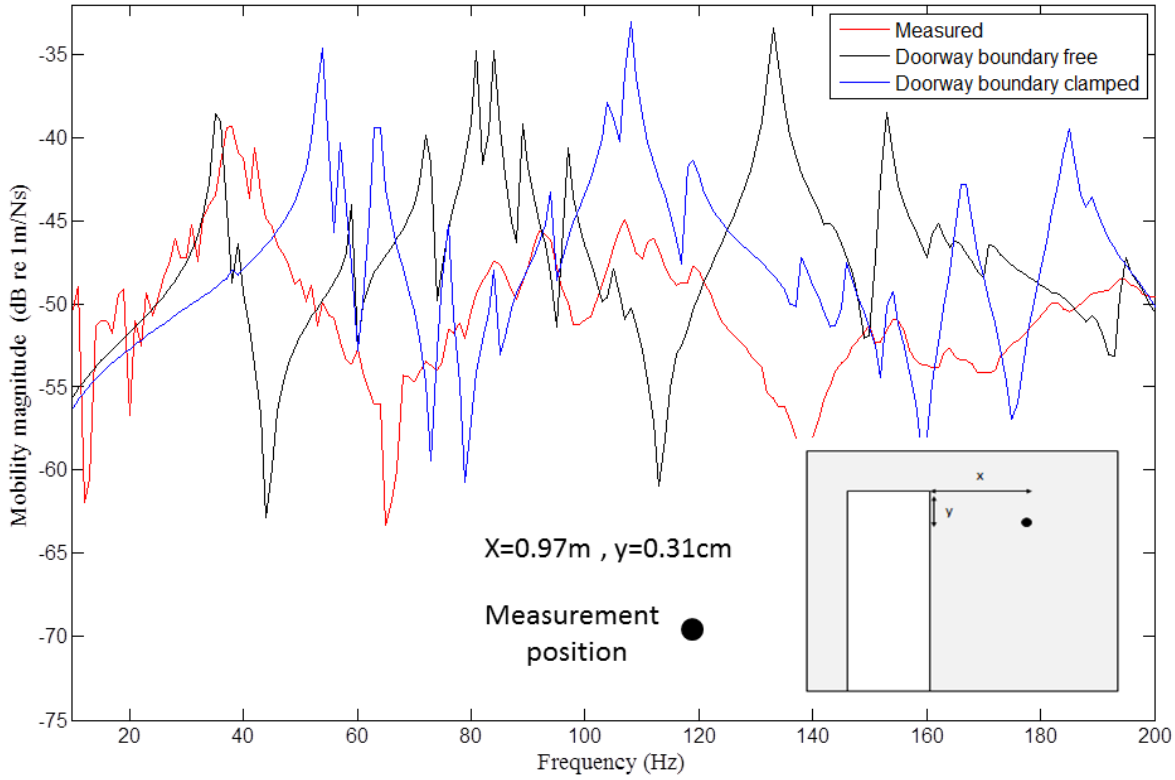

Figure 4.9. FEM driving point mobility for the case of clamped edge doorway and free edge doorway for comparison with the measured mobility at a point on the western wall of the building.

Quasi-longitudinal local modes are only predicted to occur in all the plates above 1100Hz so it was assumed that bending waves dominate the structure-borne sound transmission in the frequency region 50-1000Hz. Therefore a pinned boundary condition was applied to the plate junctions. The coupling to the air volume was assumed not to affect the structure borne sound transmission between plates. As a result the fluid-structure interaction was not modelled in the FEM models.

4.4.2 Introducing uncertainty to the FEM model

To introduce uncertainty for the material properties for MCFEM analysis, an ensemble of 'similar' buildings was defined using the same procedure as described in Section 2.4.2 with the Young's modulus of the individual walls and floors selected randomly from a normal distribution and different sets of ROTR applied to each of the resulting buildings. Fifteen members of the ensemble were generated using this procedure for two separate choices of source plate. Measurements of the quasi-longitudinal phase velocity on the North, West and East walls suggest a mean value of 2000ms^{-1} with standard deviation of 200ms^{-1}. The standard deviation of the quasi-longitudinal phase velocity on the southern wall was estimated to be 200ms^{-1} and the measured value of 2300ms^{-1} was used as the sample mean. Previous measurements carried out on concrete floors by Hopkins [35] suggest that 200ms^{-1} is also a reasonable estimate of the standard deviation of the concrete floor and the measured value of 3500ms^{-1} was used as the sample mean. The measured values of the quasi-longitudinal phase velocity and density of all the walls and floors are shown in Table 4.2 with the results Section 4.5.1. Due to the small sample size any sample lying more than three standard deviations from the mean was discarded. The Young's modulus is related to the quasi-longitudinal phase velocity by:

$$E = \rho c_{\mathrm{L}}^2 (1 - \nu^2) \qquad (4.7)$$

The Young's modulus was calculated using equation 4.6 using the mean values of density and Poisson ratio from table 4.1.

4.5 Results

The measurement results for the quasi-longitudinal phase velocity (Section 4.2) and density measurements (Section 4.3) are discussed in Section 4.5.1. Spatial-average mobility and ELD measurements are compared with the FEM predictions in Section 4.5.2 and 4.5.3 respectively.

4.5.1 Physical properties

Measured values of quasi-longitudinal phase velocity and density are given in table 4.2. Along with the estimated values of internal loss factor and Poisson ratio taken from the literature [3].

	c_L(m/s)	ρ(kg/m^3)	ν(-)	ILF(-)
Lower Floor	3500	1900	0.2	0.005
Upper Floor	3500	1900	0.2	0.005
North Wall	2000	1700	0.2	0.01
East Wall	2000	1700	0.2	0.01
South Wall	2300	1800	0.2	0.01
West Wall	2000	1700	0.2	0.01

Table 4.2. Physical properties of the plates.

The values given in the literature [3] for the quasi-longitudinal phase velocity and density are 3800ms^{-1} and 2200kgm^{-3} respectively for concrete and 2700ms^{-1} and 1500-2000kgm^{-3} for solid bricks connected with mortar. Comparison with the measured values given in Table 4.2 indicates that the measured density of concrete is 300kgm^{-3}lower than the value in the literature and the quasi-longitudinal phase velocity is 300ms^{-1} lower than expected. The measured density of the brick and mortar walls was within the expected range quoted in the literature but the quasi-longitudinal phase velocity was 700ms^{-1}lower. The ARU transmission suite was constructed in 1959, hence possible reasons for the difference between the measured and quoted values may be the deterioration of the bricks or concrete over time or that a different material composition was used in this building than described in the literature.

4.5.2 Mobility measurements

The FEM model for the North room was validated by comparing the predicted spatial-average driving-point mobility with measured values for three of the plates that form the room. Two predictions of the driving-point mobility are shown, these are the FEM model for the entire room that accounts for the global modes and a local mode model based on the local modes of an isolated simply-supported plate using the in situ total loss factor. Figures 4.10 to 4.12 compare the measured and predicted data. Only the first few resonant peaks were of interest in this analysis and hence the frequency range is limited from 10 to 200Hz.

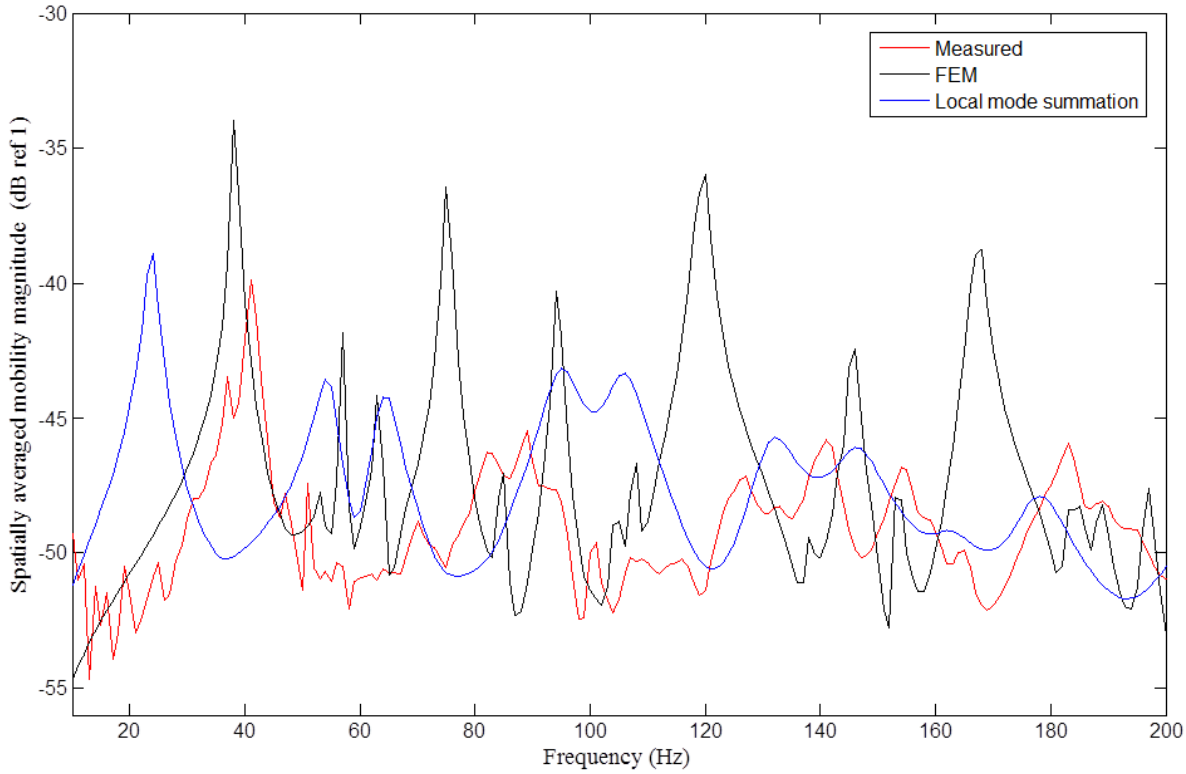

Figure 4.10. Measured and predicted spatially averaged mobility magnitude of the Eastern wall.

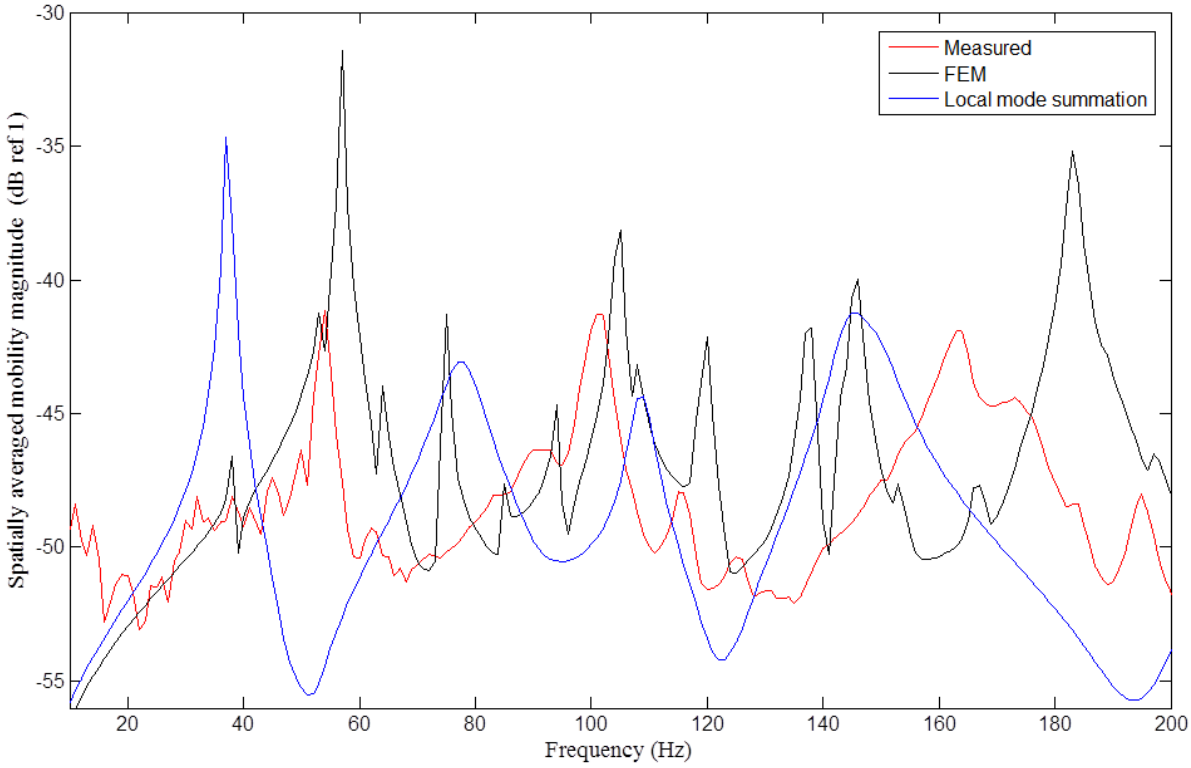

Figure 4.11. Measured and predicted spatially averaged mobility magnitude of the northern wall.

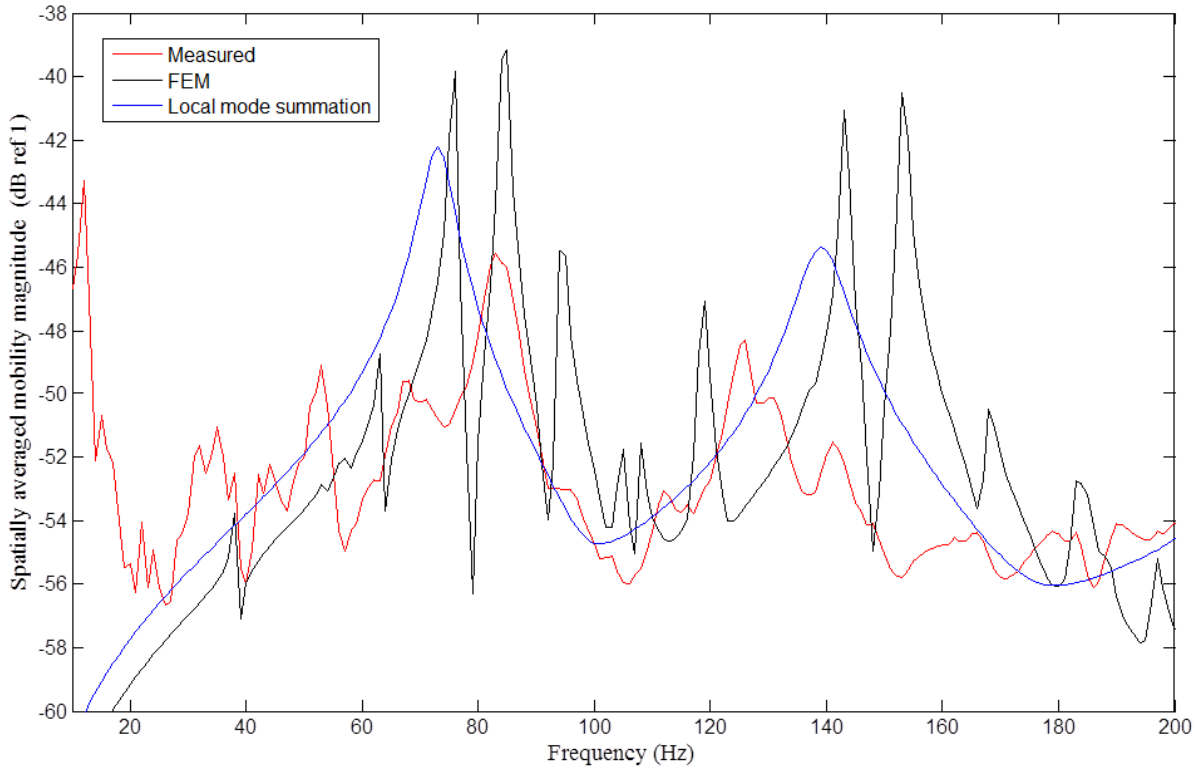

Figure 4.12. Measured and predicted spatially averaged mobility magnitude of the Upper floor.

For the east and north walls the measured peaks in the driving point mobility coincide with the peak in the FEM prediction in the region of the fundamental resonance although FEM consistently predicts a larger value for the amplitude of this peak. The predicted mobility using the local modes of the isolated plate consistently gives a lower frequency for the first resonant peak than was observed experimentally. This provides evidence that a local mode model is inadequate and that the FEM model which accounts for global modes is more appropriate. For the upper floor both the FEM model and the local mode model show discrepancies with measured data. Above the first modal peaks there is little agreement between the measurements and the theoretical predictions.

4.5.3 Energy level differences

The MCFEM approach was validated by comparing the predicted ELD's with the measured values in third-octave bands. For the case of excitation applied to the East wall the results are shown in Figures 4.13 to 4.17. The results in Figures 4.18 to 4.22 show the ELD's when excitation is applied to the upper floor. The 95% confidence limits (see Section 2.4.2) for the measured and predicted ELD's are shown as error bars in each plot, overlapping confidence limits indicate good agreement between measured and predicted values.

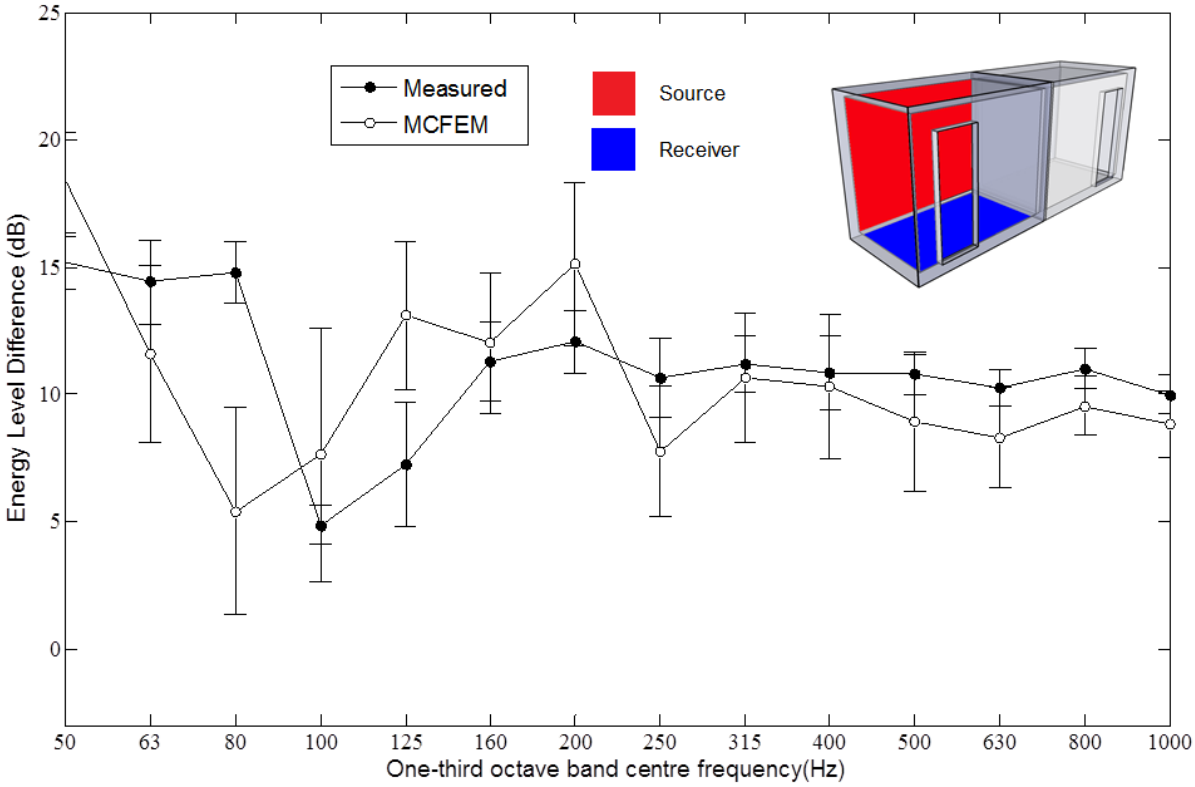

Figure 4.13. Comparison between MCFEM and measurements. ELD between east wall and lower floor of the ARU transmission suite.

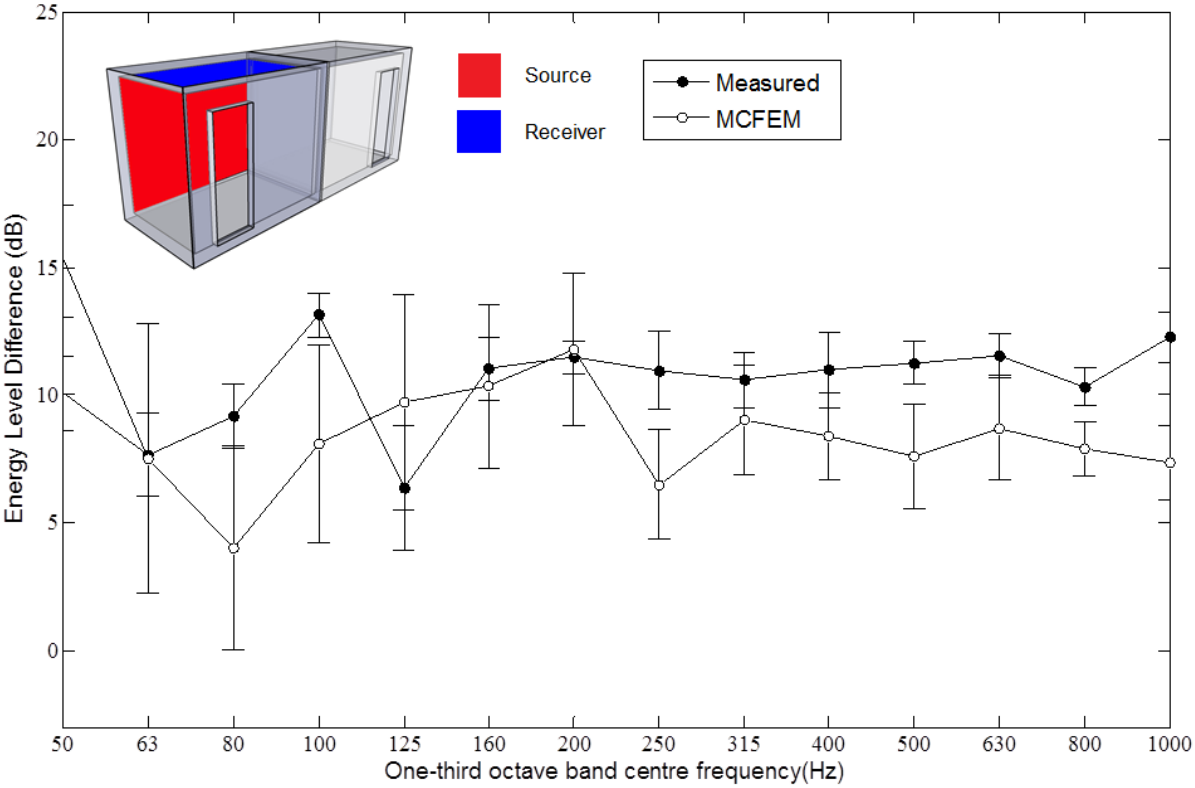

Figure 4.14. Comparison between MCFEM and measurements. ELD between east wall and upper floor of the ARU transmission suite.

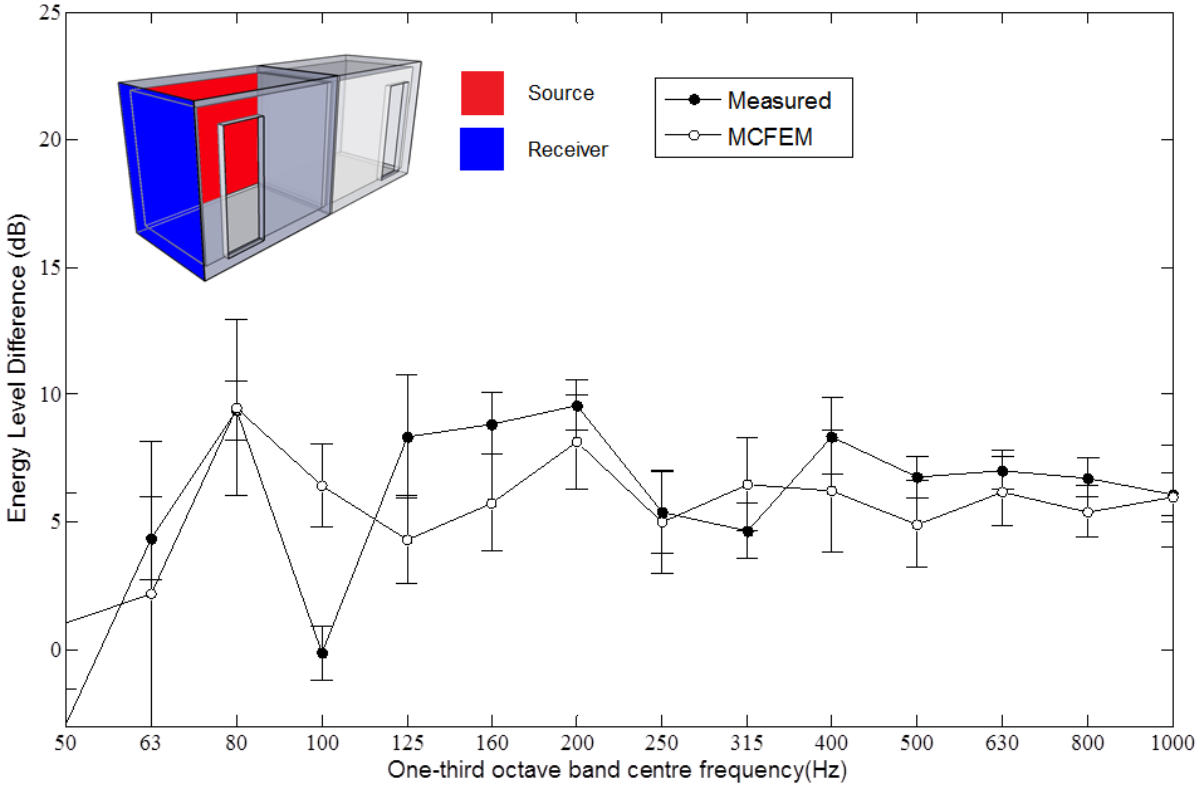

Figure 4.15. Comparison between MCFEM and measurements. ELD between east and north wall of the ARU transmission suite.

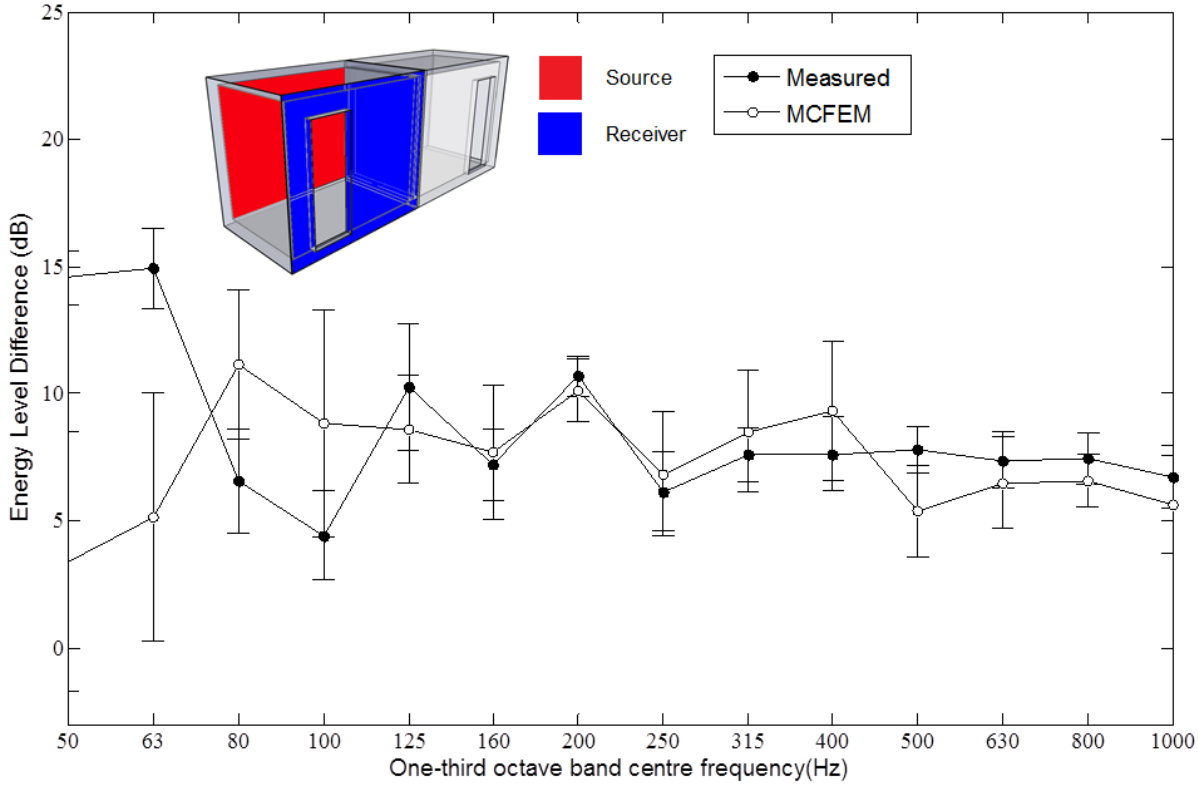

Figure 4.16. Comparison between MCFEM and measurements. ELD between east and west wall of the ARU transmission suite.

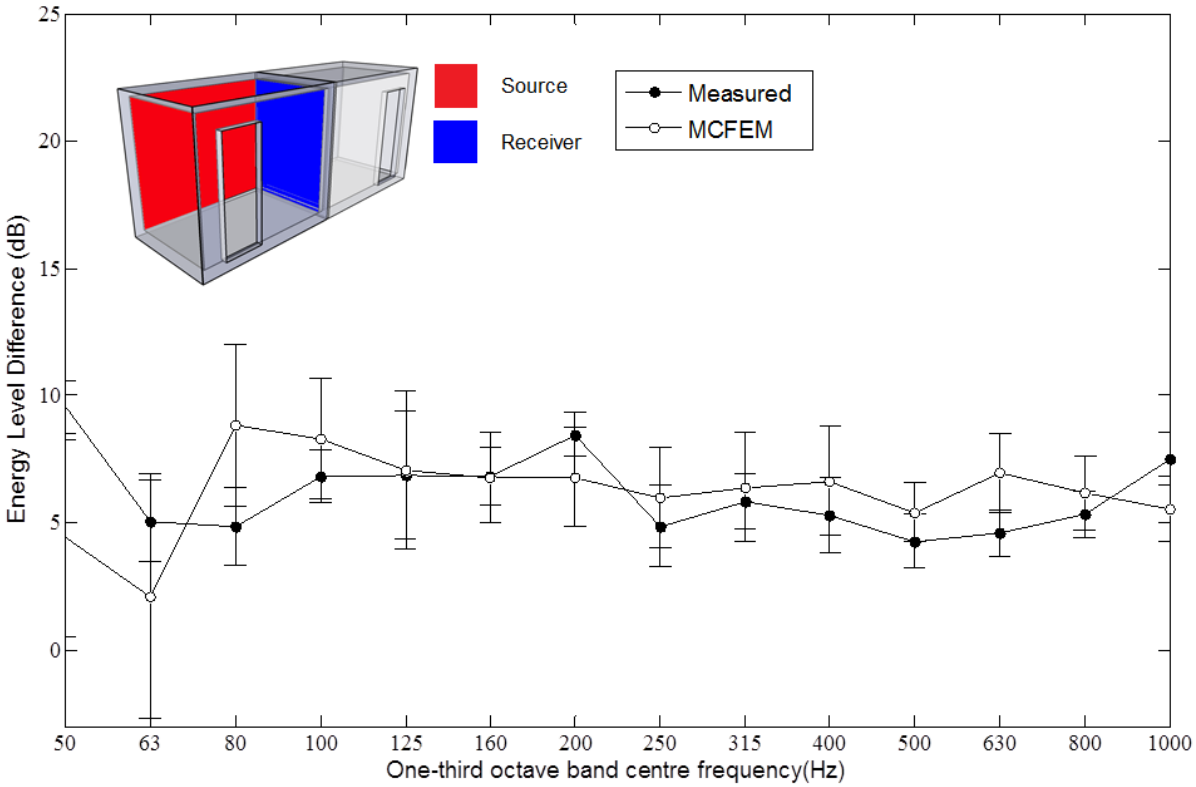

Figure 4.17. Comparison between MCFEM and measurements. ELD between east and south wall of the ARU transmission suite.

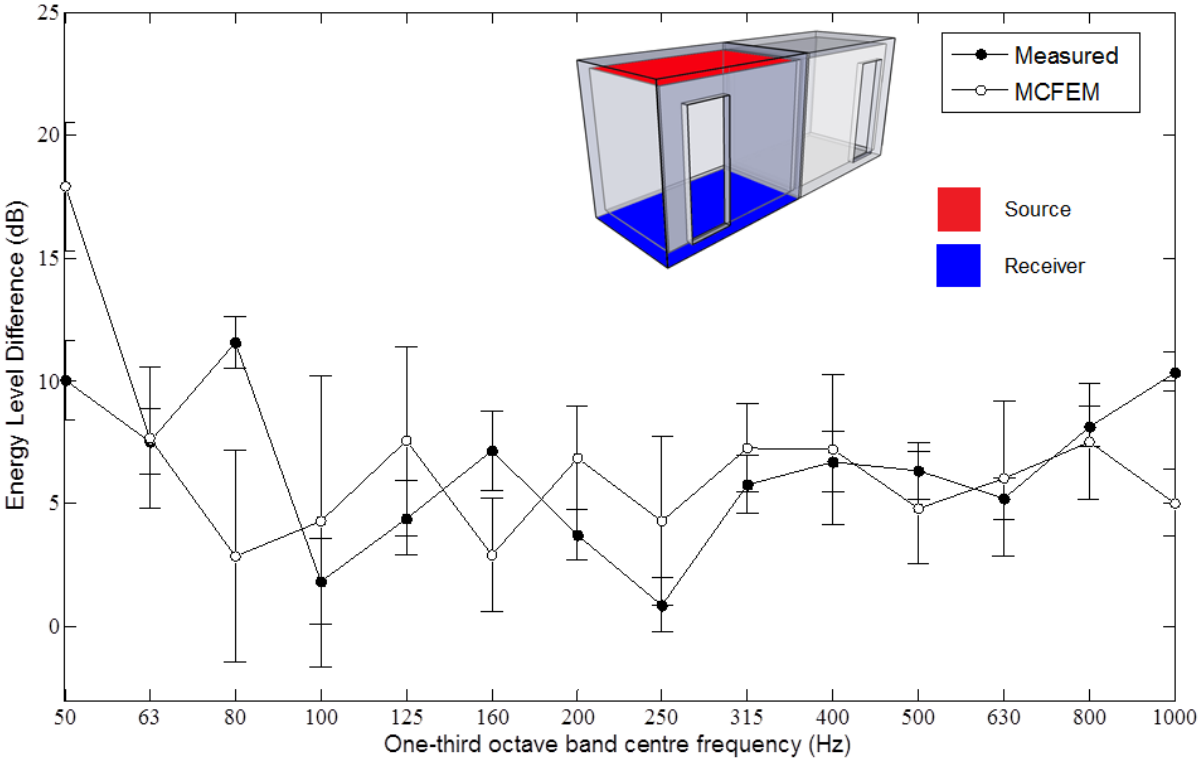

Figure 4.18. Comparison between MCFEM and measurements. ELD between upper floor and lower floor of the ARU transmission suite.

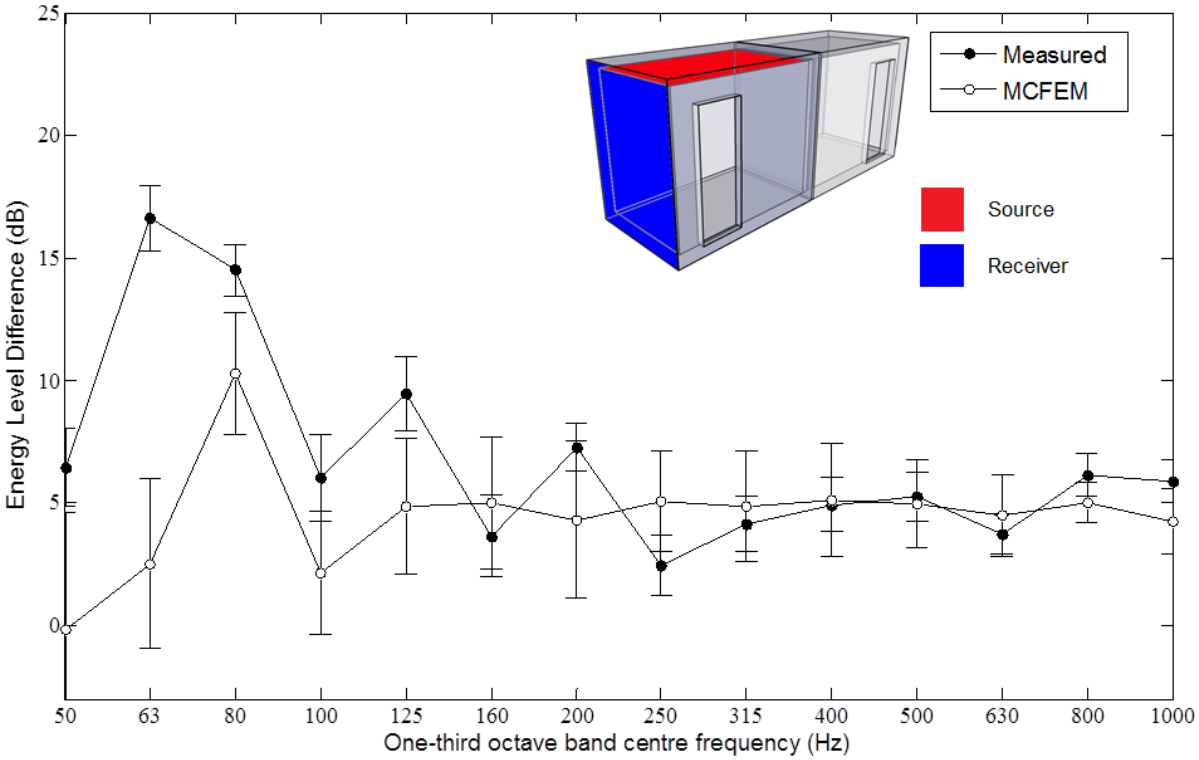

Figure 4.19. Comparison between MCFEM and measurements. ELD between upper floor and north wall of the ARU transmission suite.

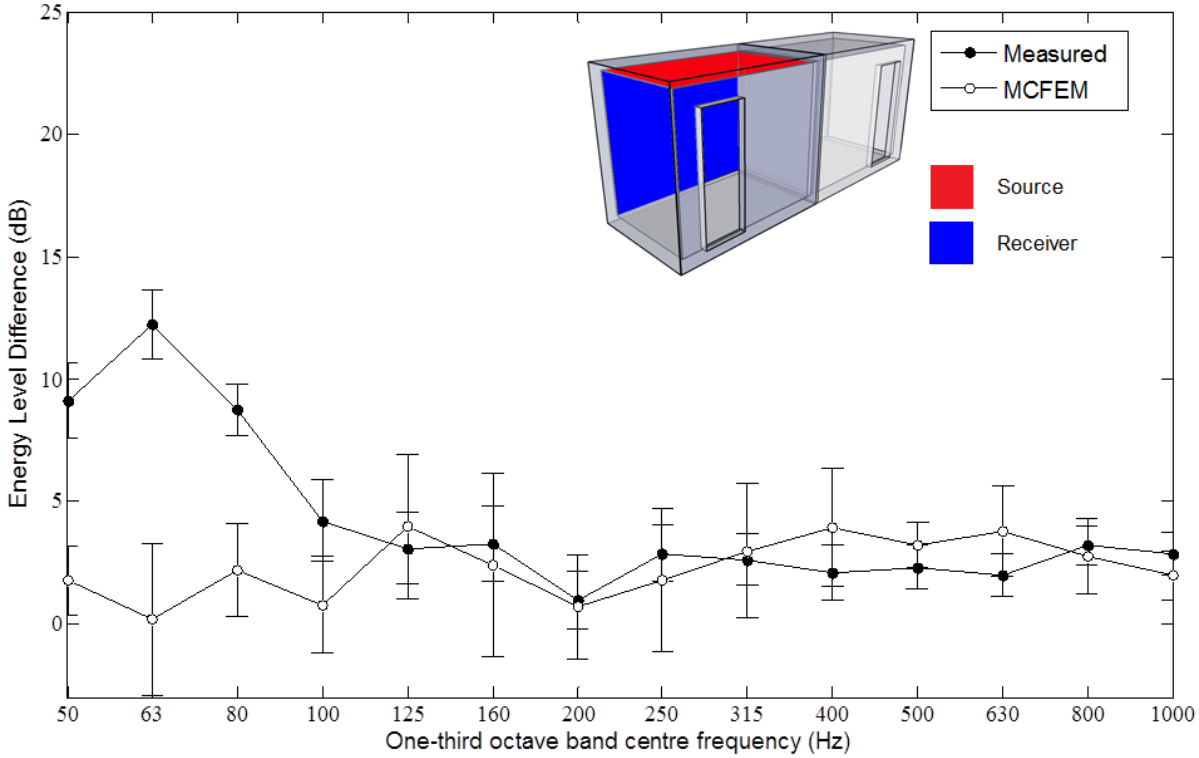

Figure 4.20. Comparison between MCFEM and measurements. ELD between upper floor and east wall of the ARU transmission suite.

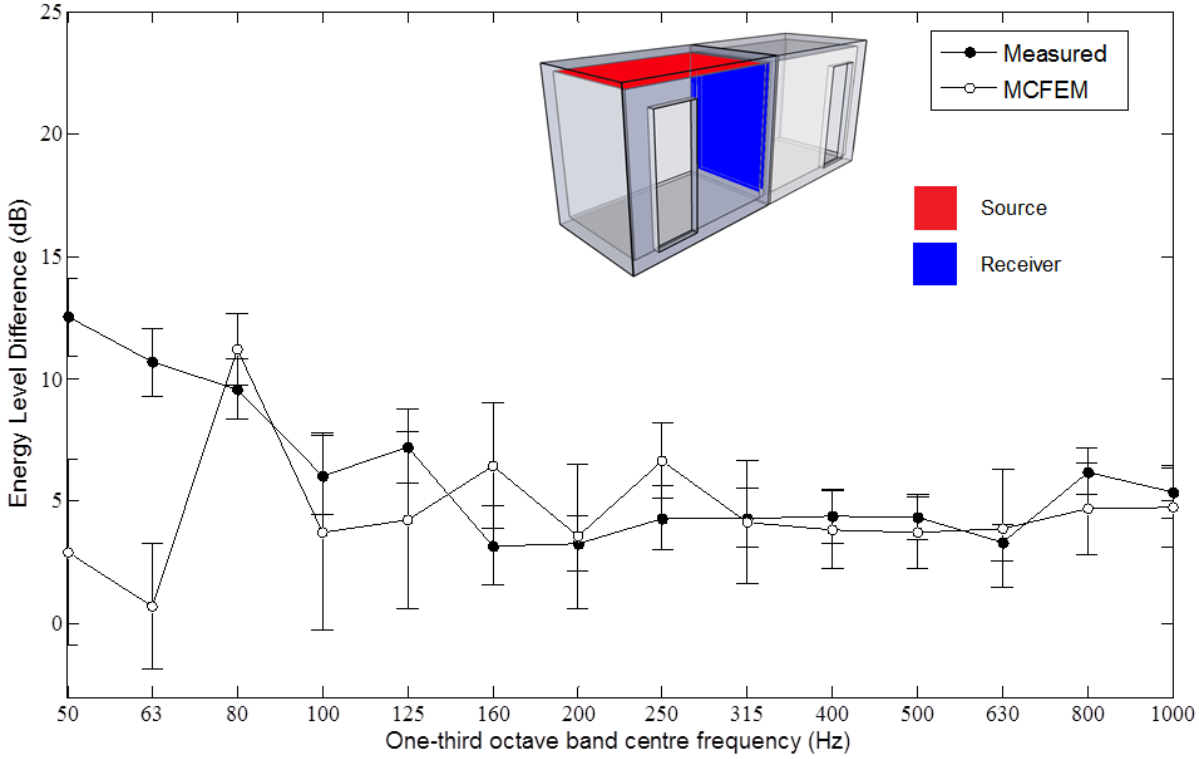

Figure 4.21. Comparison between MCFEM and measurements. ELD between upper floor and south wall of the ARU transmission suite.

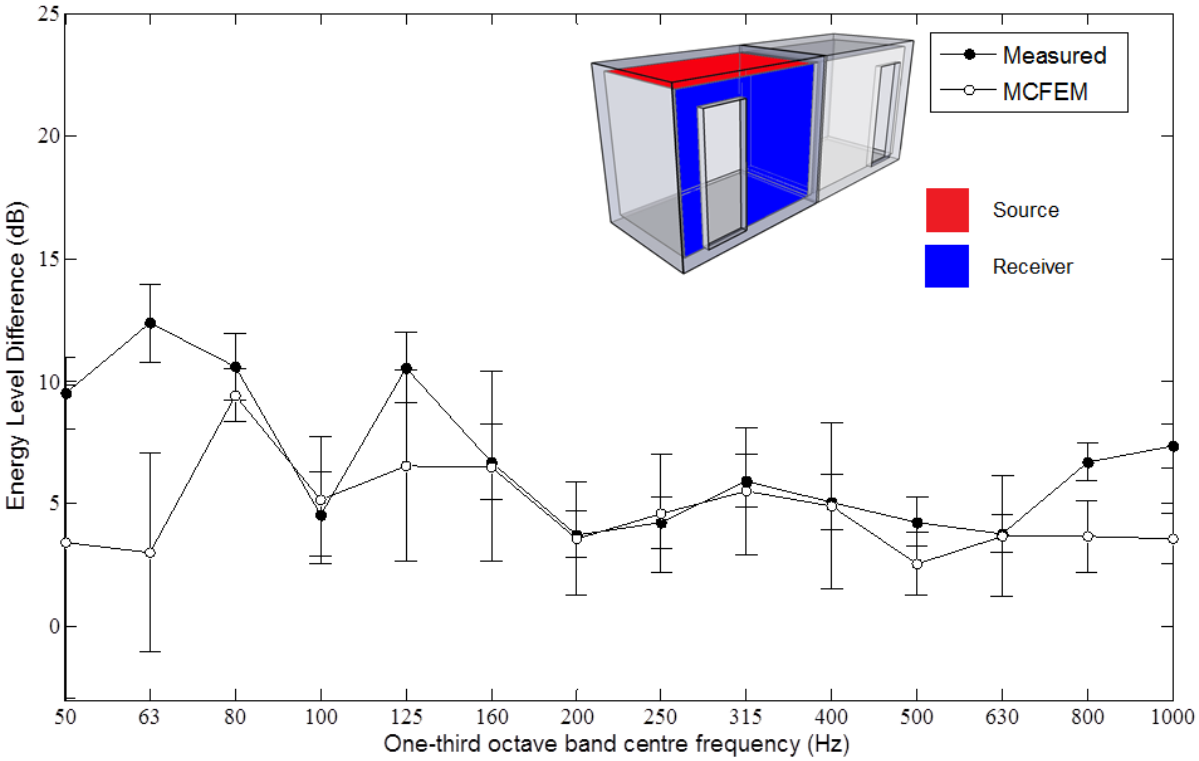

Figure 4.22. Comparison between MCFEM and measurements. ELD between upper floor and west wall of the ARU transmission suite.

The ELD results can be considered in two frequency regions; below 250Hz there are strong responses of individual modes; hence there are discrepancies between the measured and predicted response if the resonant frequency of these modes is not predicted with sufficient accuracy. Above 250Hz there is statistically more than one mode per one-third octave band in each plate of the structure and the one-third octave band response is dominated by resonant modes. The results show best agreement above 250Hz as the 95% confidence limits of MCFEM tend to overlap with those of the measurements.

The mobility measurements previously indicated that FEM is unable to accurately predict the frequency of all the resonant peaks of the driving point mobility of the structure. This is likely to be caused by a difference in the eigenfrequencies of the FEM models and the actual eigenfrequencies of the real structure. Where the statistical mode count is low the one-third octave response is sensitive to small changes in eigenfrequencies in cases where the out of band modes dominate the one-third octave band response. Hence there is poor agreement between FEM and the measured results below 250 Hz. Above 250Hz, resonant modes dominate the one-third octave band response and the exact frequency position of the modes becomes less important.

4.6 Conclusions

This chapter used measurements on a small heavyweight building structure to validate the FEM models and the MCFEM approach to account for uncertainty.

Comparison of the driving-point mobility from FEM and the measurements show good agreement in the region of the first modal peak with the peak in the predicted mobility occurring within ±8Hz of the measured peak. Although FEM overestimated the amplitude of this peak there was evidence that a global mode model (i.e. FEM) was necessary to predict the modal response because the local mode model consistently predicted a lower frequency for the first resonant peak than was observed experimentally. However the FEM model was unable to accurately predict the location of higher frequency peaks in the driving point mobility.

For the ELDs, there was good agreement between MCFEM and the measurements above 250Hz. However below 250Hz there were discrepancies with up to 15dB difference between the measurements and MCFEM in some cases. This was attributed to the FEM model predicting eigenfrequencies for the first few global modes that were different to the actual eigenfrequencies.

The results indicate that a MCFEM approach can be used to accurately predict the structure-borne sound transmission in a simple single room heavyweight building structure in one-third octave bands at frequencies where the statistical mode count is greater than one. Consequently the MCFEM approach is considered to be appropriate to predict structure borne sound transmission on larger scale buildings in Chapters 5,6 and 7.

Chapter 5 SEA and SEA-like models of heavyweight buildings

5.1 Introduction

In this chapter the use of the standard EN12354 part 2 [24] for predicting impact sound insulation between dwellings will be compared to matrix SEA (Section 2.23) using coupling loss factors from semi-infinite plate theory(which will be referred to as wave-theory SEA).

Section 5.2 contains an overview of the building structures investigated in this thesis. This thesis primarily focuses on structure-borne sound transmission *in vacuo* without considering the air cavities representing the rooms as part of the transmission path. For this reason, Section 5.3.2 investigates their influence because the focus in the remainder of the thesis is on the vibrational energy levels of the plates as obtaining the correct spatial-average sound pressure level in the receiving room requires the vibration levels of all the plates in that room to be predicted accurately.

EN12354 is a form of transmission path analysis (Section 2.2.4) which only includes paths that cross a single structural joint. In Sections 5.3.3 to 5.34 the method is compared to the matrix SEA method for two different building structures described in Section 5.2. Of particular interest is the feasibility of extending this approach to subsystems in which the minimum number of structural junctions between the subsystem and the source is greater than one.

Section 5.4 investigates the capability of matrix SEA to predict ELDs between plates with low modal overlap and low statistical mode counts. ELDs from matrix SEA are compared to those predicted by MCFEM for the two different building structures.

5.2 Building description

5.2.1 Physical properties of the plates

The models investigated in this thesis represent typical heavyweight residential buildings with dense aggregate block walls and cast in-situ concrete floors, the dimensions of the plates are based on the dimensions of rooms found in typical living spaces (see Table 5.1). The building structures consist of a minimum of two rooms separated by a 0.215m thick wall with

0.1m thick flanking walls and 0.15m thick floors. The material properties for these plates are taken from Hopkins [3] and are presented in Table 5.1. The buildings consist of homogeneous plates with no inclusions such as doorways and windows. The internal loss factor of the lower floor is set to $1/\sqrt{f}$ to account for the high radiation into the earth[3].

	L_x(m)	L_y(m)	L_z(m)	h(m)	c_L(ms^{-1})	ρ(kgm^{-3})	Poisson ratio	ILF
Floors*	3.5	-	4	0.15	3800	2200	0.2	0.005
Separating Wall	-	2.4	4	0.215	3200	2000	0.2	0.01
Flanking Wall	3.5	2.4	-	0.1	3200	2000	0.2	0.01

Table 5.1. Physical properties of the walls and floors of the test buildings. * ILF is $1/\sqrt{f}$ for the lower floors of the building.

5.2.2 Modal properties of the plates

SEA is based on the interaction between resonant modes in separate subsystems; hence SEA may only be applied when resonant modes are present in all subsystems in the structure. The fundamental frequency of the bending, $f_{11(B)}$, quasi-longitudinal, $f_{11(L)}$and transverse shear modes, $f_{11(T)}$, are given by eq. 5.1 to 5.3.

$$f_{11(B)} = \frac{\pi h c_L}{4\sqrt{3}}\left(\left(\frac{1}{L_x}\right)^2 + \left(\frac{1}{L_y}\right)^2\right) \tag{5.1}$$

$$f_{11(L)} = \frac{c_L}{2}\left(\left(\frac{1}{L_x}\right)^2 + \left(\frac{1}{L_y}\right)^2\right) \tag{5.2}$$

$$f_{11(T)} = \frac{c_L}{2}\sqrt{\frac{1-\vartheta}{2}}\left(\left(\frac{1}{L_x}\right)^2 + \left(\frac{1}{L_y}\right)^2\right) \tag{5.3}$$

Where ϑ is the poisson ratio of the material

The calculated mode frequencies for each of the mode types is given in Table 5.2.

	$f_{11(B)}$ (Hz)	$f_{11(L)}$(Hz)	$f_{11(T)}$ (Hz)	Modal density (Bending)
Floors	37.2	721.0	456.2	0.0425
Separating Walls	73.7	777.5	491.7	0.0242
Flanking Walls	37.0	808.3	511.2	0.0455

Table 5.2. Modal properties of the plates.

Bending modes are present in all plates above 74Hz, quasi-longitudinal modes are present in all plates above 809Hz and transverse-shear modes are present from 511Hz. For all models in this thesis, the plate boundaries were pinned to prevent excitation of in-plane waves at the junctions. These fundamental frequencies indicate that only bending modes occur up to 500Hz one-third octave band. However, evidence from [15] indicates that it should also be a reasonable assumption up to ≈1kHz.

The bending wave modal density of the walls and floors was calculated using eq.2.5 and the results are shown in Table 5.2. These values were used to determine the statistical mode count of the walls and floors as shown in Table 5.3.

	50	63	80	100	125	160	200	250	315	400	500	630	800	1k
Floors	0.49	0.62	0.78	0.98	1.24	1.56	1.96	2.47	3.1	3.91	4.92	6.19	7.8	9.82
Separating walls	0.28	0.35	0.44	0.56	0.7	0.88	1.11	1.4	1.76	2.22	2.8	3.52	4.43	5.58
Flanking wall	0.53	0.66	0.83	1.05	1.32	1.66	2.09	2.64	3.32	4.18	5.26	6.62	8.33	10.5

Table 5.3. Statistical mode count for bending modes in one-third octave bands.

The modal overlap factor is commonly defined as [48, 55]

$$M = \omega n_{\omega} \eta_{int} \tag{5.4}$$

where $\eta_{int}$is the internal loss factor, ω is the band centre frequency and n_{ω} is the modal density in units of angular frequency.

However for building structures in which the total loss factor is dominated by the coupling loss factor the modal overlap factor is defined [33].

$$M = \omega n_{\omega} \eta_{total} \tag{5.5}$$

where η_{total} is the total loss factor.

5.2.3 Layout of the building structures

The building types are denoted according to the number of rooms along each of the three dimensions, N_x, N_y and N_z. For example, a building with two rooms along the *x*-direction, one room along the *y*-direction and three rooms in the *z*-direction would be denoted as a 2_1_3 building. The walls facing into a particular room are labelled according to the room number using their compass orientation (North-South axis runs across the thick separating walls of the dwellings and the East-West axis runs across the thin flanking walls). For example: on the eastern side (*E*) of room 1, the wall (*W*) would be labelled *EW1,* the upper floor of room 1 would be labelled *UF1*, the lower floor of room 1 would be labelled *LF1*.

The building structures investigated in this thesis are shown in Figures 5.1 to 5.3. The 2_1_1 building shown in Figure 5.1 is used to investigate the influence of the airborne paths on the vibration levels of the plate subsystems. The 5_1_1 model shown in Figure 5.2 allows transmission across several identical junctions to be tested and to some degree can be viewed as a periodic structure. The 2_2_2 building shown in Figure 5.3 was designed to test transmission diagonally across the structure from plates connected to the room in the lower right hand corner to plates connected to the room in the upper left hand corner.

In building acoustics the aim of most prediction models is to determine the spatial-average SPL in the receiving room. It is assumed that in order to obtain an accurate estimate of the spatial-average SPL in the receiving room the energy levels of the walls and floors must also be predicted accurately. In the models investigated here, the plates are all decoupled from the air and it is assumed that the plate to plate coupling will not affected by the presence of the air volumes. The validity of these assumptions will be investigated using an SEA model in Section 5.3.2.

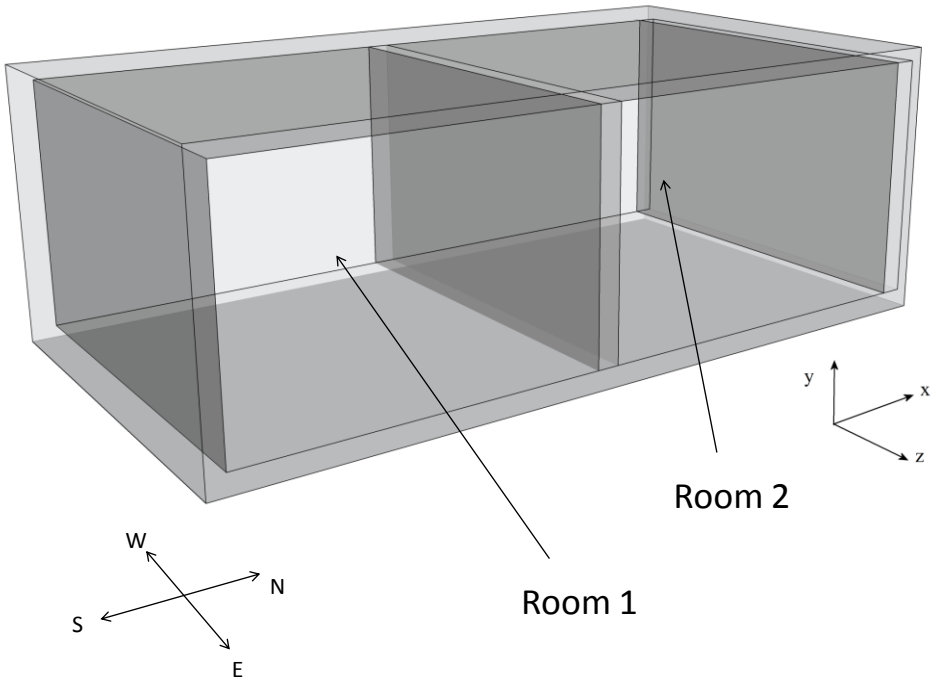

Figure. 5.1. Schematic of the 2_1_1 model

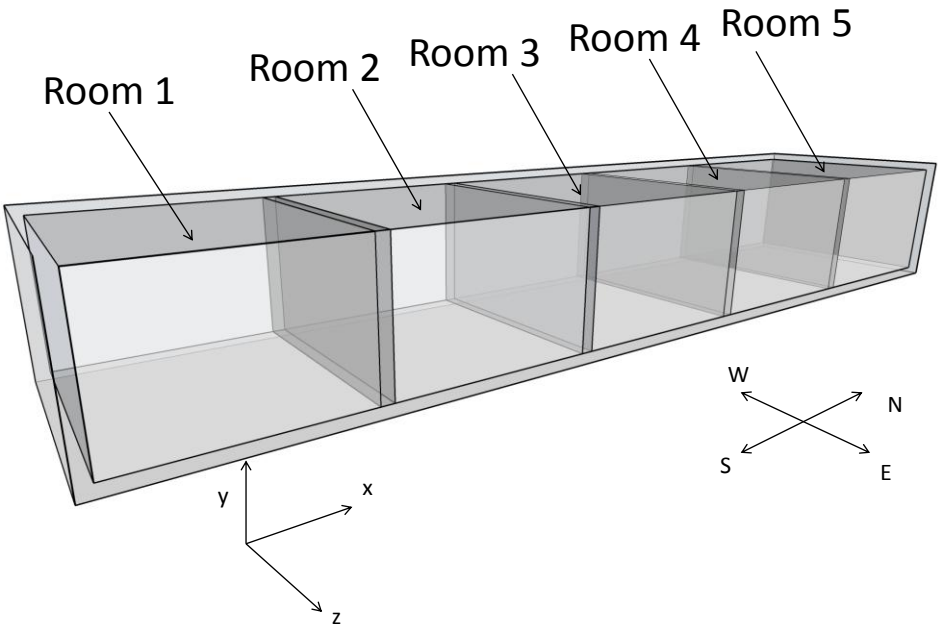

Figure. 5.2. Schematic of the 5_1_1 model

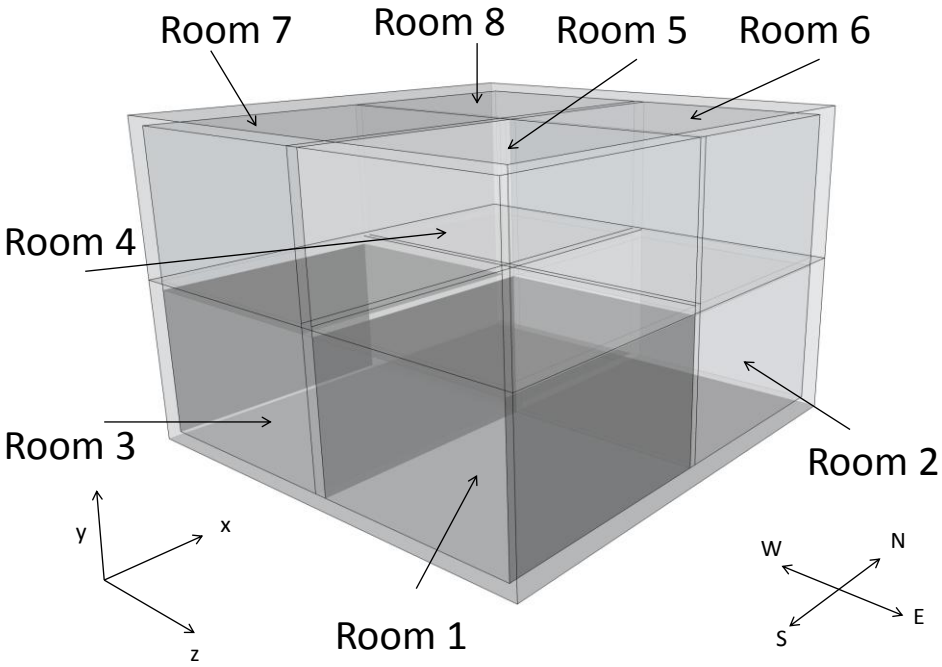

Figure. 5.3. Schematic of the 2_2_2 model

5.2.4 Comparison between ROTR excitation and excitation from simulated white goods appliances

The statistical models used in this thesis to model structure-borne sound transmission rely on the use of ROTR forces which are applied over the surface of the source plate. However, most mechanical equipment used in buildings will only excite the plate at a discrete number of points, for example, white goods appliances. Such appliances are more likely to be installed around the edges of the floor although in some modern kitchens the appliance may be located in the centre of the floor. It is therefore of interest to investigate how well ROTR excitation approximates the case where an appliance is installed at a specific location within a room.

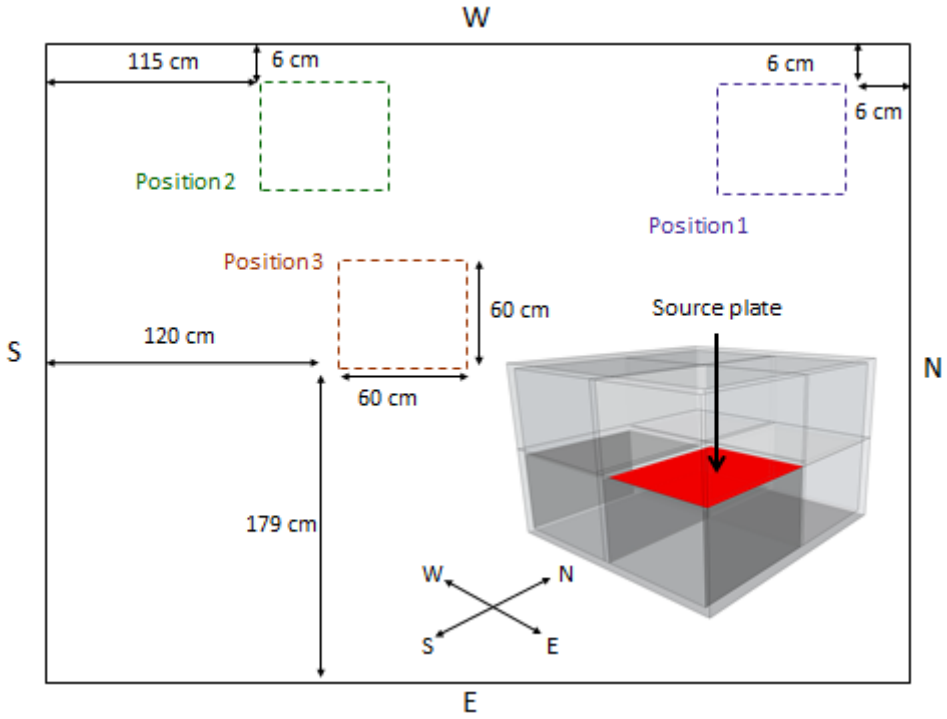

Figure 5.4. Schematic diagram of the force positions on the source plate. The plate edges are labelled North(N), East(E), South (S) and West (W) corresponding to the edges of the source plate as indicated in the inset building diagram in the bottom left corner.

An ensemble of similar 2_2_2 buildings was generated by randomly sampling the Young's modulus of the walls and floors of the building described in Section 2.42. The ELD between the upper floor of room 1 and a receiving wall/floor was computed for each ensemble member and for four different cases of excitation on the source plate. The first case is when ROTR forces are applied over the surface of the source plate and the remaining three cases are for excitation at specific locations on the source plate. To represent the driving points of the four feet of a white goods appliance, four forces with random phase (a different set of four random phases was selected for each ensemble member) were applied to the four corners of a 60cm by 60cm square. The three locations of the simulated white goods appliance on the source plate are shown in Figure 5.4.

The ensemble average ELDs with 95% confidence limits for the four cases of excitation are plotted for various receiving subsystems in the 2_2_2 buildings in Figures 5.5 to 5.. The case of ROTR excitation is represented by the solid blue line with solid markers and the remaining three dotted curves show the results for the three individual cases of white goods excitation.

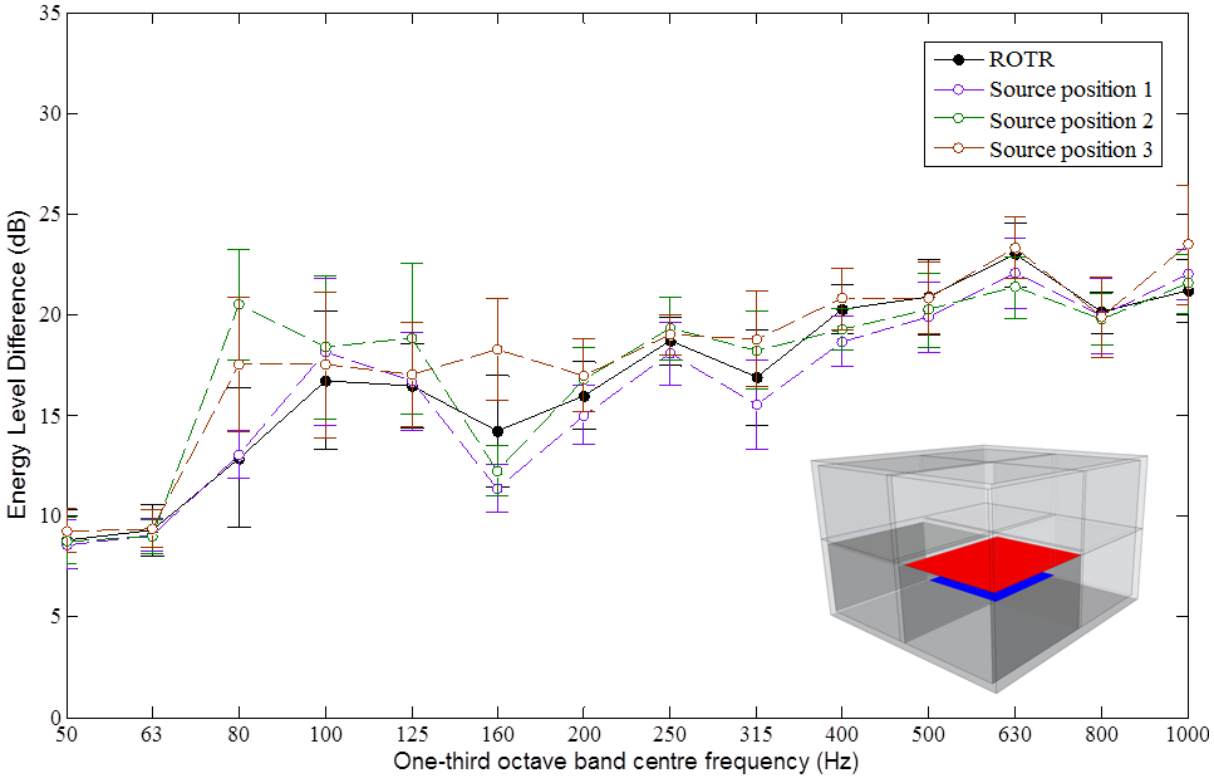

Figure 5.5. ELD between the upper floor of room 1 and the lower floor of room 4 for the case of ROTR excitation and the three cases of different white goods source position.

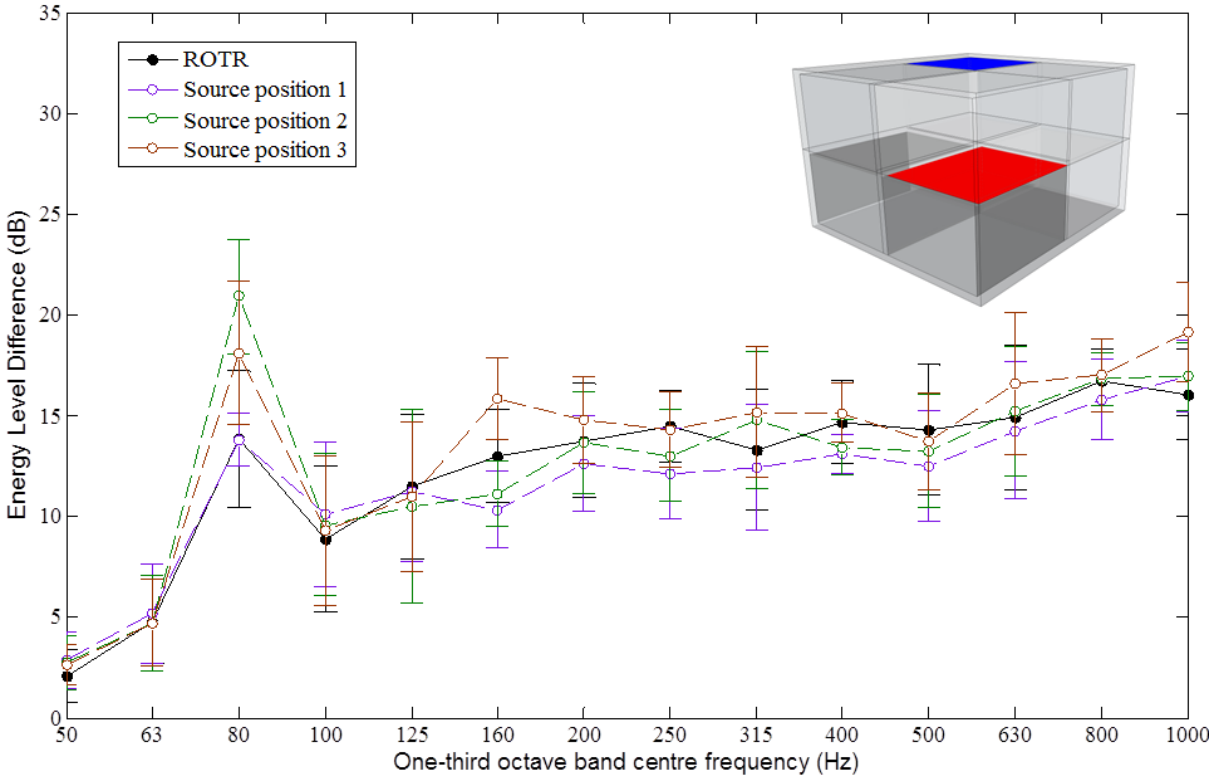

Figure 5.6. ELD between the upper floor of room 1 and the upper floor of room 8 for the case of ROTR excitation and the three cases of different white goods source position.

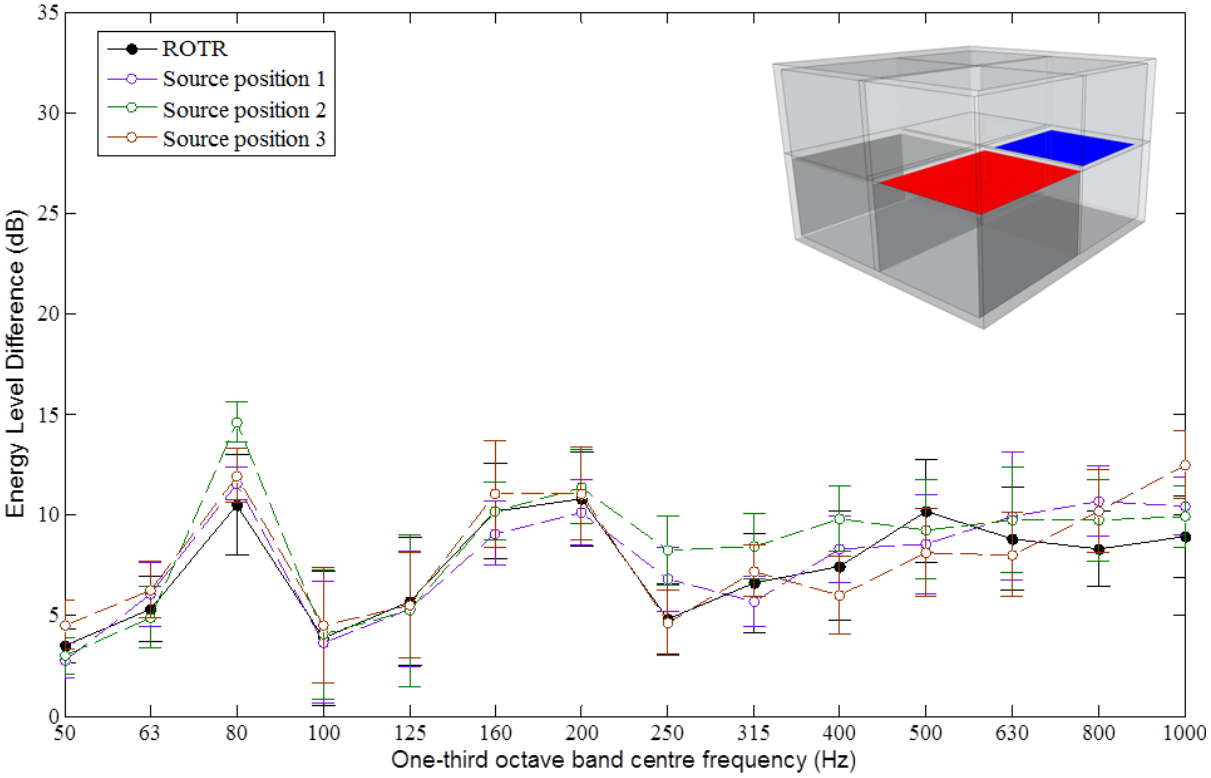

Figure 5.7. ELD between the upper floor of room 1 and the upper floor of room 2 for the case of ROTR excitation and the three cases of different white goods source position.

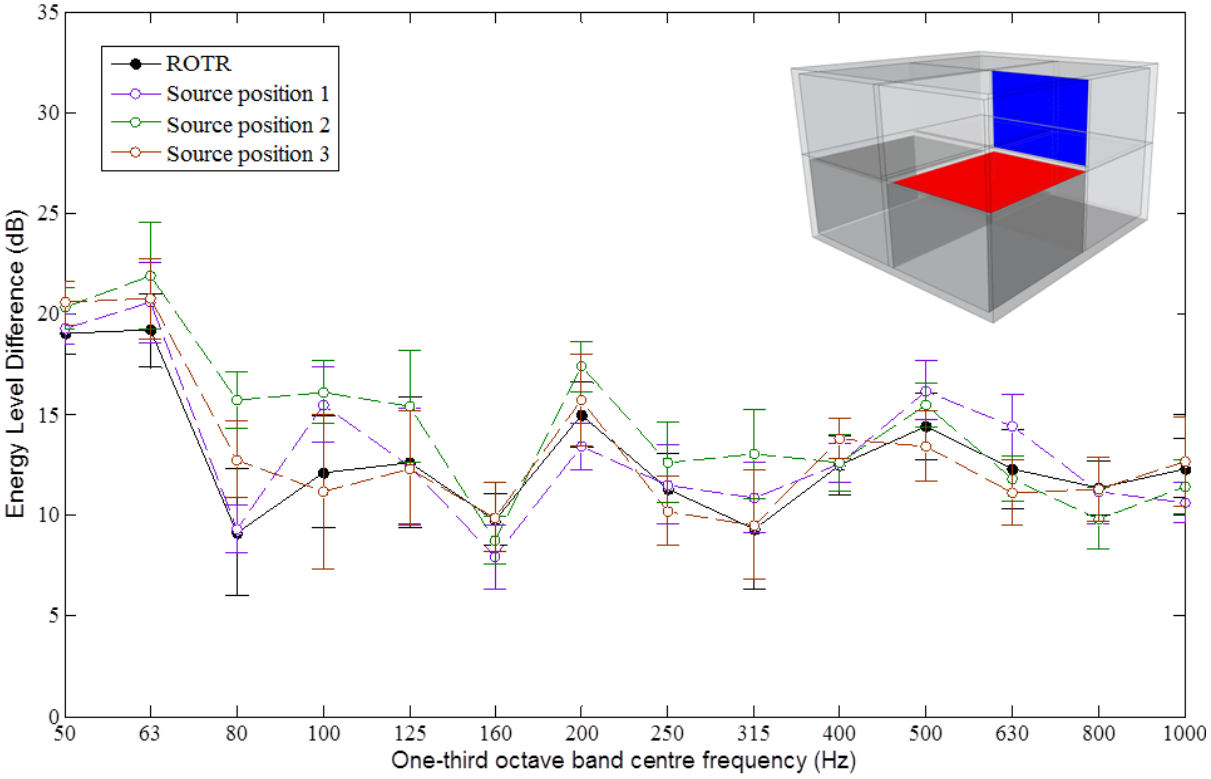

Figure 5.8. ELD between the upper floor of room 1 and the north wall of room 5 for the case of ROTR excitation and the three cases of different white goods source position.

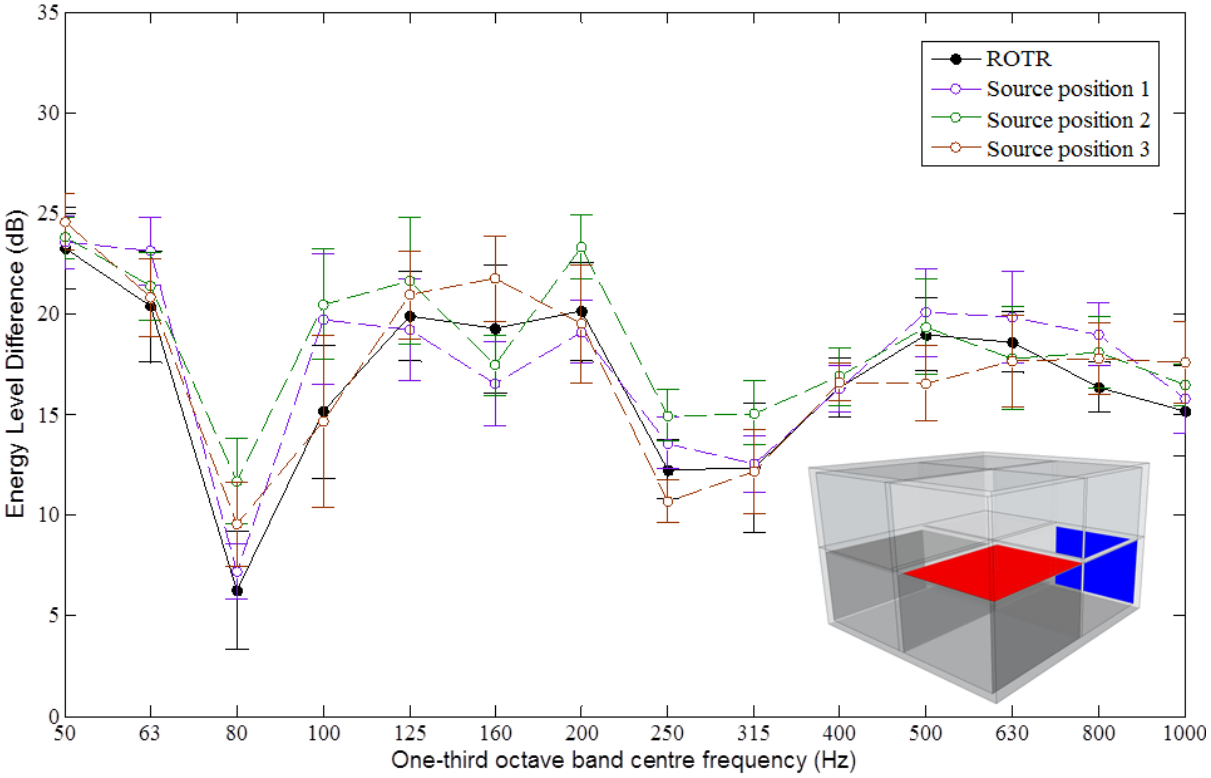

Figure 5.9. ELD between the upper floor of room 1 and the north wall of room 2 for the case of ROTR excitation and the three cases of different white goods source position.

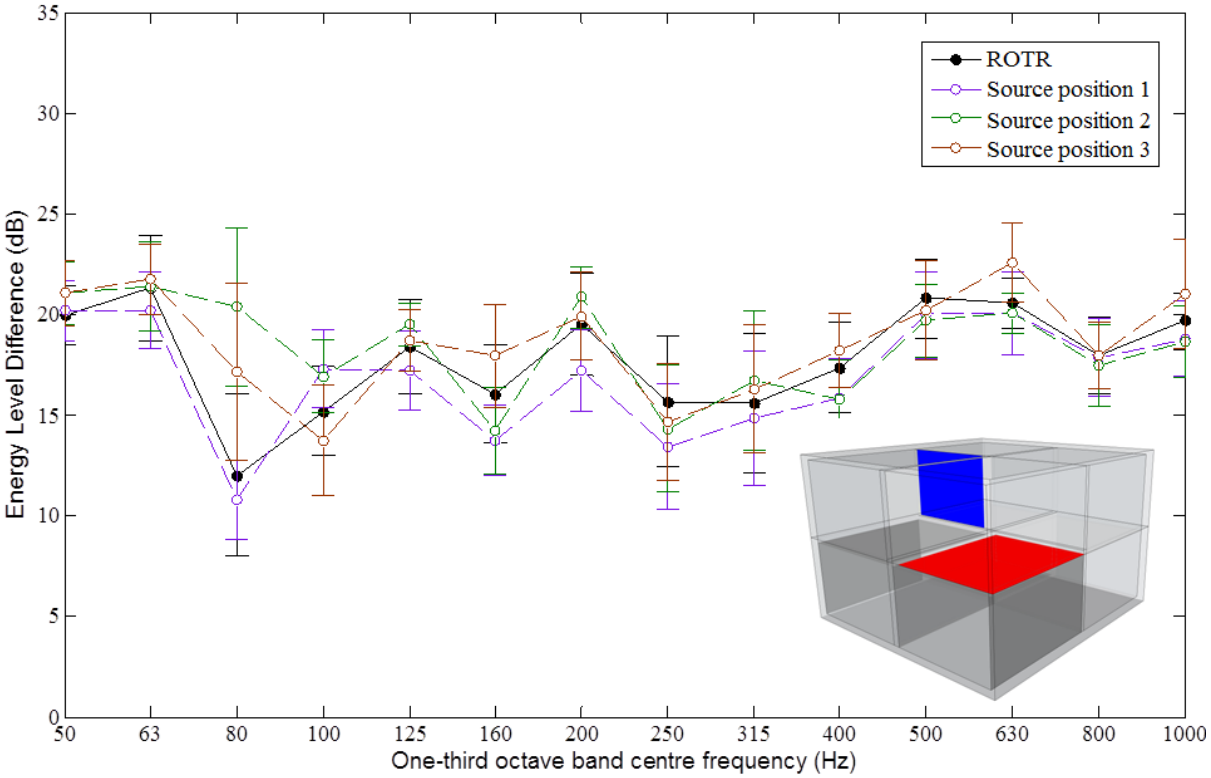

Figure 5.10. ELD between the upper floor of room 1 and the north wall of room 7 for the case of ROTR excitation and the three cases of different white goods source position.

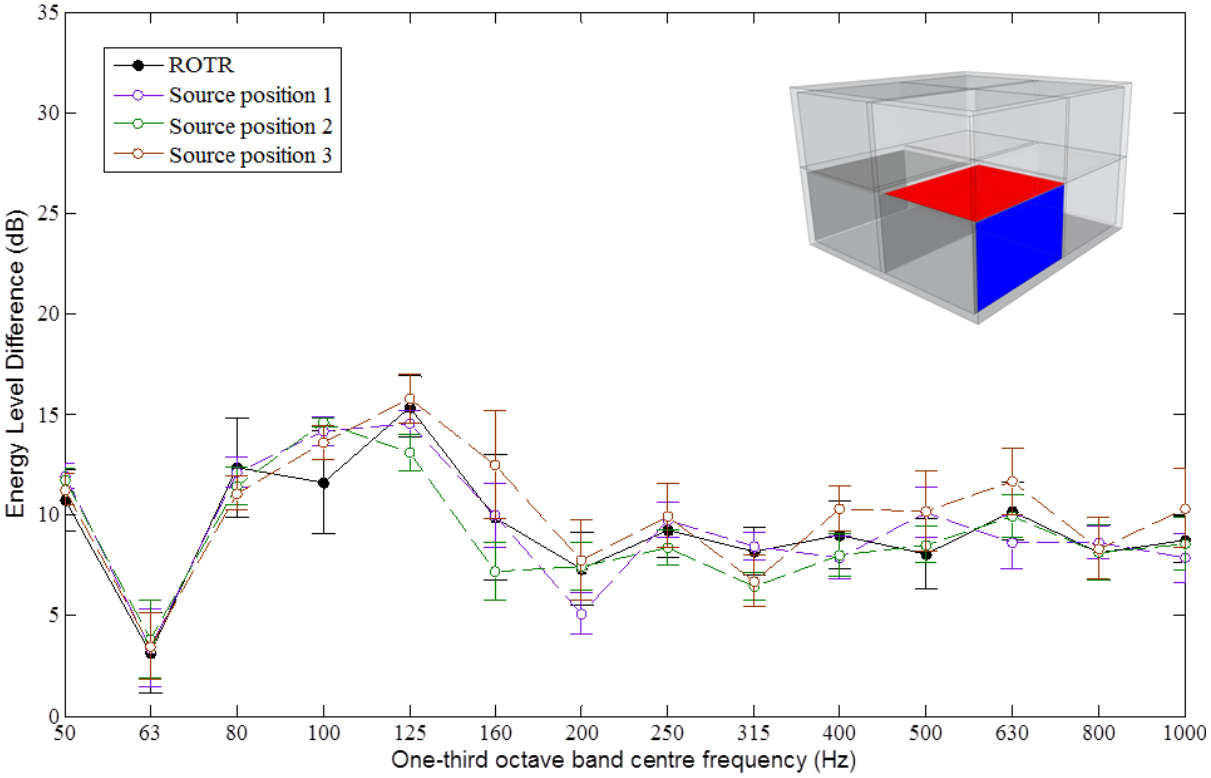

Figure 5.11. ELD between the upper floor of room 1 and the east wall of room 1 for the case of ROTR excitation and the three cases of different white goods source position

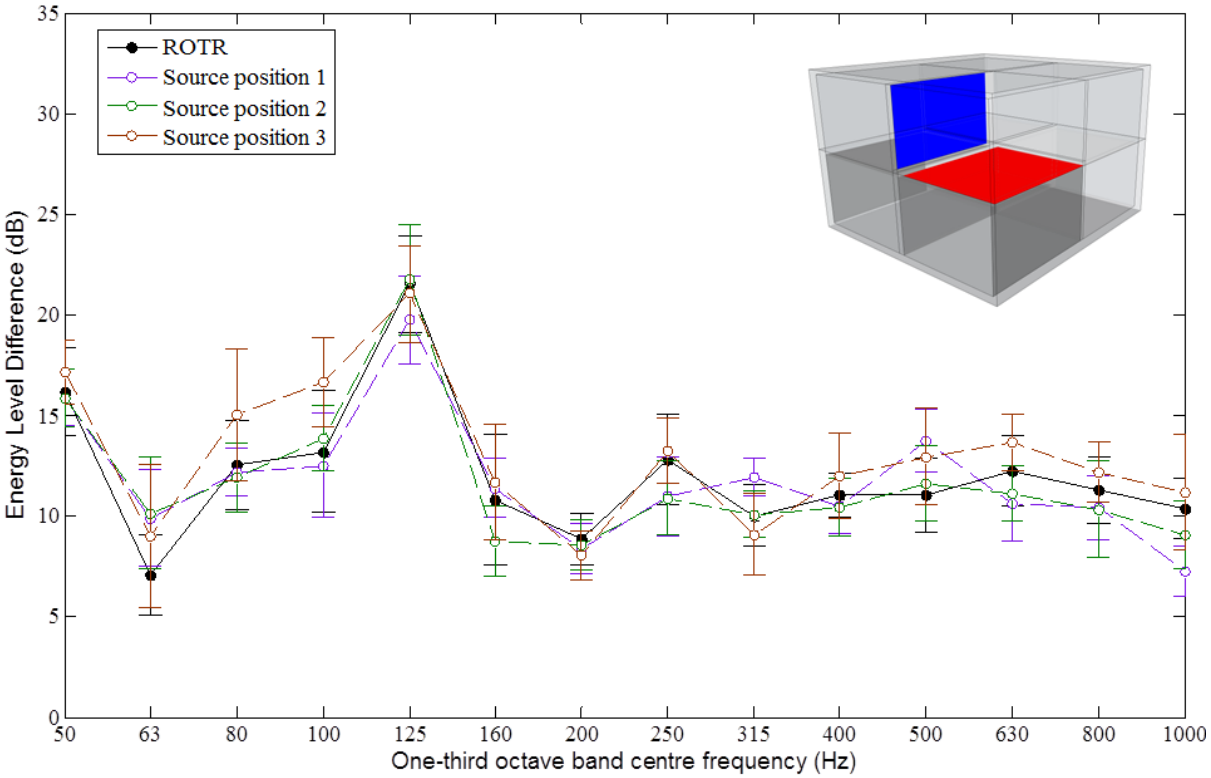

Figure 5.12. ELD between the upper floor of room 1 and the west wall of room 5 for the case of ROTR excitation and the three cases of different white goods source position

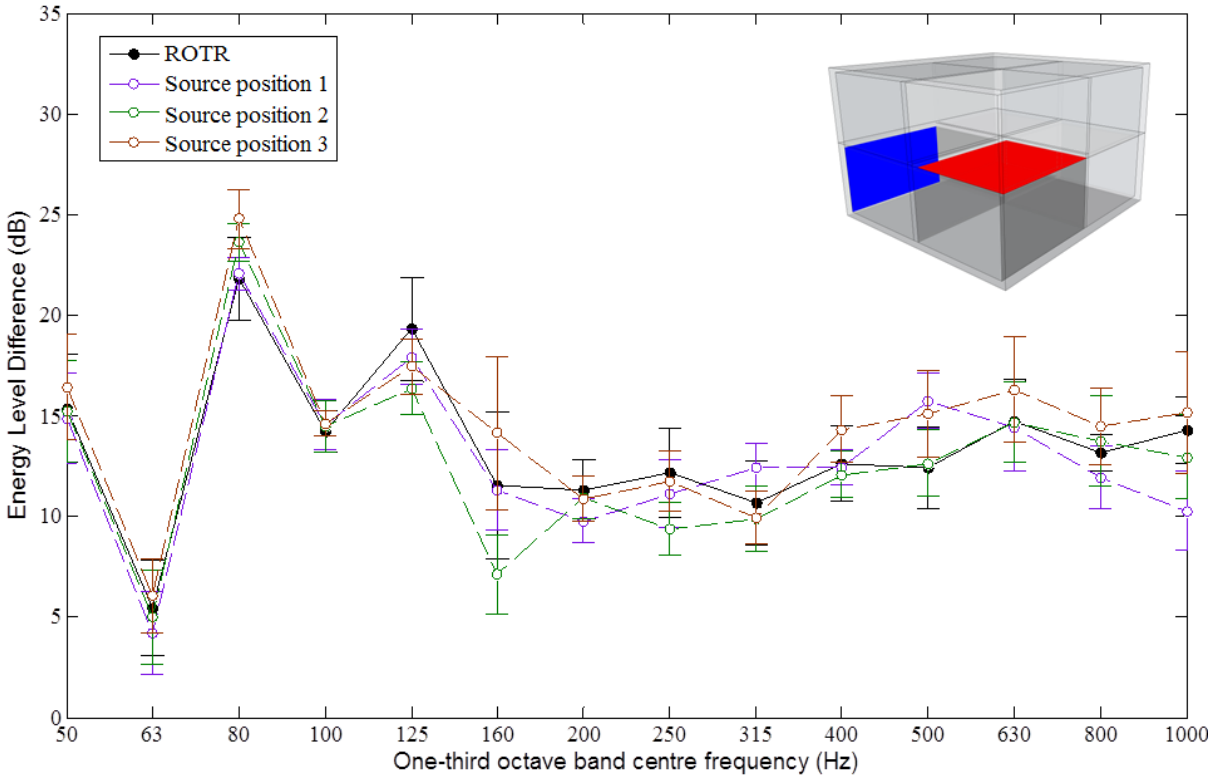

Figure 5.13. ELD between the upper floor of room 1 and the west wall of room 3 for the case of ROTR excitation and the three cases of different white goods source position

The results in Figures 2 to 10 show the ELD in receiver plates which have varying physical properties and which are can be directly connected to the source plate and separated from it by several structural junctions. The results can be generalised such that above 200Hz the 95% confidence limits between the ROTR ELDs and the three individual cases of white good excitation overlap. Below 200 Hz the 95% confidence limits overlap in the majority of one-third octave bands with a few exceptions (see for example 80Hz band in Figure 5.6.). This indicates that ROTR excitation is a good approximation to the case of white goods excitation positioned at specific locations on the source floor. Hence in the remainder of this thesis only ROTR excitation will be used to assess the validity of the predictive models. If the ELD falls within the 95% confidence limits of the ROTR result then it is reasonable to expect there will be acceptable agreement between the ELD and the case of white goods excitation.

5.3 The effect of a limited number of paths in SEA models

This section considers SEA models incorporating CLFs determined from semi-infinite plate theory to assess the effect of predicting the subsystem response using a limited number of transmission paths. Existing literature indicates that for plates with low modal overlap and low mode counts, CLFs determined from semi-infinite plate theory tend to overestimate the

strength of the coupling, see for example [17, 19, 33]. However, it is not until Chapters 6 and 7 that alternative approaches will be assessed to calculate these CLFs; hence at this stage it is reasonable to draw conclusions using semi-infinite plate theory.

5.3.1 Overview of the standard EN12354

The standard method of predicting impact sound is described in EN12354-2 [24] and considers the direct and flanking paths shown in Figure 5.14. For situations where the structure-borne sound source is located directly above the receiver room a total of four flanking paths are considered along with the direct path. When the source is located in the room next to the receiver room only two flanking paths are considered.

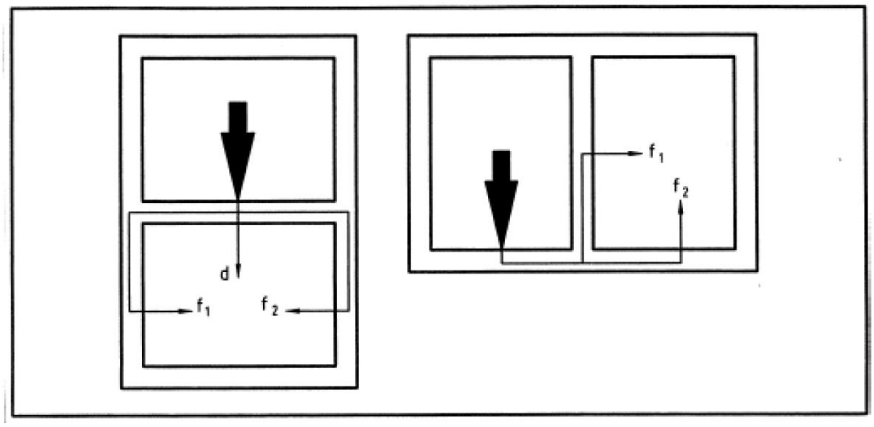

Figure. 5.14. Schematic diagram of the two situations outlined in the standard EN12354 2.

EN 12354 states that "when there are many transmission paths the use of a complete SEA model could be more appropriate" [53]. The aim of this section is to use several case studies to investigate when path analysis can and cannot give a good estimate of the total receiver subsystem energy as compared to matrix SEA.

In Section 2.2.4 it was shown that the subsystem energies calculated using matrix SEA could be written in the form of eq.2.9. Rewriting eq.2.9 for the energy , E_j, in a single subsystem j for the case of power input, $\pi_{\text{in},i}$, to subsystem i gives

$$E_j = \left[[S^1]_{ji} + [S^2]_{ji} + [S^3]_{ji} + \cdots\right]\frac{\pi_{\text{in},i}}{\omega\eta_{ii}} = \left[\frac{\eta_{ij}}{\eta_{jj}} + \sum_{k=1}^{N}\frac{\eta_{ik}\eta_{kj}}{\eta_{kk}\eta_{jj}} + \sum_{k=1}^{N}\sum_{l=1}^{M}\frac{\eta_{il}\eta_{lk}\eta_{kj}}{\eta_{ll}\eta_{kk}\eta_{jj}} + \cdots\right]\frac{\pi_{\text{in},i}}{\omega\eta_{ii}} \tag{5.6}$$

The summations in eq.5.6 are taken over all subsystems in the model. Using this definition, CLFs exist between all subsystems in the model although the value of the CLFs between

physically unconnected subsystems is set to zero. In eq.5.6 an element $[S^n]_{ji}$ multiplied by a factor $\frac{\pi_{\text{in},i}}{\omega\eta_{ii}}$ gives the contribution to the receiver subsystem energy,E_j, from the total sum of the energy contributions of all paths containing *n* coupling loss factors.

Using the approach by Magrans [26] the total number of paths containing *n* CLFs can be found by replacing all non-zero elements of S with a value of one. The element $[S^n]_{ji}$ then gives the total number of paths between subsystem *i* and subsystem *j* that contain *n* CLFs. Calculation of the number of paths and the energy contribution from all paths that contain a certain number of CLFs allows the feasibility of path analysis to be assessed. For example, if there are many of paths that contain *n* CLFs and these paths only contribute a small fraction of the total receiver subsystems energy then it is not necessary to conduct a path-by-path analysis that including paths containing *n* CLFs.

Using eq.5.6 it is also possible to determine the influence of certain groups of paths on the receiving subsystem energy. For example, the total energy contribution of all paths between source subsystem *i* and receiving subsystem *j* that contain the CLF η_{kj} can be calculated by setting the element S_{jk} equal to zero and calculating the energy in subsystem *j* using eq.2.8, $E_j^{'}$. Subtracting $E_j^{'}$ from the original value, E_j, gives the energy contribution to subsystem *j* from all paths containing the CLFs η_{kj} when power is injected into subsystem *i* this is referred to as, $E_{kj,ij}$ and this can be presented as a percentage of the total receiver subsystem energy

$$E_{kj,ij} = 100 \times \frac{E_j - E_j^{'}}{E_j} \tag{5.6}$$

5.3.2 Influence of airborne paths on plate vibration

Equation 5.6 shows that the matrix SEA solution for the energy level of a room subsystem will contain contributions from paths which include more than one CLF that couples the plate to the cavity. The assumption that the plate vibration can be predicted *in vacuo* requires that the presence of the cavity does not significantly affect the energy of the plate subsystems.

The percentage contribution from airborne paths to the energy levels of the walls and floors of the 2_1_1 building (Figure 5.1) was determined for the case of power input to the upper floor of the room 1. The process was exactly the same as outlined in Section 5.3.1 but instead of investigating the influence of a single coupling loss factor, the influence of groups of coupling loss factors connecting the plates to the air volumes was investigated. The percentage contribution of the airborne paths to the one-third octave band energy level of each plate subsystem is shown in Figure 5.15.

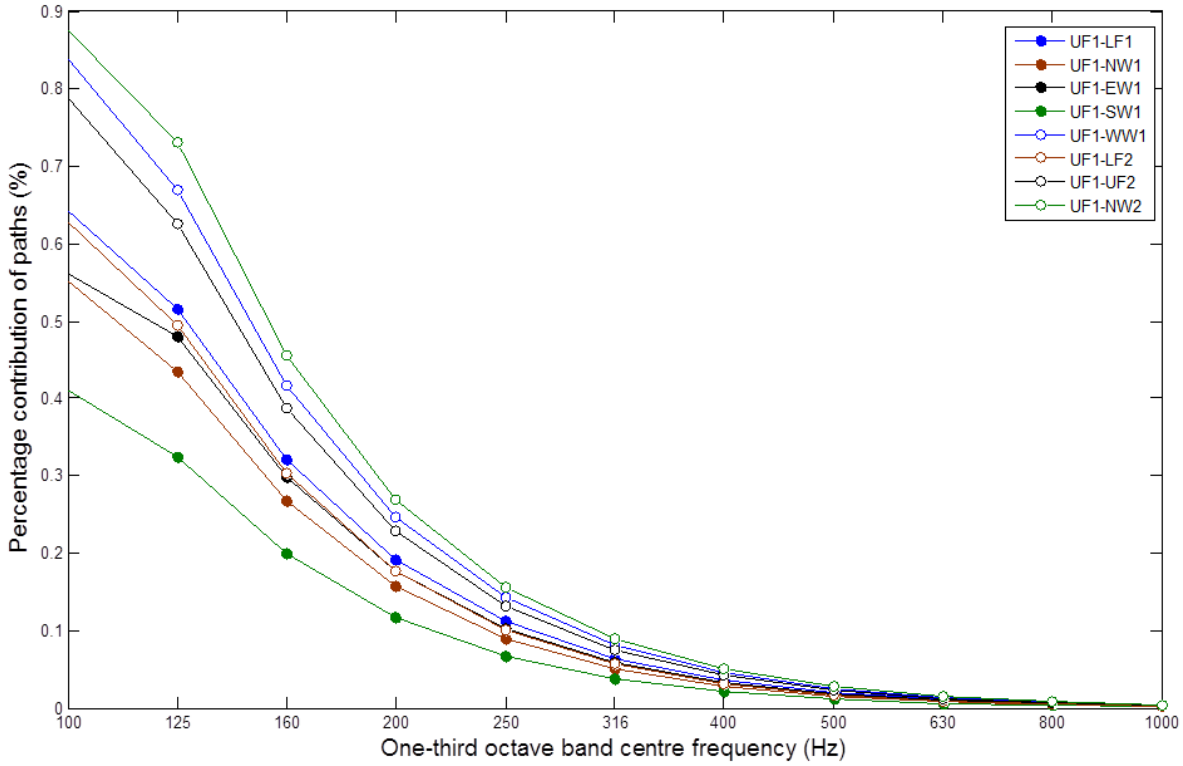

Figure 5.15. Percentage contribution to the energy levels of the walls and floors from airborne paths

Figure 5.15 shows that less than 1% of the energy in the plate subsystems arrives via airborne paths across the frequency range 100 to 1000Hz. This is an important finding as it indicates that the influence of the airborne paths on the vibration level of the walls and floors is negligible. Hence, the prediction of structure-borne sound transmission in of heavyweight buildings *in vacuo* gives a good approximation to their vibration when coupled to the air cavities contained in the rooms.

The same approach is now used to investigate the influence of the CLFs between the air volumes and the plates. These CLFs are present in all paths which enter the air volumes more

than once, hence by setting these CLFs to zero in an SEA model the energy in the air volume may be written as

$$E_{\mathrm{air,j}} = \left[E_1 \frac{\eta_{1j}}{\eta_{jj}} + E_2 \frac{\eta_{2j}}{\eta_{jj}} + E_3 \frac{\eta_{3j}}{\eta_{jj}} \ldots \right] \tag{5.7}$$

where E_k is the energy level in plate subsystem k when structure-borne power is input to plate subsystem i and all plates are completely decoupled from the air cavities.

The percentage difference in the air cavity energy levels calculated using eq.5.7 compared to eq.5.6 is shown in Figure 5.16.

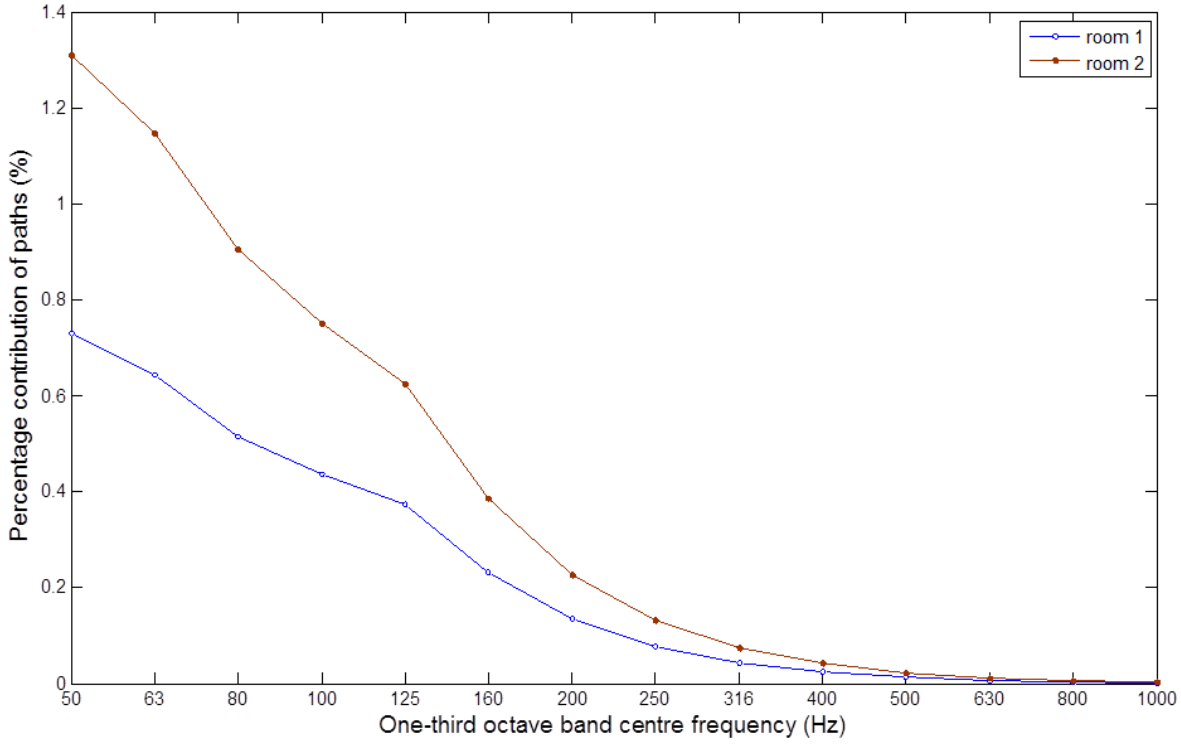

Figure 5.16. Percentage contribution to the air cavity energy arriving via paths which include more than one air volume to structure coupling loss factor.

Figure 5.16 shows that the total percentage contribution to the air volume subsystem energy from paths which include more than one air cavity to plate CLF is less than 1% across the frequency range 100 to1000Hz. This indicates that eq.5.7 is a good approximation to the result obtained through a full matrix SEA model and clearly shows that the energy in the receiver room is primarily determined by the energy of the plate subsystems.

5.3.3 Transmission to plates adjoining the source plate

This section investigates the assumption in EN12354 -2 that for flanking paths between adjacent rooms it is sufficient to include no more than one plate to plate CLF.

The approach considers the subsystem energies obtained through inverting the loss factor matrix describing the SEA power balance equations (eq.2.8). ROTR excitation is applied to the upper floor of room 1 in a 2_2_2 building (see Figure 5.3 for plate labelling). The receiver subsystems are all directly connected to the source plate so that the method described in EN12354 can be applied. To make the analysis, the energy contribution to a subsystem from all paths that contain *n* CLFs or less, E_{path}, was compared to the total energy in each subsystem as calculated by the loss factor matrix inversion, E_{Total}. A level difference between E_{Total} and E_{Path} was therefore defined as

$$10\lg\left(\frac{E_{\text{Total}}}{E_{\text{Path}}}\right) \tag{5.8}$$

which gives the difference in decibels between the full SEA solution and a path analysis where the paths contain *n* coupling loss factors or less. The results for the 100Hz and 1000Hz one-third octave bands are shown in Figures 5.17 and 5.18 respectively. The total number of paths containing *n* coupling loss factors or less was also calculated (see Section 5.3.1) and the results are plotted against *n* in Figure 5.19.

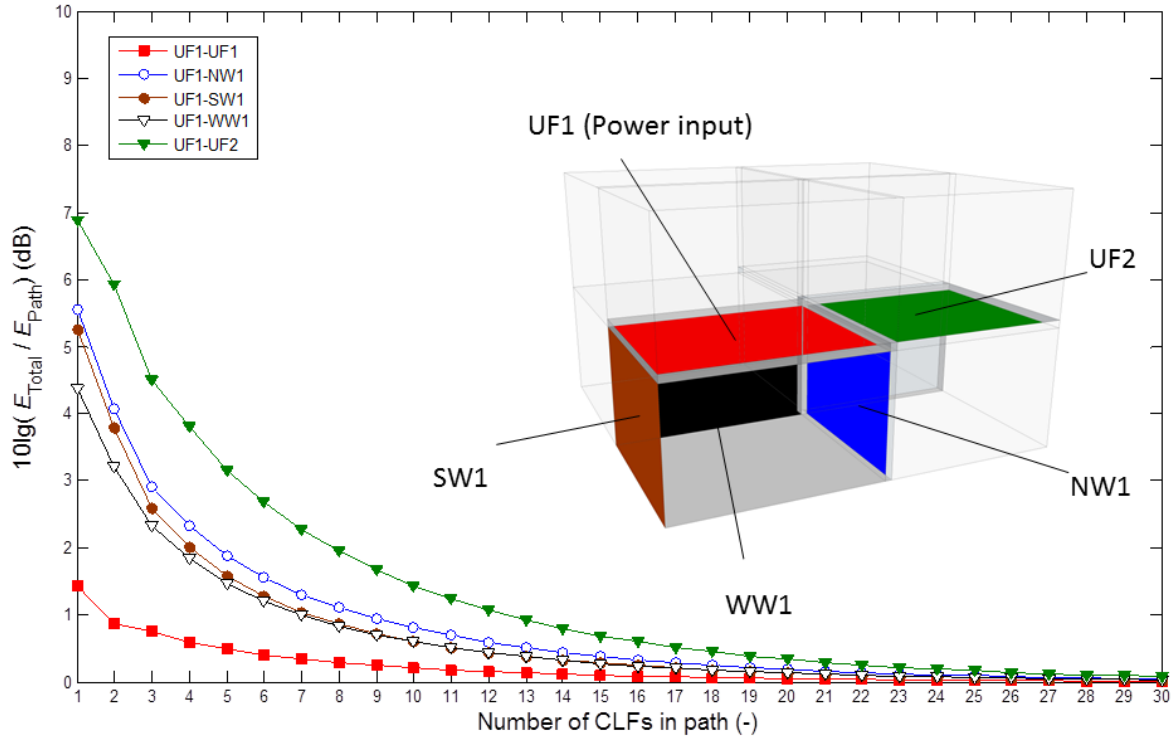

Figure 5.17. Difference between the total energy in each subsystem and the cumulative sum of all contributions from paths up to and including paths containing *n* CLFs: 100Hz one-third octave band

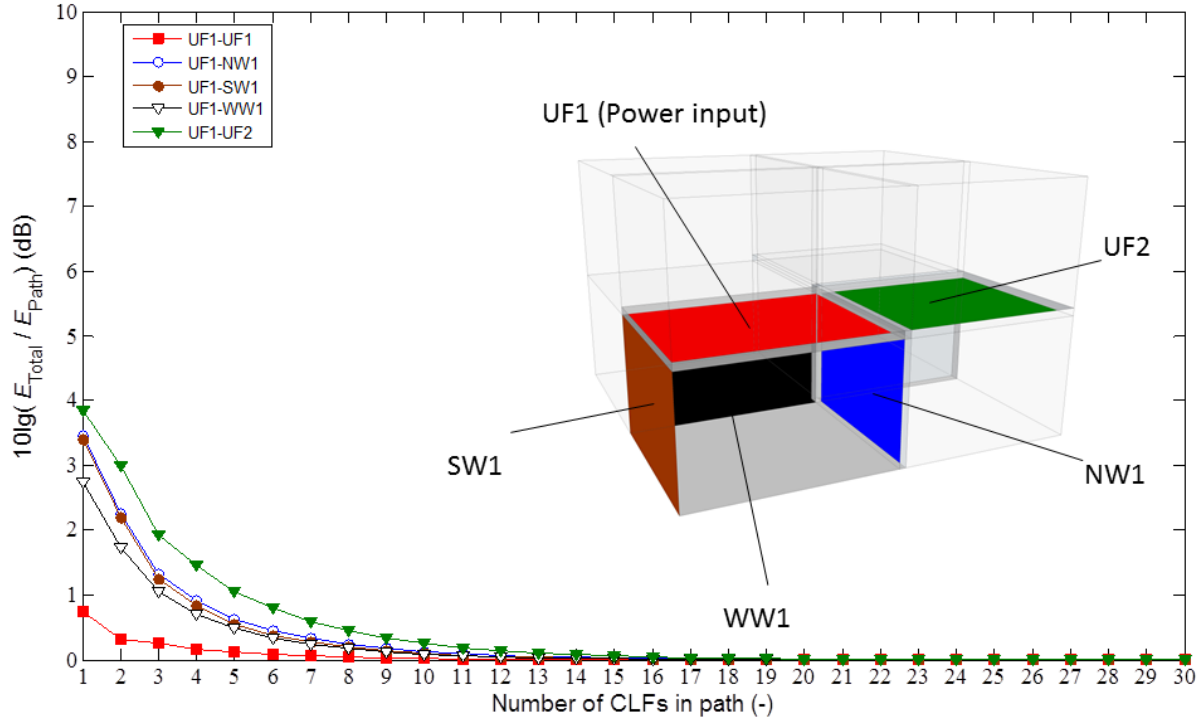

Figure 5.18. Difference between the total energy in each subsystem and the cumulative sum of all contributions from paths up to and including paths containing *n* CLFs: 1000Hz one-third octave band.

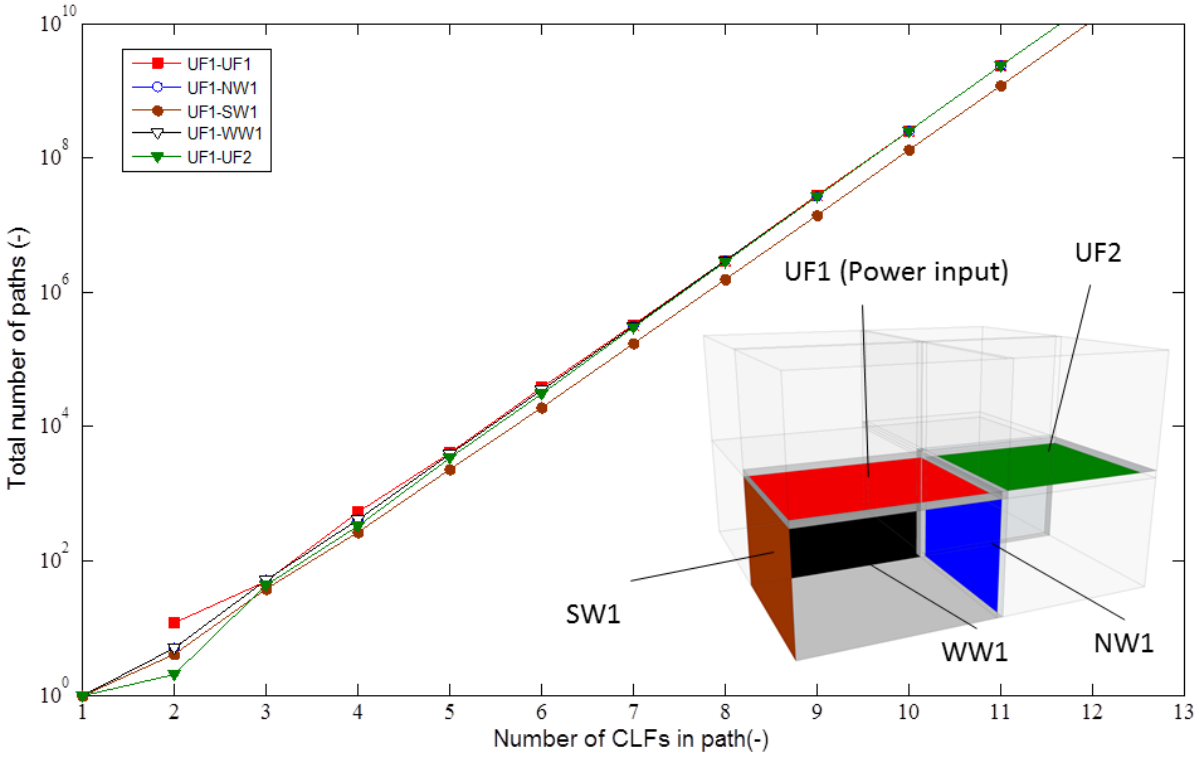

Figure 5.19. Total number of paths up to and including paths containing *n* CLFs.

Figure 5.19 shows that there is one path containing a single CLF between the source and each of the receiver subsystems: UF2, SW1, NW1 and WW1. There are no paths returning to the source subsystem that contain less than two coupling loss factors. Hence, the total energy in the source subsystem containing paths which have less than two coupling loss factors is given by eq.2.11. From Figures 5.17 and 5.18 this approximation is between 1.5dB to 0.7dB lower than the total energy calculated by matrix SEA. At 100Hz, using EN12354 to estimate the energy levels of the receiver subsystems gives results which differ from matrix SEA by 4.4 to 6.9dB. At 1000Hz the agreement slightly improves and the energy levels predicted by EN12354 are between 2.8 to 3.9dB lower than matrix SEA.

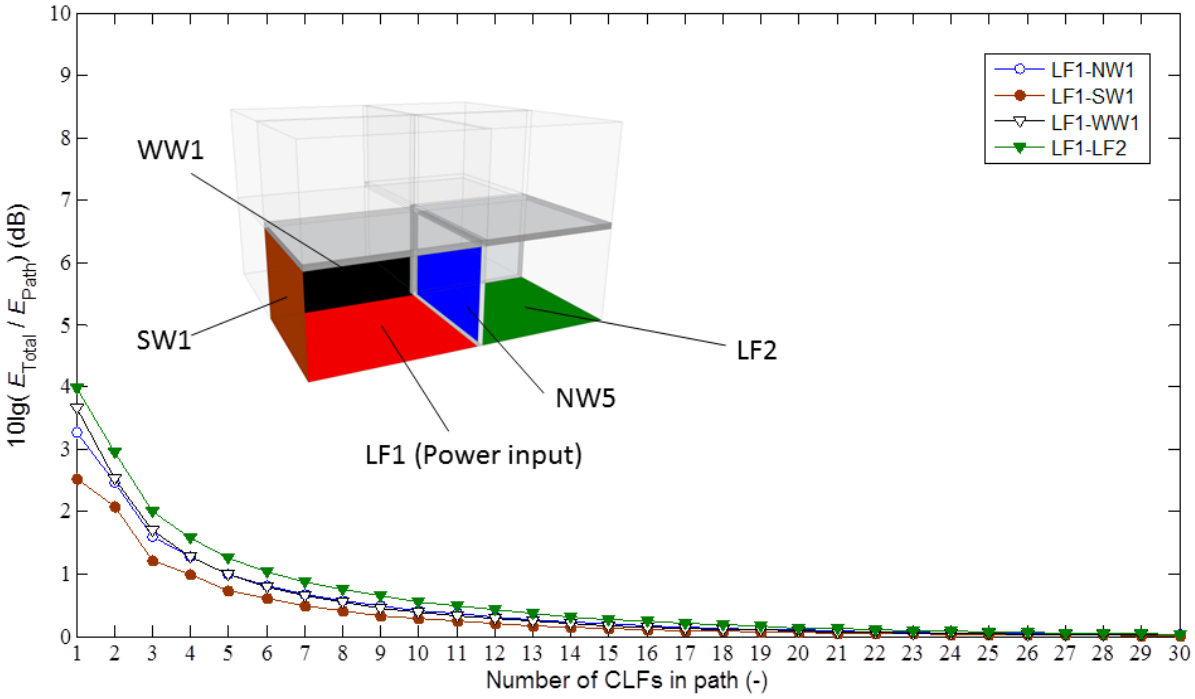

Figure.5.20. Difference between the total energy in each subsystem and the cumulative sum of all contributions from paths up to and including paths containing *n* CLFs: 100Hz one-third octave band, power input to lower floor of room 1.

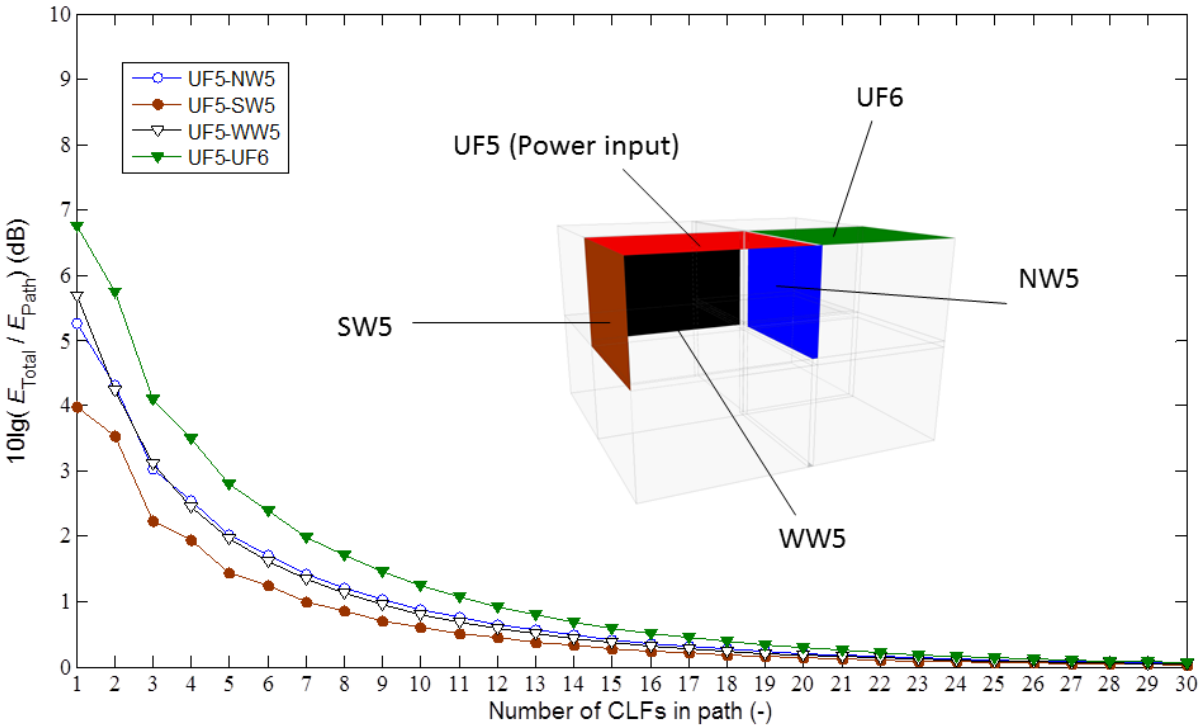

Figure.5.21. Difference between the total energy in each subsystem and the cumulative sum of all contributions from paths up to and including paths containing *n* CLFs: 100Hz one-third octave band, power input to upper floor of room 5.

Figures 5.10 and 5.11 show the results in the 100Hz one-third octave band when power is input to the lower floor of room 1 and the upper floor of room 5 respectively. Due to the symmetry of the building around the plane of the middle floor both cases are identical except that the total loss factor of the lower floor is significantly higher than the upper floor (see Section 5.2.1). When the lower floor is excited all energy levels calculated using EN12354 in the adjoining plates are within 4dB of matrix SEA. However for the case of power input to the upper floor of room 5 the energies in the adjoining plates calculated using EN12354 are within 7dB of matrix SEA. This indicates that EN12354 has lower errors when the internal losses of the source subsystem are high; although it could also be questioned whether a highly-damped plates are always sufficiently reverberant to be considered as SEA subsystems.

Figure 5.19 shows that the number of paths grows exponentially. Hence Figures 5.17 and 5.18 show that the difference between matrix SEA and path analysis results tends towards zero with an increasing number of paths.

5.3.4 Transmission to non-contiguous subsystems

In this section the feasibility of the path analysis approach to receiving subsystems that are not directly connected to the source subsystem is investigated. EN12354 does not give direct instructions about which paths should be included in the analysis but it does state that more paths will be necessary in these situations. Two cases are considered here: (1) when the receiving room is connected diagonally across an X-junction from the source room and when the receiving room is located several junctions away from the source room. For case (1) power is input to the upper floor of room 1 of the 2_2_2 building and the receiving plates are located in rooms 4 and 8 (see Figure 5.22a to 5.24c). For case (2) power is input to the upper floor of room 1 of the 5_1_1 building (see Figure 5.25a to 5.26e) and the energy levels in all the remaining plates in the building are investigated (note that the eastern and western walls are identical for the 5_1_1 building hence only the results for the eastern walls are shown).
The results for subsystems connected to the two receiver rooms in the 100Hz and 1000Hz one-third octave bands for the 2_2_2 building are shown in Figures 5.22 and 5.23 respectively. The total number of paths containing *n* CLFs or less is shown in Figures 5.24.

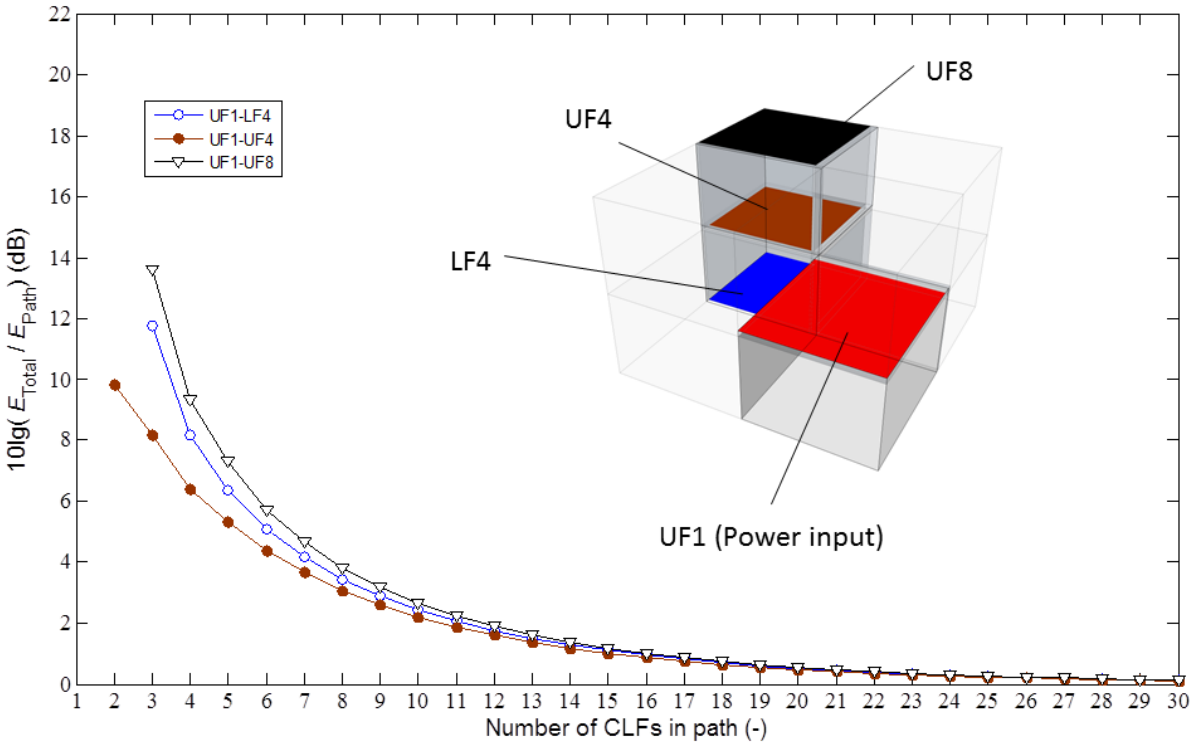

Figure 5.22.a) Difference between the total energy in each subsystem and the cumulative sum of all contributions from paths up to and including paths containing *n* CLFs: 100Hz one-third octave band level. Floors of room 4 and 8 of the 2_2_2 building..

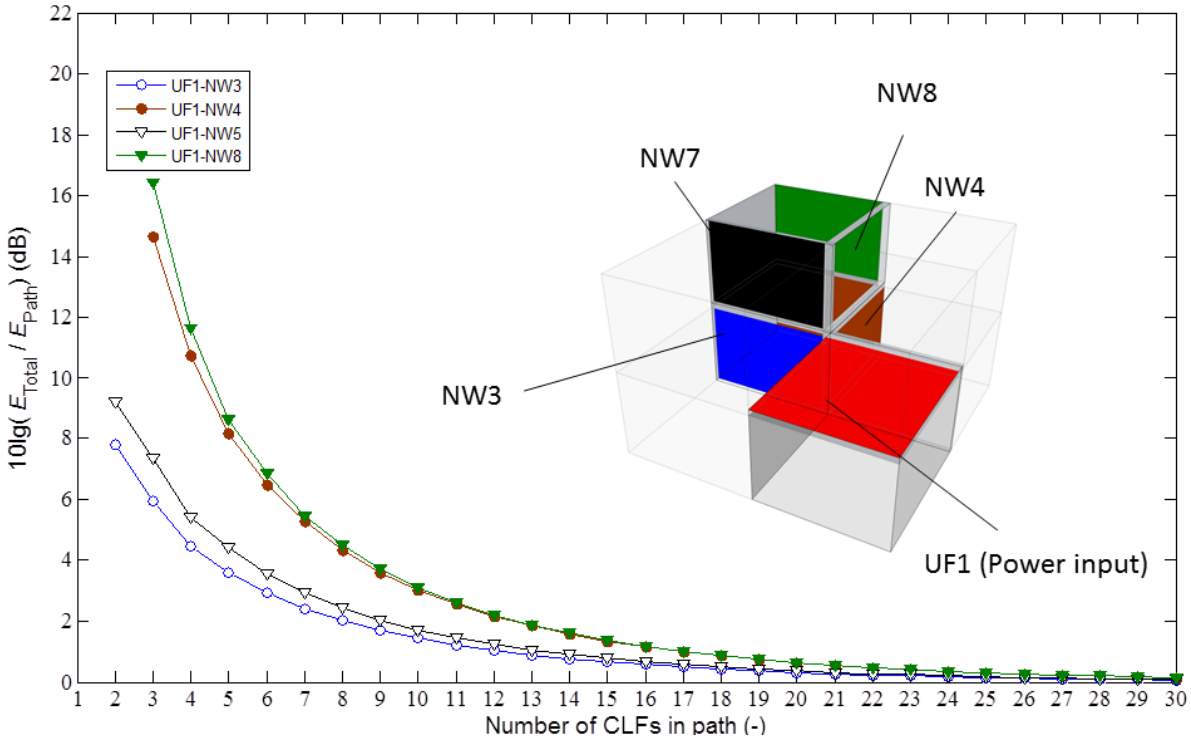

Figure 5.22.b) Difference between the total energy in each subsystem and the cumulative sum of all contributions from paths up to and including paths containing *n* CLFs: 100Hz one-third octave band level. Separating walls of room 4 and 8 of the 2_2_2 building.

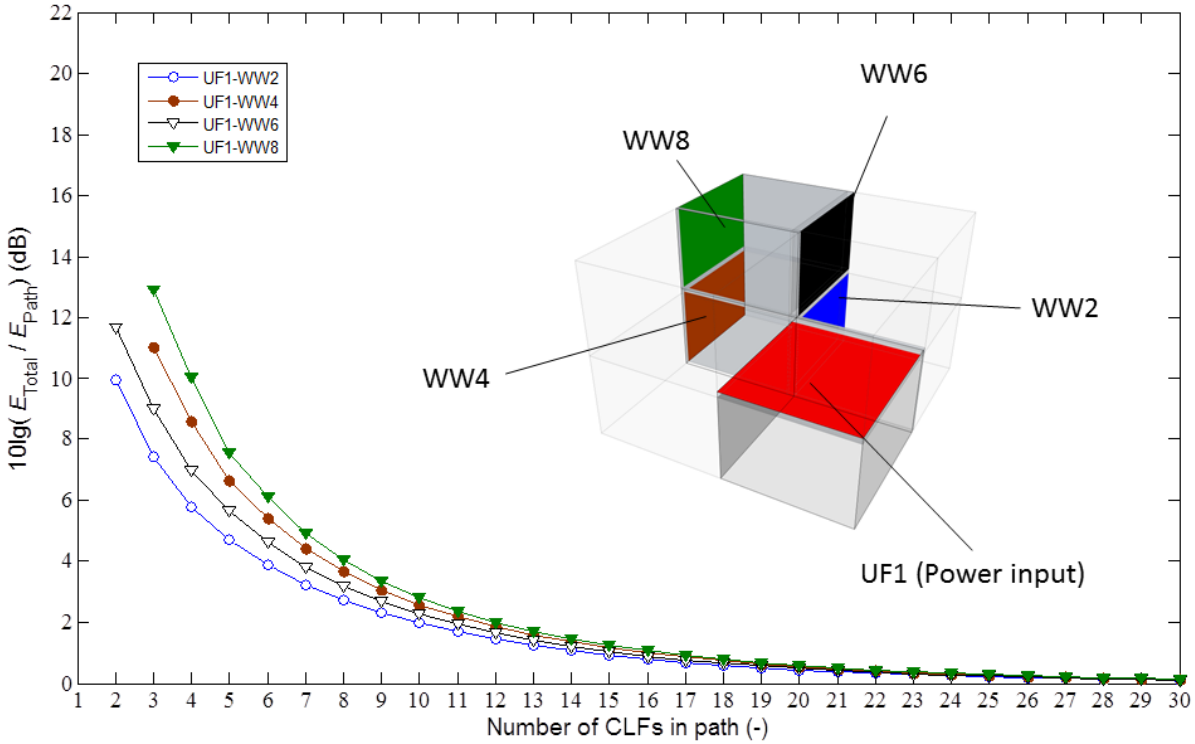

Figure 5.22c). Difference between the total energy in each subsystem and the cumulative sum of all contributions from paths up to and including paths containing *n* CLFs: 100Hz one-third octave band level. Flanking walls of room 4 and 8 of the 2_2_2 building.

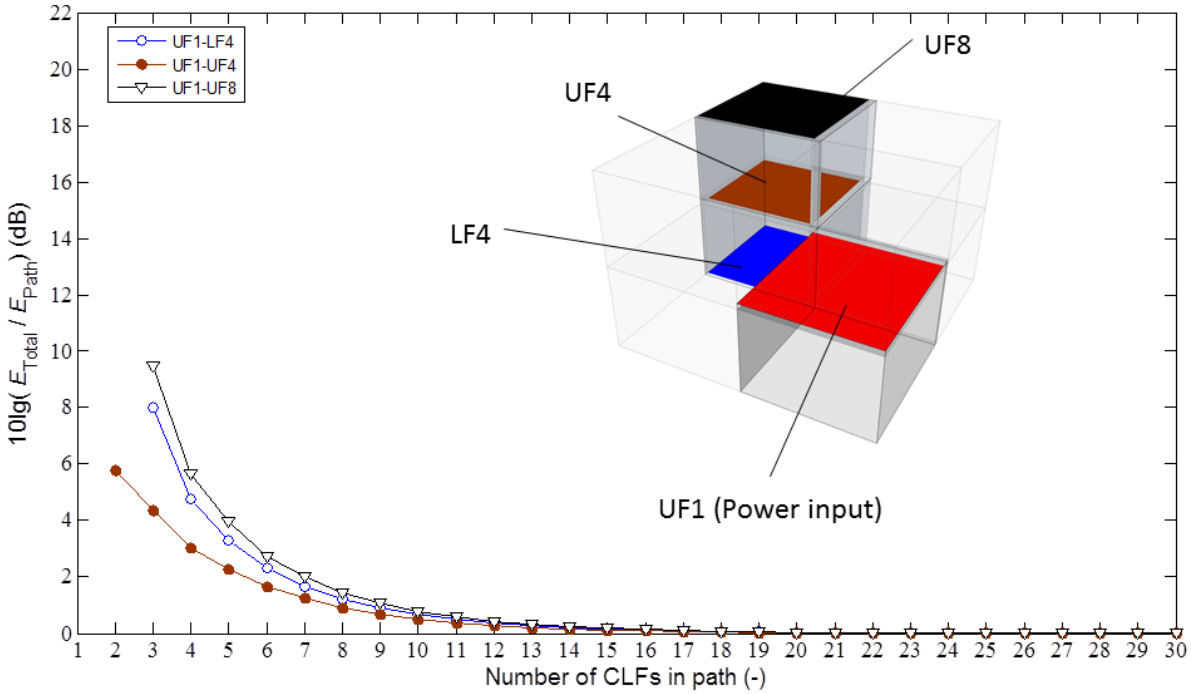

Figure 5.23a). Difference between the total energy in each subsystem and the cumulative sum of all contributions from paths up to and including paths containing *n* CLFs: 1000Hz one-third octave band. Floors of room 4 and 8 of the 2_2_2 building.

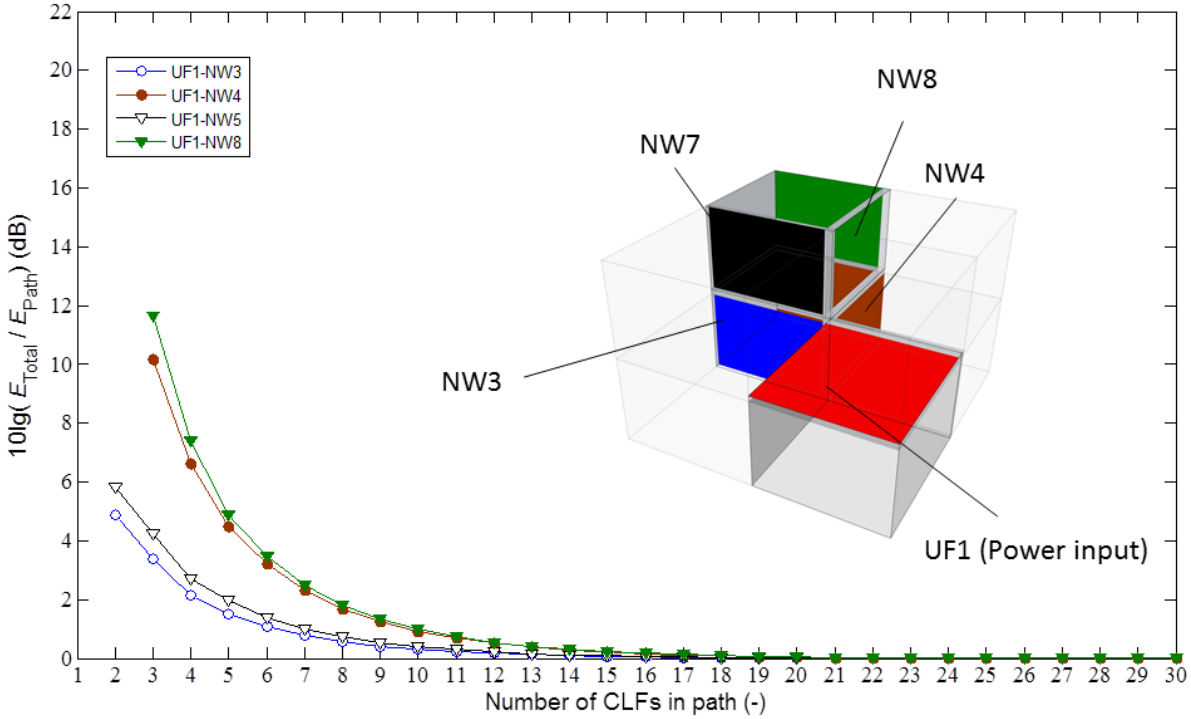

Figure 5.23b). Difference between the total energy in each subsystem and the cumulative sum of all contributions from paths up to and including paths containing *n* CLFs: 1000Hz one-third octave band. Separating walls of room 4 and 8 of the 2_2_2 building.

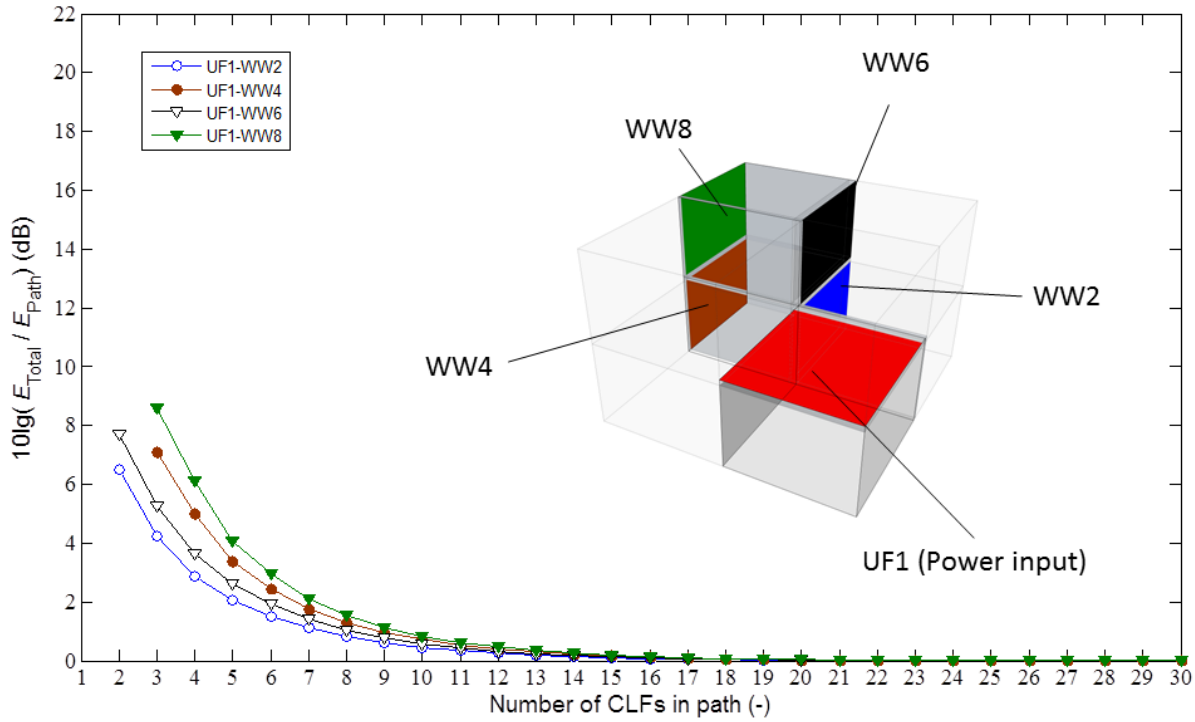

Figure 5.23c). Difference between the total energy in each subsystem and the cumulative sum of all contributions from paths up to and including paths containing *n* CLFs: 1000Hz one-third octave band. Flanking walls of room 4 and 8 2_2_2 building.

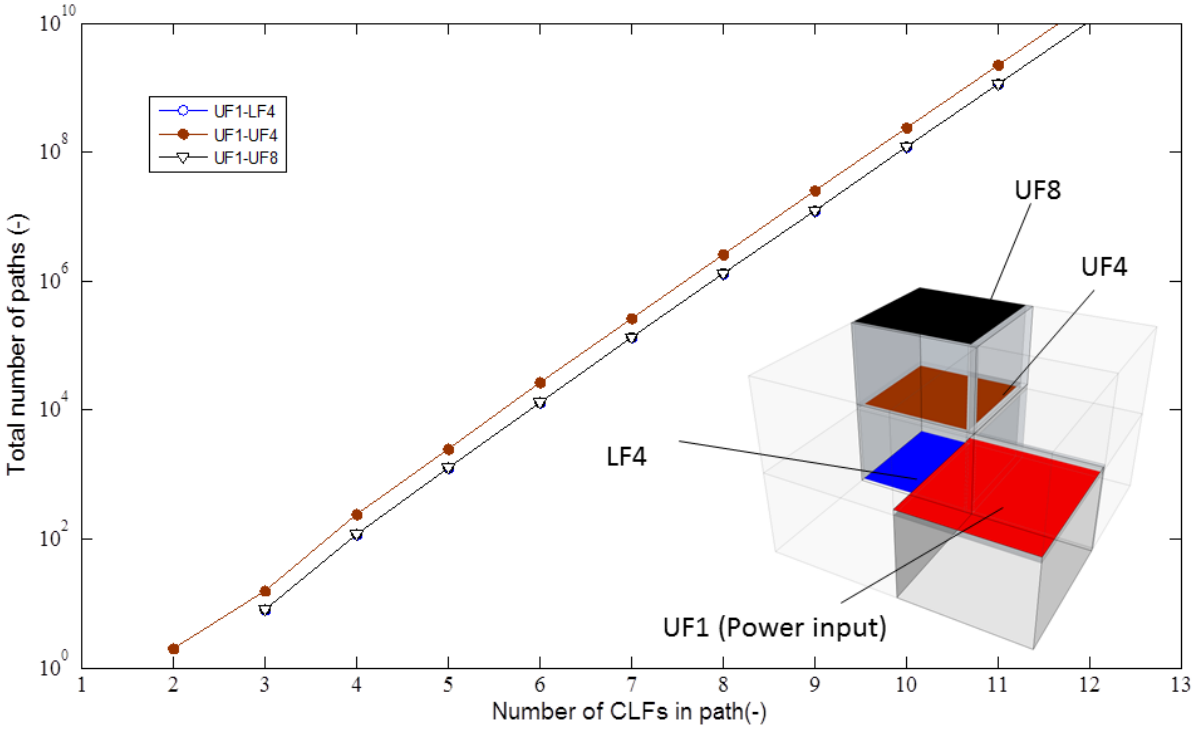

Figure 5.24a). Total number of paths up to and including paths containing *n* CLFs. Floors walls of room 4 and 8 2_2_2 building.

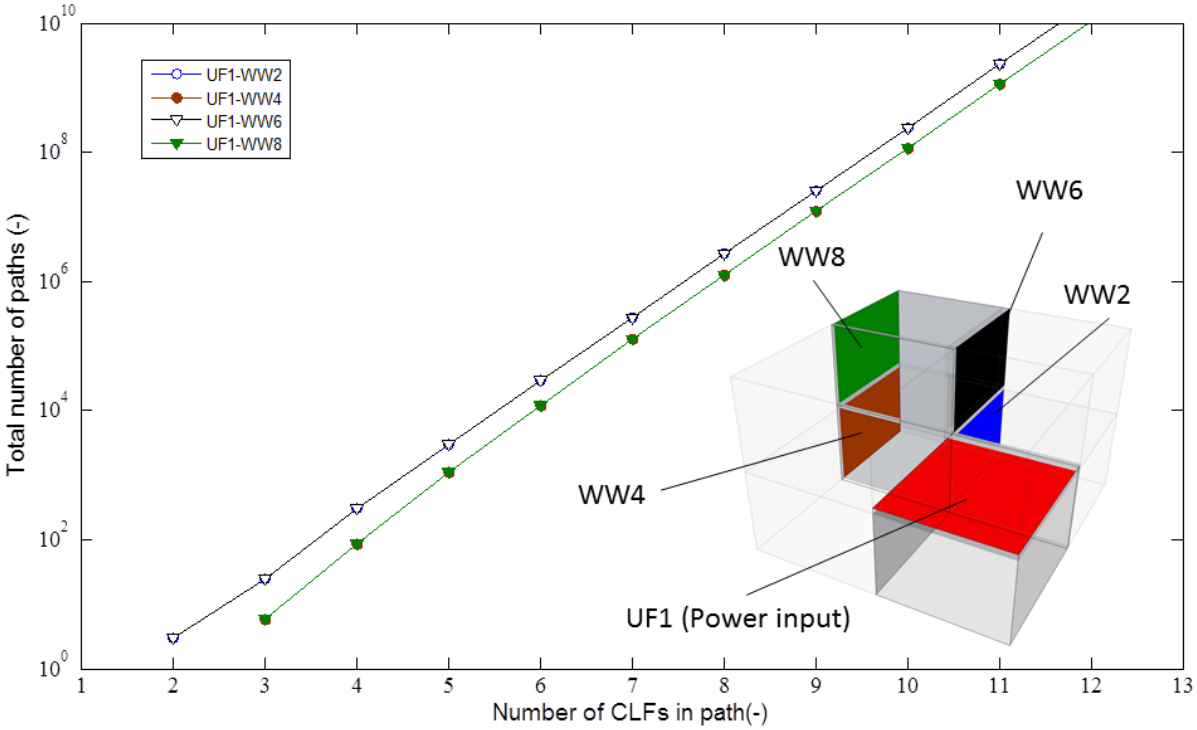

Figure 5.24b). Total number of paths up to and including paths containing *n* CLFs. Separating walls of room 4 and 8 2_2_2 building.

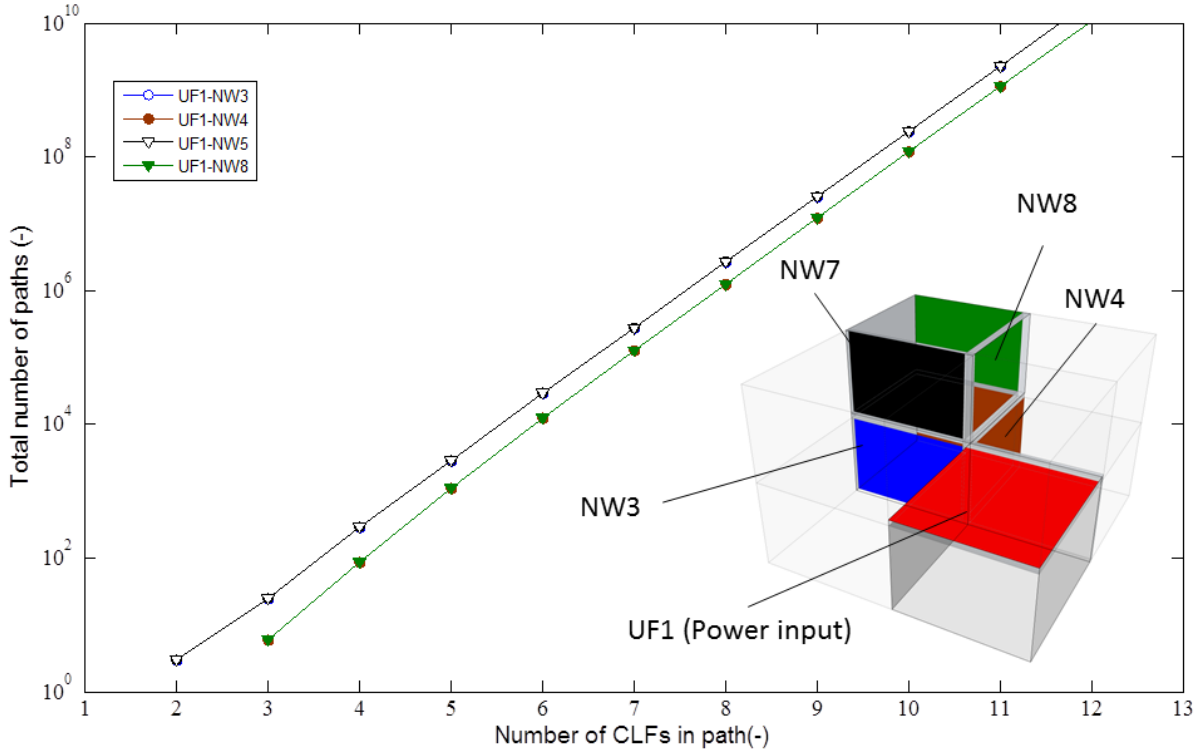

Figure 5.24c). Total number of paths up to and including paths containing *n* CLFs. Flanking walls of room 4 and 8 2_2_2 building.

The receiver subsystems are divided into two sets: the minimum number of CLFs in any path from the source subsystem to the receiver subsystems in the first set is two and in the second

set the minimum number of CLFs in any path from the source subsystem to the receiver subsystems is three. The minimum number of CLFs in any path between subsystem A and subsystem B will be referred to as the direct path.

In a majority of cases the contribution to the total energy from the direct path is larger for subsystems belonging to the first set, than for subsystems in the second set. The energies of the subsystems belonging to the first set, calculated using the direct paths only, are between 8 and 12dB lower than the matrix SEA calculations in the 100Hz one-third octave band. In the 1000Hz one-third octave band the level difference is between 5 and 8dB. For the second set these values are between 11 and 16.5dB for the 100Hz one-third octave band and between 7.3 and 12dB in the 1000Hz one-third octave band.

The gradient of the curves in Figures 5.22 and 5.23 suggests that the effect of adding paths containing large numbers of CLFs decreases as the maximum number of CLFs in the path increases. After including energy contributions from paths which contain two or more CLFs than the direct path, the convergence to matrix SEA slows considerably. Figures 5.22a and 5.23 show that including these paths would give a result that is between 3 and 8dB at 100Hz and 2 and 4dB at 1000Hz. Figures 5.24a to 5.24c show that there are 300 to 3000 such paths between the source and receiving subsystems.

The 100Hz one-third octave band results for the case of power input to the upper floor of room 1 of the 5_1_1 building are shown in Figures 5.25a to 5.25d and the 1000Hz one-third octave band results are shown in Figures 5.26a to 5.26d. The total number of paths containing *n* CLFs or less is shown in Figure 5.27a to 5.27d.

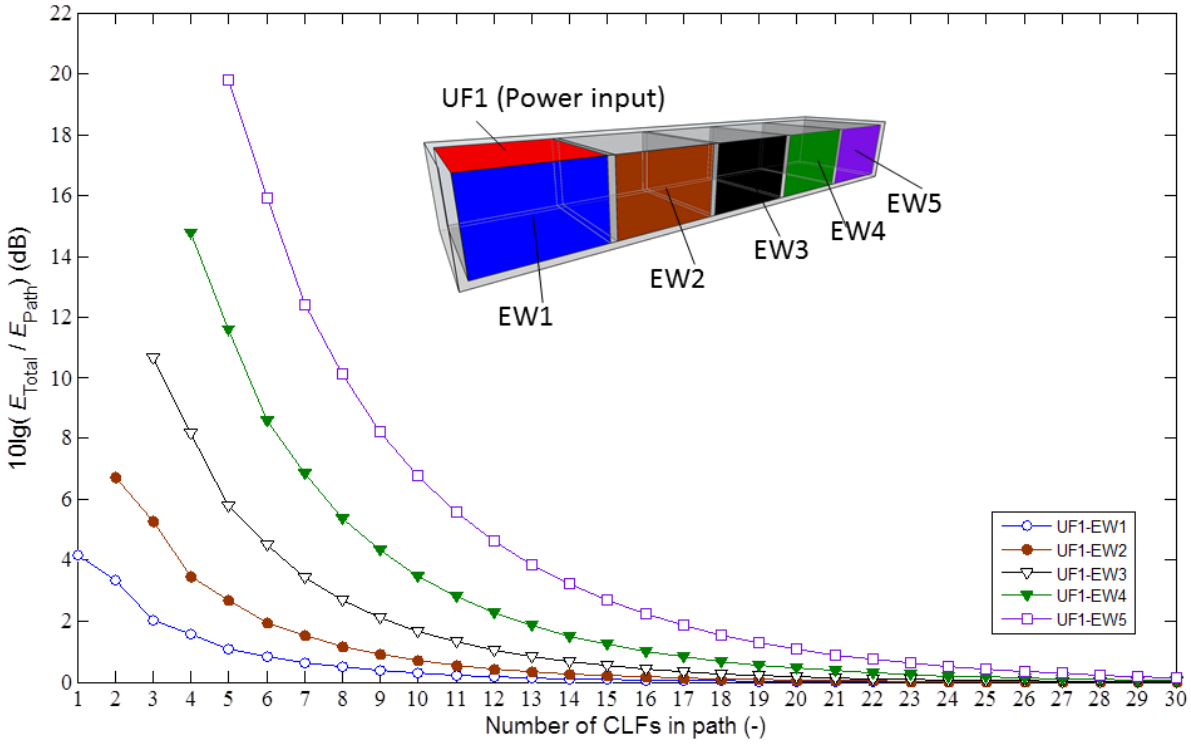

Figure 5.25a. 100Hz one-third octave band level difference between the total energy in each subsystem and the cumulative sum of all contributions from paths up to and including paths containing *n* CLFs. Flanking walls of 5_1_1 building.

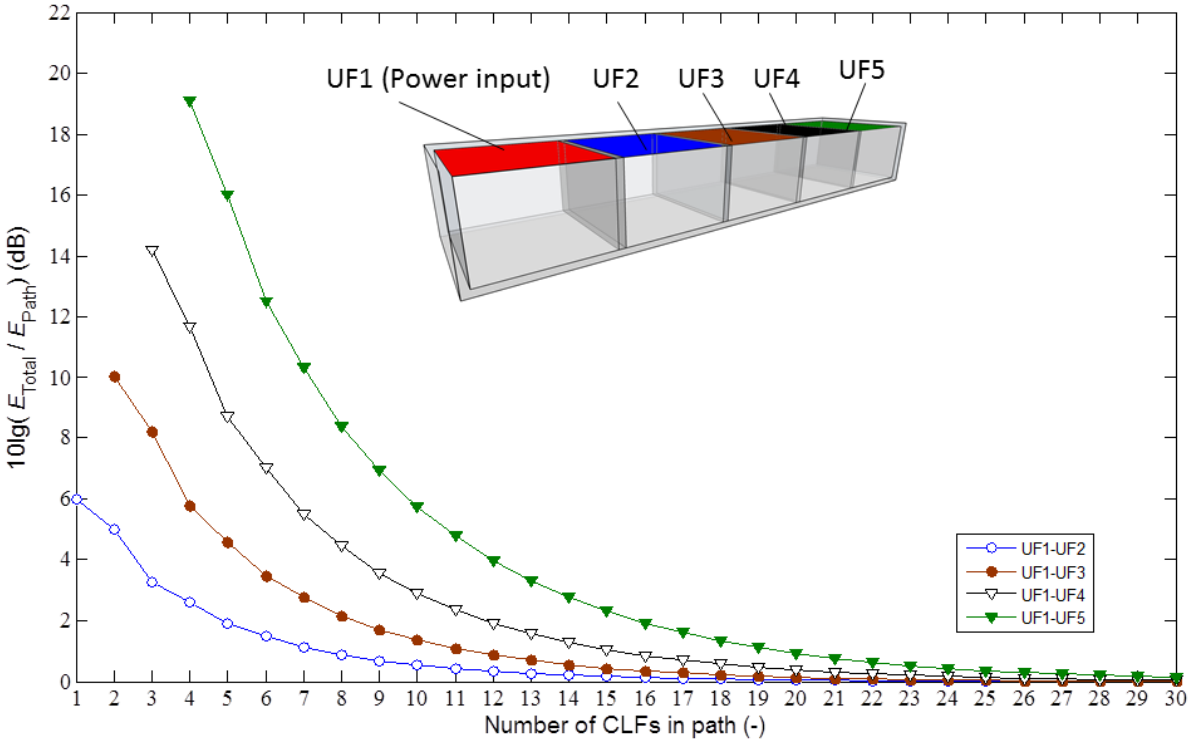

Figure 5.25b. 100Hz one-third octave band level difference between the total energy in each subsystem and the cumulative sum of all contributions from paths up to and including paths containing *n* CLFs. Upper floors of 5_1_1 building.

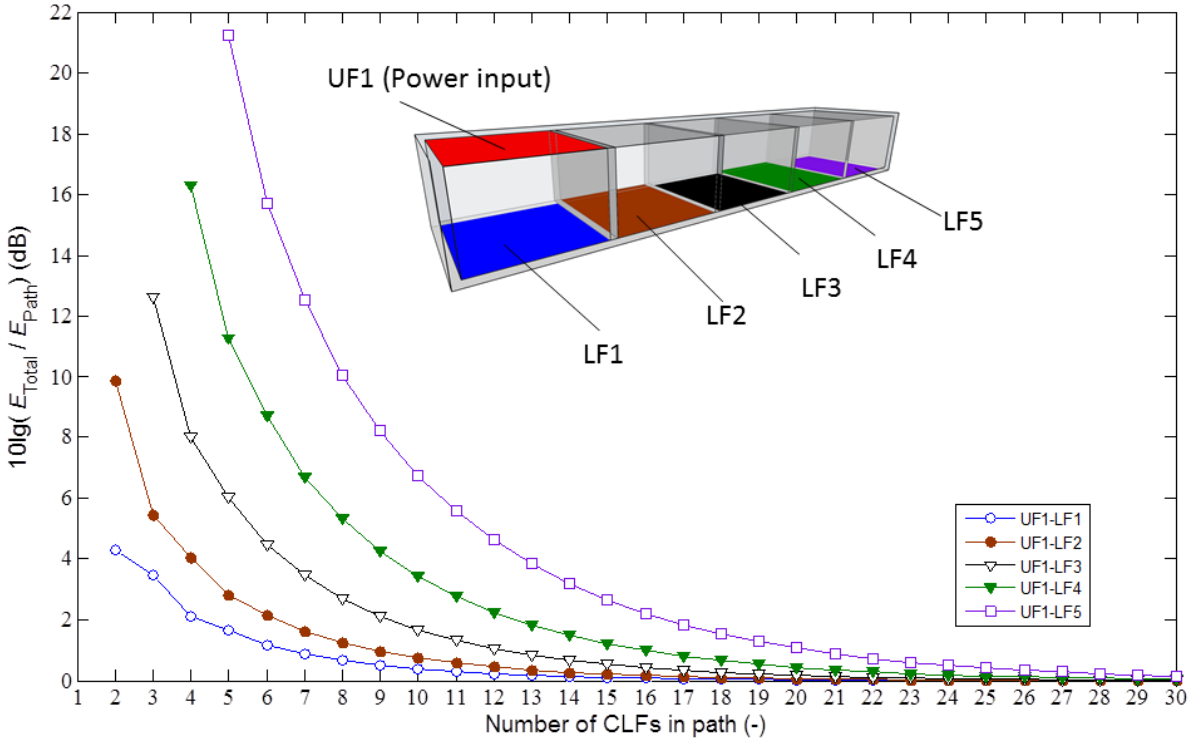

Figure 5.25c. 100Hz one-third octave band level difference between the total energy in each subsystem and the cumulative sum of all contributions from paths up to and including paths containing *n* CLFs. Lower floors of 5_1_1 building.

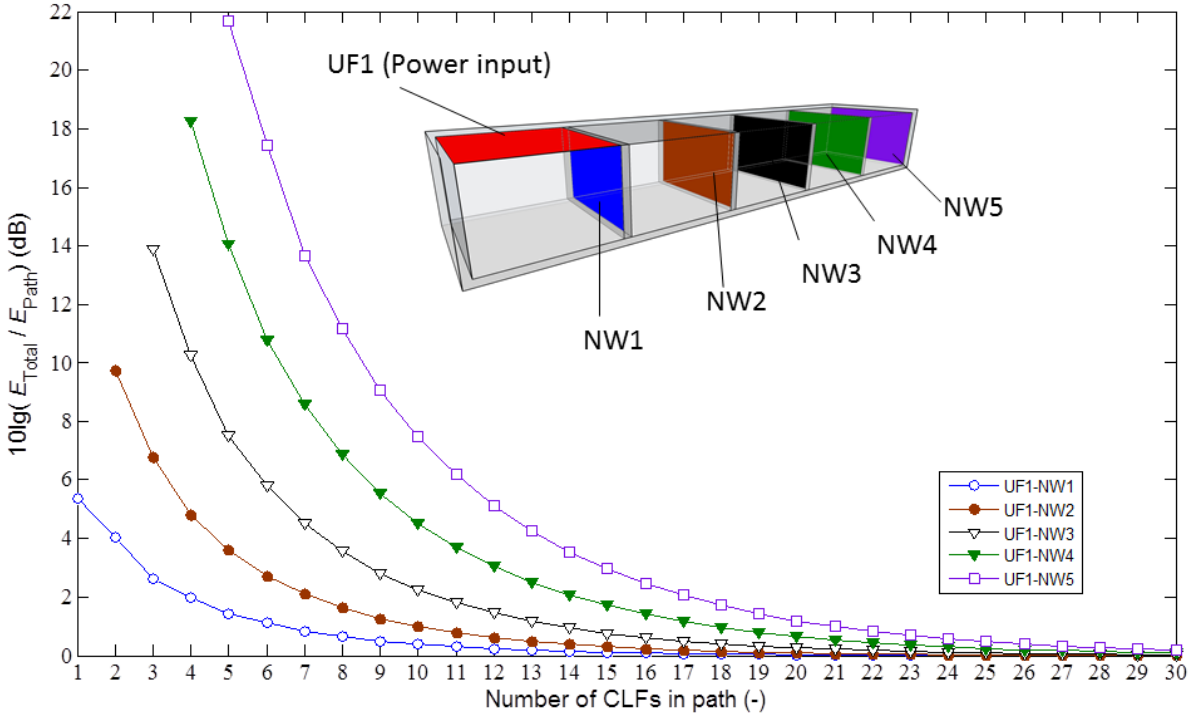

Figure 5.25d.100Hz one-third octave band level difference between the total energy in each subsystem and the cumulative sum of all contributions from paths up to and including paths containing *n* CLFs. Separating walls of 5_1_1 building.

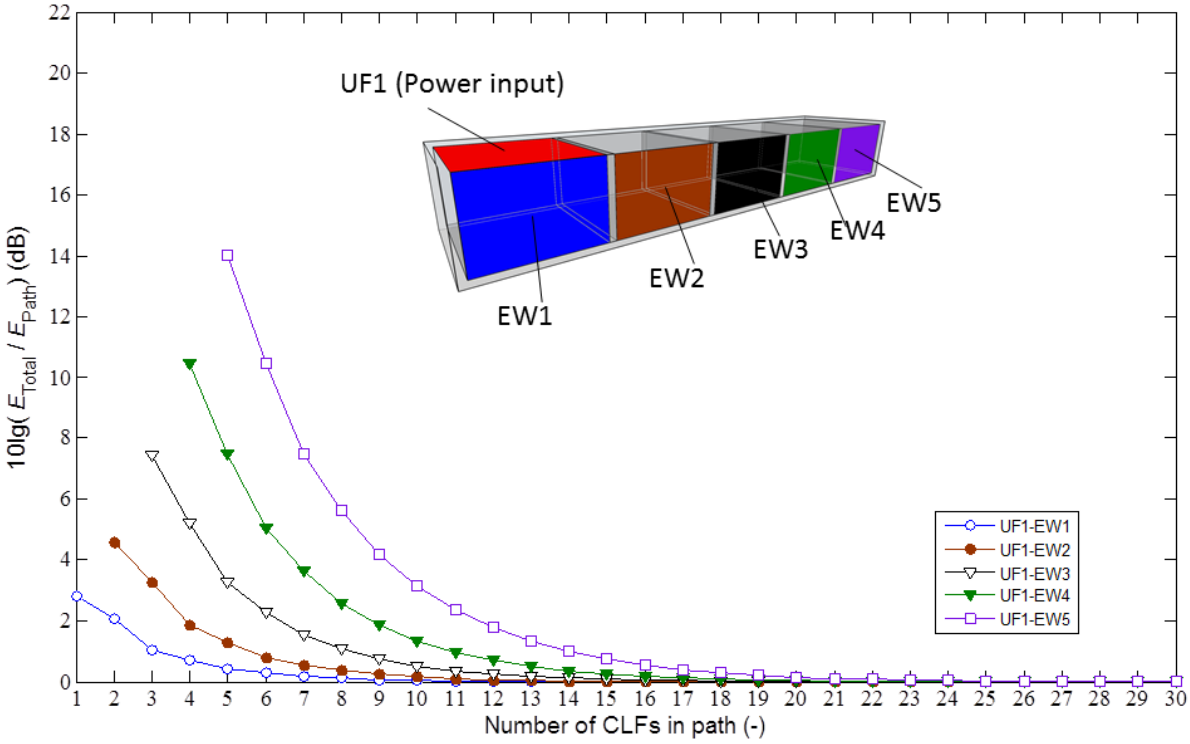

Figure 5.26a.1000Hz one-third octave band level difference between the total energy in each subsystem and the cumulative sum of all contributions from paths up to and including paths containing *n* CLFs. Flanking walls of 5_1_1 building.

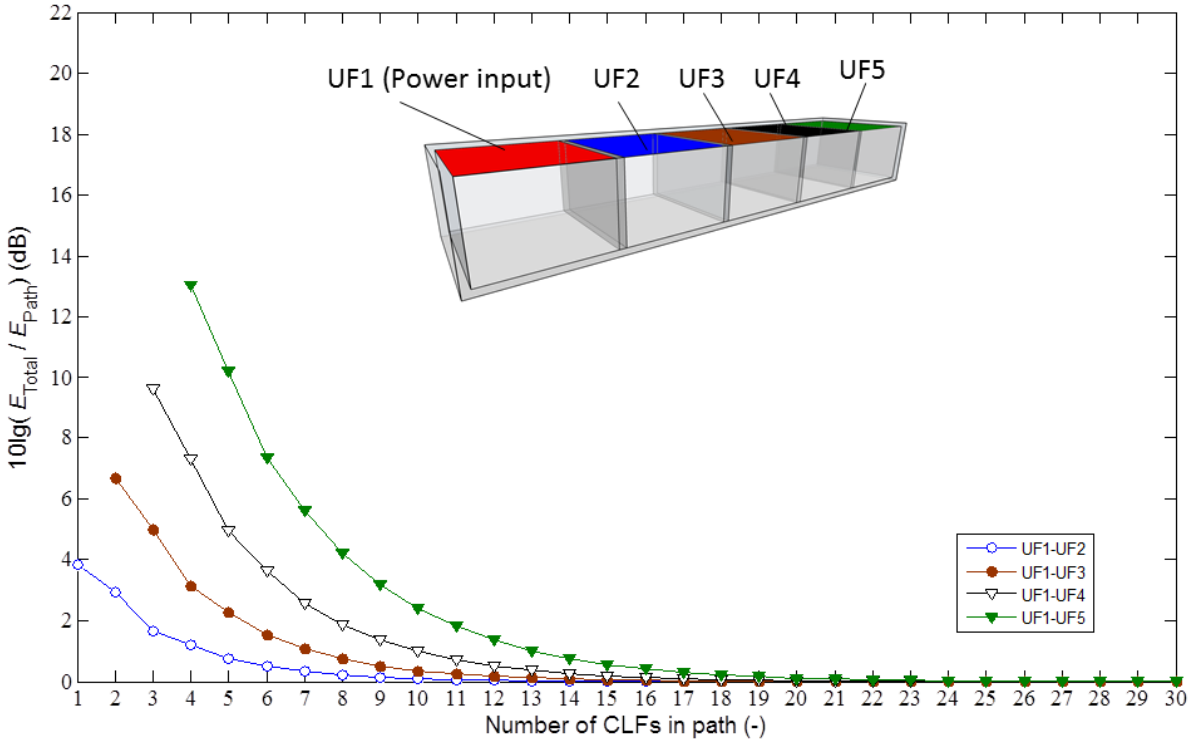

Figure 5.26b.1000Hz one-third octave band level difference between the total energy in each subsystem and the cumulative sum of all contributions from paths up to and including paths containing *n* CLFs. Upper floors of 5_1_1 building.

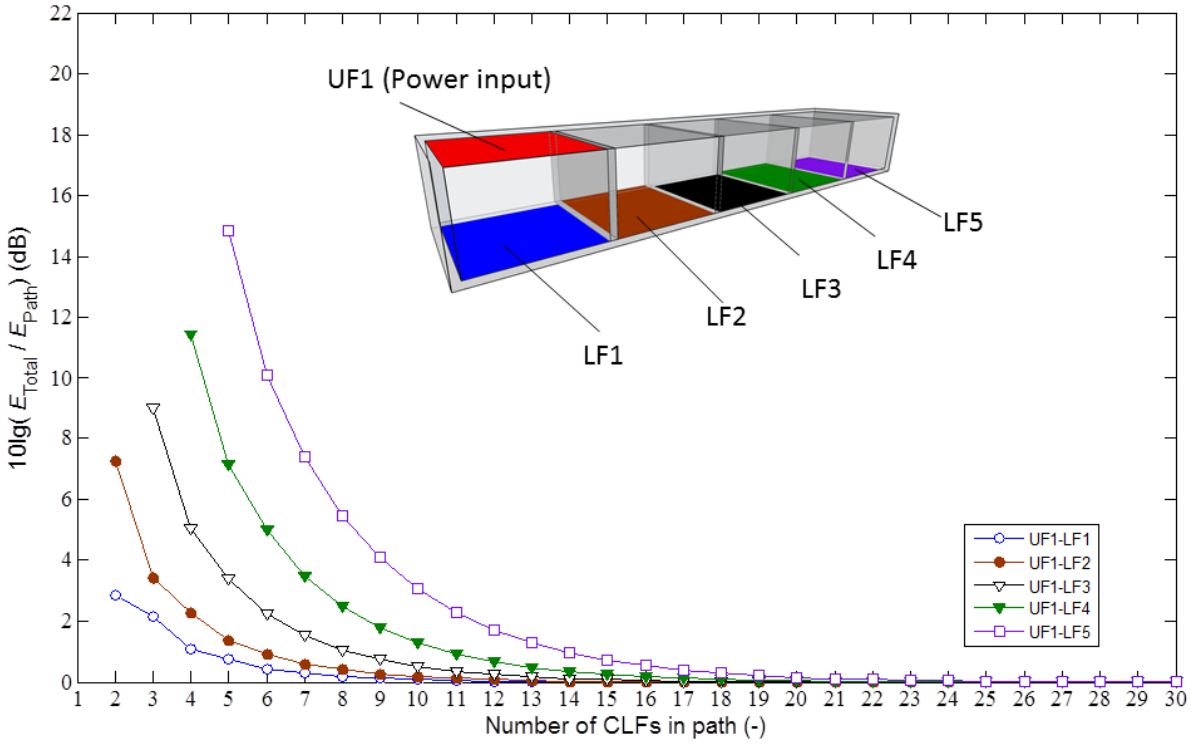

Figure 5.26c.1000Hz one-third octave band level difference between the total energy in each subsystem and the cumulative sum of all contributions from paths up to and including paths containing *n* CLFs. Lower floors of 5_1_1 building.

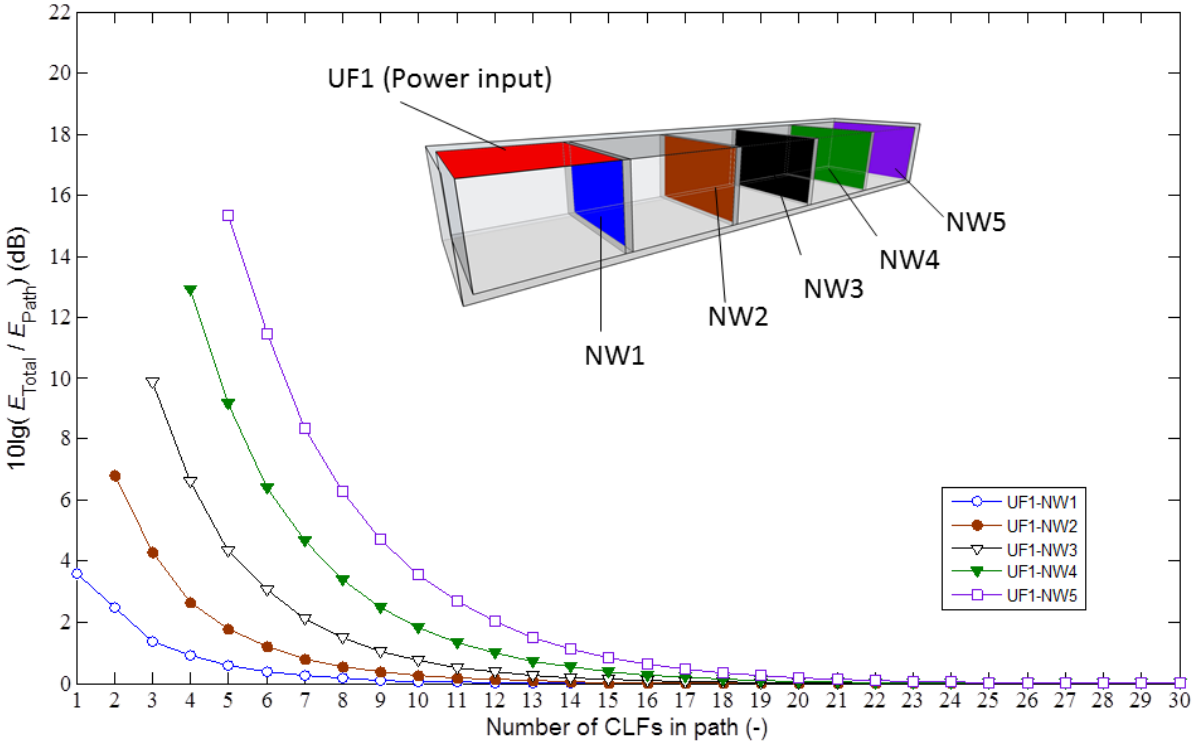

Figure 5.26d.1000Hz one-third octave band level difference between the total energy in each subsystem and the cumulative sum of all contributions from paths up to and including paths containing *n* CLFs. Separating walls of 5_1_1 building.

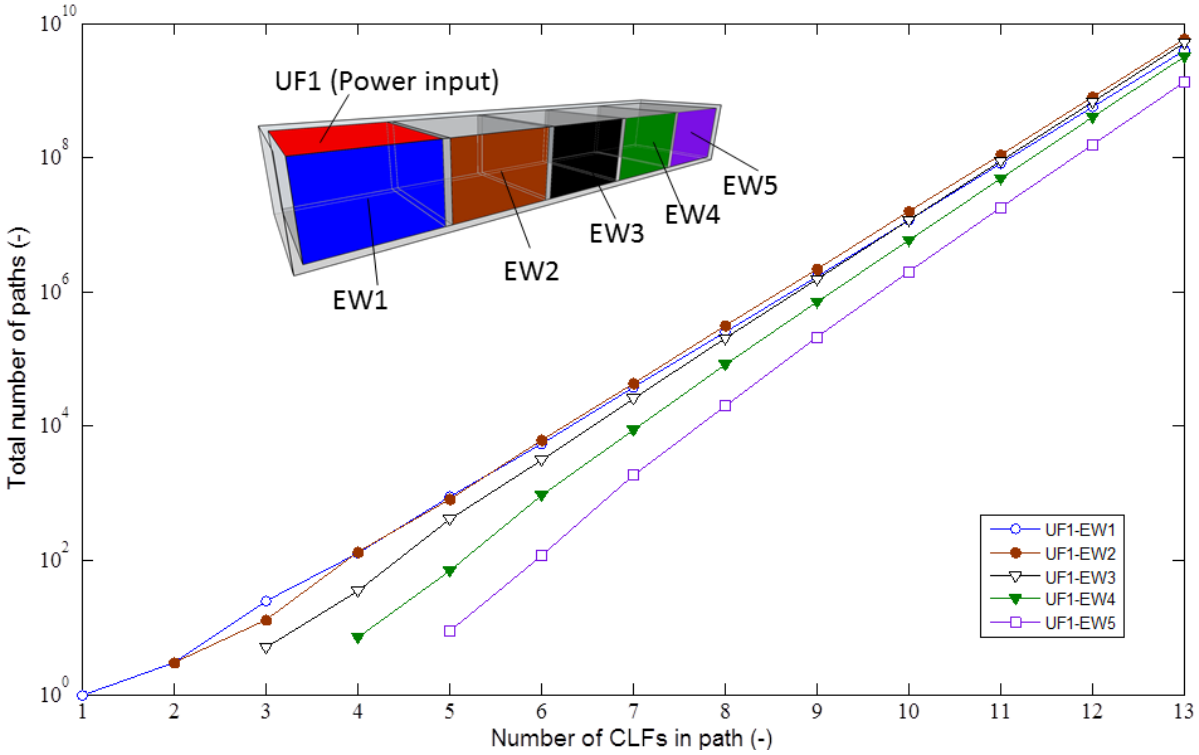

Figure 5.27a. Total number of paths up to and including paths containing *n* CLFs. Flanking walls of 5_1_1 building.

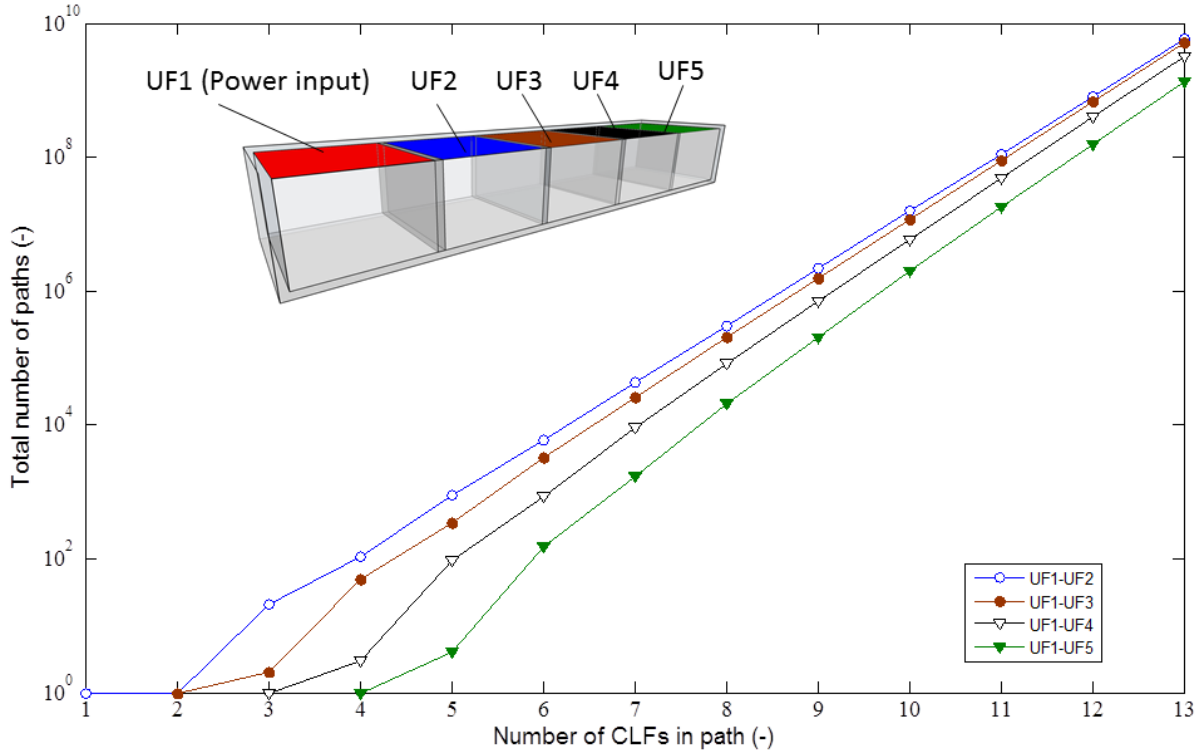

Figure 5.27b. Total number of paths up to and including paths containing *n* CLFs. Upper floor of 5_1_1 building.

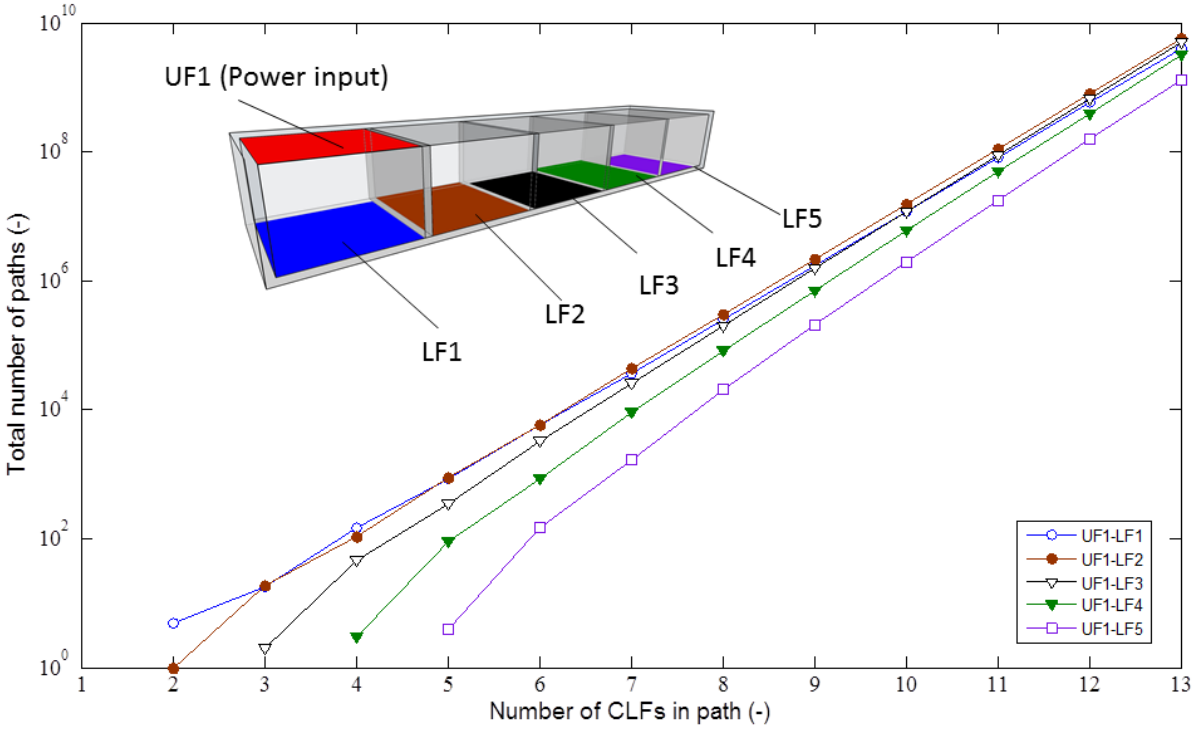

Figure 5.27c. Total number of paths up to and including paths containing *n* CLFs. Lower floor of 5_1_1 building.

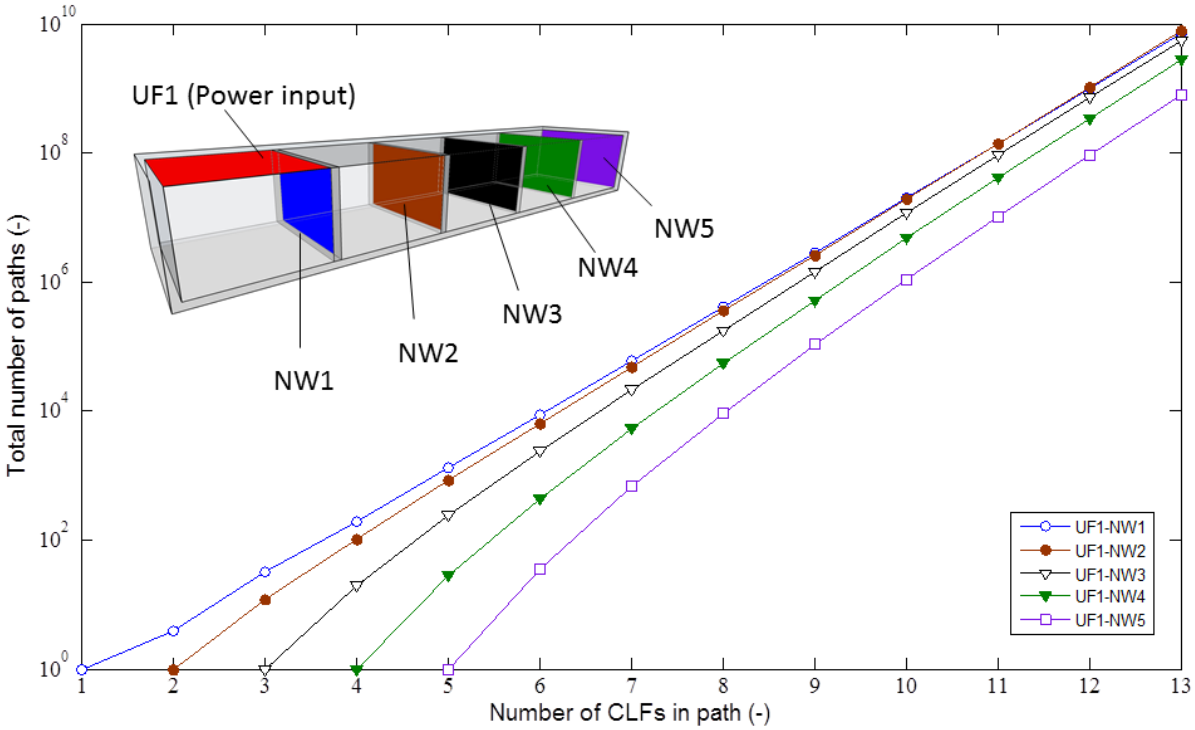

Figure 5.27d. Total number of paths up to and including paths containing *n* CLFs. Separating walls of 5_1_1 building.

From Figure 5.25a to 5.25d the direct paths between the upper floor of room 1 to the plates connected to room 5 are between 18.3 and 22dB lower than the matrix SEA prediction in the 100Hz one-third octave band. Figures 5.26a to 5.26d shows that at 1000Hz the results are 13

to 15dB lower. From Figures 5.27a to 5.27d the number of direct paths to subsystems in room 5 is between 1 and 10 and the number of paths rapidly increases with increasing path length for the subsystems connected to room 5. There is a large difference between the energy calculated using the direct path from the source to the upper floor of room 5 and the energy calculated using matrix SEA. Including paths that contain up to ten CLFs reduces the difference between the path analysis and matrix SEA to 6.5dB in the 100Hz one-third octave band. However, Figures 5.27a to 5.27d shows that there are approximately 10^6 paths containing up to ten CLFs. Similar results are found for the other plates in room 5 and hence it is not feasible to carry out a path analysis approach when several structural junctions exist between source and receiving subsystems in this model due to the large errors incurred.

5.4 The effect of low mode counts and low modal overlap

5.4.1 General comparison between SEA and MCFEM ELDs

The plates that form the heavyweight buildings described in Section 5.2 have low modal overlap factors and low statistical mode counts (see Table 5.3) for one-third octave bands in the range 50 to 1000Hz. In these conditions SEA using CLFs from semi-infinite plate theory tends to overestimate the strength of the coupling, see for example [17, 18, 33, 69]. In this section ELDs predicted by matrix SEA will be compared against the MCFEM results for the case of ROTR excitation applied to the upper floor of the first room of the building types described in Section 5.2.3. Note that for brevity, matrix SEA will simply be referred to as SEA.

The results in Figure 5.28 show the difference between the ELD predicted by MCFEM with 95% confidence limits and the ELD predicted by SEA for each of the subsystems in the 2_2_2 building. Above 200Hz the statistical mode count is greater than one for all plates in the building and the results indicate that in this region there is generally between -5dB and +10dB difference between MCFEM and SEA. The geometric average modal overlap factor between the source plate and the receiver plates is shown in Table 5.5. From Tables 5.3 and 5.5 it is seen that $M>1$ and $N>5$ at 1000Hz; however no convergence between SEA and MCFEM are observed in this band.

Below 200Hz the maximum difference between ELDs from MCFEM and SEA is 16dB; however most SEA results fall within 10dB of MCFEM. Below 80Hz there are no bending

modes present in some of the plates (see Table 5.2) and therefore it is not appropriate to compare SEA and MCFEM in this frequency range. Figure 5.28 also indicates that there is a tendency for SEA to underestimate the ELD between the source and receiving subsystems below 1kHz which is in agreement with some findings in the literature [3]

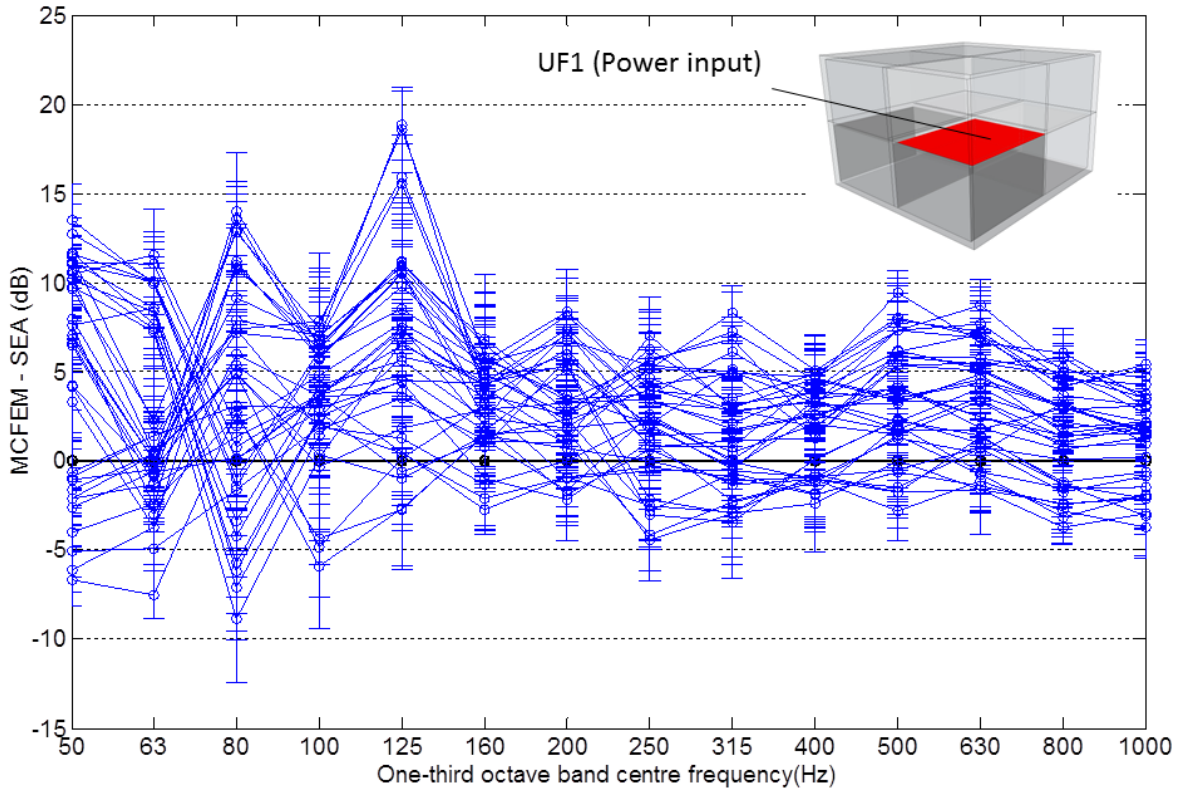

Figure 5.28. ELDs between the upper floor of room 1 in the 2_2_2 building and the remaining plates in the building. Error bars indicate the 95% confidence limit for each ELD.

	50	63	80	100	125	160	200	250	315	400	500	630	800	1k
Floors1	0.41	0.46	0.53	0.59	0.66	0.75	0.84	0.94	1.06	1.21	1.35	1.53	1.74	1.96
Floors2	0.29	0.32	0.37	0.41	0.46	0.53	0.59	0.67	0.76	0.87	0.98	1.11	1.28	1.44
Separating walls 1	0.28	0.31	0.35	0.4	0.45	0.51	0.58	0.65	0.74	0.84	0.95	1.08	1.24	1.41
Flanking walls 1	0.23	0.26	0.3	0.33	0.38	0.43	0.49	0.56	0.64	0.74	0.84	0.97	1.13	1.3
Flanking walls 2	0.18	0.21	0.24	0.27	0.31	0.36	0.41	0.47	0.54	0.63	0.72	0.84	0.98	1.13
Floors 3	0.29	0.33	0.38	0.42	0.47	0.54	0.61	0.69	0.78	0.89	1	1.14	1.31	1.48
Separating walls 2	0.27	0.3	0.35	0.39	0.43	0.5	0.56	0.63	0.72	0.82	0.93	1.06	1.22	1.38

Table 5.7 Geometrical mean of the modal overlap factors of the source and receiver plates in the 2_2_2 building.. The modal overlap factors are calculated using the TLFs (Eq.5.5). Floors 1 – LF1, LF2, LF3,LF4. Floors 2 – UF1,UF2,UF3,UF4. Floors 3 – UF5,UF6,UF7,UF8 Separating walls 1 – NW1,NW3,NW5,NW7. Flanking walls 1-WW1,WW2,WW5,WW6. Flanking walls 2 – EW1,EW2, EW5, EW6, WW3,WW4,WW7,WW8. Separating walls 2 – SW1,NW2, SW3,NW4,SW5,NW6,SW7,NW8.

The results for the 5_1_1 building are shown in Figure 5.29. The geometric mean of the modal overlap factors for each case is shown in Table 5.8. Below 200Hz the SEA ELDs are

between -10dB and 15dB of the MCFEM ELDs. Above 200Hz the difference between SEA and MCFEM is typically between -15dB and 5dB. However in some cases such as the 315Hz one-third octave band, MCFEM ELDs are approximately 15dB lower than those predicted by SEA. This differs from the general trend that SEA underestimates the ELD in this frequency range; hence it may be related to the periodic arrangement of T-junctions in the 5_1_1 building which is not present in the other buildings that are investigated.

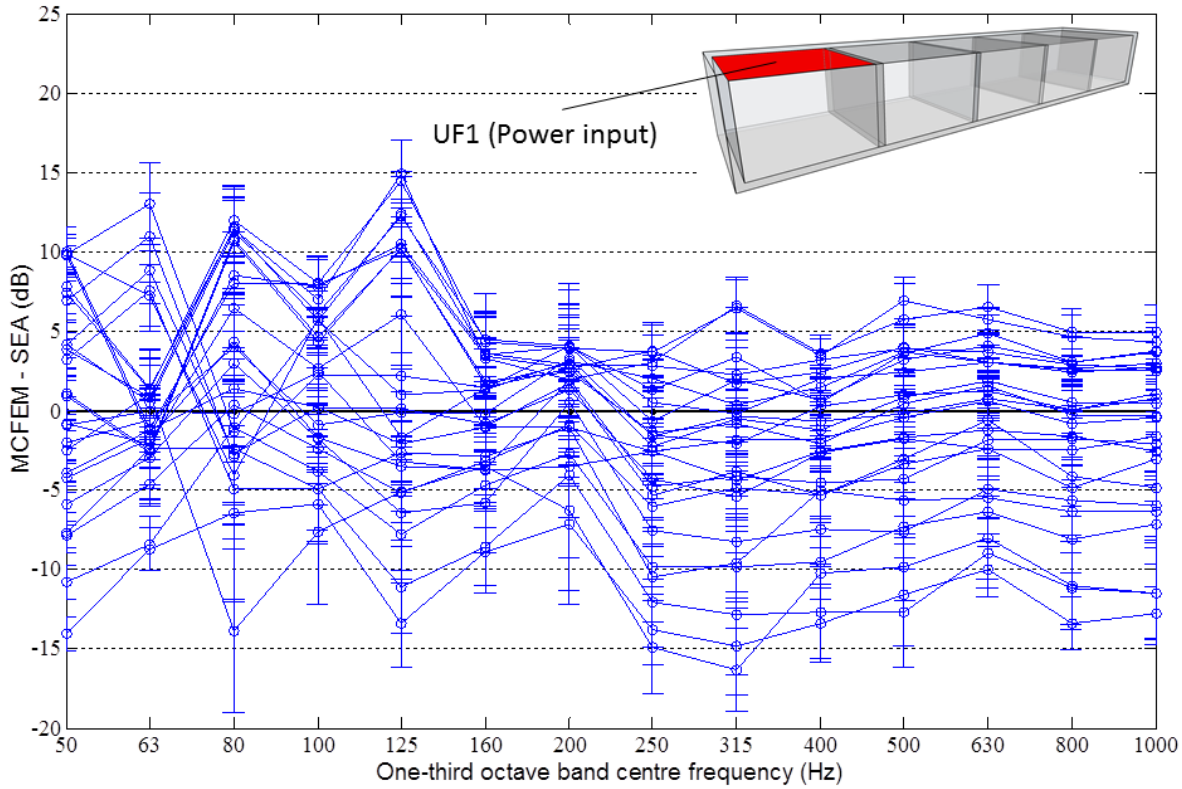

Figure.5.29. ELDs between the upper floor of room 1 in the 5_1_1 building and the remaining plates in the building. Error bars indicate the 95% confidence limit for each ELD.

	50	63	80	100	125	160	200	250	315	400	500	630	800	1k
Floors 1	0.39	0.44	0.5	0.56	0.63	0.72	0.8	0.9	1.02	1.16	1.3	1.47	1.67	1.88
Floors 2	0.4	0.45	0.51	0.57	0.63	0.73	0.81	0.91	1.03	1.17	1.31	1.48	1.69	1.89
Floors 3	0.28	0.31	0.36	0.4	0.45	0.52	0.58	0.65	0.74	0.84	0.95	1.08	1.25	1.41
Floors 4	0.27	0.31	0.35	0.39	0.44	0.51	0.57	0.64	0.73	0.83	0.94	1.06	1.22	1.39
Flanking walls 1	0.23	0.26	0.3	0.33	0.38	0.44	0.49	0.56	0.64	0.74	0.84	0.97	1.13	1.3
Flanking walls 2	0.23	0.26	0.29	0.33	0.37	0.43	0.49	0.56	0.64	0.74	0.84	0.97	1.13	1.29
Separating walls 1	0.25	0.28	0.33	0.37	0.41	0.47	0.53	0.6	0.69	0.79	0.9	1.03	1.19	1.35
Separating walls 2	0.25	0.28	0.32	0.36	0.41	0.47	0.53	0.59	0.68	0.77	0.87	1	1.15	1.3

Table 5.8. Geometrical mean of the modal overlap factors of the source and receiver plates in the 5_1_1 building. The modal overlap factors are calculated using the TLFs (Eq.5.5). Floors 1 – LF1, LF5. Floors 2 –LF2,LF3,LF4. Floors 3 – UF1, UF5, Floors 4 – UF2, UF3,UF4. Separating walls 1 – NW1,NW2,NW3,NW4. Flanking walls 1-WW1,WW5,EW2,EW5. Flanking walls 2 –EW2, EW3, EW4, WW2,WW3,WW4. Separating walls 2 – SW1,NW5.

5.4.2 Individual case comparison between SEA and MCFEM

The analysis so far has focussed on the full set of ELD results obtained for each building. In this section, SEA is compared to MCFEM for individual pairs of source and receiver plates. Particular attention is given to the frequency region where the statistical mode count is greater than unity in all subsystems in the building (above 200Hz).

In Figure 5.30 the ELDs calculated using both methods are plotted for a set of subsystems that are directly attached to the source in the 2_2_2 building. The source plate is coloured in red with the other coloured lines representing the ELD between the source and the corresponding coloured subsystem of the 2_2_2 building (note this applies to all subsequent figures). Above 200Hz, SEA results for the upper floors are within 3dB of MCFEM with most values lying within the 95% confidence limits. The remaining SEA results are within 5dB of MCFEM and close to the lower limit of the MCFEM 95% confidence limits. It is noteworthy that SEA underestimates the level difference on these plates by approximately the same amount that path analysis using EN12354 would underestimate the receiving subsystem energy compared to SEA (refer back to Figures 5.17 and 5.18). Using EN12354 only gives better agreement with MCFEM for an invalid reason; namely that insufficient paths are included in EN12354.

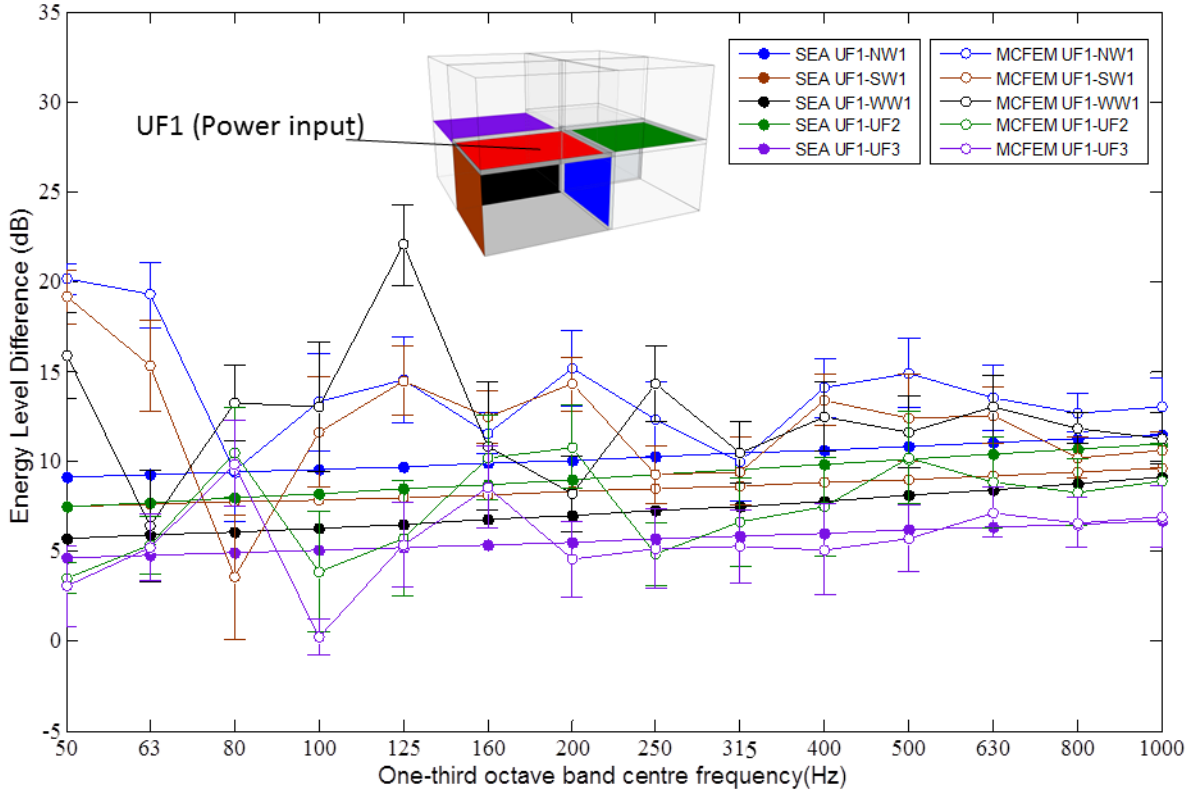

Figure. 5.30. ELD between the upper floor or room 1and the directly attached plates.. Error bars indicate the 95% confidence limit for each ELD.

The SEA and MCFEM ELDs between the upper floor of room 1 and the walls and floors of the diagonally opposite rooms are shown in Figures 5.31 to 5.33. In some cases the SEA results below 200Hz are closer to the MCFEM results than at higher frequencies. For example, in Figure 5.31 the SEA ELD for the lower floor of room 4 is within the 95% confidence limits between 80Hz and 315Hz wheras above 315Hz this does not occur. This is contradictory to the expectation that SEA is suited to higher frequencies when a large number of modes are present and the modal overlap factor is high. This could again be regarded as an example of SEA giving the right answer for the wrong reasons. Chapter 6 will investigate whether non-diffuse vibration fields and spatial filtering could be the cause of this.

Above 200Hz the difference between the MCFEM and SEA ELDs is between -1 and +8dB. Comparing Figures 5.31 to 5.33 with Figure 5.30 shows that in general the SEA results are closer to MCFEM for subsystems that are directly connected to the source subsystem. For 500Hz to 1000Hz none of the SEA results (with the exception of the 500Hz and 630Hz ELD to the upper floor of room 4) are within the 95% confidence limits of the MCFEM results. This highlights a potential problem when using SEA with CLFs from semi-infinite plate theory to determine the vibration level of plates in rooms that are diagonally connected to the room containing the source plate.

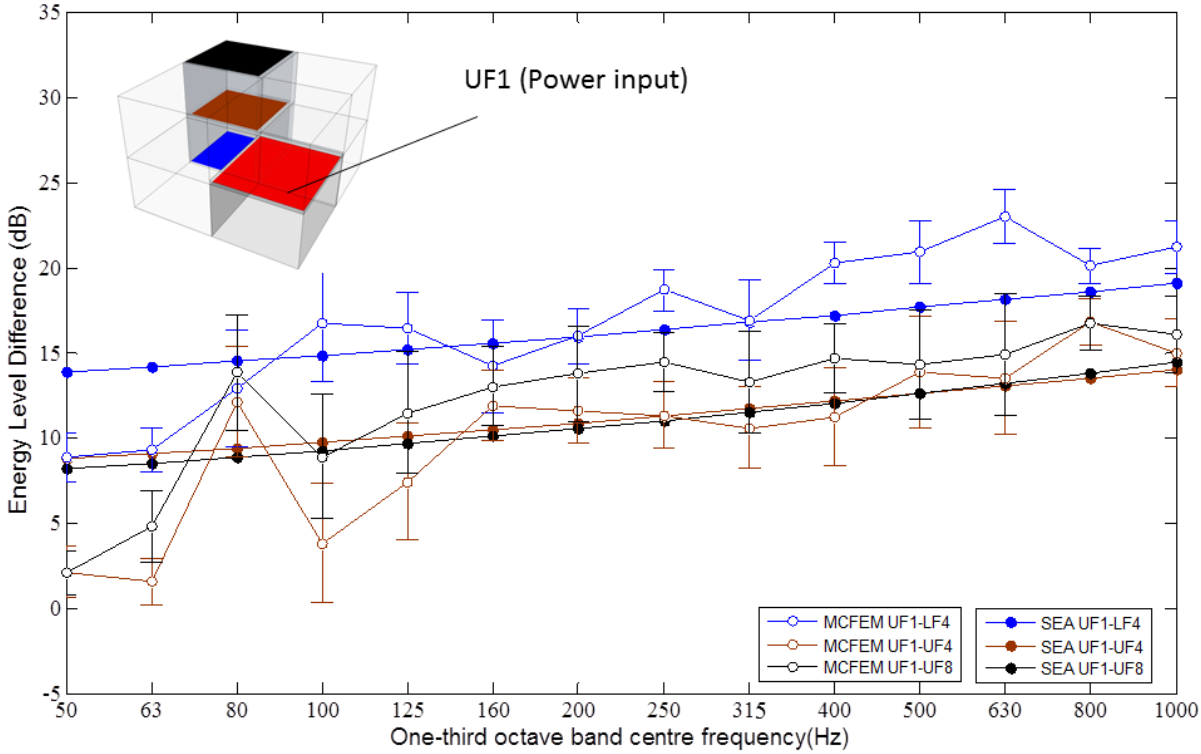

Figure.5.31. ELD between the upper floor of room 1and the floors of the diagonally opposite rooms.. Error bars indicate the 95% confidence limit for each ELD.

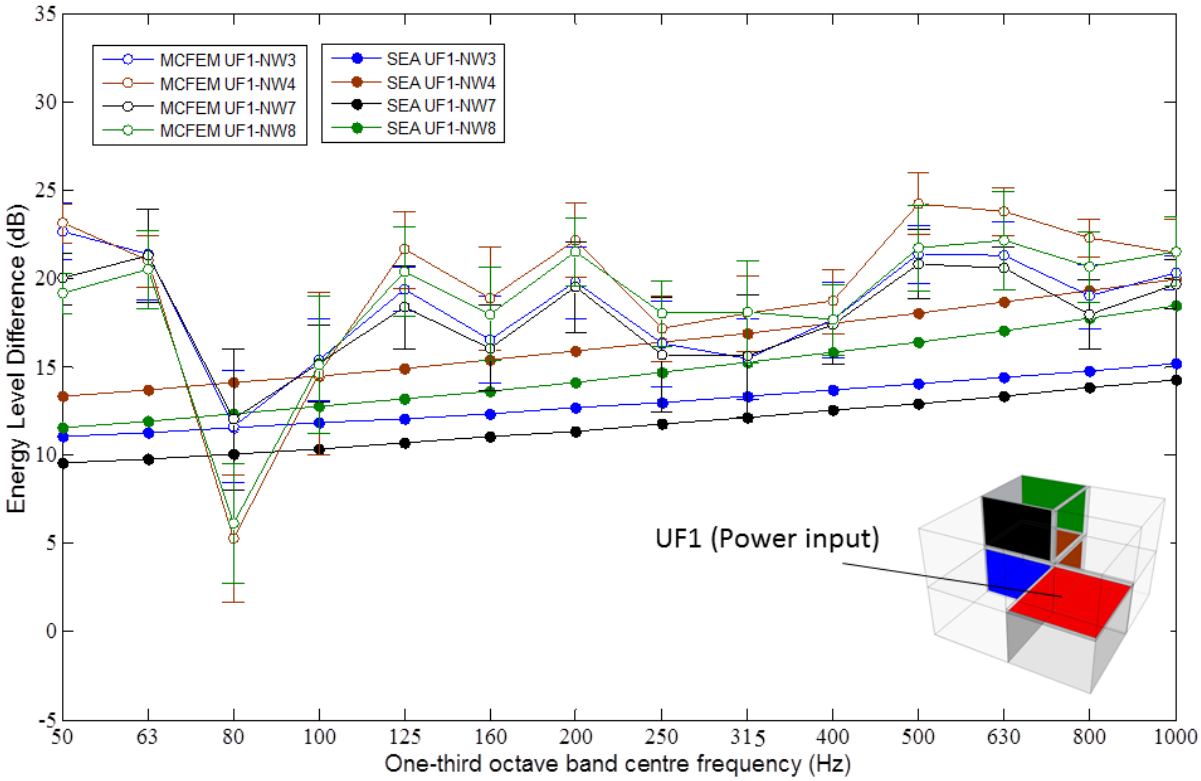

Figure 5.32. ELD between the upper floor of room 1and the separating walls of the diagonally opposite rooms. Error bars indicate the 95% confidence limit for each ELD.

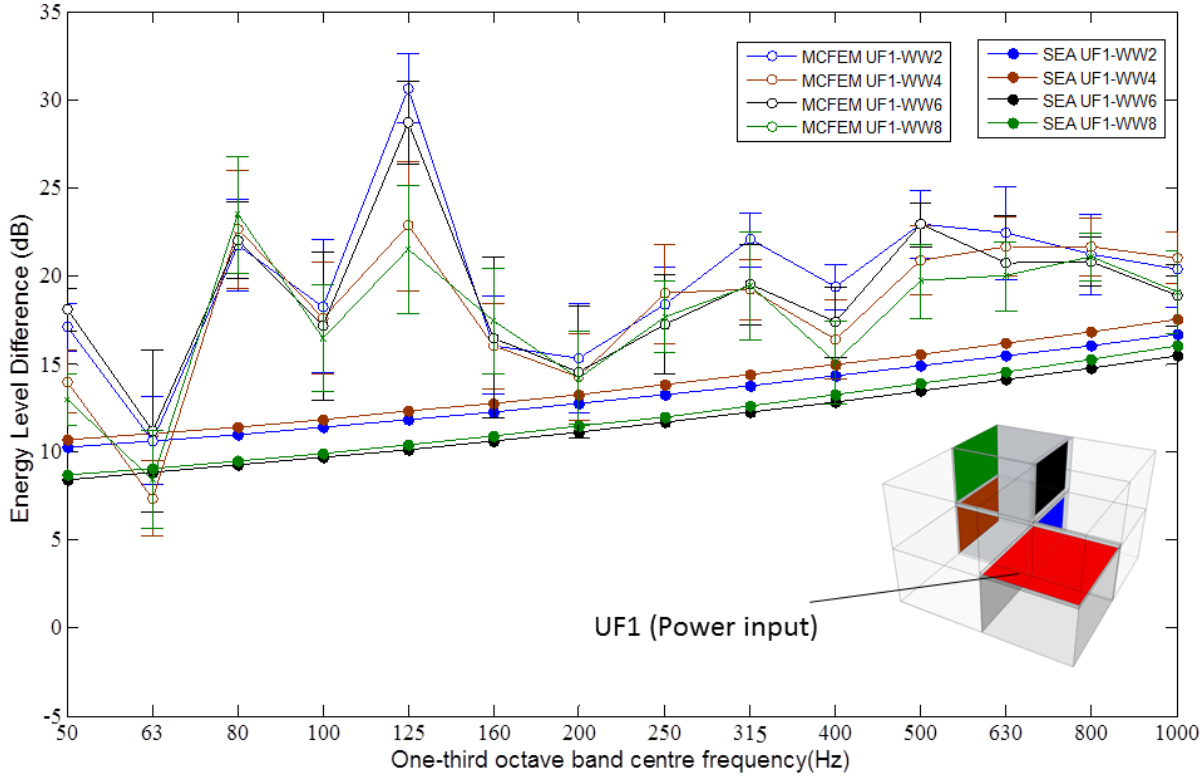

Figure.5.33. ELD between the upper floor of room 1and the flanking walls of the diagonally opposite rooms. Error bars indicate the 95% confidence limit for each ELD.

In Figures 5.34 – 5.37 the ELD predicted by SEA is compared against MCFEM for the case of excitation applied to the upper floor of room 1 of the 5_1_1 building.

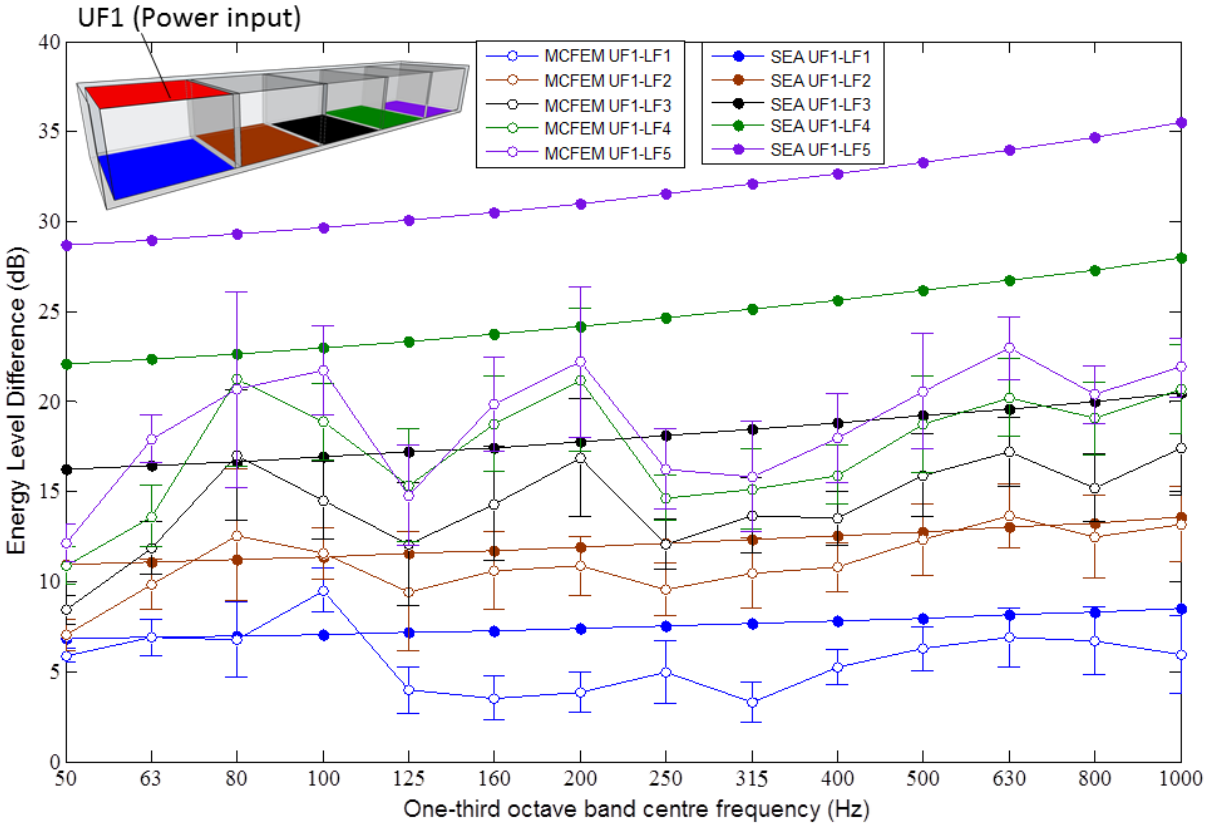

Figure 5.34. ELD between the upper floor of room 1and the lower floors. Error bars indicate the 95% confidence limit for each ELD.

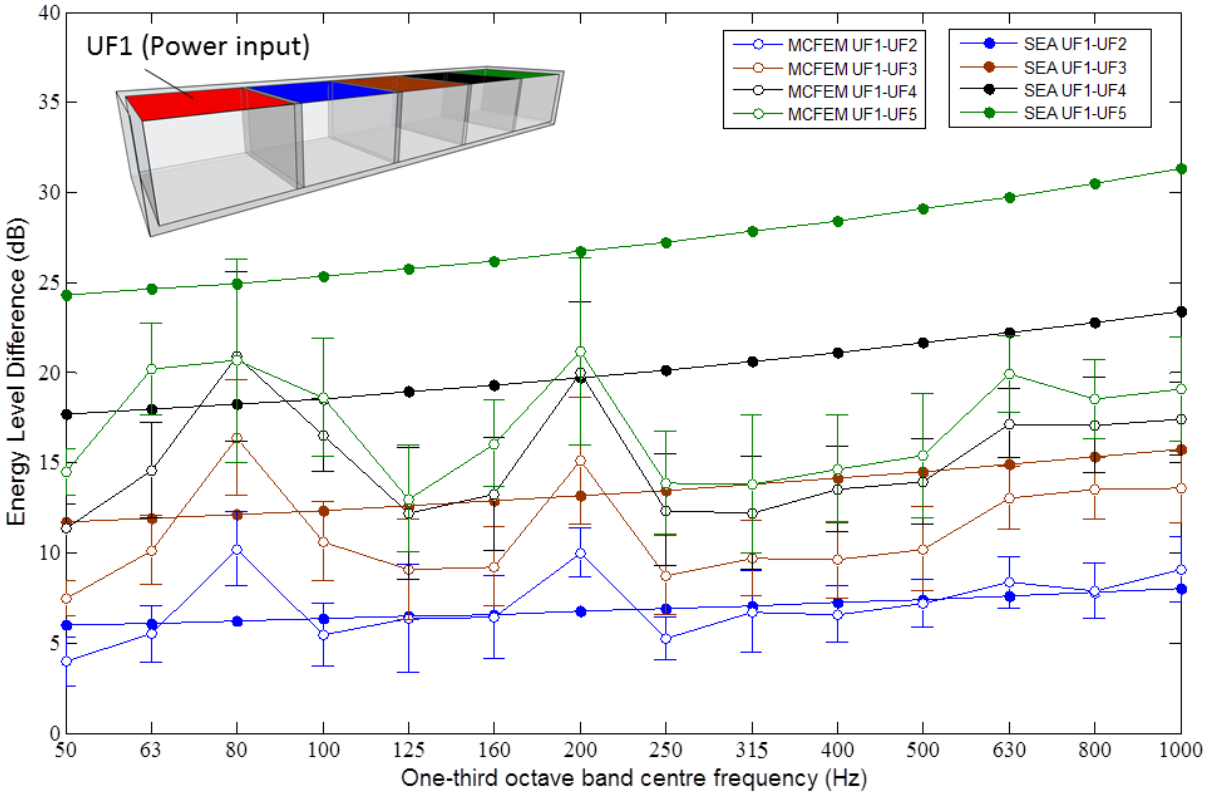

Figure 5.35. ELD between the upper floor of room 1and the upper floors. Error bars indicate the 95% confidence limit for each ELD.

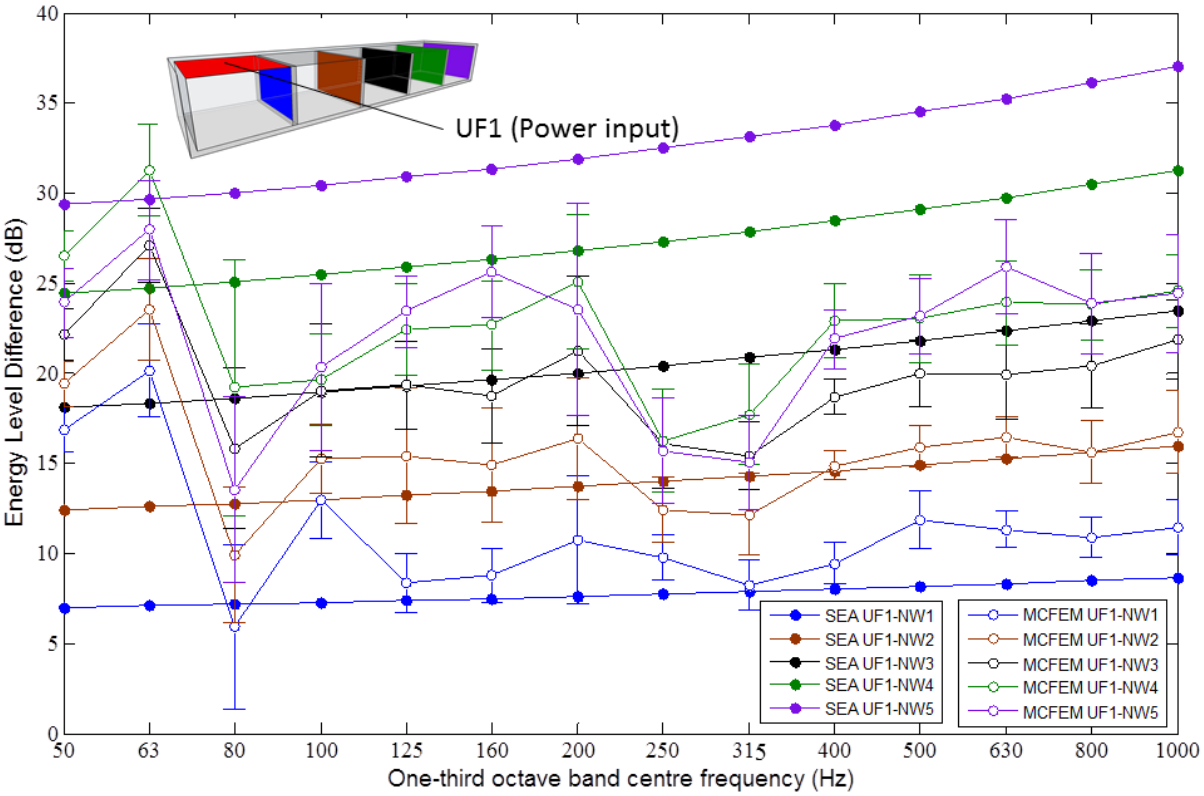

Figure 5.36. ELD between the upper floor of room 1and the separating walls. Error bars indicate the 95% confidence limit for each ELD.

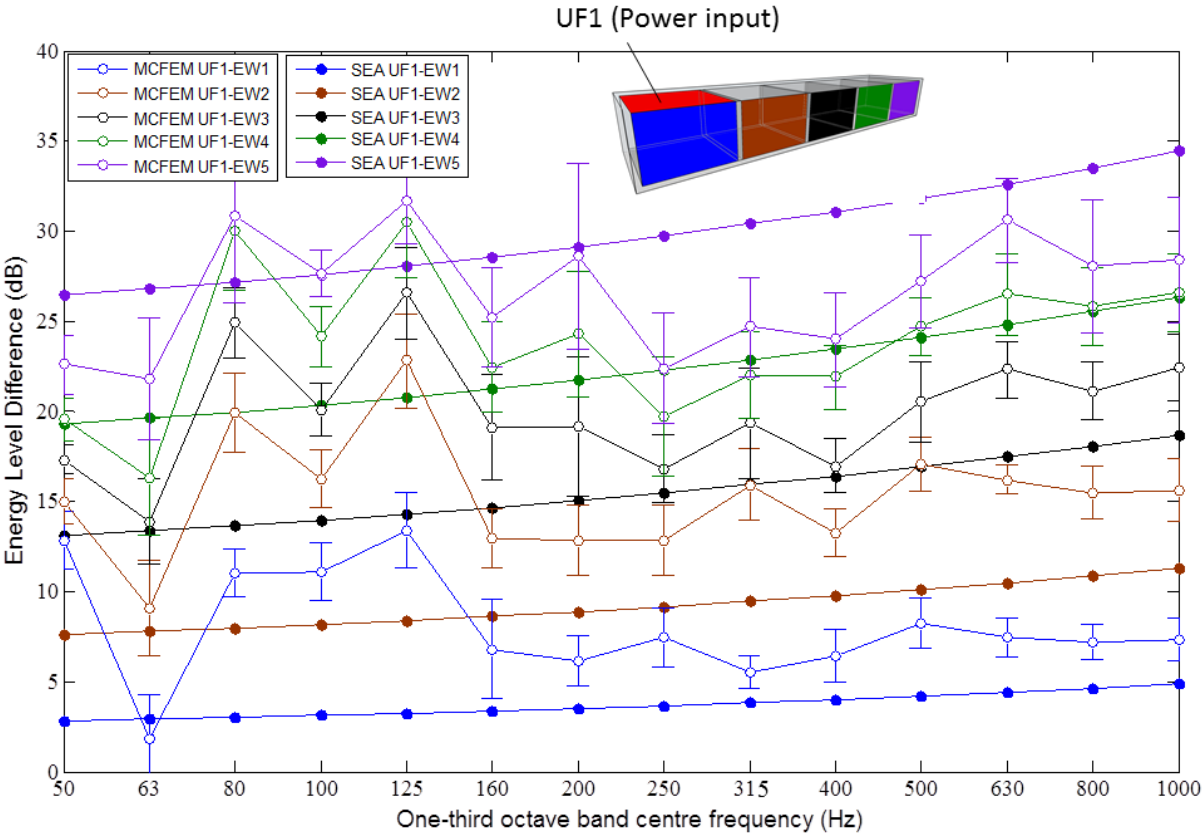

Figure 5.37. ELD between the upper floor of room 1and the flanking walls. Error bars indicate the 95% confidence limit for each ELD.

In general, Figures 5.34 to 5.37 show close agreement between ELDs predicted by SEA and MCFEM for subsystems which are connected to the source across one or two structural junctions. Most of the SEA results lie within or close to the MCFEM 95% confidence limits at and above 200Hz. However, as shown in Figure 5.37, the ELD between the upper floor of room 1 and the eastern wall of room 2 is an exception to this general trend with SEA underestimating the ELD by approximately 5 to 7dB in the frequency range 200 to 1000Hz. There appears to be good agreement between SEA and MCFEM for the eastern wall of room 4 and room 5. However the results for the eastern wall subsystems in rooms 1, 2 and 3 indicate that SEA overestimates the transmission across the structural junctions. This provides another example of a case where SEA gives the right answers for the wrong reason.
Between 200 and 500Hz there is a feature in the MCFEM ELD which is common to all the plates belonging to room 3 (except the south wall), room 4 and room 5. This feature is a distinctive peak in the ELD in the 200 or 250Hz band followed by a trough spanning three to four bands. This feature is most prominent in Figure 5.26 where the MCFEM ELDs between the upper floor of room 1 and the north walls of room 3, 4 and 5 have overlapping confidence limits. This indicates much stronger transmission between the subsystems of these rooms than would normally be expected and could be due to the periodic structure.

5.5 Conclusion

This chapter analysed results from SEA models using CLFs from semi-infinite plate theory for comparison with MCFEM for 2_2_2 and 5_1_1 buildings.

For a 2_1_1 building, comparison of SEA models with and without air cavities representing the room subsystems indicated that the structure-borne sound transmission in heavyweight buildings can be modelled *in vacuo* without the need to include radiation coupling between the plates and the air cavities. Hence for the remainder of this thesis the focus is on the prediction of the vibration levels on plates without further consideration of the effect of the sound fields in the rooms.

An investigation was carried out into the effect of using a limited number of short transmission paths to predict energy levels of walls and floors in heavyweight buildings. For power input to the upper floor of room 1 in a 2_2_2 building, the approach used in EN12354 (first-order path analysis) underestimates the energy level in the source plate. For receiving subsystems which are attached directly to the source subsystem, EN12354 underestimates the

energy levels by up to 7dB. When using path analysis, the effect of adding paths higher than first-order paths is to increase the receiving subsystem energy. When including energy contributions from paths which contain two or more CLFs than the direct path it was shown that the convergence to matrix SEA slows considerably. This is because most of the energy is transmitted to the receiver via a large number of paths. For example, in the 5_1_1 building with the source as the upper floor of room 1, the energy in the upper floor of room 5 predicted using only the direct path was 13dB lower than matrix SEA. In some cases it was shown to be necessary to include up to a million paths in order to converge on the matrix SEA result. Hence it is concluded that a path analysis approach such as EN12354 is not a feasible predictive method in heavyweight buildings for plates that are not directly attached to the source plate.

To assess the effect of low mode counts and low modal overlap factors when using one-third octave bands, matrix SEA was compared to MCFEM. ELDS were predicted between plates where the power was injected into the upper floor of room 1 of the 2_2_2 and 5_1_1 buildings. Between 80Hz and 200Hz the low statistical mode count leads to large fluctuations in the plate responses and therefore SEA gave poor agreement with MCFEM with differences typically between -5dB and 15dB. In Chapter 6 the use of CLFs derived from finite plate theory will be used to investigate whether the matrix-SEA predictions can be improved in this low-frequency range. For the 2_2_2 building there was reasonable agreement between SEA and MCFEM above 200Hz where statistically there was more than one mode per band in all plates; although SEA underestimated the ELD by up to 10dB or overestimated by up to 5dB. However for the 5_1_1 building above 200Hz there was a wider spread of results above 200Hz where SEA underestimated by up to 7dB or overestimated the ELD by up to 15dB.

For the 2_2_2 building it was found that SEA underpredicted the ELD by between 3 and 5dB above 200Hz which is approximately the same amount that EN12354 underestimates the total energy calculated by matrix SEA in these receiving subsystems. Hence EN12354 gives the right answer for the wrong reason. ELDs from MCFEM and SEA were then compared for the case of walls and floors connected to rooms that were located diagonally opposite to room 1. In this case SEA results underestimated the ELDs by between 5 and 10dB between 500 and 1000Hz. It is hypothesised that this occurs due to the spatial filtering of the wave field in subsystems connected to the source across a minimum of two junctions; hence in Chapter 7 Advanced SEA will be used to investigate this further.

The results from the 5_1_1 building are distinctly different from the 2_2_2 building. In some bands the ELD predicted by SEA is around 15dB higher than predicted by MCFEM for certain source and receiving subsystems. The results show very strong transmission from the upper floors to the north walls of rooms 2 to 5 in the 250Hz and 316Hz bands. Subsequently, troughs occur in the MCFEM ELDs between the upper floors and the lower/upper floors of room 3 to 5. In Chapter 6 finite plate theory CLFs will be used to investigate whether this feature can be predicted when CLFs from isolated plate junctions are incorporated into an SEA model rather than using CLFs from semi-infinite plate theory.

Chapter 6 Incorporating coupling parameters from isolated plate junctions with low mode counts into SEA models of building structures

6.1 Introduction

In this chapter, CLFs for isolated junctions of finite plates are incorporated into SEA models to try and improve the predictions in Chapter 5 that used CLFs from semi-infinite plate theory. In Section 6.2, EICs from the global mode approach are used to compute the ELDs directly (Section 3.3.1) these are then compared to MCFEM ELDs for isolated junctions. Different methods for inverting the ESEA energy matrix (Section 2.2.5) to obtain the finite plate CLFs are investigated. The CLFs are incorporated into SEA models of the isolated junctions and the ELDs resulting from the inverse SEA matrix are compared to the MCFEM ELDs. In Section 6.3 the CLFs for junctions of finite plates are incorporated into SEA models of large building structures and the resulting ELDs from matrix SEA are compared against MCFEM. In Section 6.4 ESEA is used on a section of the 5_1_1 building structure to explore the reasons behind the mixed performance of the approach in Section 6.3; particular attention is given to the role of CLFs between plate subsystems which are not directly connected (i.e. non-resonant transmission via tunnelling mechanisms).

6.2 Global mode approach for isolated junctions

6.2.1 Validation of Global mode model

The global mode method described in Section 3.3 can be used to determine the Energy Influence Coefficients (EICs), A_{rs} using eq. 3.53 In terms of the EICs the ELD between a source subsystem *s* and receiver subsystem *r* is given by

$$D_{\mathrm{E},ij} = 10\lg\left(\frac{A_{ii}}{A_{ji}}\right) \tag{6.1}$$

To validate the global mode approach the ELDs calculated using eq. 6.1 were compared to ELDs calculated using MCFEM for various junctions present in the building structures described in Section 5.2.3. The internal loss factors for plates in the isolated junctions are set to $1/\sqrt{f}$ which is typical of the total loss factor of plates found in heavyweight building structures [70]. A total of 10 different ensemble members were generated for each junction

by randomly selecting the Young's modulus of the plates in the junction from assumed normal distributions. A different set of ROTR forces was generated for each MCFEM ensemble member. The global mode approach calculates the EICs by assuming an ideal set of ROTR forces is applied to each of the plates in the ensemble.

In Figure 6.1 the mean ELDs in one-third octave bands with 95% confidence limits are shown for an L-junction of an upper floor and a separating wall or thick exterior wall (see Table 5.1 for physical properties of the plates) with ROTR excitation applied to the upper floor plate. The results are in close agreement with overlapping confidence limits across the whole frequency range. The agreement between mean values is not exact because the set of ROTR forces applied in MCFEM are not 'ideal' ROTR forces as applied in the global mode approach. However by using an ensemble of different ROTR values in the MCFEM approach, the mean value is in good agreement with 'ideal' ROTR in the global mode approach. Figure 6.2 and 6.3 show a T-junction connecting the upper floor to the separating wall. The two predictions are also in close agreement for both the ELD around the corner to the cantilever plate and straight across the T-junction to the upper floor. Many of the modal features below 500 Hz appear in both ELDs and the 95% confidence limits overlap in most frequency bands.

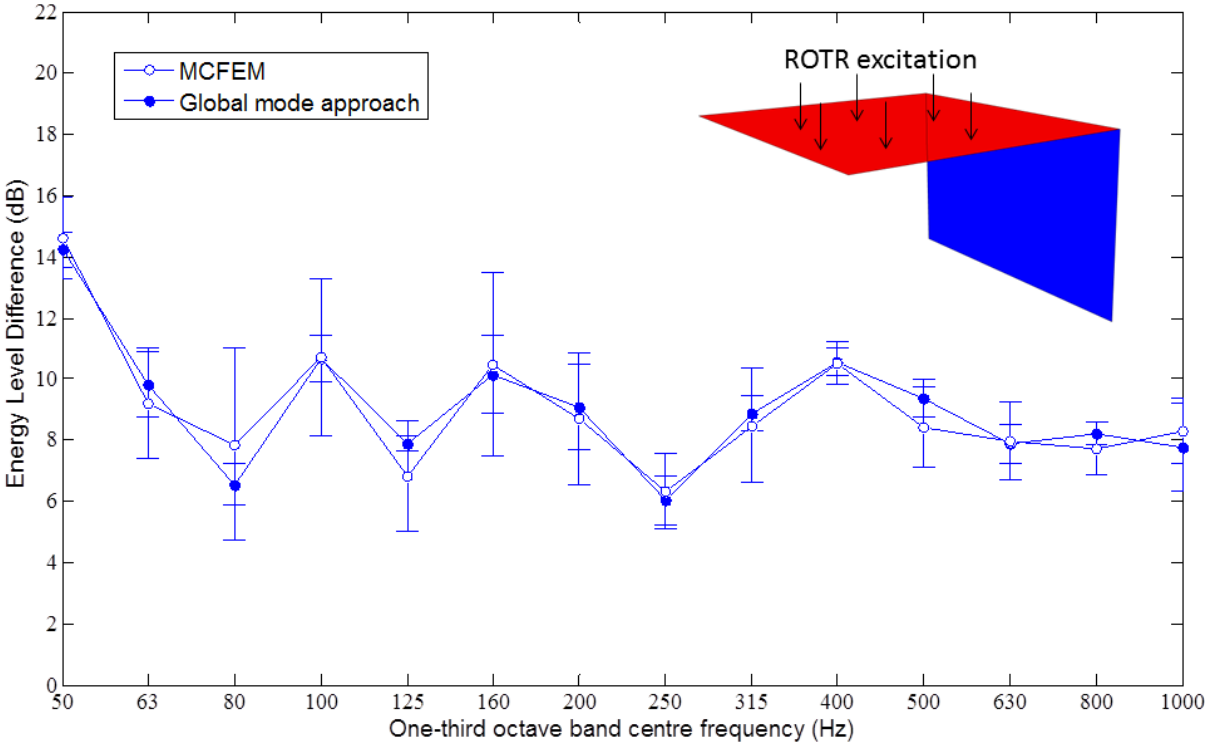

Figure 6.1. L-junction ELD from upper floor to separating wall. Comparison between global mode method ensemble and MCFEM.

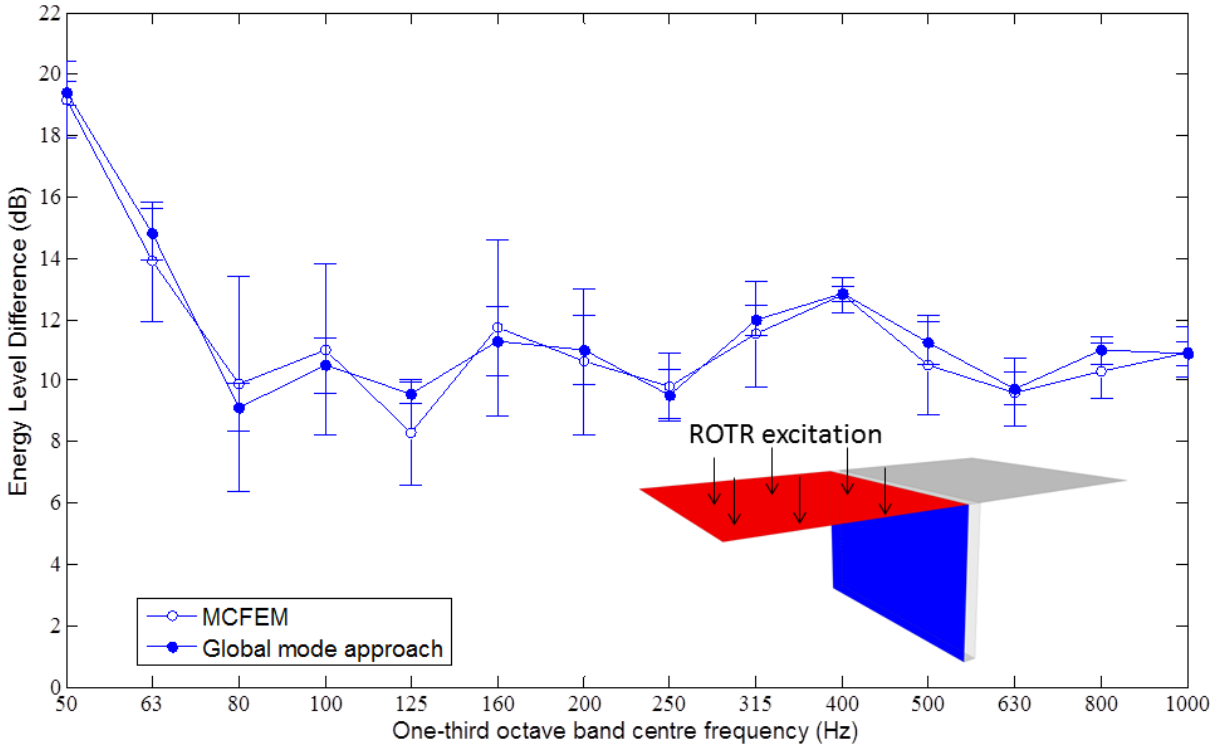

Figure 6.2. T-junction ELD from upper floor to separating wall. Comparison between global mode approach and MCFEM.

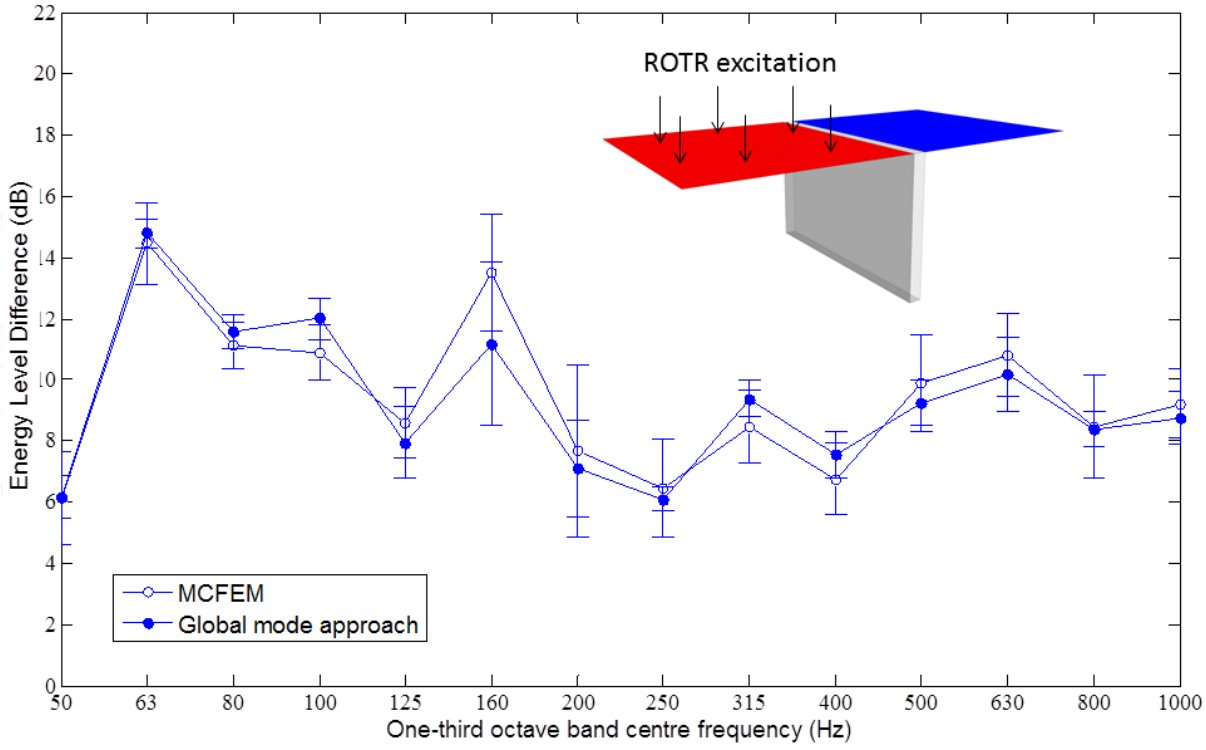

Figure 6.3 T-junction ELD from upper floor to upper floor. Comparison between global mode approach and MCFEM.

Figures 6.4 and 6.5 shows the results for an X-junction comprising two upper floors and two separating walls. Good agreement between the two predicted energy level differences is also observed.

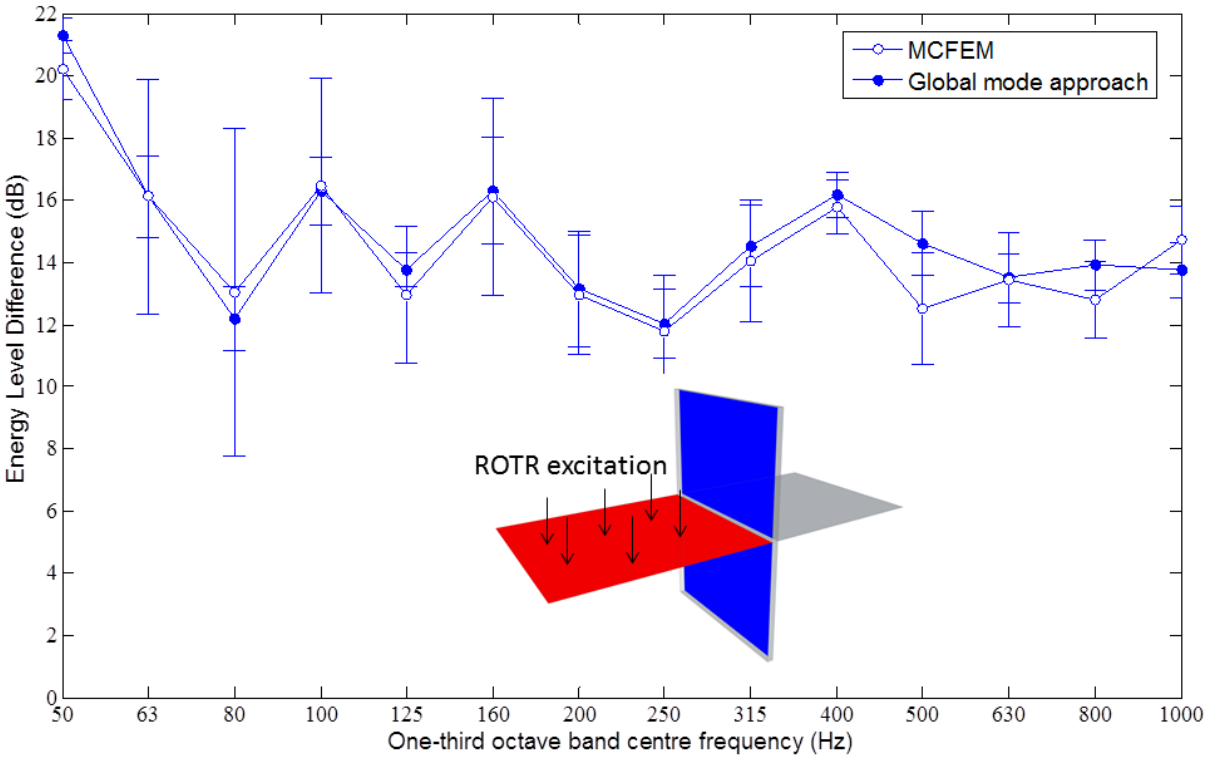

Figure 6.4 X-junction ELD from upper floor to separating walls. Comparison between global mode approach and MCFEM.

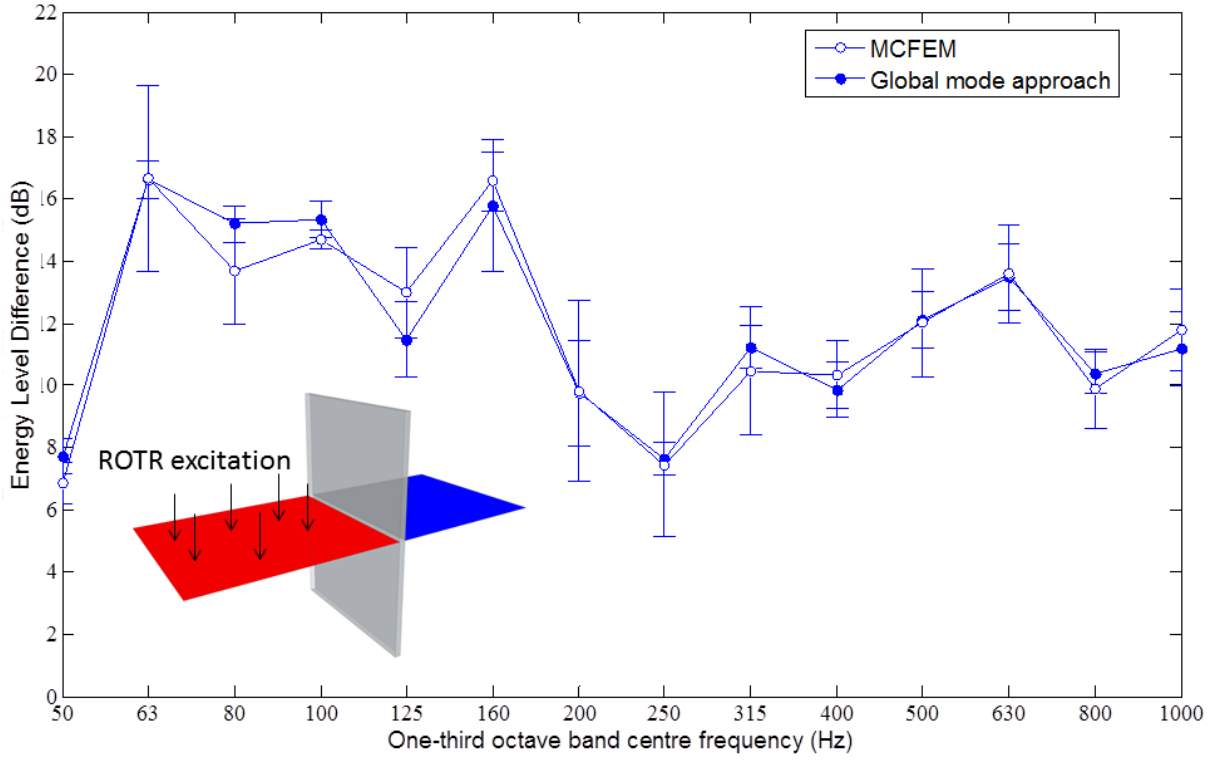

Figure 6.5. X-junction ELD from upper floor to upper floor. Comparison between global mode approach and MCFEM.

6.2.2 Inverting the EIC coefficients

There are two methods that can be used to convert the calculated ensemble of EICs into CLFs. The first method involves inverting the EIC matrix using eq. 3.54 to obtain a set of CLFs for each ensemble member. The set of ensemble CLFs is averaged to obain the ensemble-average CLF. The second method averages the ensemble EICs to obtain the ensemble-average EIC which is then inverted to obtain the CLF. The first method has the advantage that the statistics of the ensemble CLFs can be obtained. Using the SEA permutation method [33] the 95% confidence limits of the CLFs can be used in an SEA matrix to give an estimate of the statistical distribution of the ELD. However in some bands the calculated CLFs belonging to a particular ensemble member may be negative and cannot be used in an SEA model. A negative CLF at a specific frequency has no physical meaning and indicates that there are problems when fitting an SEA model to the system for the individual enemble member within the band. The solution adopted here was to eliminate negative CLFs from the ensemble of CLFs before linear averaging to predict the mean one-third octave band CLFs.

There are several methods available to invert the EIC matrix. Lalor [56] has developed two approaches to determine the CLFs from input powers and subsystem energies. The first approach, which is descibed in Section 2.2.5, divides the ESEA energy balance equations into two parts which can be solved separately to give the coupling and internal loss factors independently. This method will be referred to as the Lalor method and its main advantage is that it reduces the size of an N subsystem ESEA matrix from an NxN matrix to an (N-1) x (N-1) matrix and should reduce the error in the calculation of the CLFs. The second approach is referred to as simplified ESEA (eq. 2.20) and gives the CLFs between subsystems i and j in terms of the energy in subsystem j when power is input to subsystem i , the energy in subsystem i when power is input to subsystem i and the TLF of subystem j. Simplified ESEA always gives a positive value for the CLF and avoids the inversion of a matrix in the calculation of the CLFs.

Note that ESEA using eq. 2.13 was compared to Lalors method for the L-, T- and X-junctions but there was no significant difference between the calculated CLFs.

In Figure 6.6 the ELD computed using matrix SEA incorporating ESEA CLFs is compared to the ELD calculated directly from the EICs (eq. 6.1) for the case of excitation into the floor of the L-junction. The EICs were calculated using the global mode approach and the CLFs were derived from EICs using Lalors method. The internal loss factor in the SEA models was set to the value of $1/\sqrt{f}$ which is the same value as used in the global mode models used to obain the EICs. The black straight line is the SEA ELD calculated using angular averaged wave theory transmission coefficients. The 95% confidence limits derived using the SEA permutations method are represented by the purple dashed lines.

For the case of the L junction the SEA permutation method gives a good representation of the mean value and the 95% confidence limits of the ELD. The results show that using CLFs from semi-infinite plate theory in matrix SEA underestimates the ELD by around 3dB in the frequency region 100 to 1000Hz.

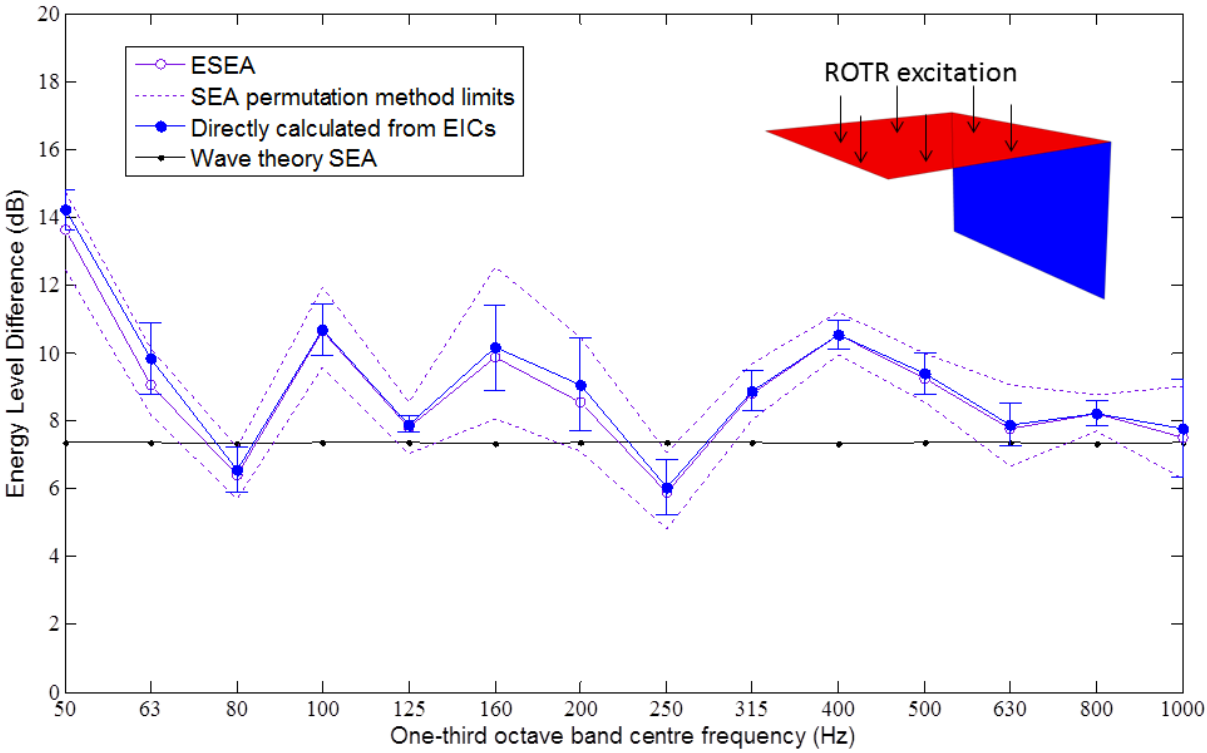

Figure 6.6. Comparison of ELDs calculated using the EICs directly and matrix SEA incorporating ESEA CLFs for the case of the L-junction. Power input to the upper floor (red) receiving subsystem is the separating wall (blue).

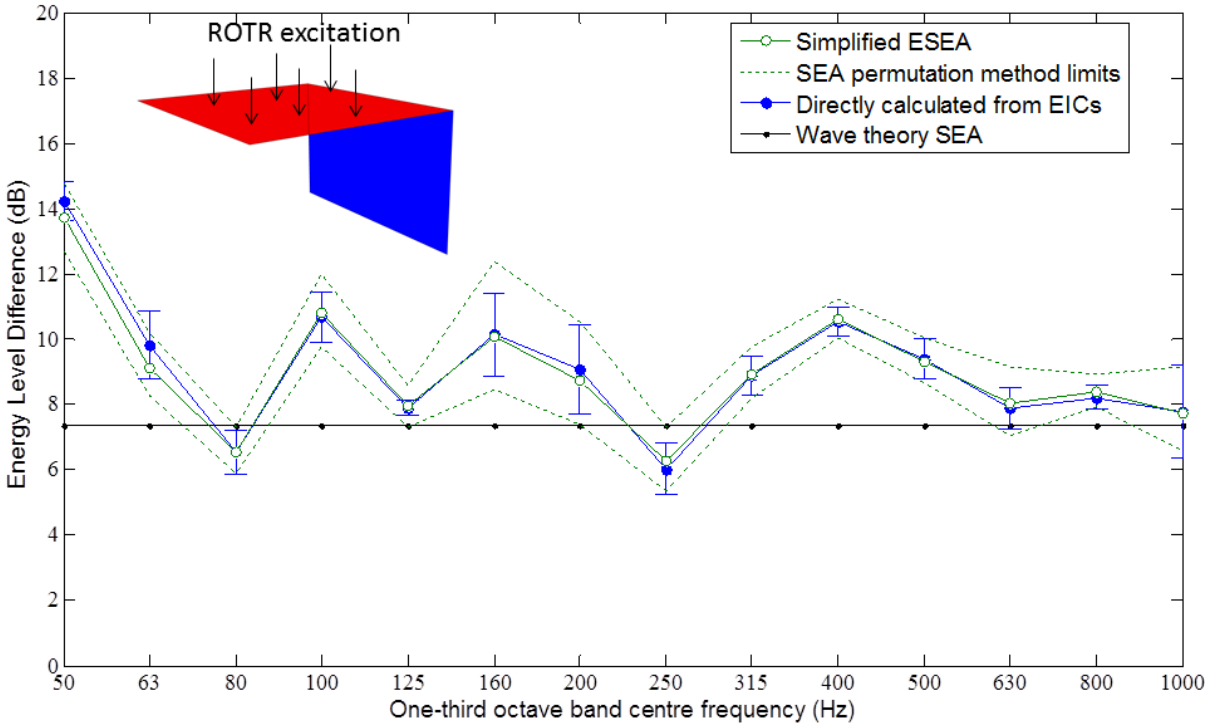

Figure 6.7 Comparison of ELDs calculated using the EICs directly and matrix SEA incorporating simplified ESEA CLFs for the case of the L-junction. Power input to the upper floor (red) receiving subsystem is the separating wall (blue)

The procedure was repeated for the case of the X-junction described in Section 6.2.1. The results are shown in Figures 6.8 to 6.11. In Figure 6.8 an interesting feature occurs in the 80Hz and 100Hz bands for the ELD predicted using the ESEA CLFs. The mean ESEA result is quite close to the ELD calculated using the EICs; however the ESEA permutation method over-predicts the 95% confidence limits. Comparing this result to Figure 6.9 shows that a significant improvement in the range of response is obtained by using simplified ESEA. All members of the simplified ESEA ensemble contain positive CLFs whereas the ESEA members that contain negative CLFs are removed. It is therefore proposed that this feature is a result of the removal of some ensemble members from the ESEA ensemble.

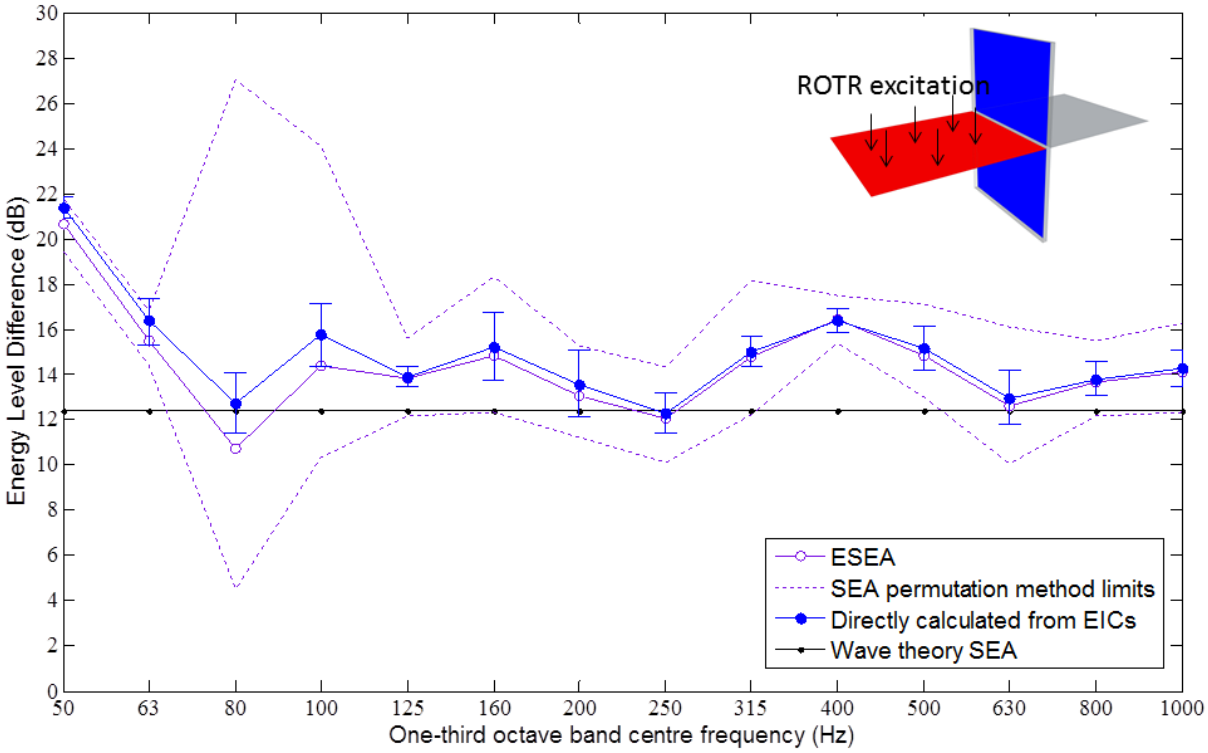

Figure 6.8. Comparison of ELDs calculated using the EICs directly and matrix SEA incorporating ESEA CLFs for the case of the X-junction. Power input to the upper floor (red) receiving subsystem are the separating walls (blue)

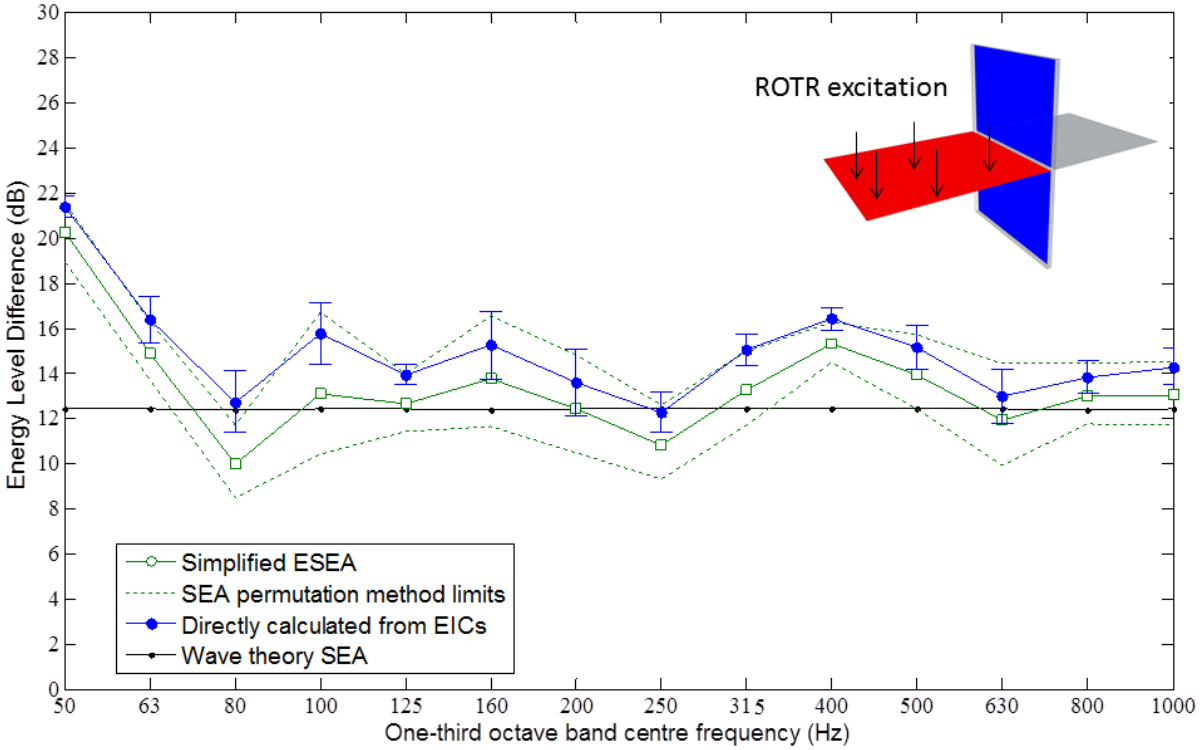

Figure 6.9. Comparison of ELDs calculated using the EICs directly and matrix SEA incorporating simplified ESEA CLFs for the case of the X-junction. Power input to the upper floor (red) receiving subsystems are the separating walls (blue)

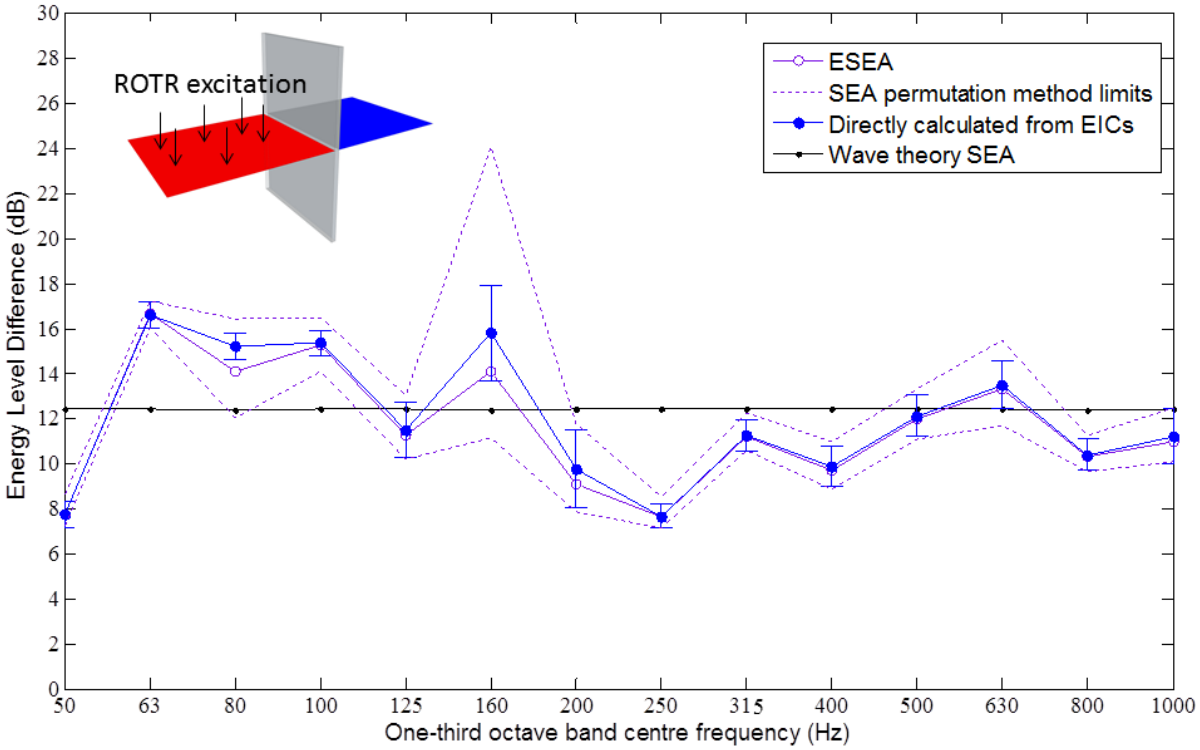

Figure 6.10. Comparison of ELDs calculated using the EICs directly and matrix SEA incorporating ESEA CLFs for the case of the X-junction. Power input to the floor (red) receiving subsystem is the floor in the adjacent room (blue)

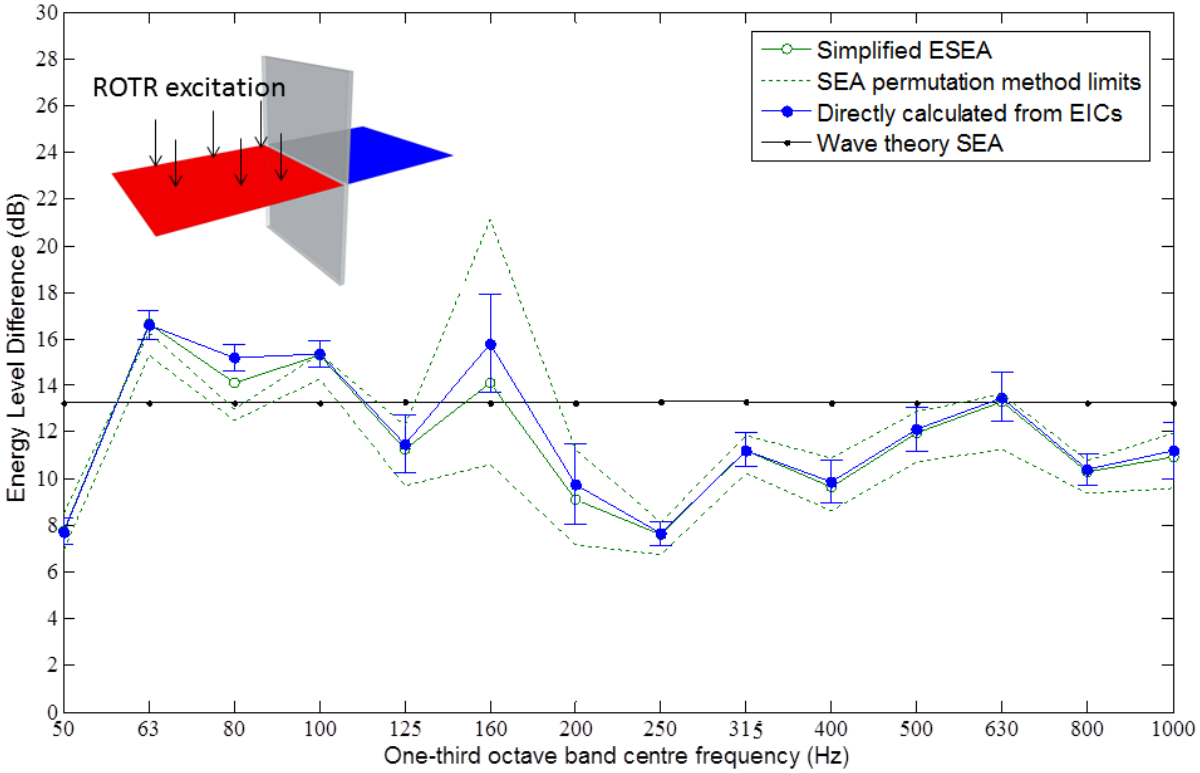

Figure 6.11. Comparison of ELDs calculated using the EICs directly and matrix SEA incorporating simplified ESEA CLFs for the case of the X-junction. Power input to the floor (red) receiving subsystem is the floor in the adjacent room (blue)

Using CLFs from semi-infinite plate theory in the SEA model under-predicts the ensemble-average ELD by approximately 2 to 3dB going around the corner to the separating wall subsystem. Going straight across the X-junction to the other floor subsystem overestimates the ensemble average ELD by 3 to 4dB at frequencies above 160Hz. In general there is good agreement between the ensemble-average ELD calculated using ESEA CLFS in an SEA model and the ensemble-average ELD calculated using the EICs. Using ESEA CLFs can capture some of the modal features which do not occur with wave theory SEA. For example, Figure 6.10 shows that at 250Hz there is high transmission across the X-junction which results in a difference of 5dB between the SEA prediction using wave theory CLFs and ESEA CLFs. However using the SEA permutations method with ESEA CLFs tends to over predict the 95% confidence limits significantly at frequencies below 200Hz (see Figures 6.8 and 6.10).

Compared to the case of the L-junction shown in Figure 6.7 simplified ESEA CLFs are less accurate for the case of the X-junction. For example, in Figure 6.9 the ensemble average ELD predicted by matrix SEA using simplified ESEA CLFs under predicts the ELD by around 2dB across the frequency range.

The simplified ESEA equation (eq. 2.20) can be rewritten in terms of the energy in subsystem *j* when power is input to subsystem *i*.

$$E_{ji} = \frac{\eta_{ij}}{\eta_{jj}} E_{ii} \tag{6.2}$$

Comparing eq. 6.2 to eq. 2.12 shows that using simplified ESEA assumes the energy in the receiver subsystem *j* is transmitted via a direct path from the source subsystem. Comparing Figures 6.6 and 6.7 this assumption seems to be valid for the L-junction where there is only one transmission path between source and receiving subsystems. However, for the X-junction there are several paths between source and receiving subsystems which are accounted for in ESEA but are not considered when using eq. 6.2.

To test this hypothesis the energy in the receiver subsystem was written in terms of the sum of the direct path (i.e. first-order) and second-order paths

$$\frac{E_{ji}}{E_{ii}} = \frac{\eta_{ij}}{\eta_{jj}} + \sum_{k \neq i,j} \frac{\eta_{ik}}{\eta_{kk}} \frac{\eta_{kj}}{\eta_{jj}} \tag{6.3}$$

Equation 6.3 can be rearranged to give an expression for the coupling loss factor η_{ij}

$$\eta_{ij} = \frac{E_{ji}}{E_{ii}} \eta_{jj} - \left(\sum_{k \neq i,j} \frac{\eta_{ik} \eta_{kj}}{\eta_{kk}} \right) \tag{6.4}$$

This may be solved for η_{ij} by making the substitutions $\eta_{jj} \approx \frac{\pi_{\text{in},j}}{\omega E_{jj}}$ and $\frac{\eta_{ij}}{\eta_{jj}} = \frac{E_{ji}}{E_{ii}}$ in eqn. 6.4 which gives

$$\eta_{ij} = \frac{E_{ji}}{E_{ii}} - \left(\sum_{k \neq i,j} \frac{E_{ki}}{E_{ii}} \frac{E_{jk}}{E_{kk}} \right) \tag{6.5}$$

Equation 6.5 was used to calculate the CLFs between the subsystems in the X-junction. These were then used in matrix SEA to calculate the ELD for comparison with the ELD calculated directly from the EICs and the ELD calculated using CLFs from Lalor's method and simplified ESEA. The ensemble-average ELD results are shown in Figures 6.12 and 6.13.

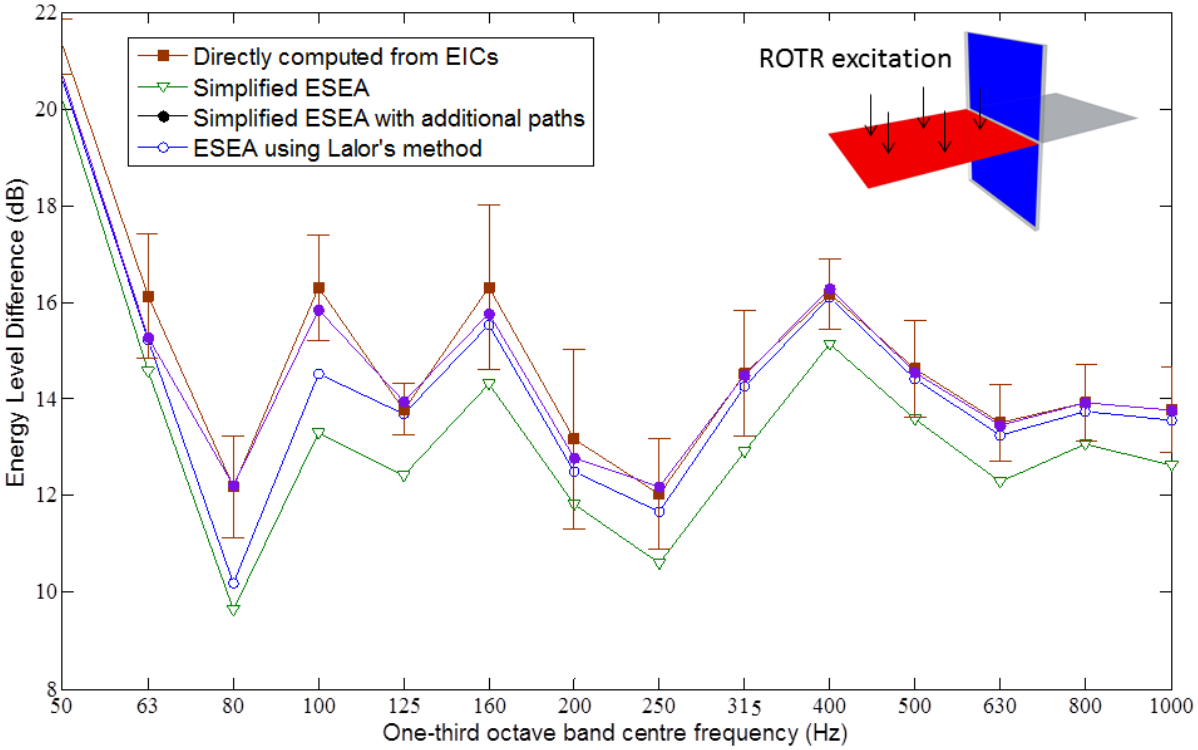

Figure.6.12. Comparison of the ELD obtained using CLFs computed from the three different methods. Excitation is applied to the upper floor and the energy level difference is taken between the source plate and the separating walls.

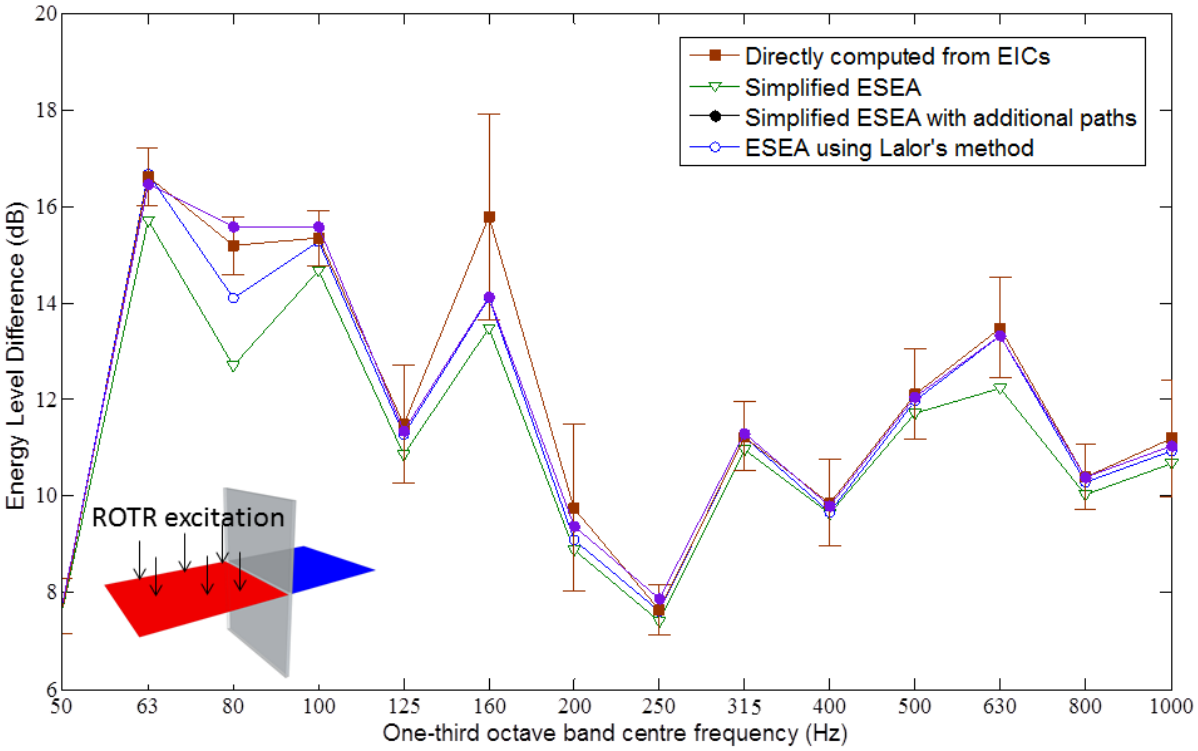

Figure.6.13. Comparison of the ELD obtained using CLFs computed from the three different methods. Excitation is applied to the upper floor and the energy level difference is taken between the source plate and the upper floor.

Using the CLFs computed with eq. 6.5 gives a result which is closer to the Lalor method and in some cases gives results which are closer to the true ELD calculated directly from the EICs. For example in Figure 6.13 the method shows a marginal improvement over Lalor's ESEA method in the 100 and 125Hz bands. For this particular case it was found that the number of negative CLFs computed using eq.6.5 was less than the number of negative CLFs computed using Lalor's method in these two bands. Hence the ensemble of CLFs calculated using Lalor's method included a smaller fraction of positive CLFs that would be required to accurately predict the ensemble-average CLF.

6.3 Incorporating CLFs calculated from finite plates in SEA models of large buildings

In this section the CLFs for isolated junctions are calculated using the global mode approach (Section 6.2) and incorporated into SEA models of large heavyweight buildings. In this process each plate in the isolated junction is assigned a TLF which is calculated from an SEA model which uses CLFs from semi-infinite plate theory (Chapter 2). The junction line boundary is assigned conditions of continuity, balance of moments and zero displacement. The remaining boundaries are assumed to be simply supported. The CLFs are calculated as

described in Section 6.2 and incorporated into the SEA power balance equations for the building. The ELDs resulting from the matrix inversion of the power balance equations are referred to here as being determined using the global mode SEA approach.

6.3.1 General comparison between global mode SEA and MCFEM ELDs

In Figure 6.14 a general comparison is made between MCFEM and the global mode SEA approach for the case of excitation applied to the upper floor of room 1 in the 2_2_2 building. Each blue line in the figure shows the difference in dB between ELDs calculated using the two methods with 95% confidence limits. Hence for good agreement between the two methods a set of blue lines which fit tightly around the zero dB line would be expected.

At frequencies where the one-third octave band statistical mode count is less than one (below 200Hz) the difference between MCFEM and the global mode SEA approach is between -10 dB and +20 dB. At frequencies above 200Hz the difference is between -5dB and +10dB.

In Figure 6.15 the difference between the MCFEM and SEA ELDs are plotted when using CLFs from semi-infinite plate theory for the SEA model. Comparing Figure 6.14 to Figure 6.15 indicates that the SEA model predictions are not improved by incorporating global mode CLFs for this particular case.

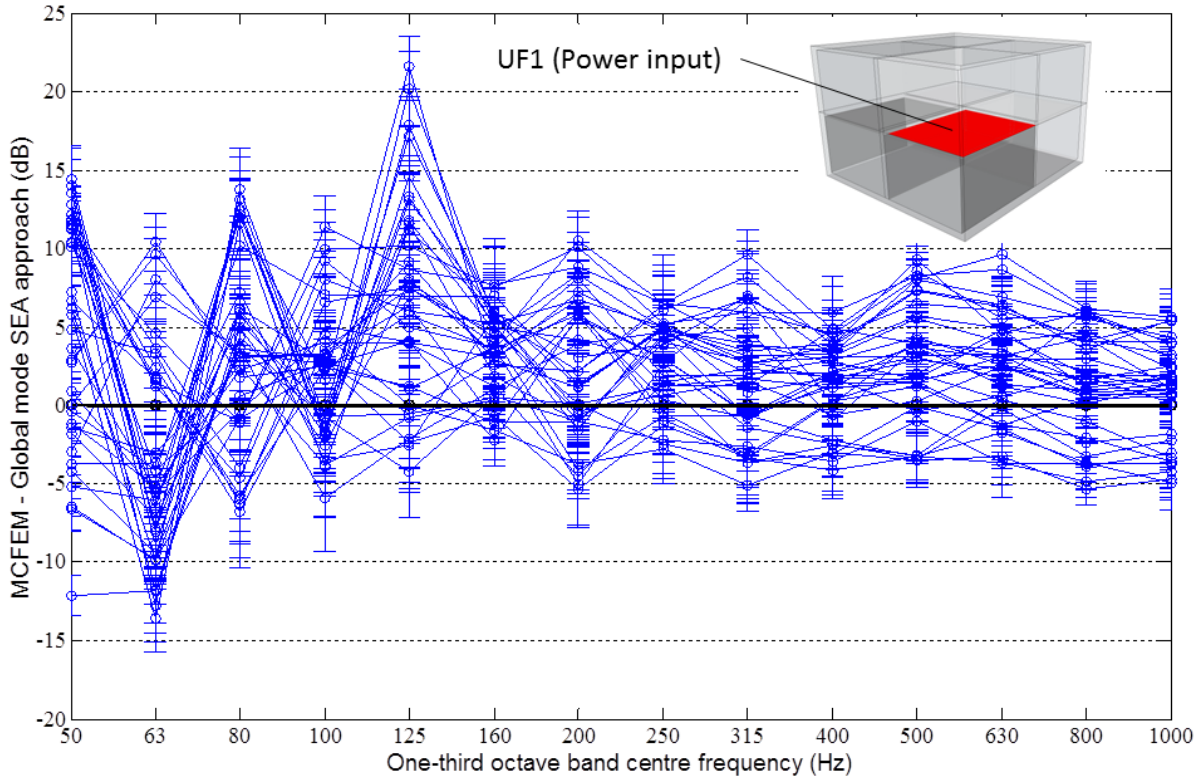

Figure 6.14. Difference between MCFEM ELDs and Matrix SEA ELDs for a 2_2_2 building with power input to the upper floor of room 1. Global mode CLFs used.

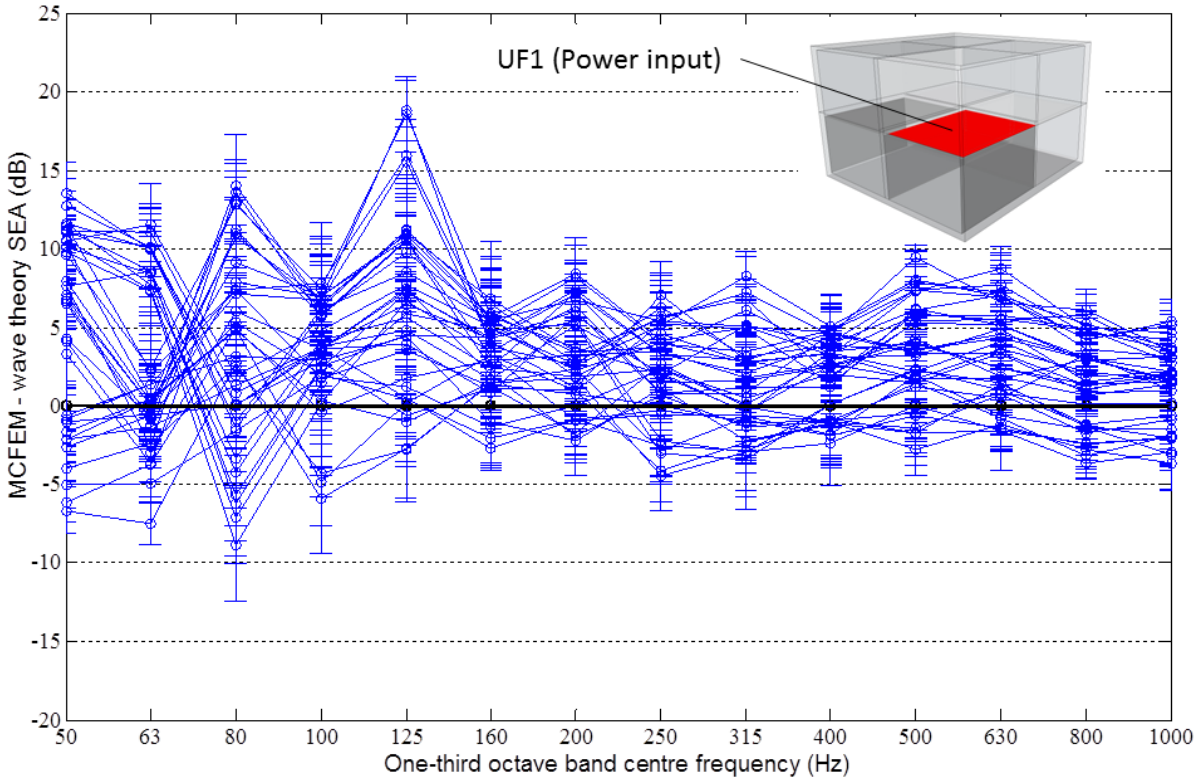

Figure 6.15. Difference between MCFEM ELDs and Matrix SEA ELDs for a 2_2_2 building with power input to the upper floor of room 1. . SEA uses CLFs from semi-infinite plate theory CLFs.

In Figure 6.16 a general comparison is made between MCFEM and the global mode SEA approach for the case of excitation applied to the upper floor of room 1 in the 5_1_1 building. The results using semi-infinite plate transmission coefficients are shown in Figure 6.17. Comparing both figures at frequencies below 200Hz indicates that generally no improvement is made by incorporating global mode CLFs in the SEA model with differences between -15dB and +20dB. At frequencies above 200Hz there is marginal improvement in the global mode SEA approach over SEA using CLFs from semi-infinite plate theory. The differences between MCFEM and SEA using CLFs from semi-infinite plate theory are between -15dB to +8dB of the MCFEM result in this frequency range and between MCFEM and global mode SEA approach are -10dB to +8dB. The most significant improvement occurs in the 250Hz band and the 400 Hz bands.

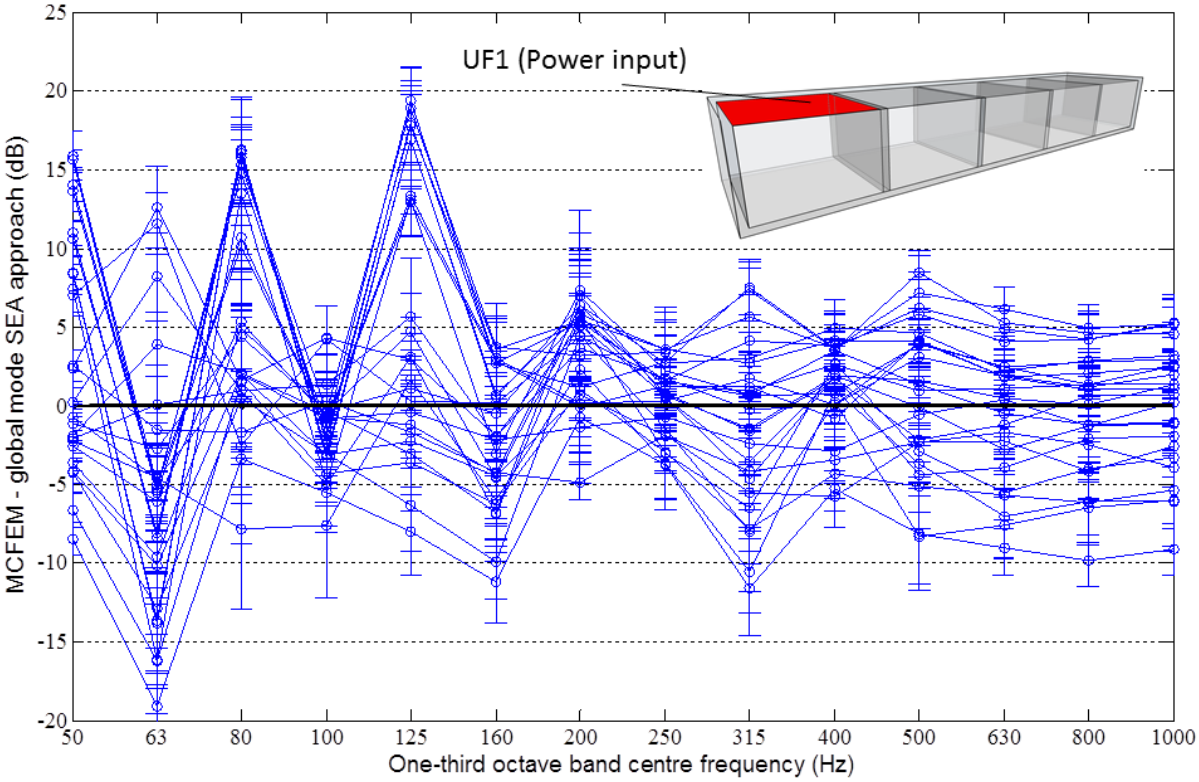

Figure 6.16. Difference between MCFEM ELDs and Matrix SEA ELDs for a 5_1_1 building with power input to the upper floor of room 1. Global mode CLFs used.

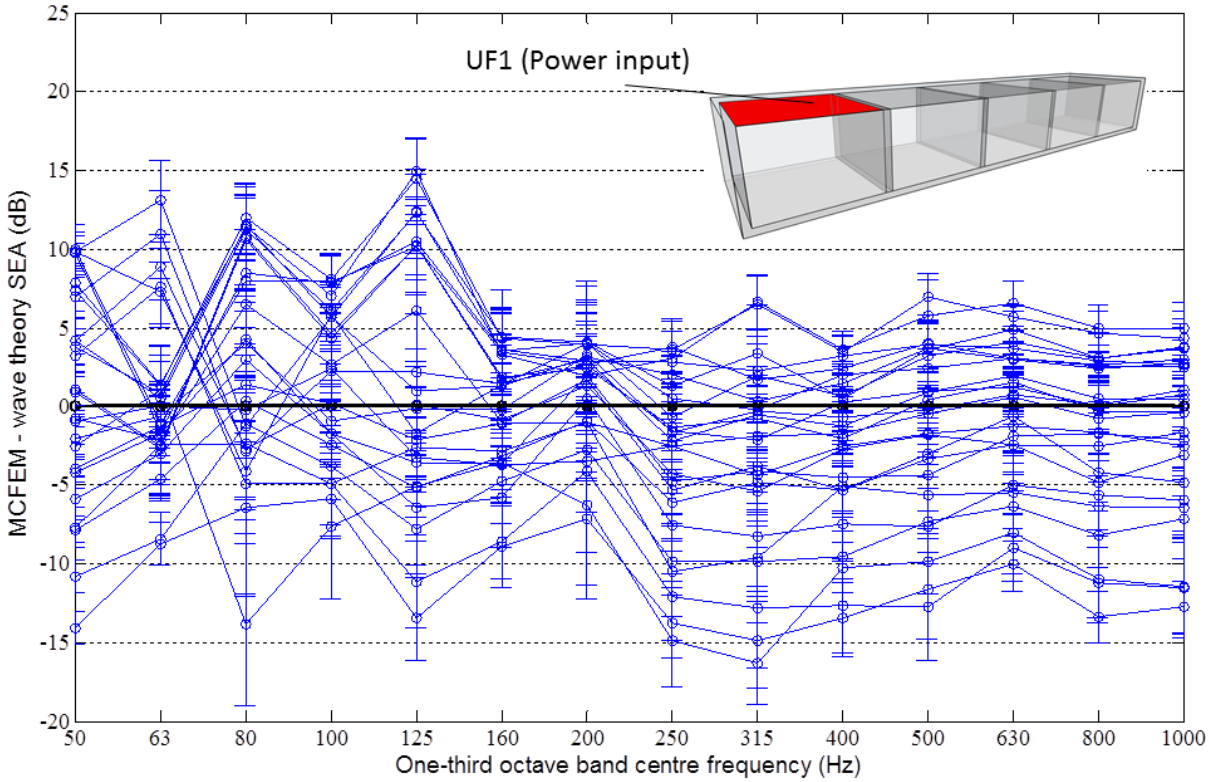

Figure 6.17. Difference between MCFEM ELDs and Matrix SEA ELDs for a 5_1_1 building with power input to the upper floor of room 1. Wave theory CLFs used.

6.3.2 Comparison between the global mode SEA approach and MCFEM – specific cases

In this section the MCFEM results are compared to the global mode SEA results for specific sets of source and receiver subsystems.

In Figure 6.18 a comparison is made between MCFEM and the global mode SEA approach for the case of excitation applied to the upper floor of room 1 of the 2_2_2 building. The figure shows the difference in dB between the two predictions. Each curve corresponds to the level difference between the source plate and the plate with the corresponding colour as the curve indicated on the diagram. All the global mode SEA ELDs are between -1dB and 5dB of the MCFEM results at frequencies above 200Hz. In Figure 6.19 the same plots are shown only this time the CLFs have been calculated using semi-infinite plate theory and are between -5 and +5 dB of the MCFEM results. Comparison of the two figures indicates that using global mode CLFs can improve the SEA predictions above 200Hz for plates directly connected to the source plate. At frequencies below 200Hz the figures indicate no significant difference between SEA using CLFs from semi-infinite plate theory and global mode SEA predictions.

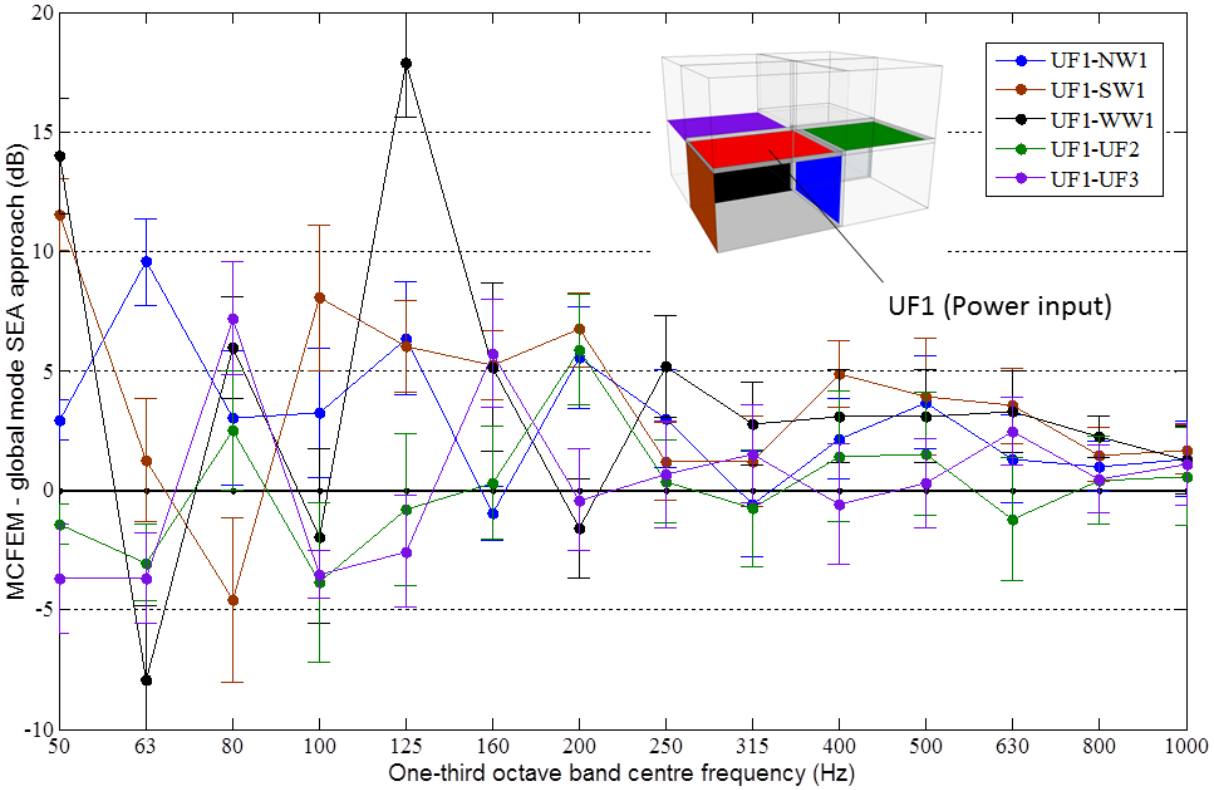

Figure 6.18. Difference between the MCFEM and global mode SEA approach for the 2_2_2 building with power input to the upper floor of room 1.

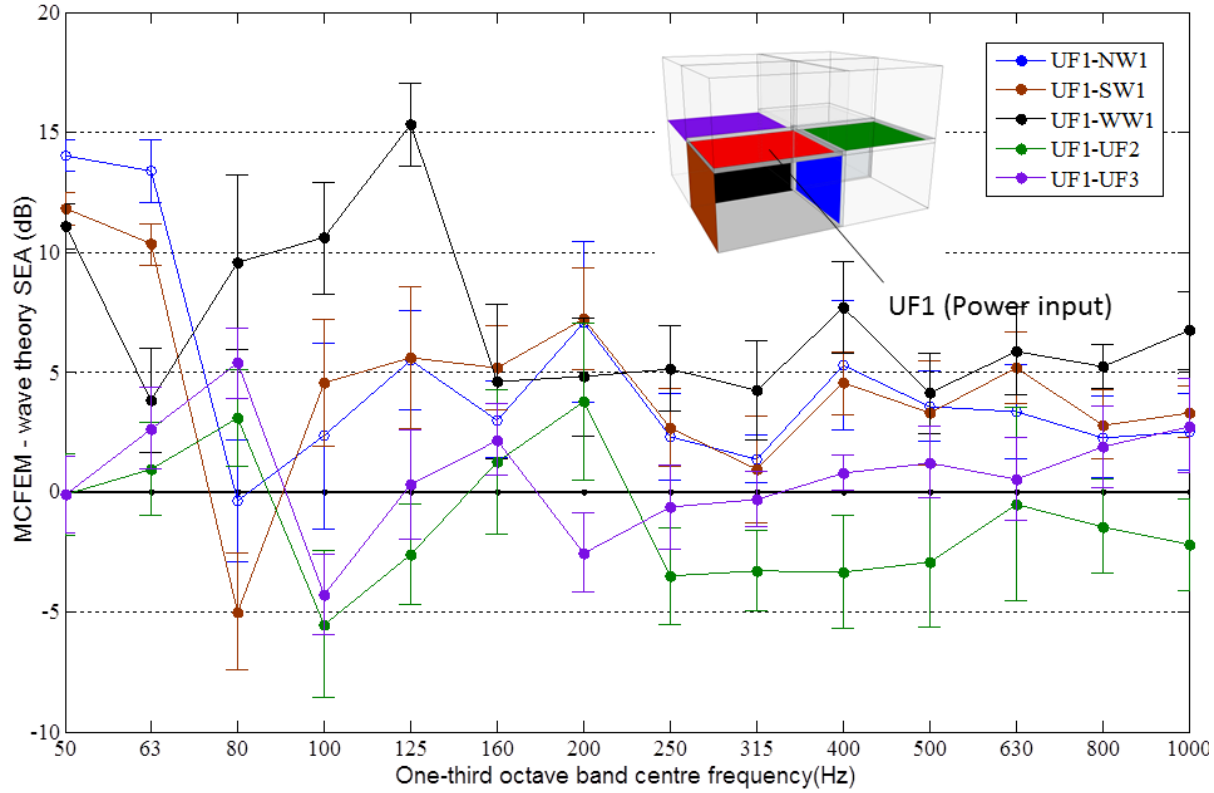

Figure 6.19. Difference between MCFEM and wave theory SEA for the 2_2_2 building with power input to the upper floor of room 1.

In Chapter 5 it was noted that in some cases the receiver plates would form the room that is diagonally opposite the source room. To test this case excitation is applied to the upper floor of room 1 and the level difference between this plate and the plates connected to rooms 4 and 8 (see Figure 5.3) are taken.

The ELDs from SEA using CLFs from semi-infinite plate theory differed from MCFEM by -1dB to +8dB at frequencies above 200Hz (see Section 5.4.2). In Figures 6.20 to 6.22 the difference between the MCFEM ELD and the global mode SEA ELD for the plates connected to room 4 and 8 is shown. There is a difference of between 0 and + 10dB in the MCFEM and the global mode SEA approach for the flanking walls (see Figure 6.20) above 200Hz. In Figure 6.22 the difference between MCFEM and the global mode SEA approach for the floor subsystems in room 4 and 8 is generally between -3dB and 5dB above 200 Hz. In Figure 6.22 the difference between MCFEM and global mode SEA is between +3dB and 10dB above 200Hz. The closest agreement occurs with transmission from the upper floor of room 1 to the floor subsystems of rooms 4 and 8 (see Figure 6.21); however this is misleading because all paths from the upper floor of room 1 to the upper floor of room 8 (or the lower floor of room 4) must pass through a flanking or separating wall.

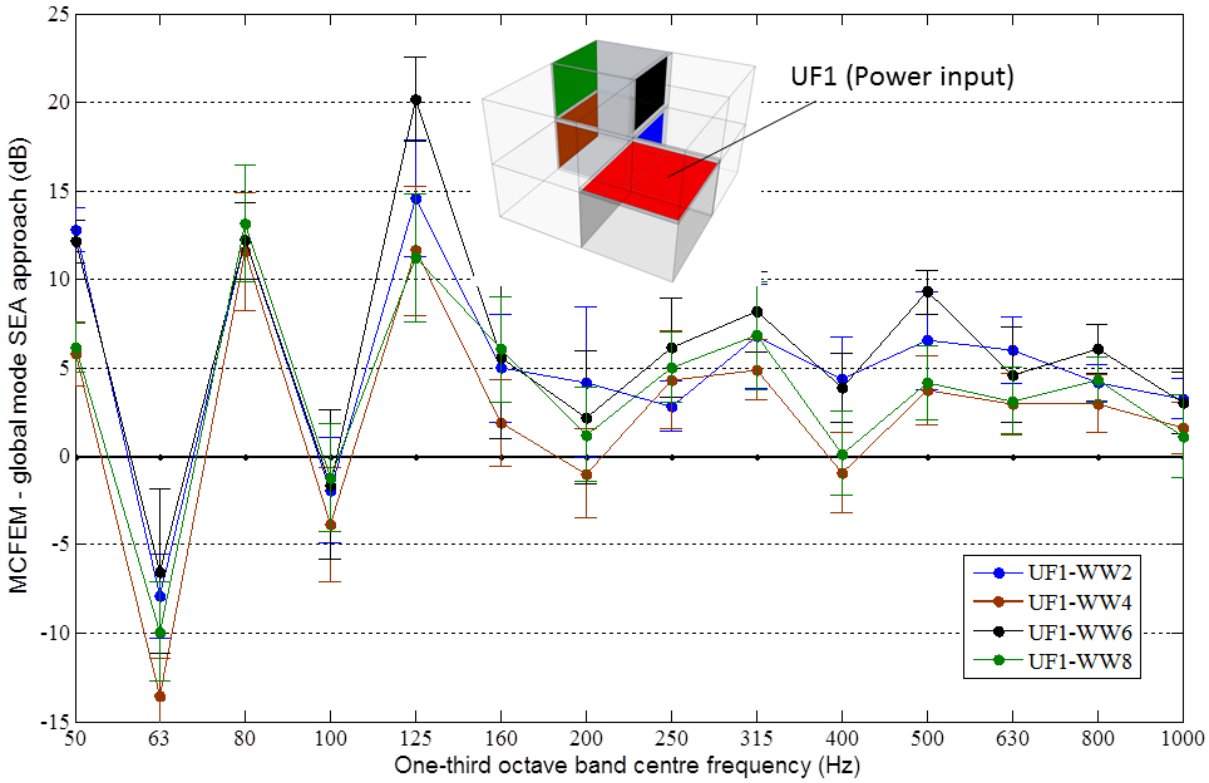

Figure 6.20 Difference between the MCFEM and global mode SEA predictions for the ELD between the upper floor and room 1 and the flanking walls in rooms 4 and 8

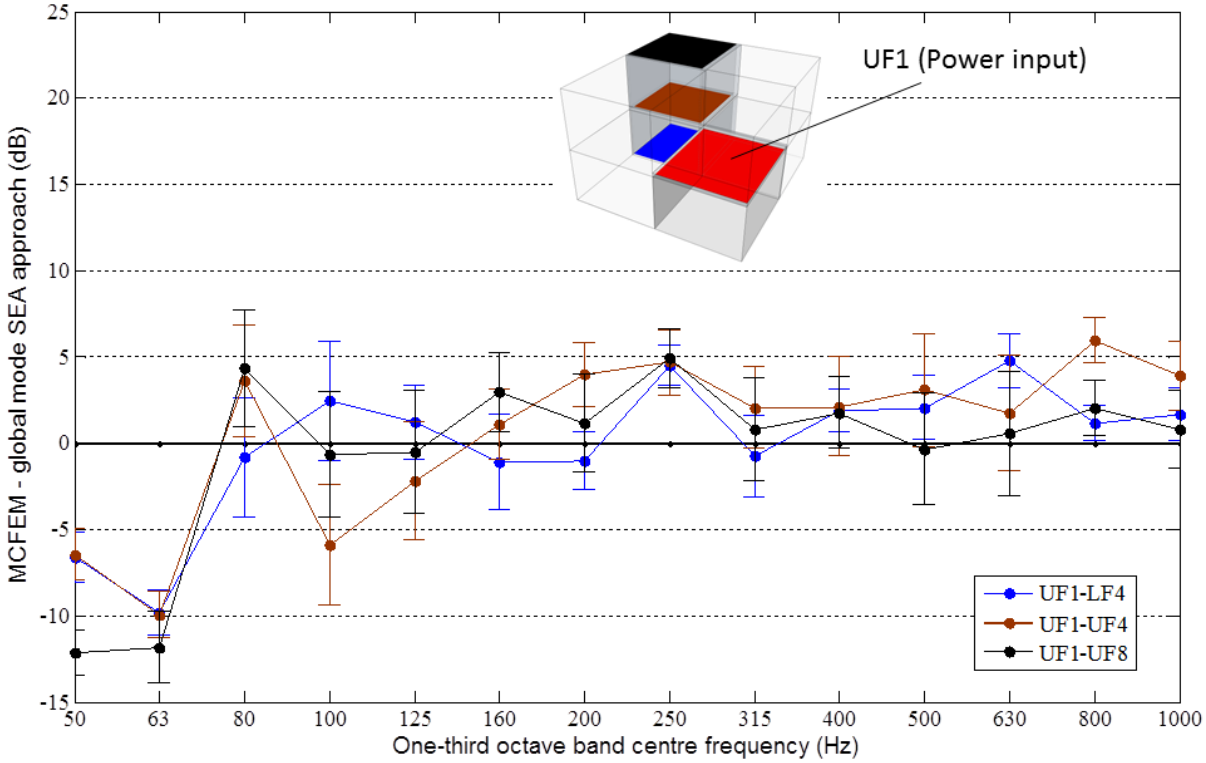

Figure 6.21 Difference between MCFEM and global mode SEA predictions for the ELD between the upper floor and room 1 and the floors in rooms 4 and 8

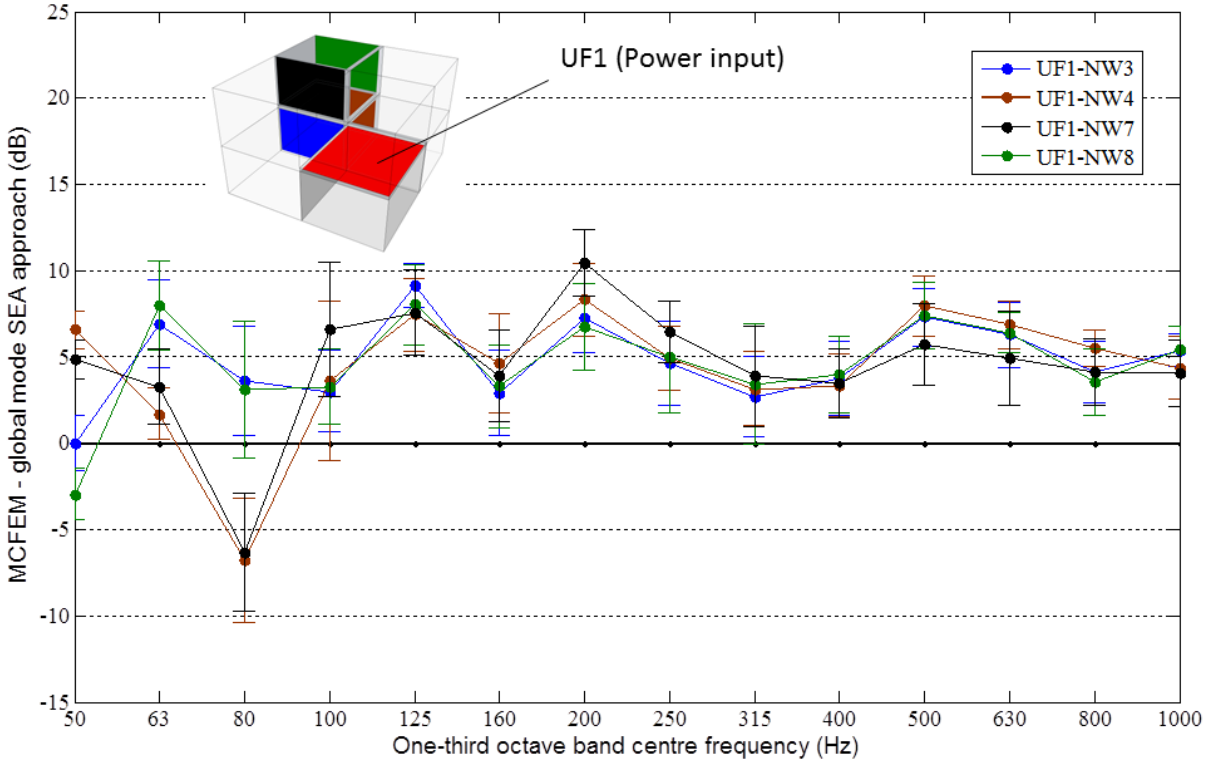

Figure 6.22 Difference between MCFEM and global mode SEA predictions for the ELD between the upper floor and room 1 and the separating walls in rooms 4 and 8

Figures 6.23 to 6.26 show a direct comparison between MCFEM and the global mode SEA approach for the ELD between the upper floor of room 1 and the remaining plates in the

5_1_1 building. The global mode SEA ELDs are represented by lines with colour filled circular markers and the MCFEM results are represented by open circular markers. Each ELD curve is colour coded according to the inset diagram on each plot.

In Figure 6.23 the MCFEM and global mode SEA results are compared for the ELDs between the upper floor of room 1 and the flanking walls of the 5_1_1 building. (note that due to symmetry it is not nessesary to show the ELDs to the flanking walls on the other side of the building). Above 200Hz the global mode SEA results are very close to MCFEM when predicting the ELD to the flanking wall of room one.

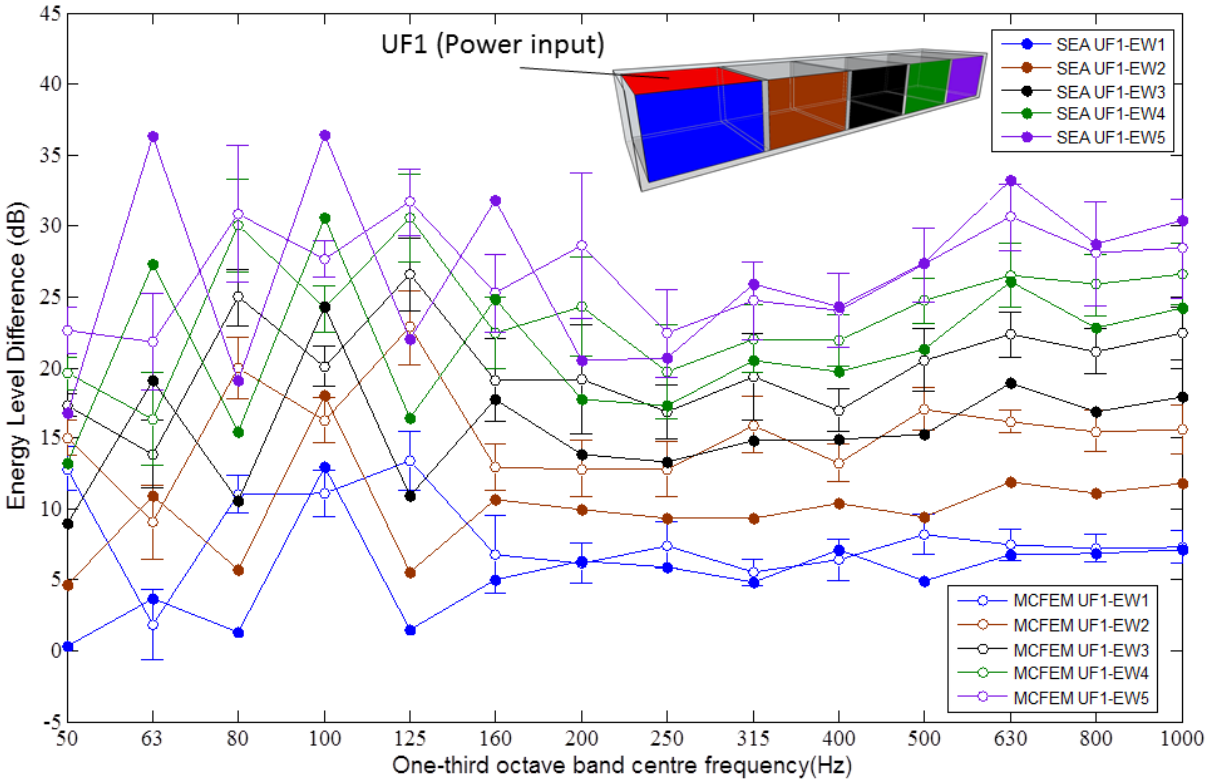

Figure 6.23 MCFEM and global mode SEA predictions for the ELD between the upper floor and room 1 and the flanking walls of 5_1_1 building.

However, there is an offset of aprroximately 5dB between the two predictions for the ELD to the flanking wall of room two and an offset of approximately 3dB to room 3. The global mode SEA ELD to the flanking wall of room four is generally within 2dB of the MCFEM result and close agreement between the two predictions is shown for the ELD to the flanking wall of room 5 with global mode SEA ELD within approximately 3dB of MCFEM.

Figure 6.24 shows the ELDs from the upper floor of room 1 to the remaining upper floors of the 5_1_1 building.

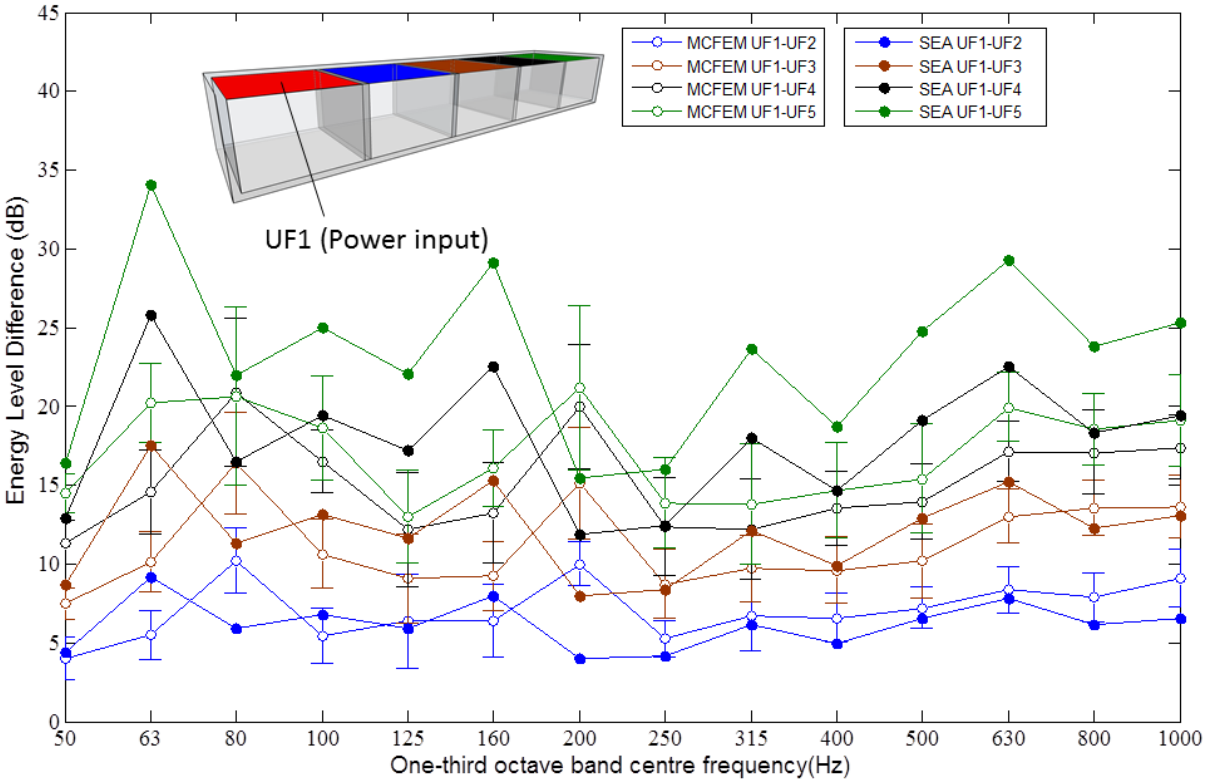

Figure 6.24 MCFEM and global mode SEA predictions for the ELD between the upper floor of room 1 and the upper floors of the 5_1_1 building.

There is good agreement between the two methods for the ELDs to the upper floors of rooms 2, 3 and 4 with most global mode SEA results lying within or close to the 95% confidence limits of MCFEM. The MCFEM results predict relatively high transmission in the 125Hz, 160Hz, 250 Hz, 316Hz and 400Hz one-third octave bands which has a slight peak in the ELD in the 200Hz one-third octave band. The global mode SEA ELDs predict a slight peak in the ELD in the 160Hz and 315 Hz bands and appears to capture the feature of the high transmission in some of the adjacent bands.

Figure 6.25 shows the ELDs from the upper floor of room 1 to the separating walls of the 5_1_1 building.

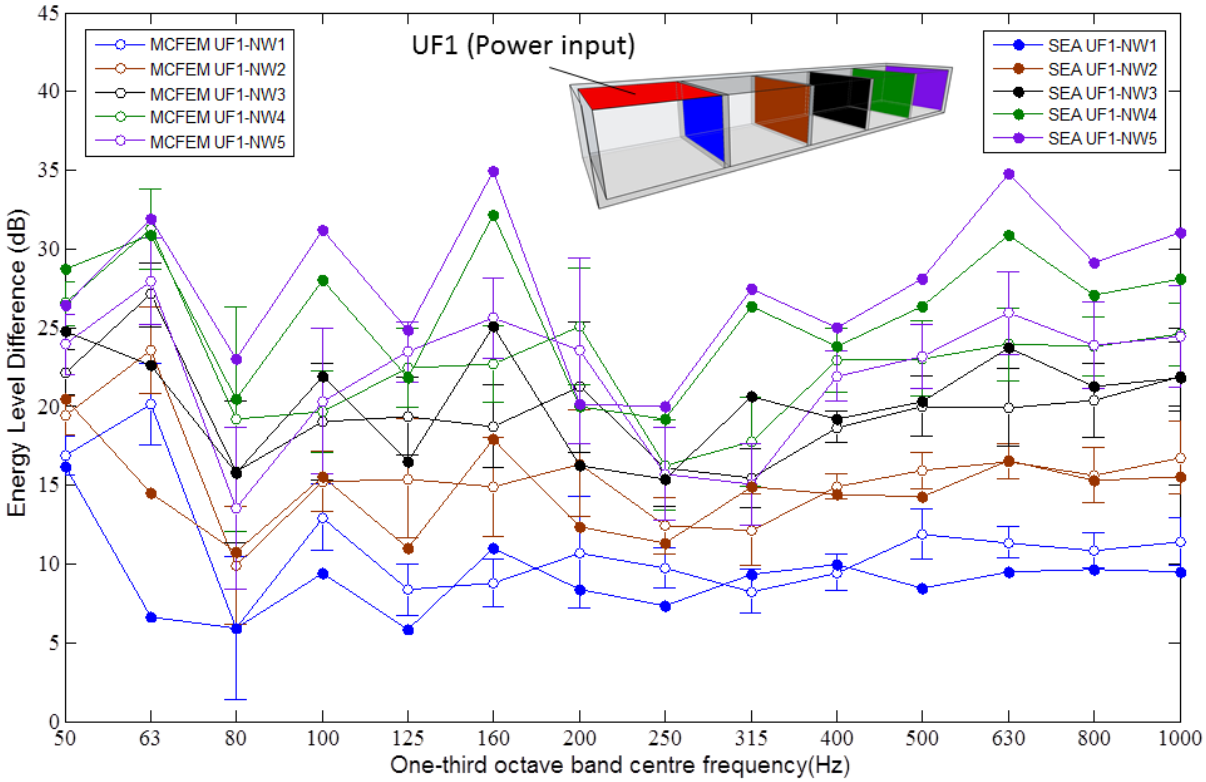

Figure 6.25 MCFEM and global mode SEA predictions for the ELD between the upper floor and room 1 and the separating walls (North walls) of the 5_1_1 building.

There is a notable feature in the 250 and 315 Hz bands with the MCFEM results. In these bands the ELD from the upper floor of room 1 to the north wall of room 3, 4 and 5 is approximately the same. A typical estimate for structure borne sound attenuation is 3dB per structural junction between source and receiver; hence this result indicates very high transmission in these two bands. At frequencies above 200 Hz the global mode SEA approach is generally within 2dB of MCFEM for north walls of rooms 1 to 2 and 3 and are within 6dB for for the north walls of rooms 4 and 5. The 315Hz band is an exception to this general result as there is a difference of approximately 10dB between MCFEM and the global mode approach going to the north wall of rooms 4 and 5. This is due to the fact that the global mode SEA approach cannot predict the peaks and troughs to an accuracy better than one-third octave band.

Figure 6.26 shows the ELDs from the upper floor of room 1 to the lower floors of the 5_1_1 building. The global mode SEA approach generally overestimates the ELD to the floor subsystems by 3 to 10dB at frequencies above 200Hz. Compared to the ELDs to the upper floors (see Figure 6.25) the difference between the MCFEM and global mode SEA ELDs is significantly greater. It is expected [51] that SEA will be most accurate for subsystems in

which the geometrical mean of the modal overlap factors is large. However, these results indicate that that this is not the case for these buildings.

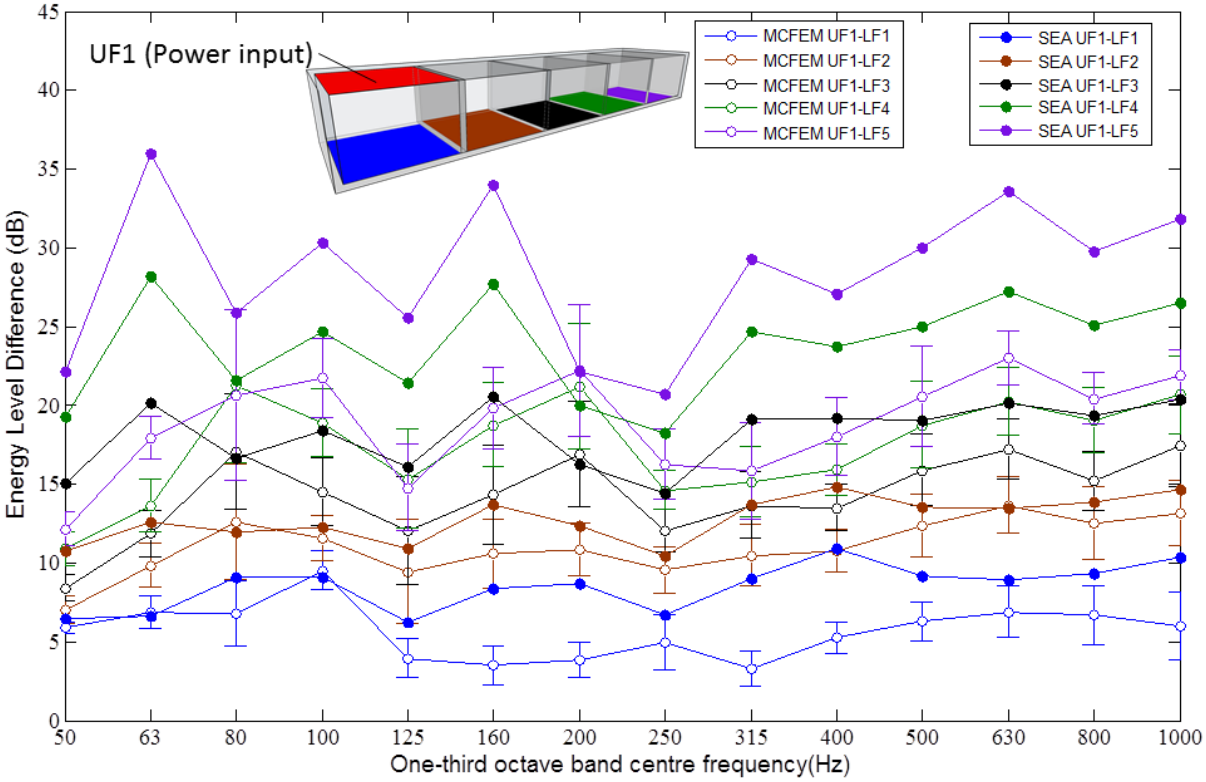

Figure 6.26 MCFEM and global mode SEA predictions for the ELD between the upper floor and room 1 and the lower floors of the 5_1_1 building.

To summarise, in all cases investigated here the global mode SEA approach is closest to MCFEM for plates that are attached directly to the source plate and shows marginal improvement over SEA using CLFs from semi-infinite plate theory. For the other plates in each building the accuracy of global mode SEA depends on the number of structural junctions between source and receiver and on the orientation of the receiver plate relative to the source plate. These aspects are considered further in the next section.

6.4 Using ESEA on an isolated section of the 5_1_1 building

In the previous section it was found that in some cases the use of global mode SEA gave a marginal improvement over SEA using CLFs from semi-infinite plate theory when compared with MCFEM whilst in other cases neither approach gave close agreement with MCFEM. For example in Figure 6.23 there is an offset of around 5dB between the MCFEM and global mode SEA from the upper floor of room 1 to the eastern wall of room 2. However, good agreement between the two methods is found for the ELD from the upper floor of room 1 to the east wall and north wall of room 1 and to the upper floor of room 2. In large built-up structures it is difficult to identify the reasons for this because it is impractical to apply the ESEA procedure to the entire structure in order to investigate the CLFs. For this reason the focus here will be on a smaller section of the 5_1_1 building as shown in Figure 6.27.

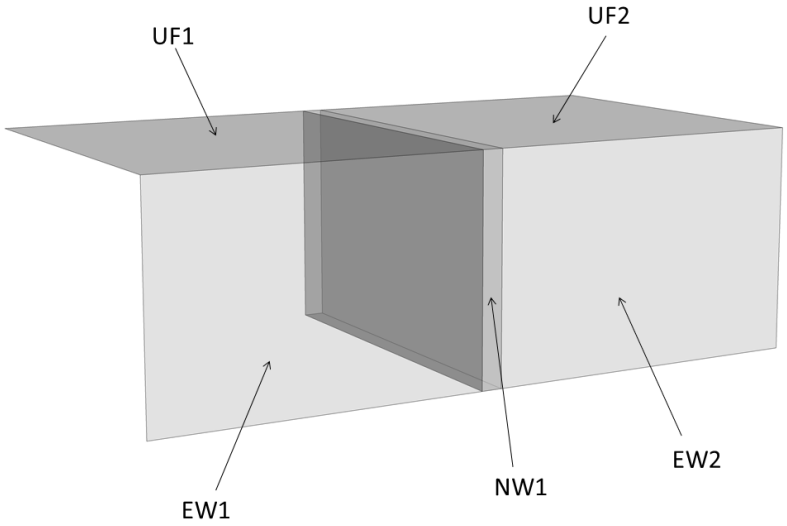

Figure 6.27. Schematic diagram of the five plate model showing the plate labels.

The section consists of the upper floors, separating wall and flanking walls of rooms 1 and 2 of the 5_1_1 building and will be referred to here as the five plate model. The ILF of the plates was set to the TLF using CLFs from semi-infinite plate theory from the plates in the full 5_1_1 building minus these CLFs that were present in the five plate model. The simply supported boundary condition was applied to both external boundaries and plate junctions in the five plate model. Ten ensemble members of the five plate model were generated for the MCFEM models where each plate was assigned the same Young's modulus as the corresponding plate in the 5_1_1 ensemble.

The difference between MCFEM and global mode SEA ELDs is shown for the case of ROTR excitation into the upper floor of room 1, the north wall of room 1 and the east wall of room 1 in Figures 6.28, 6.29 and 6.30 respectively

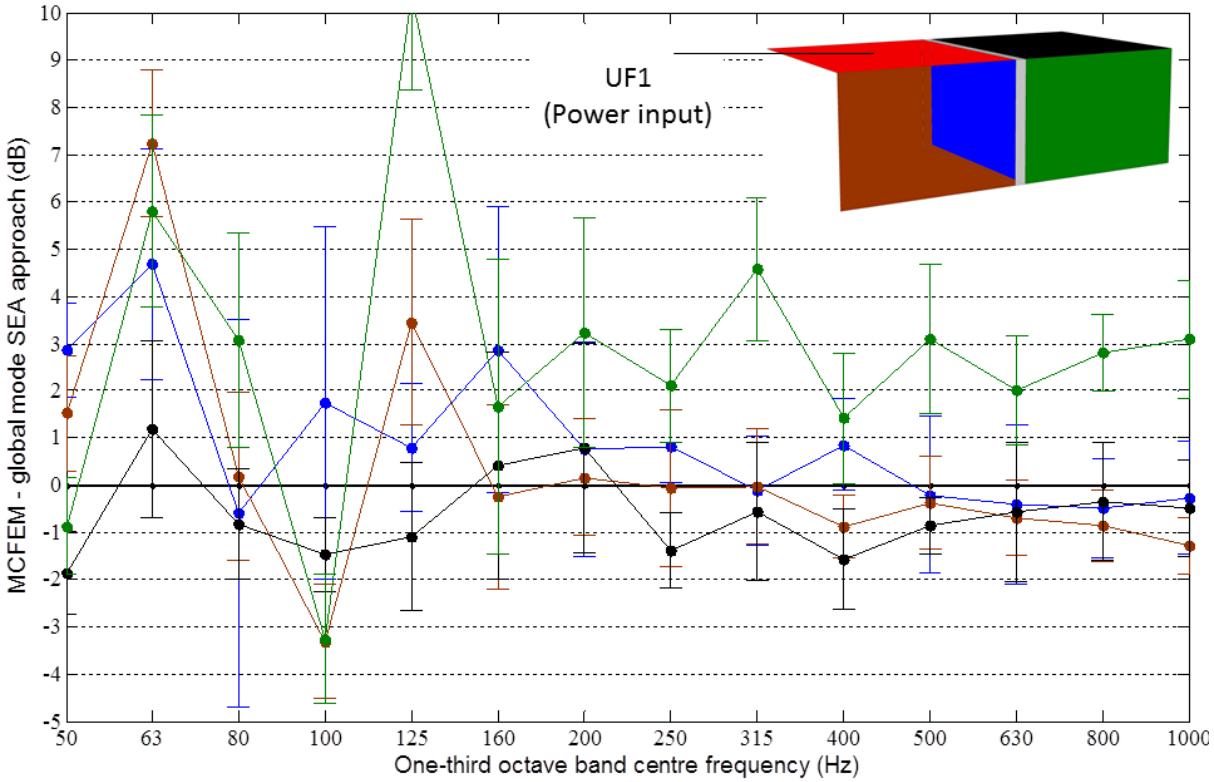

Figure 6.28. Difference between MCFEM and global mode SEA ELDs for the case of power input to the upper floor of room 1.

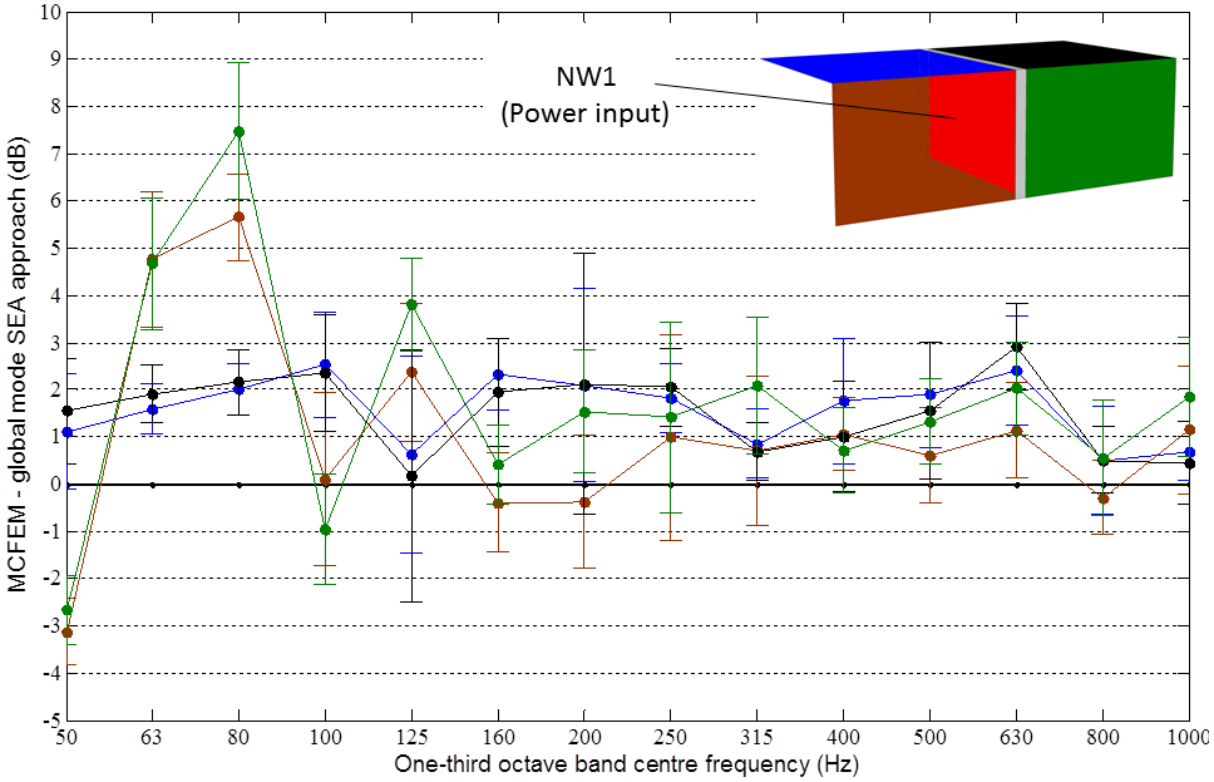

Figure 6.29. Difference between MCFEM and global mode SEA ELDs for the case of power input to the north wall of room 1.

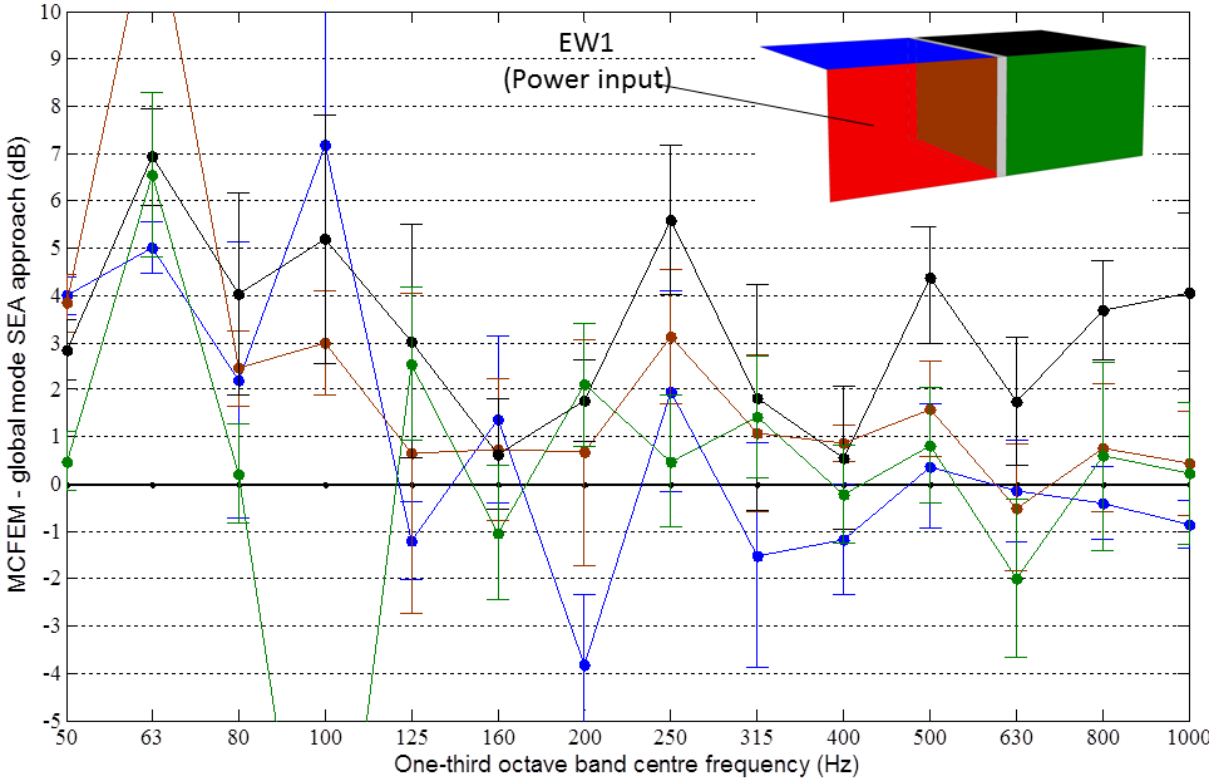

Figure 6.30. Difference between MCFEM and global mode SEA ELDs for the case of power input to the east wall of room 1.

Figures 6.28 to 6.30 show that in all cases where the receiving subsystem is directly connected to the source, global mode SEA is within approximately 1.5dB of MCFEM above 200 Hz. For cases where the receiving subsystem is indirectly coupled to the source subsystem via another plate there is approximately a 3dB difference between the two predictions above 200Hz. This compares to approximately 4dB observed with the five plates in the 5_1_1 building (see Figure 6.23). To investigate this further ESEA was carried out on each member of the MCFEM ensemble. From Section 2.2.5 the ESEA matrix for the five plate model may be written in block matrix form as:

$$\begin{bmatrix} [\boldsymbol{E_1}] & [\boldsymbol{0}] & [\boldsymbol{0}] & [\boldsymbol{0}] & [\boldsymbol{0}] \\ [\boldsymbol{0}] & [\boldsymbol{E_2}] & [\boldsymbol{0}] & [\boldsymbol{0}] & [\boldsymbol{0}] \\ [\boldsymbol{0}] & [\boldsymbol{0}] & [\boldsymbol{E_3}] & [\boldsymbol{0}] & [\boldsymbol{0}] \\ [\boldsymbol{0}] & [\boldsymbol{0}] & [\boldsymbol{0}] & [\boldsymbol{E_4}] & [\boldsymbol{0}] \\ [\boldsymbol{0}] & [\boldsymbol{0}] & [\boldsymbol{0}] & [\boldsymbol{0}] & [\boldsymbol{E_5}] \end{bmatrix} \begin{bmatrix} \boldsymbol{\eta_1} \\ \boldsymbol{\eta_2} \\ \boldsymbol{\eta_3} \\ \boldsymbol{\eta_4} \\ \boldsymbol{\eta_5} \end{bmatrix} = \begin{bmatrix} \boldsymbol{\pi_1} \\ \boldsymbol{\pi_2} \\ \boldsymbol{\pi_3} \\ \boldsymbol{\pi_4} \\ \boldsymbol{\pi_5} \end{bmatrix} \tag{6.6}$$

The elements of the block matrices and vectors are given by eqns. 6.7a) to 6.9. The 'zero' matrices are 4x4 matrices whose elements are zeros.

$$[\boldsymbol{E_1}] = \begin{bmatrix} \left(\frac{E_{22}}{E_{12}} - \frac{E_{21}}{E_{11}}\right) & \left(\frac{E_{32}}{E_{12}} - \frac{E_{31}}{E_{11}}\right) & \left(\frac{E_{42}}{E_{12}} - \frac{E_{41}}{E_{11}}\right) & \left(\frac{E_{52}}{E_{12}} - \frac{E_{51}}{E_{11}}\right) \\ \left(\frac{E_{23}}{E_{13}} - \frac{E_{21}}{E_{11}}\right) & \left(\frac{E_{33}}{E_{13}} - \frac{E_{31}}{E_{11}}\right) & \left(\frac{E_{43}}{E_{13}} - \frac{E_{41}}{E_{11}}\right) & \left(\frac{E_{52}}{E_{13}} - \frac{E_{51}}{E_{11}}\right) \\ \left(\frac{E_{24}}{E_{14}} - \frac{E_{21}}{E_{11}}\right) & \left(\frac{E_{34}}{E_{14}} - \frac{E_{31}}{E_{11}}\right) & \left(\frac{E_{44}}{E_{14}} - \frac{E_{41}}{E_{11}}\right) & \left(\frac{E_{53}}{E_{14}} - \frac{E_{51}}{E_{11}}\right) \\ \left(\frac{E_{25}}{E_{15}} - \frac{E_{21}}{E_{11}}\right) & \left(\frac{E_{35}}{E_{15}} - \frac{E_{31}}{E_{11}}\right) & \left(\frac{E_{45}}{E_{15}} - \frac{E_{41}}{E_{11}}\right) & \left(\frac{E_{55}}{E_{15}} - \frac{E_{51}}{E_{11}}\right) \end{bmatrix} \tag{6.7a}$$

$$[\boldsymbol{E_2}] = \begin{bmatrix} \left(\frac{E_{11}}{E_{21}} - \frac{E_{12}}{E_{22}}\right) & \left(\frac{E_{31}}{E_{21}} - \frac{E_{32}}{E_{22}}\right) & \left(\frac{E_{41}}{E_{21}} - \frac{E_{42}}{E_{22}}\right) & \left(\frac{E_{51}}{E_{21}} - \frac{E_{52}}{E_{22}}\right) \\ \left(\frac{E_{13}}{E_{23}} - \frac{E_{12}}{E_{22}}\right) & \left(\frac{E_{33}}{E_{23}} - \frac{E_{32}}{E_{22}}\right) & \left(\frac{E_{43}}{E_{23}} - \frac{E_{42}}{E_{22}}\right) & \left(\frac{E_{53}}{E_{23}} - \frac{E_{52}}{E_{22}}\right) \\ \left(\frac{E_{14}}{E_{24}} - \frac{E_{12}}{E_{22}}\right) & \left(\frac{E_{34}}{E_{24}} - \frac{E_{32}}{E_{22}}\right) & \left(\frac{E_{44}}{E_{24}} - \frac{E_{42}}{E_{22}}\right) & \left(\frac{E_{54}}{E_{24}} - \frac{E_{52}}{E_{22}}\right) \\ \left(\frac{E_{15}}{E_{25}} - \frac{E_{12}}{E_{22}}\right) & \left(\frac{E_{35}}{E_{25}} - \frac{E_{32}}{E_{22}}\right) & \left(\frac{E_{45}}{E_{25}} - \frac{E_{42}}{E_{22}}\right) & \left(\frac{E_{55}}{E_{25}} - \frac{E_{52}}{E_{22}}\right) \end{bmatrix} \tag{6.7b}$$

$$[\boldsymbol{E_3}] = \begin{bmatrix} \left(\frac{E_{11}}{E_{31}} - \frac{E_{13}}{E_{33}}\right) & \left(\frac{E_{21}}{E_{31}} - \frac{E_{23}}{E_{33}}\right) & \left(\frac{E_{41}}{E_{31}} - \frac{E_{43}}{E_{33}}\right) & \left(\frac{E_{51}}{E_{31}} - \frac{E_{53}}{E_{33}}\right) \\ \left(\frac{E_{12}}{E_{32}} - \frac{E_{13}}{E_{33}}\right) & \left(\frac{E_{22}}{E_{32}} - \frac{E_{23}}{E_{33}}\right) & \left(\frac{E_{42}}{E_{32}} - \frac{E_{43}}{E_{33}}\right) & \left(\frac{E_{52}}{E_{32}} - \frac{E_{53}}{E_{33}}\right) \\ \left(\frac{E_{14}}{E_{34}} - \frac{E_{13}}{E_{33}}\right) & \left(\frac{E_{24}}{E_{34}} - \frac{E_{23}}{E_{33}}\right) & \left(\frac{E_{44}}{E_{34}} - \frac{E_{43}}{E_{33}}\right) & \left(\frac{E_{54}}{E_{34}} - \frac{E_{53}}{E_{33}}\right) \\ \left(\frac{E_{15}}{E_{35}} - \frac{E_{13}}{E_{33}}\right) & \left(\frac{E_{25}}{E_{35}} - \frac{E_{23}}{E_{33}}\right) & \left(\frac{E_{45}}{E_{35}} - \frac{E_{43}}{E_{33}}\right) & \left(\frac{E_{55}}{E_{35}} - \frac{E_{53}}{E_{33}}\right) \end{bmatrix} \tag{6.7c}$$

$$[\boldsymbol{E_4}] = \begin{bmatrix} \left(\frac{E_{11}}{E_{41}} - \frac{E_{14}}{E_{44}}\right) & \left(\frac{E_{21}}{E_{41}} - \frac{E_{24}}{E_{44}}\right) & \left(\frac{E_{31}}{E_{41}} - \frac{E_{34}}{E_{44}}\right) & \left(\frac{E_{41}}{E_{41}} - \frac{E_{54}}{E_{44}}\right) \\ \left(\frac{E_{12}}{E_{42}} - \frac{E_{14}}{E_{44}}\right) & \left(\frac{E_{22}}{E_{42}} - \frac{E_{24}}{E_{55}}\right) & \left(\frac{E_{32}}{E_{42}} - \frac{E_{34}}{E_{44}}\right) & \left(\frac{E_{42}}{E_{42}} - \frac{E_{54}}{E_{44}}\right) \\ \left(\frac{E_{13}}{E_{43}} - \frac{E_{14}}{E_{44}}\right) & \left(\frac{E_{23}}{E_{43}} - \frac{E_{24}}{E_{44}}\right) & \left(\frac{E_{33}}{E_{43}} - \frac{E_{34}}{E_{44}}\right) & \left(\frac{E_{43}}{E_{43}} - \frac{E_{54}}{E_{44}}\right) \\ \left(\frac{E_{15}}{E_{45}} - \frac{E_{14}}{E_{44}}\right) & \left(\frac{E_{25}}{E_{45}} - \frac{E_{24}}{E_{44}}\right) & \left(\frac{E_{35}}{E_{45}} - \frac{E_{34}}{E_{44}}\right) & \left(\frac{E_{45}}{E_{45}} - \frac{E_{54}}{E_{44}}\right) \end{bmatrix} \tag{6.7d}$$

$$[\boldsymbol{E_5}] = \begin{bmatrix} \left(\frac{E_{11}}{E_{51}} - \frac{E_{15}}{E_{55}}\right) & \left(\frac{E_{21}}{E_{51}} - \frac{E_{25}}{E_{55}}\right) & \left(\frac{E_{31}}{E_{51}} - \frac{E_{35}}{E_{55}}\right) & \left(\frac{E_{41}}{E_{51}} - \frac{E_{45}}{E_{55}}\right) \\ \left(\frac{E_{12}}{E_{52}} - \frac{E_{15}}{E_{55}}\right) & \left(\frac{E_{22}}{E_{52}} - \frac{E_{25}}{E_{55}}\right) & \left(\frac{E_{32}}{E_{52}} - \frac{E_{35}}{E_{55}}\right) & \left(\frac{E_{42}}{E_{52}} - \frac{E_{45}}{E_{55}}\right) \\ \left(\frac{E_{13}}{E_{53}} - \frac{E_{15}}{E_{55}}\right) & \left(\frac{E_{23}}{E_{53}} - \frac{E_{25}}{E_{55}}\right) & \left(\frac{E_{33}}{E_{53}} - \frac{E_{35}}{E_{55}}\right) & \left(\frac{E_{43}}{E_{53}} - \frac{E_{45}}{E_{55}}\right) \\ \left(\frac{E_{14}}{E_{54}} - \frac{E_{15}}{E_{55}}\right) & \left(\frac{E_{24}}{E_{54}} - \frac{E_{25}}{E_{55}}\right) & \left(\frac{E_{34}}{E_{54}} - \frac{E_{35}}{E_{55}}\right) & \left(\frac{E_{44}}{E_{54}} - \frac{E_{45}}{E_{55}}\right) \end{bmatrix} \tag{6.7e}$$

$$\boldsymbol{\eta_1} = \begin{bmatrix} \eta_{21} \\ \eta_{31} \\ \eta_{41} \\ \eta_{51} \end{bmatrix}, \boldsymbol{\eta_2} = \begin{bmatrix} \eta_{12} \\ \eta_{32} \\ \eta_{42} \\ \eta_{52} \end{bmatrix}, \boldsymbol{\eta_3} = \begin{bmatrix} \eta_{13} \\ \eta_{23} \\ \eta_{43} \\ \eta_{53} \end{bmatrix}, \boldsymbol{\eta_4} = \begin{bmatrix} \eta_{14} \\ \eta_{24} \\ \eta_{34} \\ \eta_{54} \end{bmatrix}, \boldsymbol{\eta_5} = \begin{bmatrix} \eta_{15} \\ \eta_{25} \\ \eta_{35} \\ \eta_{45} \end{bmatrix} \tag{6.8}$$

$$\boldsymbol{\pi_1} = \begin{bmatrix} \frac{\pi_{\text{in},1}}{\omega E_{11}} \\ \frac{\pi_{\text{in},1}}{\omega E_{11}} \\ \frac{\pi_{\text{in},1}}{\omega E_{11}} \\ \frac{\pi_{\text{in},1}}{\omega E_{11}} \end{bmatrix}, \boldsymbol{\pi_2} = \begin{bmatrix} \frac{\pi_{\text{in},2}}{\omega E_{22}} \\ \frac{\pi_{\text{in},2}}{\omega E_{22}} \\ \frac{\pi_{\text{in},2}}{\omega E_{22}} \\ \frac{\pi_{\text{in},2}}{\omega E_{22}} \end{bmatrix}, \boldsymbol{\pi_3} = \begin{bmatrix} \frac{\pi_{\text{in},3}}{\omega E_{33}} \\ \frac{\pi_{\text{in},3}}{\omega E_{33}} \\ \frac{\pi_{\text{in},3}}{\omega E_{33}} \\ \frac{\pi_{\text{in},3}}{\omega E_{33}} \end{bmatrix}, \boldsymbol{\pi_4} = \begin{bmatrix} \frac{\pi_{\text{in},4}}{\omega E_{44}} \\ \frac{\pi_{\text{in},4}}{\omega E_{44}} \\ \frac{\pi_{\text{in},4}}{\omega E_{44}} \\ \frac{\pi_{\text{in},4}}{\omega E_{44}} \end{bmatrix}, \boldsymbol{\pi_5} = \begin{bmatrix} \frac{\pi_{\text{in},5}}{\omega E_{55}} \\ \frac{\pi_{\text{in},5}}{\omega E_{55}} \\ \frac{\pi_{\text{in},5}}{\omega E_{55}} \\ \frac{\pi_{\text{in},5}}{\omega E_{55}} \end{bmatrix} \tag{6.9}$$

The ESEA subsystems were labelled as indicated in Table 6.1.

Plate	Subsystem label
Upper floor of room 1 (UF1)	1
North wall of room 1 (NW1)	2
East wall of room 1 (EW1)	3
Upper floor of room 2 (UF2)	4
East wall of room 2 (EW2)	5

Table 6.1. Plate subsystem labelling.

Multiplying eq. 6.6 by the inverse energy matrix gives the column vector of CLFs which includes terms between subsystems which are not directly connected. This process was repeated for each ensemble member to generate ten separate CLF column vectors in each one-third octave band. The CLF vectors were averaged over the ensemble to generate a vector of ensemble-average CLFs. CLFs between directly connected subsystems which were negative were not included in the averaging; however negative CLFs between indirectly connected subsystems were included in the averaging. This follows work by Mace [39] in which the negative CLFs between indirectly coupled subsystems are considered to be 'correctional terms' and do not represent physical power flow between subsystems which are not directly connected.

An SEA model was generated which incorporated the ensemble-average CLFs from ESEA. The difference between the ELDs output from this SEA model and MCFEM are compared for three different source subsystems in Figures 6.31 to 6.33.

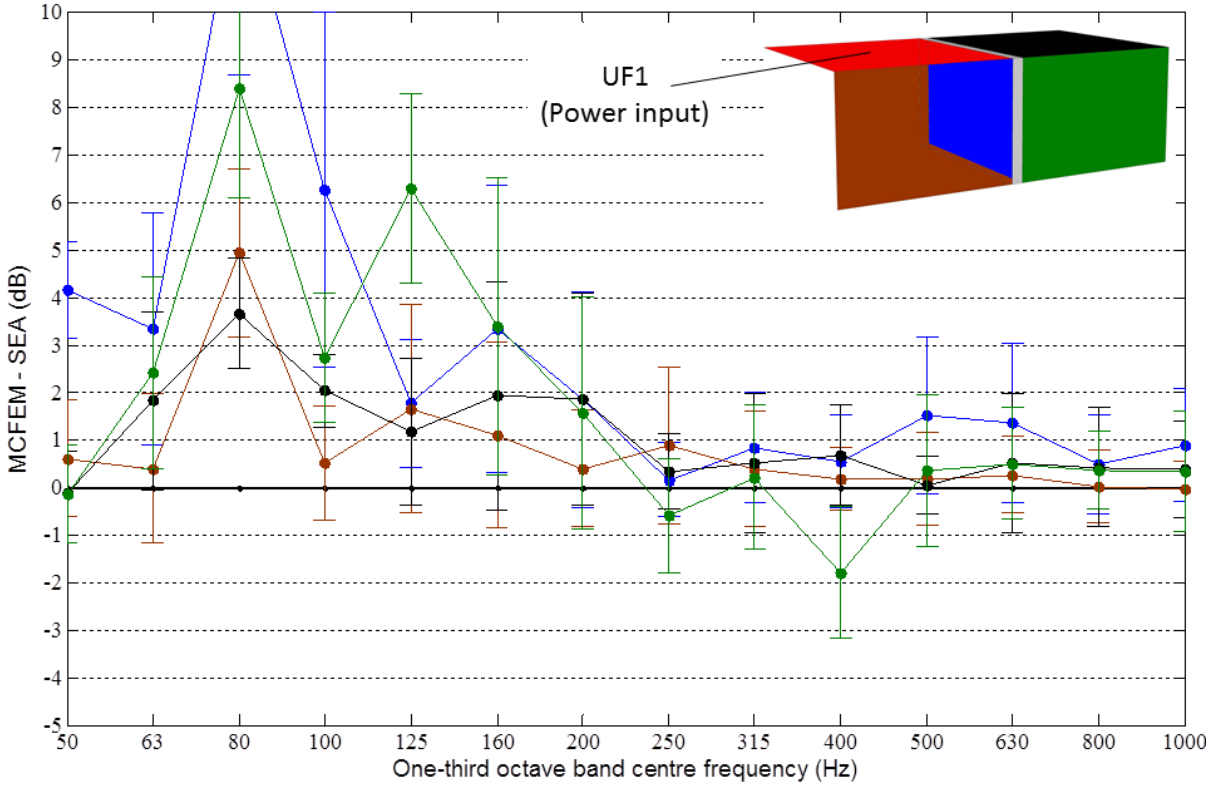

Figure 6.31. Difference between MCFEM and ESEA ELDs for the case of power input to the upper floor of room 1. Non-adjacent CLFs are included in the ESEA model.

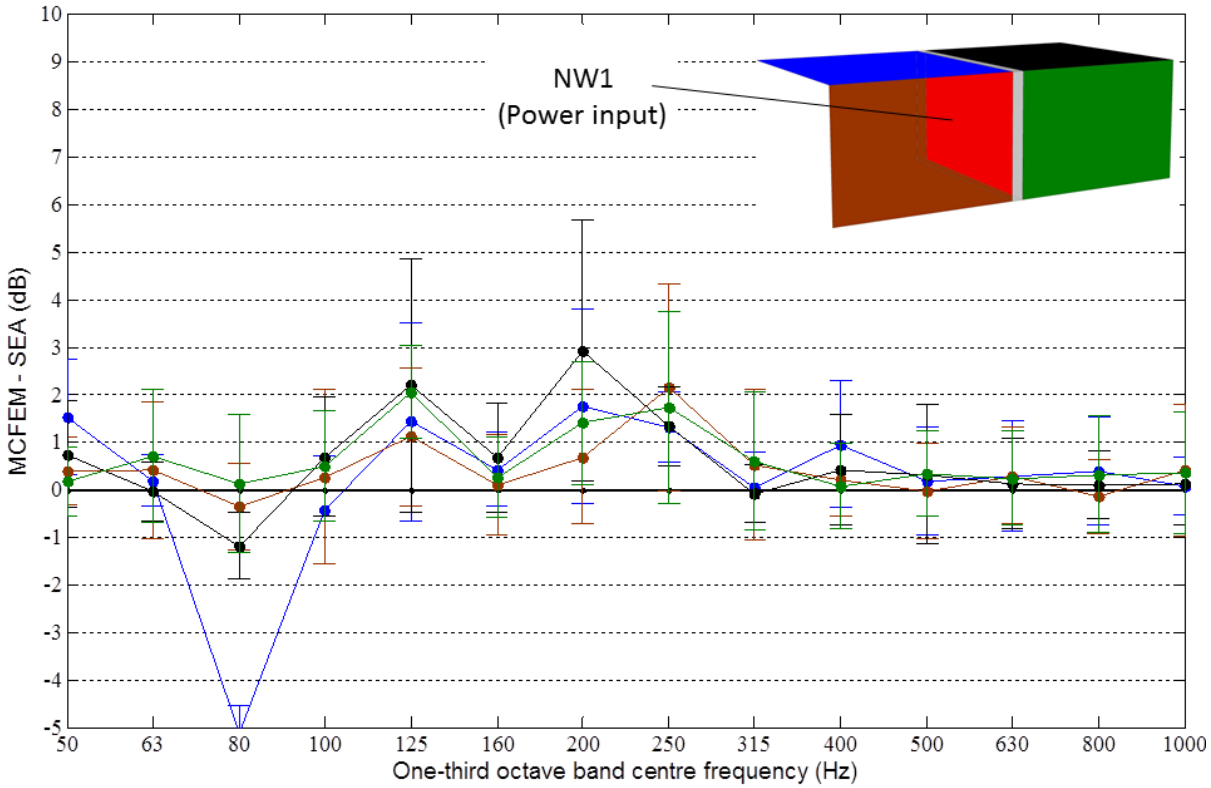

Figure 6.32. Difference between MCFEM and ESEA ELDs for the case of power input to the north wall of room 1. Non-adjacent CLFs are included in the ESEA model.

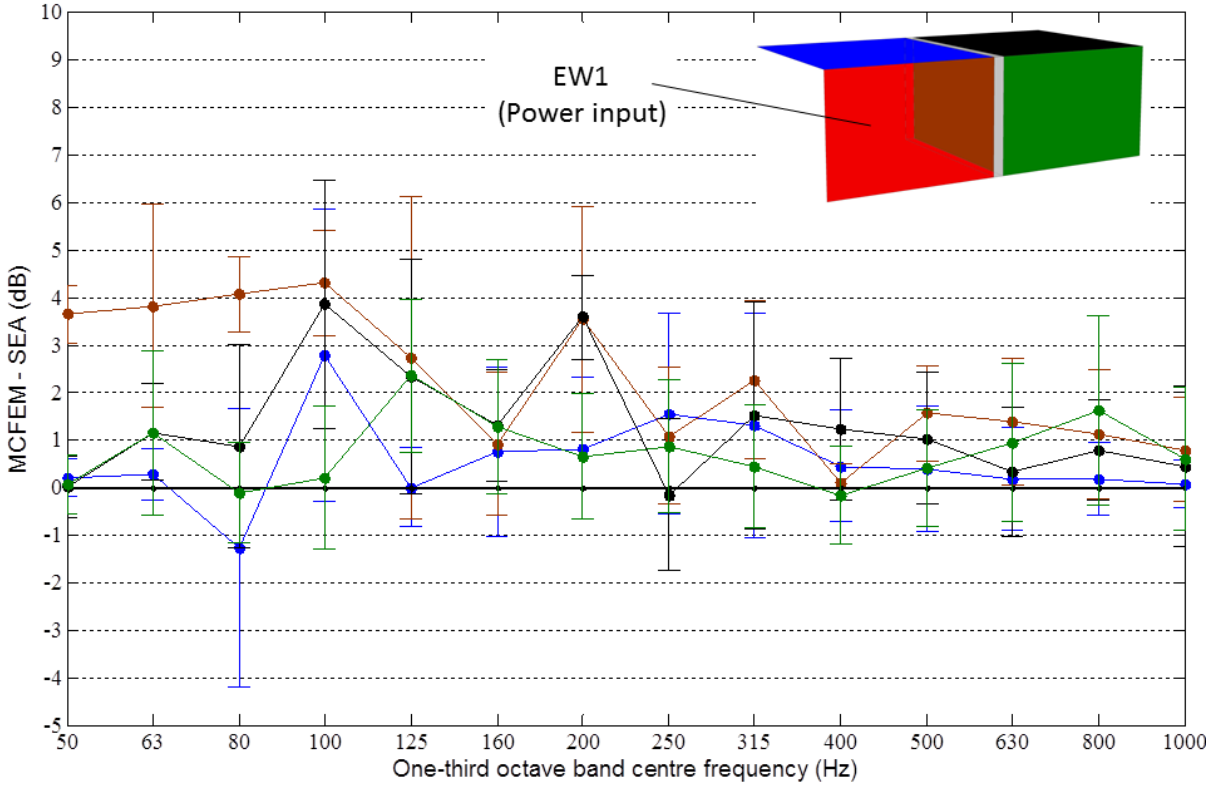

Figure 6.33. Difference between MCFEM and ESEA ELDs for the case of power input to the east wall of room 1. Non adjacent CLFs are included in the ESEA model.

Above 200Hz most results are within 1.5dB of MCFEM . It is notable that this also occurs for ELDs between subsystems which are not directly connected. For example, the ELD between the upper floor of room 1 and the east wall of room 2(see Figure 6.32) is less than 0.5dB from the MCFEM result compared to a 3dB difference between global mode SEA and MCFEM for the same ELD (see Figure 6.29). The small difference between MCFEM and ESEA can be attributed to inversion errors. Also the removal of negative CLFs between directly connected subsystems before calculating the ensemble-average CLFs implies that the ESEA ensemble differs slightly from the original MCFEM ensemble. This is particularly relevant to the results below 200Hz and can lead to large differences of up to 12dB between the ESEA and MCFEM results.

The ESEA model included four negative indirect CLFs between the upper floors and the east walls of the five plate model and this type of coupling is not considered in standard SEA theory. Lalor [56] developed a method was developed for forcing to zero all the CLFs between subsystems which are not directly connected. The process involves rearranging eq. 6.6 to partition the matrix into terms which involve direct CLFs and terms which involve indirect CLFs.

$$\begin{bmatrix} [E_{\alpha\alpha}] & \vdots & [E_{\alpha\beta}] \\ \cdots & \cdots & \cdots \\ [E_{\beta\alpha}] & \vdots & [E_{\beta\beta}] \end{bmatrix} \begin{bmatrix} \boldsymbol{\eta}_{\alpha} \\ \cdots \\ \boldsymbol{\eta}_{\beta} \end{bmatrix} = \begin{bmatrix} \boldsymbol{\pi}_{\alpha} \\ \cdots \\ \boldsymbol{\pi}_{\beta} \end{bmatrix} \tag{6.10}$$

The elements of the block matrix $E_{\alpha\alpha}$ is given by:

$$E_{\alpha\alpha} = \begin{bmatrix} [\boldsymbol{E_1}] & [\boldsymbol{0}] & [\boldsymbol{0}] & [\boldsymbol{0}] & [\boldsymbol{0}] \\ [\boldsymbol{0}] & [\boldsymbol{E_2}] & [\boldsymbol{0}] & [\boldsymbol{0}] & [\boldsymbol{0}] \\ [\boldsymbol{0}] & [\boldsymbol{0}] & [\boldsymbol{E_3}] & [\boldsymbol{0}] & [\boldsymbol{0}] \\ [\boldsymbol{0}] & [\boldsymbol{0}] & [\boldsymbol{0}] & [\boldsymbol{E_4}] & [\boldsymbol{0}] \\ [\boldsymbol{0}] & [\boldsymbol{0}] & [\boldsymbol{0}] & [\boldsymbol{0}] & [\boldsymbol{E_5}] \end{bmatrix} \tag{6.11}$$

where the non-zero elements of the matrix $E_{\alpha\alpha}$ are

$$[\boldsymbol{E_1}] = \begin{bmatrix} \left(\frac{E_{22}}{E_{12}} - \frac{E_{21}}{E_{11}}\right) & \left(\frac{E_{32}}{E_{12}} - \frac{E_{31}}{E_{11}}\right) & \left(\frac{E_{42}}{E_{12}} - \frac{E_{41}}{E_{11}}\right) \\ \left(\frac{E_{23}}{E_{13}} - \frac{E_{21}}{E_{11}}\right) & \left(\frac{E_{33}}{E_{13}} - \frac{E_{31}}{E_{11}}\right) & \left(\frac{E_{43}}{E_{13}} - \frac{E_{41}}{E_{11}}\right) \\ \left(\frac{E_{24}}{E_{14}} - \frac{E_{21}}{E_{11}}\right) & \left(\frac{E_{34}}{E_{14}} - \frac{E_{31}}{E_{11}}\right) & \left(\frac{E_{44}}{E_{14}} - \frac{E_{41}}{E_{11}}\right) \end{bmatrix} \tag{6.12a}$$

$$[\boldsymbol{E_2}] = \begin{bmatrix} \left(\frac{E_{11}}{E_{21}} - \frac{E_{12}}{E_{22}}\right) & \left(\frac{E_{31}}{E_{21}} - \frac{E_{32}}{E_{22}}\right) & \left(\frac{E_{41}}{E_{21}} - \frac{E_{42}}{E_{22}}\right) & \left(\frac{E_{51}}{E_{21}} - \frac{E_{52}}{E_{22}}\right) \\ \left(\frac{E_{13}}{E_{23}} - \frac{E_{12}}{E_{22}}\right) & \left(\frac{E_{33}}{E_{23}} - \frac{E_{32}}{E_{22}}\right) & \left(\frac{E_{43}}{E_{23}} - \frac{E_{42}}{E_{22}}\right) & \left(\frac{E_{53}}{E_{23}} - \frac{E_{52}}{E_{22}}\right) \\ \left(\frac{E_{14}}{E_{24}} - \frac{E_{12}}{E_{22}}\right) & \left(\frac{E_{34}}{E_{24}} - \frac{E_{32}}{E_{22}}\right) & \left(\frac{E_{44}}{E_{24}} - \frac{E_{42}}{E_{22}}\right) & \left(\frac{E_{54}}{E_{24}} - \frac{E_{52}}{E_{22}}\right) \\ \left(\frac{E_{15}}{E_{25}} - \frac{E_{12}}{E_{22}}\right) & \left(\frac{E_{35}}{E_{25}} - \frac{E_{32}}{E_{22}}\right) & \left(\frac{E_{45}}{E_{25}} - \frac{E_{42}}{E_{22}}\right) & \left(\frac{E_{55}}{E_{25}} - \frac{E_{52}}{E_{22}}\right) \end{bmatrix} \tag{6.12b}$$

$$[\boldsymbol{E_3}] = \begin{bmatrix} \left(\frac{E_{11}}{E_{31}} - \frac{E_{13}}{E_{33}}\right) & \left(\frac{E_{21}}{E_{31}} - \frac{E_{23}}{E_{33}}\right) & \left(\frac{E_{51}}{E_{31}} - \frac{E_{53}}{E_{33}}\right) \\ \left(\frac{E_{12}}{E_{32}} - \frac{E_{13}}{E_{33}}\right) & \left(\frac{E_{22}}{E_{32}} - \frac{E_{23}}{E_{33}}\right) & \left(\frac{E_{52}}{E_{32}} - \frac{E_{53}}{E_{33}}\right) \\ \left(\frac{E_{15}}{E_{35}} - \frac{E_{13}}{E_{33}}\right) & \left(\frac{E_{25}}{E_{35}} - \frac{E_{23}}{E_{33}}\right) & \left(\frac{E_{55}}{E_{35}} - \frac{E_{53}}{E_{33}}\right) \end{bmatrix} \tag{6.12c}$$

$$[\boldsymbol{E_4}] = \begin{bmatrix} \left(\frac{E_{11}}{E_{41}} - \frac{E_{14}}{E_{44}}\right) & \left(\frac{E_{21}}{E_{41}} - \frac{E_{24}}{E_{44}}\right) & \left(\frac{E_{41}}{E_{41}} - \frac{E_{54}}{E_{44}}\right) \\ \left(\frac{E_{12}}{E_{42}} - \frac{E_{14}}{E_{44}}\right) & \left(\frac{E_{22}}{E_{42}} - \frac{E_{24}}{E_{55}}\right) & \left(\frac{E_{42}}{E_{42}} - \frac{E_{54}}{E_{44}}\right) \\ \left(\frac{E_{15}}{E_{45}} - \frac{E_{14}}{E_{44}}\right) & \left(\frac{E_{25}}{E_{45}} - \frac{E_{24}}{E_{44}}\right) & \left(\frac{E_{45}}{E_{45}} - \frac{E_{54}}{E_{44}}\right) \end{bmatrix} \tag{6.12d}$$

$$[\boldsymbol{E_5}] = \begin{bmatrix} \left(\frac{E_{22}}{E_{52}} - \frac{E_{25}}{E_{55}}\right) & \left(\frac{E_{32}}{E_{52}} - \frac{E_{35}}{E_{55}}\right) & \left(\frac{E_{42}}{E_{52}} - \frac{E_{45}}{E_{55}}\right) \\ \left(\frac{E_{23}}{E_{53}} - \frac{E_{25}}{E_{55}}\right) & \left(\frac{E_{33}}{E_{53}} - \frac{E_{35}}{E_{55}}\right) & \left(\frac{E_{43}}{E_{53}} - \frac{E_{45}}{E_{55}}\right) \\ \left(\frac{E_{24}}{E_{54}} - \frac{E_{25}}{E_{55}}\right) & \left(\frac{E_{34}}{E_{54}} - \frac{E_{35}}{E_{55}}\right) & \left(\frac{E_{44}}{E_{54}} - \frac{E_{45}}{E_{55}}\right) \end{bmatrix} \tag{6.12e}$$

The elements of the rearranged CLF column vectors are:

$$\boldsymbol{\eta}_\alpha = \begin{bmatrix} \boldsymbol{\eta_1} \\ \boldsymbol{\eta_2} \\ \boldsymbol{\eta_3} \\ \boldsymbol{\eta_4} \\ \boldsymbol{\eta_5} \end{bmatrix} \tag{6.13a}$$

$$\boldsymbol{\eta_1} = \begin{bmatrix} \eta_{21} \\ \eta_{31} \\ \eta_{41} \end{bmatrix}, \boldsymbol{\eta_2} = \begin{bmatrix} \eta_{12} \\ \eta_{32} \\ \eta_{42} \\ \eta_{52} \end{bmatrix}, \boldsymbol{\eta_3} = \begin{bmatrix} \eta_{13} \\ \eta_{23} \\ \eta_{53} \end{bmatrix}, \boldsymbol{\eta_4} = \begin{bmatrix} \eta_{14} \\ \eta_{24} \\ \eta_{54} \end{bmatrix}, \boldsymbol{\eta_5} = \begin{bmatrix} \eta_{25} \\ \eta_{35} \\ \eta_{45} \end{bmatrix} \tag{6.13b}$$

$$\boldsymbol{\eta}_\beta = \begin{bmatrix} \eta_{51} \\ \eta_{43} \\ \eta_{34} \\ \eta_{15} \end{bmatrix} \tag{6.13c}$$

Finally the power column vectors are given by:

$$\boldsymbol{\pi_1} = \begin{bmatrix} \frac{\pi_{\text{in},1}}{\omega E_{11}} \\ \frac{\pi_{\text{in},1}}{\omega E_{11}} \\ \frac{\pi_{\text{in},1}}{\omega E_{11}} \end{bmatrix}, \boldsymbol{\pi_2} = \begin{bmatrix} \frac{\pi_{\text{in},2}}{\omega E_{22}} \\ \frac{\pi_{\text{in},2}}{\omega E_{22}} \\ \frac{\pi_{\text{in},2}}{\omega E_{22}} \\ \frac{\pi_{\text{in},2}}{\omega E_{22}} \end{bmatrix}, \boldsymbol{\pi_3} = \begin{bmatrix} \frac{\pi_{\text{in},3}}{\omega E_{33}} \\ \frac{\pi_{\text{in},3}}{\omega E_{33}} \\ \frac{\pi_{\text{in},3}}{\omega E_{33}} \end{bmatrix}, \boldsymbol{\pi_4} = \begin{bmatrix} \frac{\pi_{\text{in},4}}{\omega E_{44}} \\ \frac{\pi_{\text{in},4}}{\omega E_{44}} \\ \frac{\pi_{\text{in},4}}{\omega E_{44}} \end{bmatrix}, \boldsymbol{\pi_5} = \begin{bmatrix} \frac{\pi_{\text{in},5}}{\omega E_{55}} \\ \frac{\pi_{\text{in},5}}{\omega E_{55}} \\ \frac{\pi_{\text{in},5}}{\omega E_{55}} \end{bmatrix}, \boldsymbol{\pi}_\beta = \begin{bmatrix} \frac{\pi_{\text{in},1}}{\omega E_{11}} \\ \frac{\pi_{\text{in},3}}{\omega E_{33}} \\ \frac{\pi_{\text{in},4}}{\omega E_{44}} \\ \frac{\pi_{\text{in},5}}{\omega E_{55}} \end{bmatrix} \tag{6.14}$$

To force the non-zero CLFs to zero the elements of $\boldsymbol{\eta}_\beta$ are set to zero in eq.6.10. Therefore equation 6.10 reduces to

$$[E_{\alpha\alpha}][\boldsymbol{\eta}_\alpha] = [\boldsymbol{\pi}_\alpha] \tag{6.14}$$

and the directly connected CLFs can be obtained by multiplying through by the inverse energy matrix:

$$[\boldsymbol{\eta}_\alpha] = [E_{\alpha\alpha}]^{-1}[\boldsymbol{\pi}_\alpha] \tag{6.15}$$

This approach was performed on the five plate model and the results are shown in Figures 6.35 to 6.37.

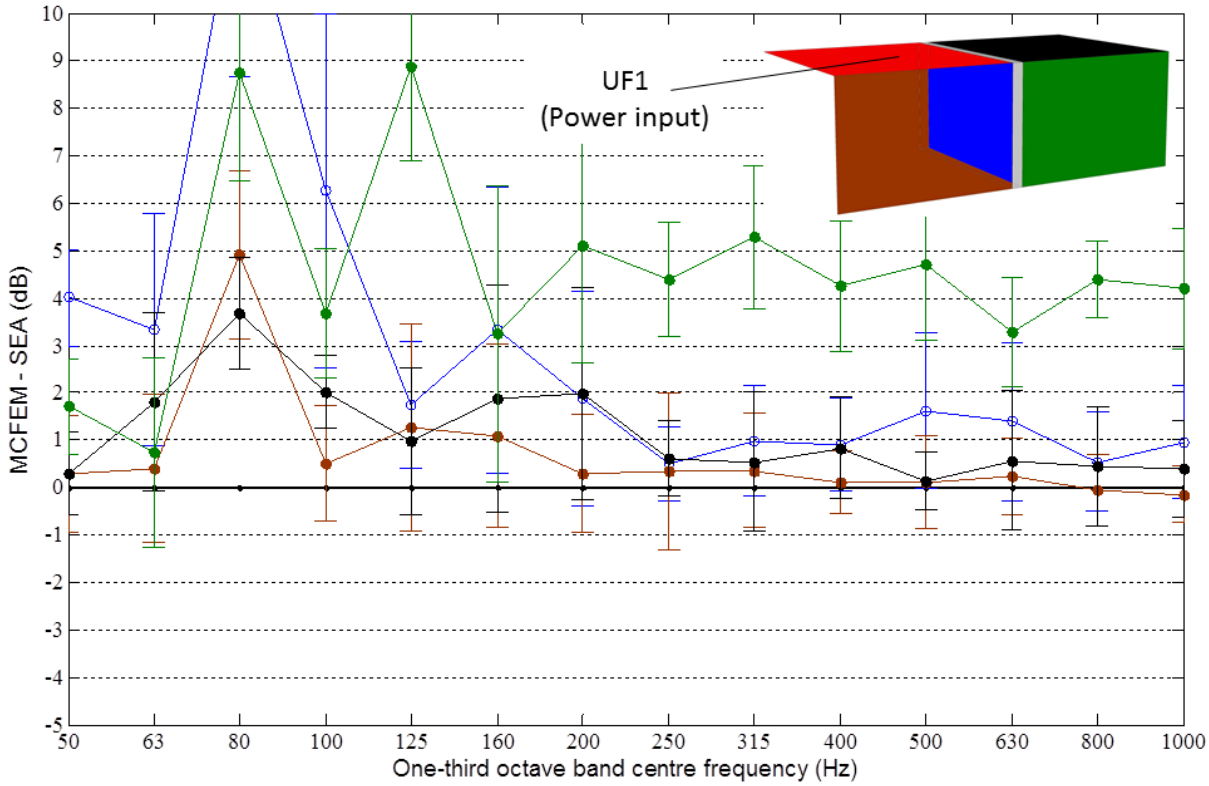

Figure 6.34. Difference between MCFEM and ESEA ELDs for the case of power input to the upper floor of room 1. All the non-adjacent CLFs are forced to zero.

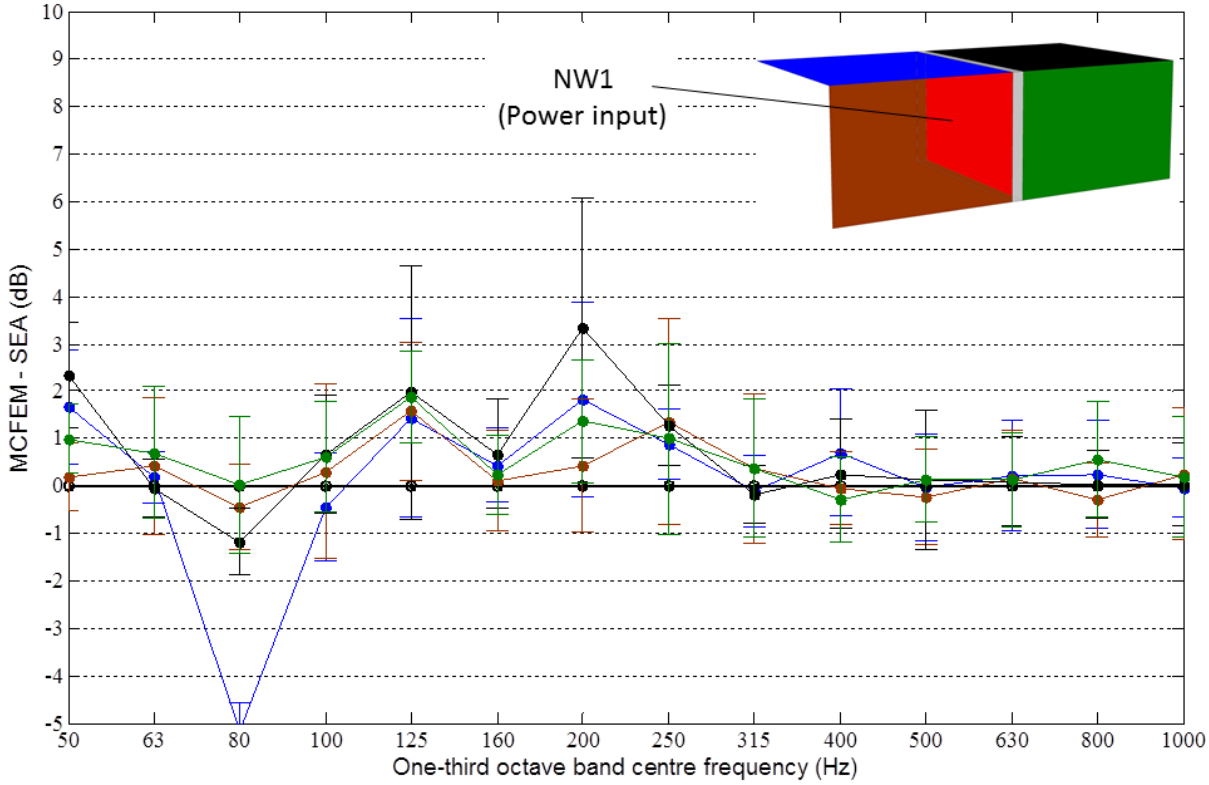

Figure 6.35. Difference between MCFEM and ESEA ELDs for the case of power input to the north wall of room 1. All the non-adjacent CLFs are forced to zero.

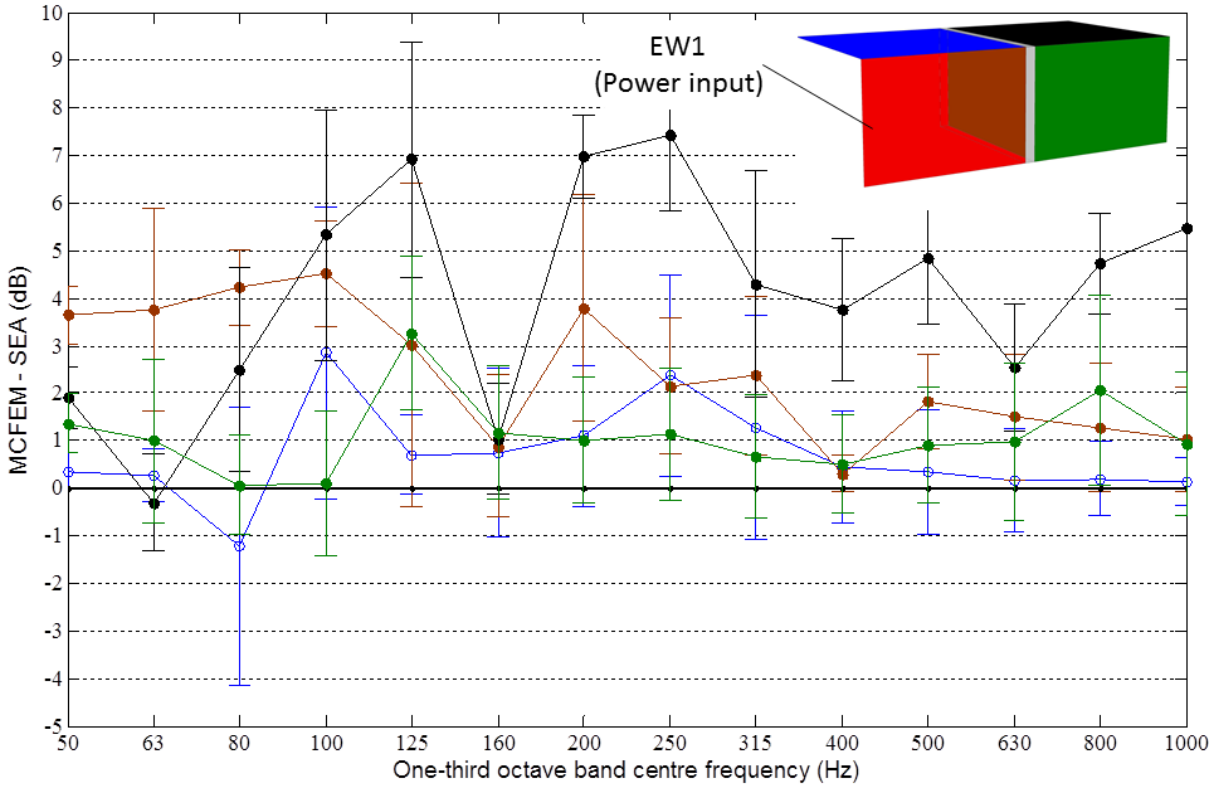

Figure 6.36. Difference between MCFEM and ESEA ELDs for the case of power input to the east wall of room 1. All the indirect CLFs are forced to zero.

The results show good agreement between ESEA and MCFEM ELDS for cases where the receiver subsystem is directly connected to the source subsystem. For example, in Figure 6.35 the difference between the ELDs from the north wall of room 1 to the remaining subsystems is generally less than 0.5dB above 200Hz. For the case of subsystems which are indirectly connected to the source there is a 4 to 5 dB offset between ESEA and MCFEM as shown in Figures 6.34 and 6.36. Comparing the results in Figures 6.34 to 6.36 to the case where indirect coupling was included (see Figures 6.31 to 6.33) shows that a significantly better approximation to MCFEM is obtained when indirect CLFs are included in the SEA model.

The results in Figures 6.34 to 6.36 are similar to the results using global mode SEA (see Figures 6.28 to 6.30) which indicates that global mode SEA can be used to improve estimates of the CLFs between directly connected subsystems over CLFs using semi-infinite plate theory. However, global mode SEA does not allow prediction of indirect CLFs and this significantly limits its usefulness in some cases.

6.5 Conclusions

This chapter considered whether CLFs determined from isolated plate junctions could be incorporated into SEA models of heavyweight buildings to improve the prediction compared to SEA models using CLFs calculated from semi-infinite plate theory.

CLFs for isolated plate junctions were calculated using EICs from the global mode approach. When these CLFs were incorporated into SEA models this was referred to as the global mode SEA approach. EICs were used to calculate the ELDs for L-, X- and T-junctions which were compared against ELDs calculated using MCFEM. The close agreement between these two methods indicates that (a) ROTR is a good approximation to the ideal ROTR used in the global mode approach (b) that the global modes of the isolated junctions calculated analytically were in close agreement with the global modes calculated using FEM.

Lalor's ESEA method which calculates the CLFs and ILFs separately was found to be reliable for these junctions to convert the EICs into CLFs.

The CLFs from isolated junctions were incorporated into SEA models of the 2_2_2 and 5_1_1 buildings and the results compared against the ELDs calculated using MCFEM.

Below 200Hz (where the statistical mode count in one-third octave bands is less than one) the global mode SEA approach was unable to predict the peaks and troughs in the ELDs in the building to one-third octave band accuracy. This is in contrast to the results for isolated junctions where good agreement was observed between MCFEM and global mode SEA.

Above 200Hz (where the statistical mode count in one-third octave bands is greater than one), good agreement was observed between MCFEM and global mode SEA for plates directly connected to the source plate (see Figure 6.18 for the 2_2_2 building and Figures 6.23 to 6.25 for the 5_1_1 building). However, for cases where the receiving subsystem is connected to the source across at least two junctions, there were significant errors in the global mode SEA approach. In some cases an offset of approximately 5dB was observed between MCFEM and global mode SEA (see Figure 6.22). To investigate these errors further a five plate MCFEM model (see Figure 6.27) was generated on which ESEA could be applied. When indirect CLFs between subsystems were forced to zero[50, 56] an offset of around 5dB was found between the MCFEM results and the SEA results for subsystems which were not directly connected to the source subsystem. Hence it is concluded that

indirect CLFs between subsystems which are not directly physically connected are essential for accurate prediction with SEA models. Comparison of the ESEA results with the global mode SEA approach indicates that the global mode SEA approach adequately predicts direct CLFs but unfortunately the method does not allow calculation of the indirect CLFs and hence is of limited use.

In the next chapter ASEA will be applied to the 5_1_1 and 2_2_2 buildings to address the issue of the importance of indirect coupling that was identified in this chapter. ASEA provides a method for calculating CLFs between subsystems which are not directly attached and hence should improve the SEA results above 200 Hz. The beam tracing method used in ASEA can also be adapted to investigate the power incident on each junction line and hence provides a method to explain the physical reasons for the occurrence of CLFs between subsystems which are not directly connected. It is hypothesised that the main error in the SEA prediction above 200Hz is not due to low modal overlap and statistical mode counts but due to spatial filtering of the wave field in subsystems connected to the source across at least two junctions which results in indirect CLFs.

Chapter 7 Using ASEA to account for spatial filtering and non-diffuse vibration fields in building structures

7.1 Introduction

In Chapters 5 and 6 MCFEM was compared against SEA with CLFs calculated using either semi-infinite plate theory or finite plate theory based on global modes. For heavyweight buildings above 200Hz the one-third octave band ELDs from MCFEM are relatively smooth functions of frequency that could be approximated by a straight line. Satisfactory agreement between MCFEM and SEA was obtained when using semi-infinite plate CLFs for receiving plates which were directly attached to the source plate with SEA being within 5dB of MCFEM. It was also shown that in some cases, SEA results could only be improved if indirect CLFs were included in the model. It has been reported in other work [39] that the existence (or inclusion) of indirect CLFs does not imply that power flows between subsystems which are not directly coupled, but that it results from an invalid SEA assumption of power flow proportionality. Therefore the existence of indirect CLFs means that the power flowing between two directly coupled subsystems depends on the energy of a third subsystem. For example an indirect CLF may be considered between plate *a* and *c* when the angular filtering of the power in plate *b* by a junction line connecting plates *a* and *b* effects the power incident on the junction line connecting plates *b* and *c*. This suggests that ASEA could potentially be used to improve the SEA predictions above 200Hz for the building structures investigated in this thesis.

In Section 7.2 the beam tracing approach that was introduced in Section 2.3.4 is used to investigate the angular distribution of the incident power on the junction lines of the 5_1_1 and 2_2_2 buildings. This distribution is compared against the diffuse field approximation used in SEA. In Section 7.3 ASEA is used to determine the ELD between the subsystems of the 5_1_1 and 2_2_2 building. The convergence of the ASEA results is discussed and the ELDs from ASEA are compared with MCFEM.

7.2 Spatial filtering in building structures

The first stage is to consider the 5_1_1 building in which spatial filtering is hypothesized to be important. A diffuse field is assumed to exist on the upper floor of room 1. The diffuse field is defined by the power incident onto the edges of the source plate, the angular dependency of which is given by eq. 3.27. The beam tracing method introduced in Section 2.3.4 was used to trace the initial diffuse power incident on the source plate edges around the entire structure. The power incident on a particular plate edge within a range of angles was summed and divided by the total power incident at all angles on that plate edge to produce a plot of the incident power versus angle. In total the number of beams incident on each edge was between 50,000 and 120,000.

Figures 7.1 to 7.4 show the results for the 5_1_1 building with diffuse power input into the upper floor of room 1 for which the power incident on the north edge of each of the upper floors was calculated. The angular distribution with angle is shown as a series of coloured curves. The inset diagram highlights the edge of the plate corresponding to the curve of the same colour. The vertical lines show the angular range over which the power was integrated, for example the marker point at $5°$ represents the total power incident on the plate edge between 0 and $10°$ normalised to the total power incident on the plate. For reference the angular distribution of the normalised power incident on a plate edge under diffuse field assumption is shown as a black line with open markers.

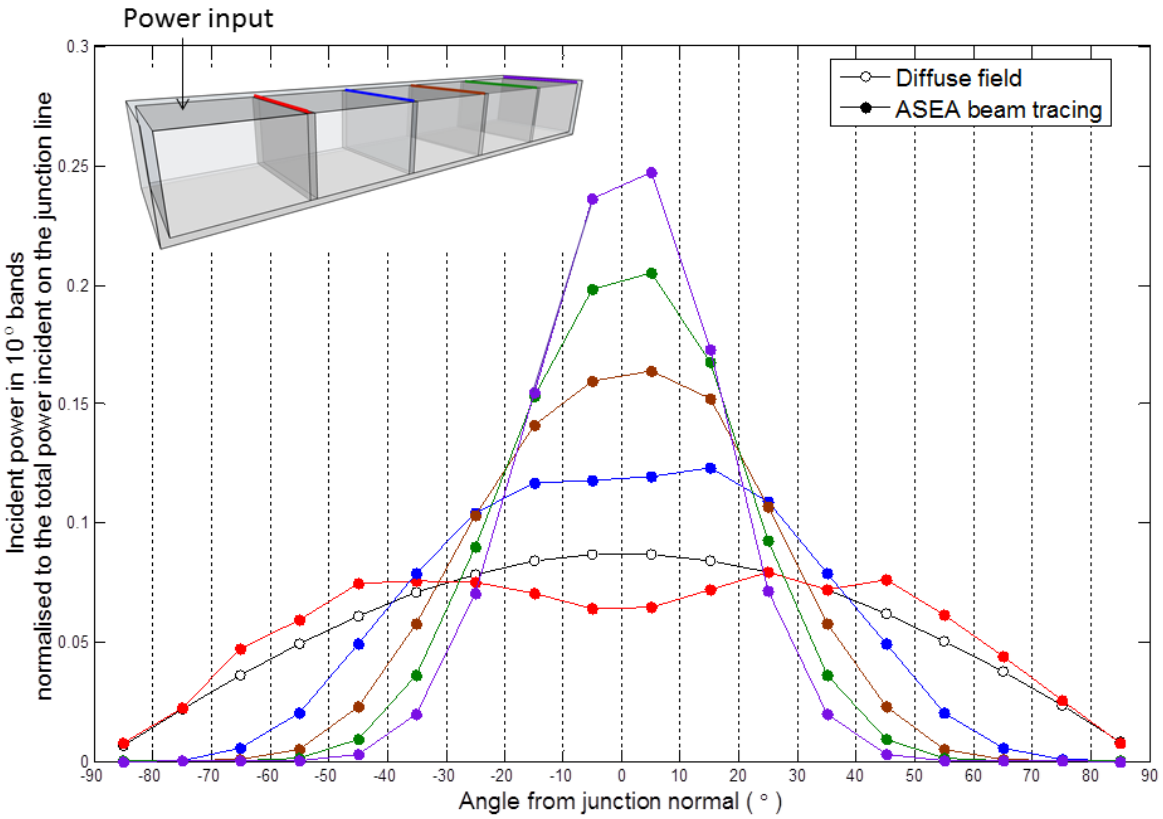

Figure 7.1. 5_1_1 building. Power incident on junctions in 10° angular bands normalised to the total power incident on the junction. Red curve with solid markers – northern edge of upper floor 1, blue curve with solid markers – northern edge of upper floor 2, brown curve with solid markers – northern edge of upper floor 3, green curve with solid markers – northern edge of upper floor 4, purple curve with solid markers – northern edge of upper floor 5. Black curve with open markers – diffuse field result.

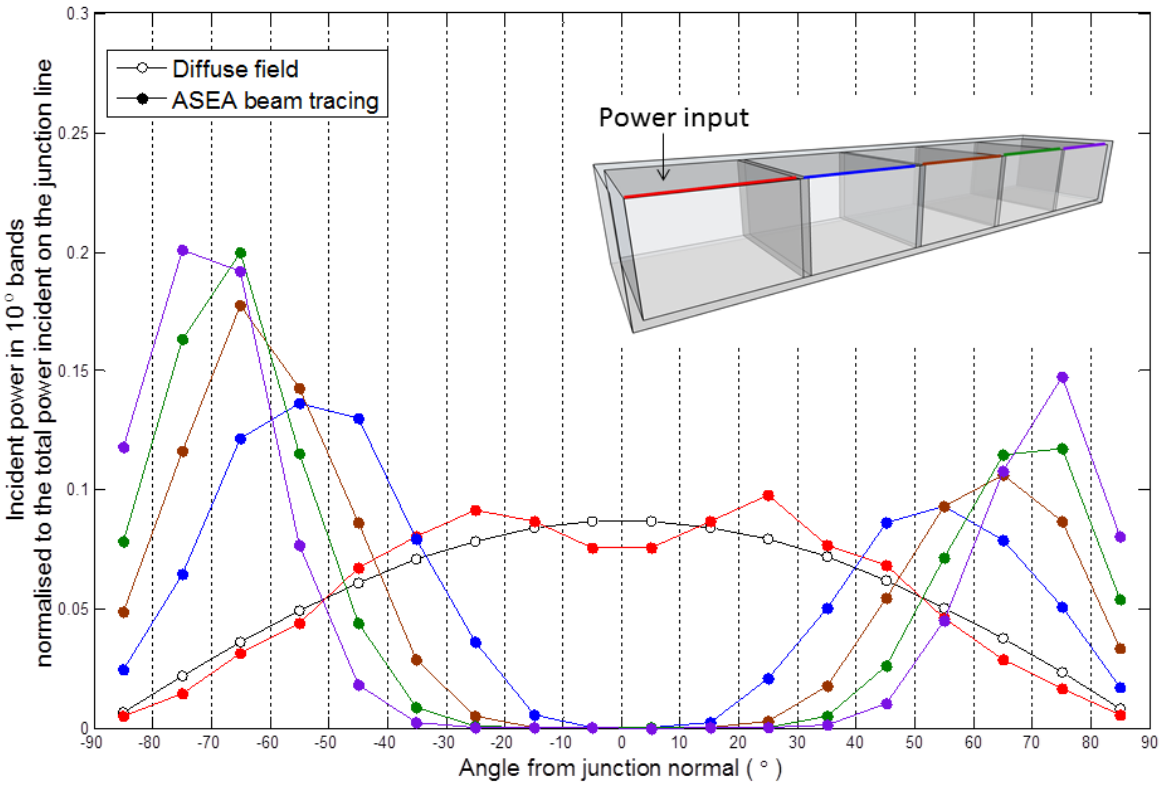

Figure 7.2. 5_1_1 building. Power incident on junction in 10° angular bands normalised to the total power incident on the junction. Red curve with solid markers – eastern edge of upper floor 1, blue curve with solid markers – eastern edge of upper floor 2, brown curve with solid markers – eastern edge of upper floor 3, green curve with solid markers – eastern edge of upper floor 4, purple curve with solid markers – eastern edge of upper floor 5. Black curve with open markers – diffuse field result.

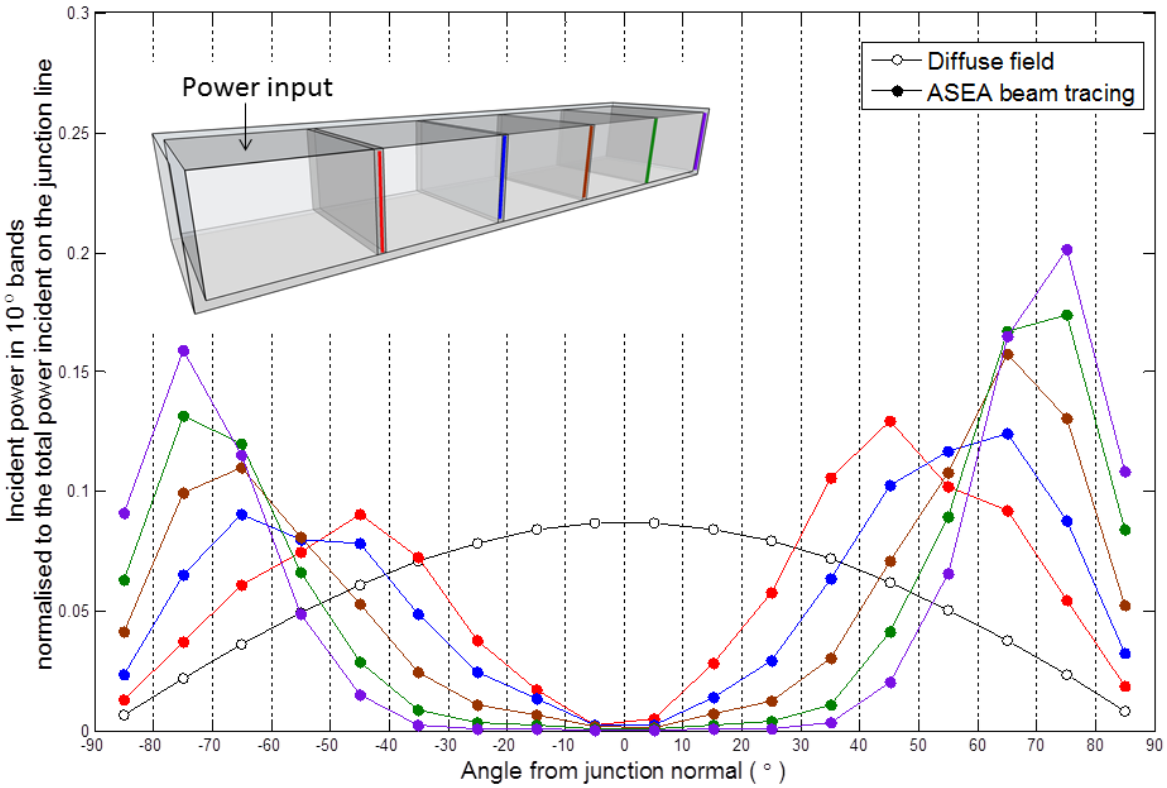

Figure 7.3. 5_1_1 building. Power incident on junction within 10° angular bands normalised to the total power incident on the junction. Red curve with solid markers – eastern edge of north wall 1, blue curve with solid markers – eastern edge of north wall 2, brown curve with solid markers – eastern edge of north wall 3, green curve with solid markers – eastern edge of north wall 4, purple curve with solid markers – eastern edge of north wall 5. Black curve with open markers – diffuse field result.

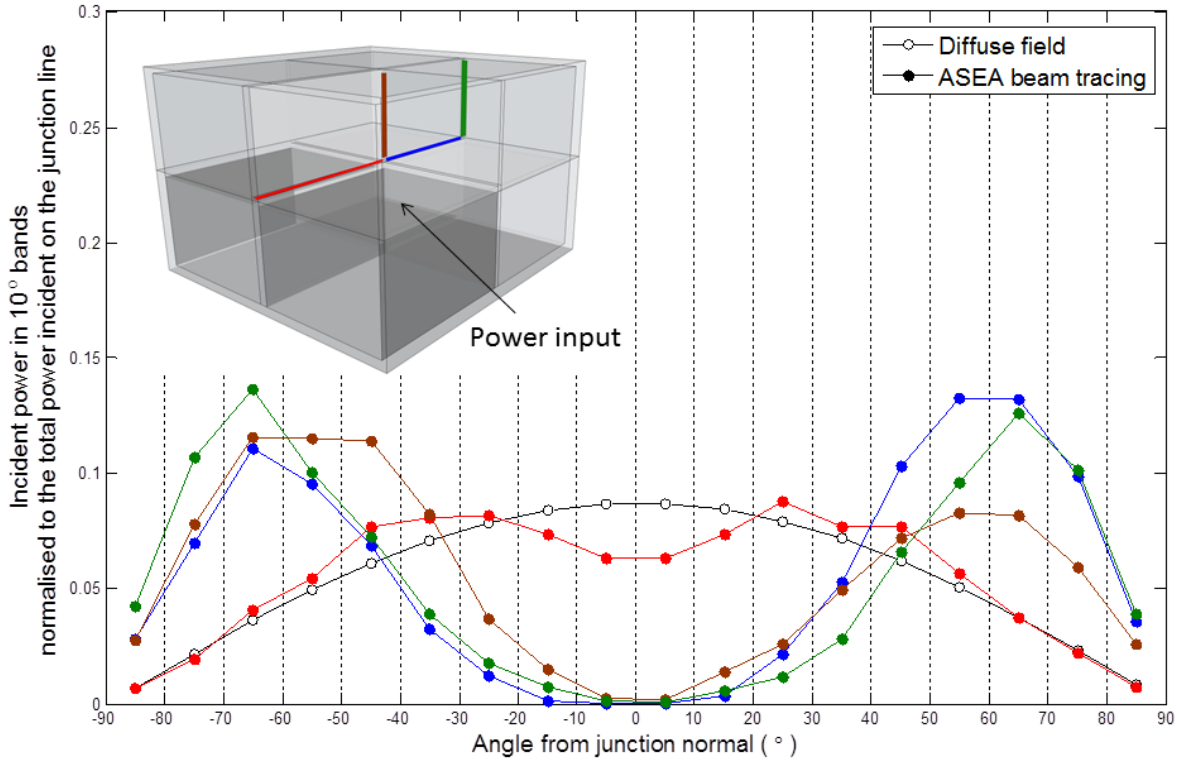

Figure 7.4. 2_2_2 building. Power incident on junction within 10° angular bands normalised to the total power incident on the junction. Red curve with solid markers – western edge of upper floor 1, blue curve with solid markers – western edge of upper floor 2, brown curve with solid markers – western edge of north wall 5, green curve with solid markers – western of north wall 6. Black curve with open markers – diffuse field result.

The angular distribution of the power incident on the edges of the source plate shows close agreement with the diffuse field assumption as shown in Figures 7.1, 7.2 and 7.4, however, the diffuse field assumption slightly overestimates the power incident on the junctions at between -20° and 20° degrees and underestimates the power at angles of incidence greater than 20°. This is caused by the rectangular shape of the source plate and the angular dependence of the reflection coefficients of the plate boundary. This combination leads to focusing of the intensity at particular angles of incidence where the transmission is weak whilst reducing the intensity in other angular bands where transmission is strong.

In Figure 7.1 it is shown that the power incident on the northern edge (see Figure 5.2 for building orientation) of the upper floors is progressively weighted towards normal incidence as the number of junction lines between source and receiver increases. The normalised angular distribution of the power incident on the eastern edge of the upper floors is shown in Figure 7.2. With the exception of the source plate most of the power incident on the eastern edges of the upper floors is incident between 20° and 90°. This is in contrast to the case of the diffuse field assumption which predicts a peak in the incident power at normal incidence.

Figure 7.3 shows a similar result for the normalised angular distribution of the power incident on the eastern edge of the north wall. Results for the 2_2_2 building are shown in Figure 7.4 and indicate that the diffuse field is a reasonable assumption in the source plate. However, spatial filtering also leads to a non-diffuse field in some plates as was found for the 5_1_1 building. For example, the normalised power incident on the western edge of the north wall of room 5, the western edge of the north wall of room 6 and the western edge of the upper floor of room 2 is mostly incident at angles with a magnitude greater than 30° from the junction normal.

These results can be considered with the aid of the diagram in Figure 7.5. This shows a receiving plate which is directly attached to a source plate via 'Edge 1'. A specific wave component of the diffuse field in the source plate which is incident on Edge 1 at an angle of incidence θ_i will generate a transmitted beam in the receiver plate as shown in the diagram. The angle between the directional vector of the beam, $\hat{k}$, and the normal vector from edge 1, y_1, is labelled, θ_1 and is related to θ_i through Snell's Law [20]. The angle between the directional vector of the transmitted beam and the normal vector to Edge 2, y_2, is labelled θ_2.

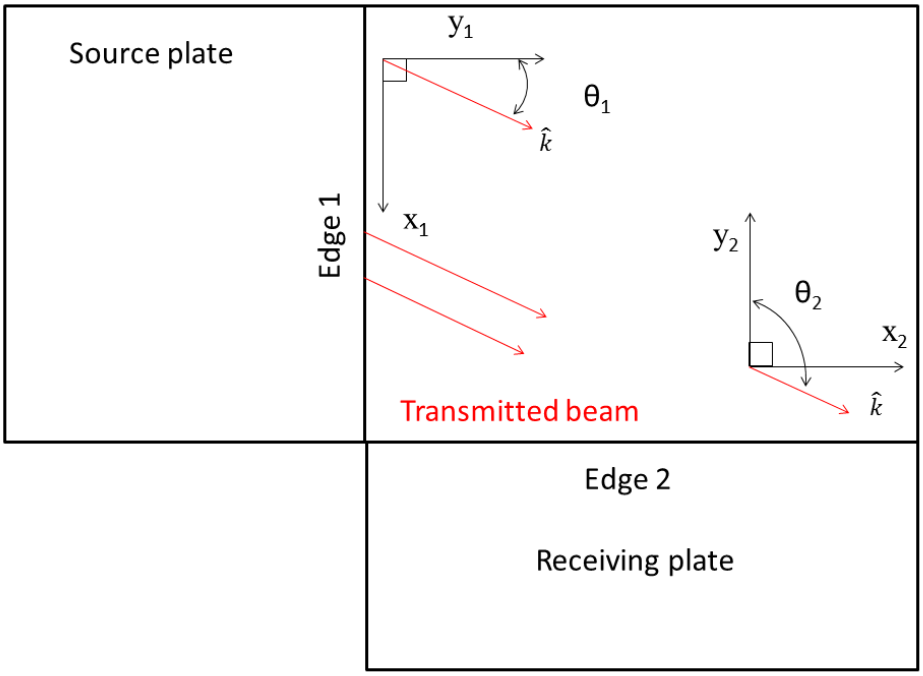

Figure 7.5. Schematic diagram of a transmitted beam from edge 1 of a plate (represented by two red parallel arrows). The systems of coordinates along each edge are shown along with the angle between the unit direction vector of the beam $\hat{k}$ and the y-axis of the edge coordinate systems.

The angle $\theta_2$is related to angle θ_1 through the relation

$$\theta_2 = \theta_1 + \pi/2 \tag{7.1}$$

Hence if there is a transmitted beam at 90° to the Edge 1 normal, this beam will be incident on Edge 2 at normal incidence. The intensity of the transmitted beam is dependent on the power transmission coefficient between the source plate and the receiver plate. The transmitted beam can only be incident on Edge 2 at normal incidence if there is a cut-off angle between the source and receiving plate or if the two plates have the same bending wavelength. A general feature of the power transmission coefficient (eq. 3.30) is that as the angle of incidence approaches the cut-off angle the power transmission coefficient tends to zero (see for example reference [3]). If there is no cut-off angle between the source and receiving plate then the directional vector of the transmitted beam will make an angle less than 90° to the Edge 1 normal vector. This explains the lack of power incident at normal incidence on some plate edges of the receiver plates.

7.3 ASEA results

7.3.1 Convergence of ASEA solution

The ASEA result changes with ASEA iteration number (see section 2.3) until after *n* iterations the difference between the ASEA result on the n^{th} iteration and the ASEA result on the $(n-1)^{th}$ iteration is close to zero. Heron [48] states that for a chain of rods the 'rule of convergence' is that the number of ASEA iterations should at least equal the number of subsystems minus two.

Using the Taylor series the ELD at ASEA iteration *n* may be approximated by the ELD at ASEA iteration $(n-1)$ plus the rate of change of the ELD evaluated at ASEA iteration $(n-1)$ plus some higher order terms:

$$ASEA_n = ASEA_{(n-1)} + \frac{\mathrm{d}}{\mathrm{d}n} ASEA_{(n-1)} + higher\ order\ terms \tag{7.2}$$

Assuming that the number of ASEA iterations is close to the number of subsystems in the model the ASEA result should be close to converging[48]. The coefficients of the higher order terms are then assumed to be much less that the first two terms in the expansion. A convergence criterion is defined that there is less than 0.1 dB difference between the ELD at the n^{th}ASEA iteration and the $(n-1)^{\mathrm{th}}$ ASEA iteration for any combination of source and

receiving plate in the model. This means that if the rate of change of the ELD with ASEA iteration number remains constant then a further ten ASEA iterations will only change the ELD by 1dB.

An example is considered here using the 5_1_1 building which has 26 subsystems. Figure 7.6 shows the difference in the 500Hz band between the 26th ASEA iteration and the 22nd ASEA iteration for the ELD between the upper floor of room 1 and the remaining plates in the 5_1_1 building. Also shown is the difference between the 30th ASEA iteration and the 26th ASEA iteration ELD for the same case of source and receivers. The *y*-axis is the difference per ASEA iteration in dB (i.e. the total difference divided by the total number of ASEA iterations (i.e. 4)) and the *x*-axis shows the subsystem label. The *y*=0 line is shown to indicate which results are closest to zero and hence are closest to convergence.

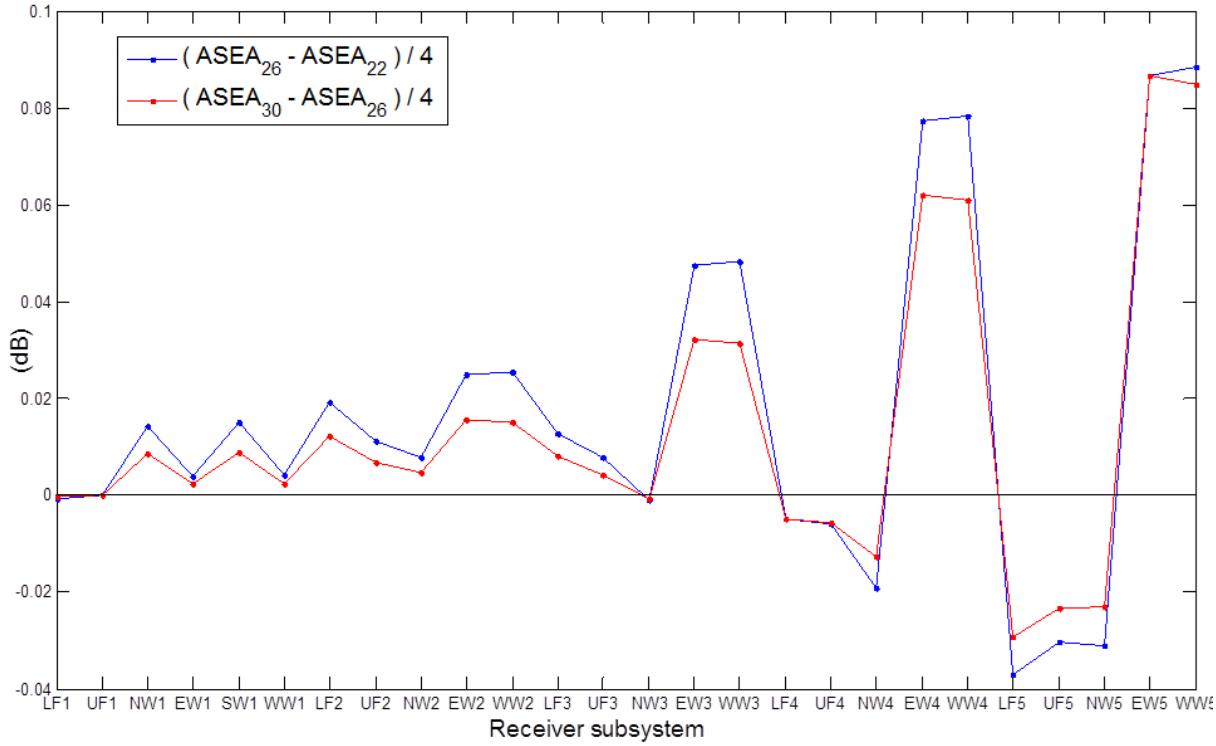

Figure 7.6. *Plot showing the difference between the ELD at the* n^{th} *ASEA iteration and the* $(n-4)^{\text{th}}$ *ASEA iteration in dB. The upper floor of room1 of the 5_1_1 building is the source plate.*

The first point to notice is that the difference between the $ASEA_{30}$ and $ASEA_{26}$ is closer to zero than the difference between $ASEA_{26}$ and $ASEA_{22}$. This indicates that the rate of change is decreasing as the ASEA iteration number increases. Hence this indicates that the ASEA solution is converging and that the actual difference between $ASEA_{30}$ and $ASEA_{40}$ will be

significantly less than 1dB predicted using the convergence criteria. The plot shows that the difference between the ELD at the n^{th} ASEA iteration and the $(n-4)^{\text{th}}$is generally closer to zero for subsystems which are closest to the source subsystem. This suggests that convergence is dependent on the number of times that the power has be traced across the plate subsystem. The results indicate that using an ASEA iteration number equal to the total number of subsystems (in the case of the 5_1_1 building investigated here this is 26) plus four (which gives $ASEA_{30}$ for the 5_1_1 building) provides a result which has converged to an acceptable level. This is similar to the findings of Yin[49, 50] and Heron[48] who suggested using an ASEA iteration number equal to the subsystems in the model minus 1 or 2. This result was used to determine that 40 ASEA iterations would be required for the 2_2_2 building.

7.3.2 Comparison between ASEA and MCFEM – overview of all results

In Figure 7.8 a general comparison is made between MCFEM and ASEA for the case of excitation applied to the upper floor of room 1 in the 2_2_2 building. Each blue line in the figure shows the difference in decibels between MCFEM and ASEA for ELDs between the source plate and other plates in the 2_2_2 building with 95% confidence limits. The zero dB line is indicated in black.

Below 200Hz where the one-third octave band statistical mode count is less than one, the differences are between -10 dB and +15 dB. At frequencies above 200Hz the differences are between -5dB and +7dB. In the 800Hz and 1000Hz bands the ASEA results are within ± 3dB of MCFEM.

Figure 7.9 shows the differences between MCFEM and SEA (or $ASEA_0$). Comparing Figure 7.8 to 7.9 shows that below 200Hz there is no real improvement when using ASEA compared to SEA. Above 200Hz the ASEA results are much more tightly grouped around the zero line with most results lying within ± 3dB. The overall spread of differences with SEA is between -5dB and +10dB. ASEA reduces this overall spread of differences to between -5dB and + 6dB.

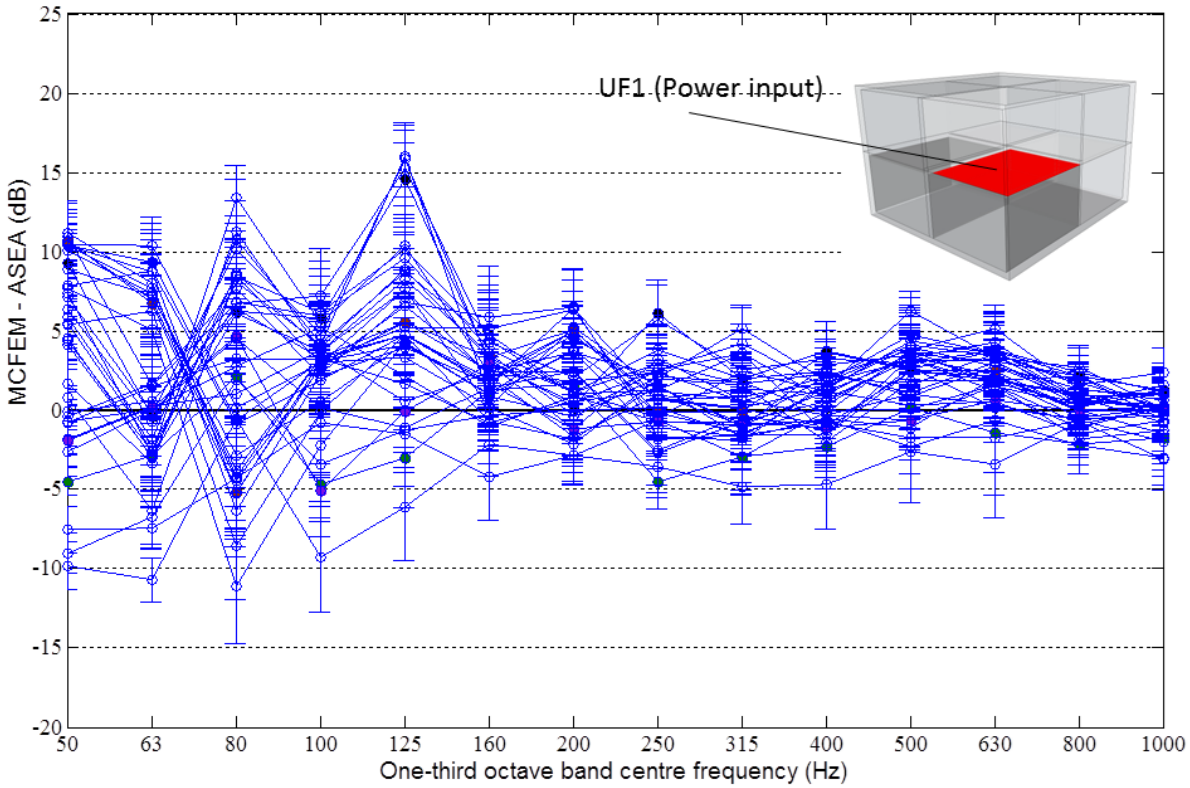

Figure 7.8. Difference between MCFEM ELDs and ASEA ELDs for a 2_2_2 building with power input to the upper floor of room 1.

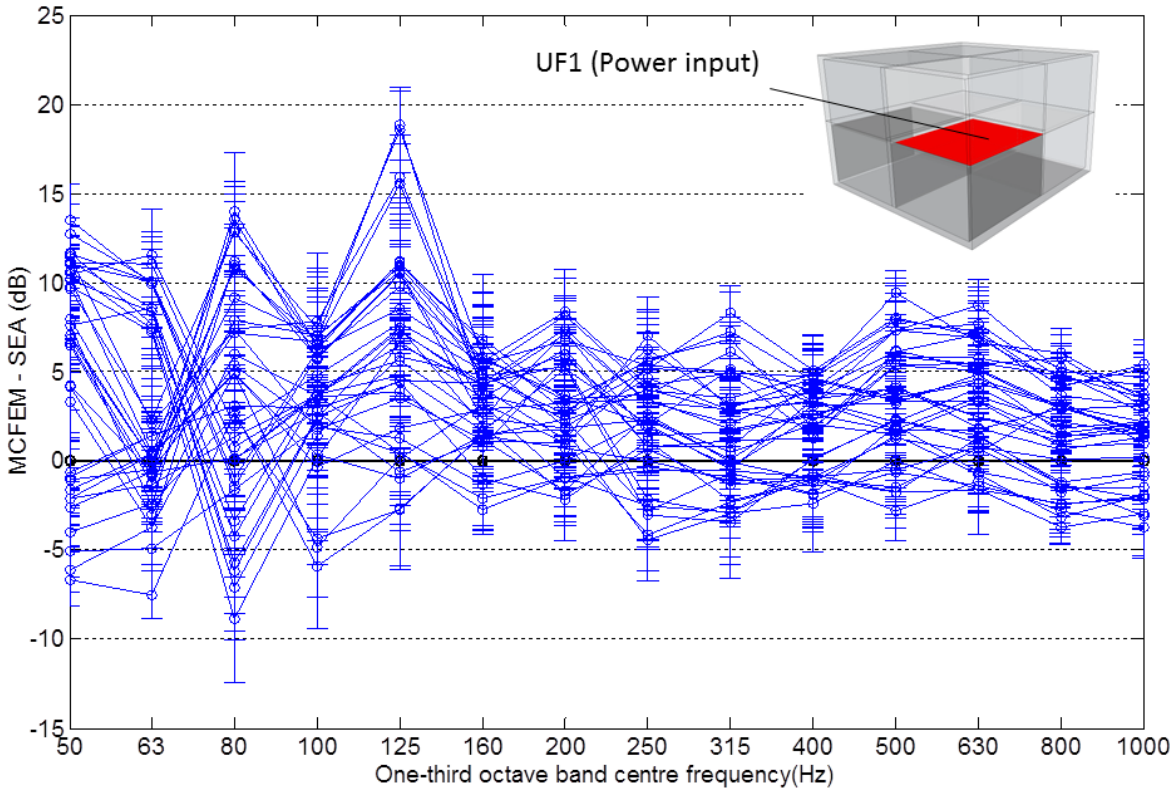

Figure 7.9. Difference between MCFEM ELDs and SEA ELDs for a 2_2_2 building with power input to the upper floor of room 1.

For the 5_1_1 building the differences between MCFEM and ASEA are shown in Figure 7.10. Below 200Hz the differences are between -10dB and 15dB, however a majority of the differences are within ±10dB. Above 200Hz most differences are between ±5dB. However in some bands the differences are as large as -11dB. Comparing ASEA results in Figure 7.10 to the SEA results in Figure 7.11 indicates that the ASEA results are more tightly concentrated around the zero line (i.e. they are close to MCFEM results). The ASEA differences are between -11dB and +5dB whereas the SEA differences are between -17dB and 7dB. In the 800Hz and 1000Hz bands the SEA differences are between -14dB and +5dB whereas the ASEA differences are between -6dB and 3dB. Hence ASEA gives a significant improvement over SEA for the case of the 5_1_1 building.

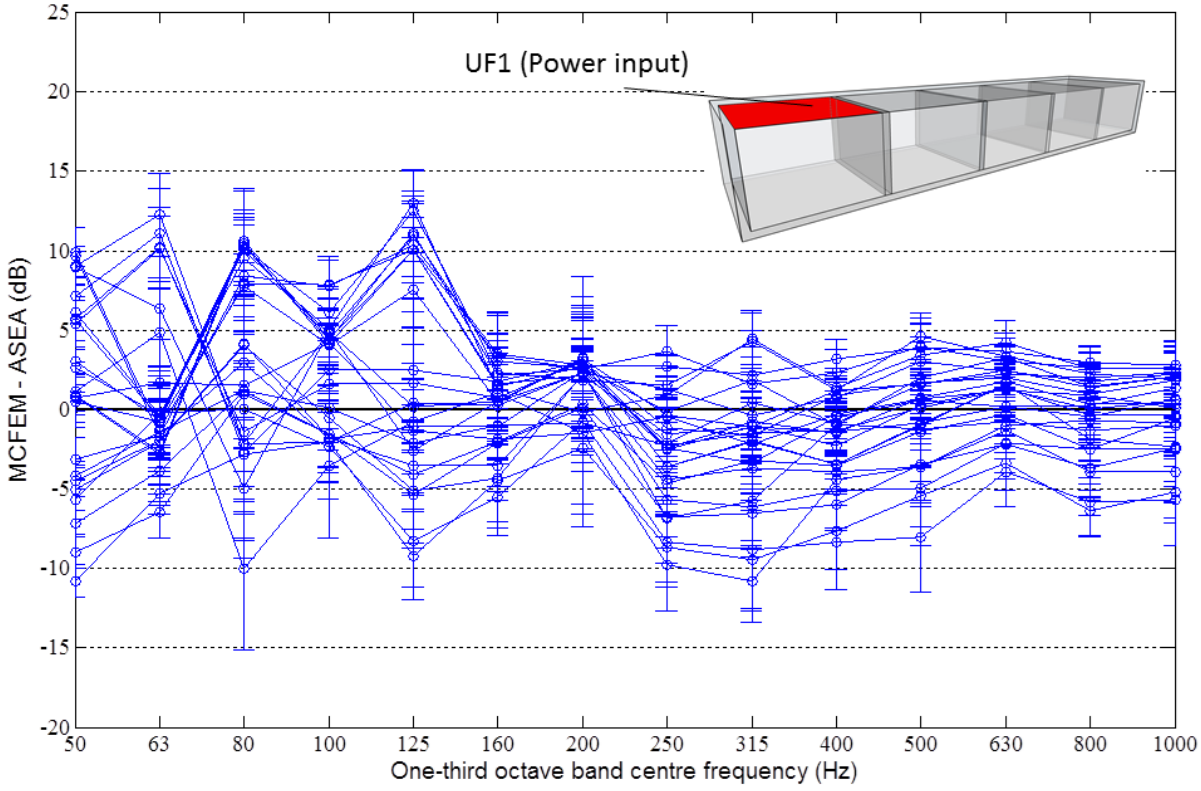

Figure 7.10. Difference between MCFEM ELDs and ASEA ELDs for a 5_1_1 building with power input to the upper floor of room 1.

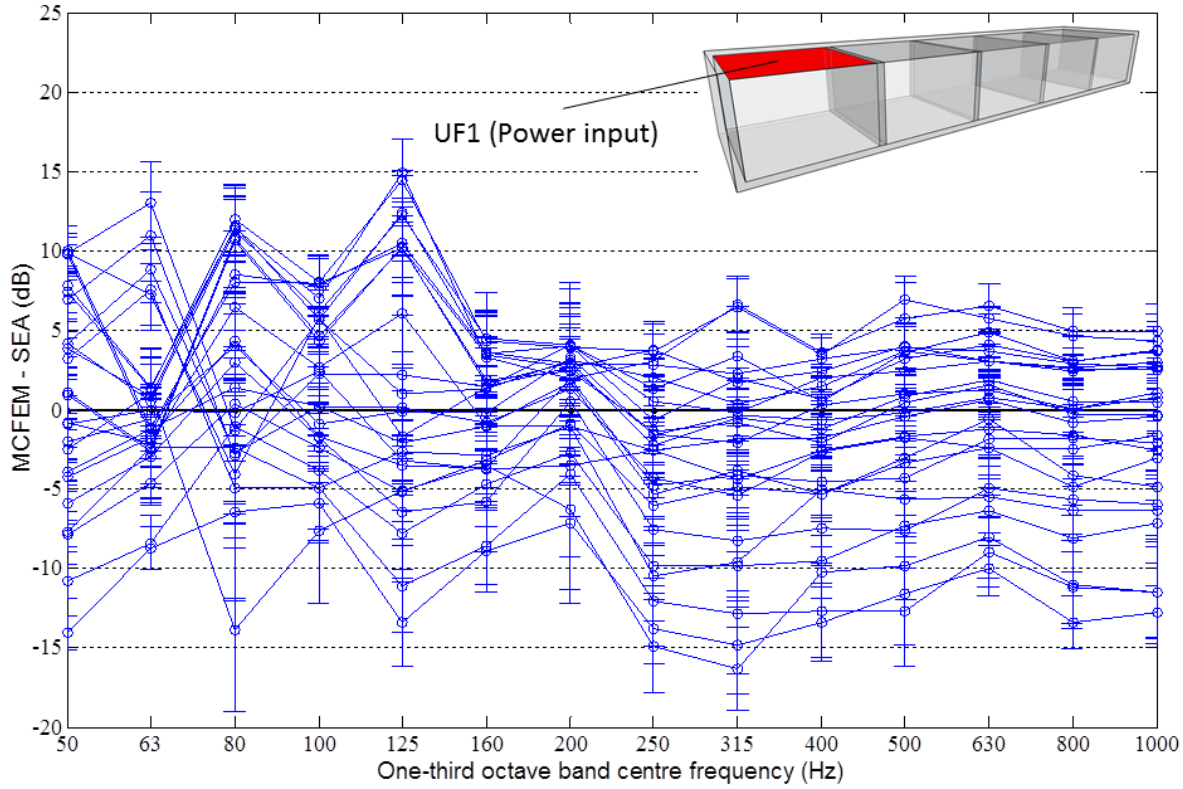

Figure 7.11. *Difference between MCFEM ELDs and SEA ELDs for a 5_1_1 building with power input to the upper floor of room 1.*

7.3.3 Individual case comparison between ASEA and MCFEM

In this section the MCFEM results are compared with ASEA for specific sets of source and receiving subsystems.

In Figure 7.12 a comparison is made between the MCFEM and the ASEA ELDs for the case of excitation applied to the upper floor of room 1 of the 2_2_2 building. This shows the difference in decibels between MCFEM and ASEA. Each curve corresponds to the ELD between the source plate and the receiver plate of the same colour as indicated on the diagram. All the differences are between -5dB and +5dB at frequencies above 200Hz. Below 200 Hz the ASEA differences are between -5 and +15dB.

Figure 7.13 shows the differences between MCFEM and SEA ELDs for the same set of plates. Comparison of the two figures indicates that ASEA gives a marginal improvement over SEA for the ELD between the upper floor and the west wall of room 1 in the bands at and above 200Hz. For the ELDs from the upper floor of room1 to the remaining plates the differences between the two results are negligible.

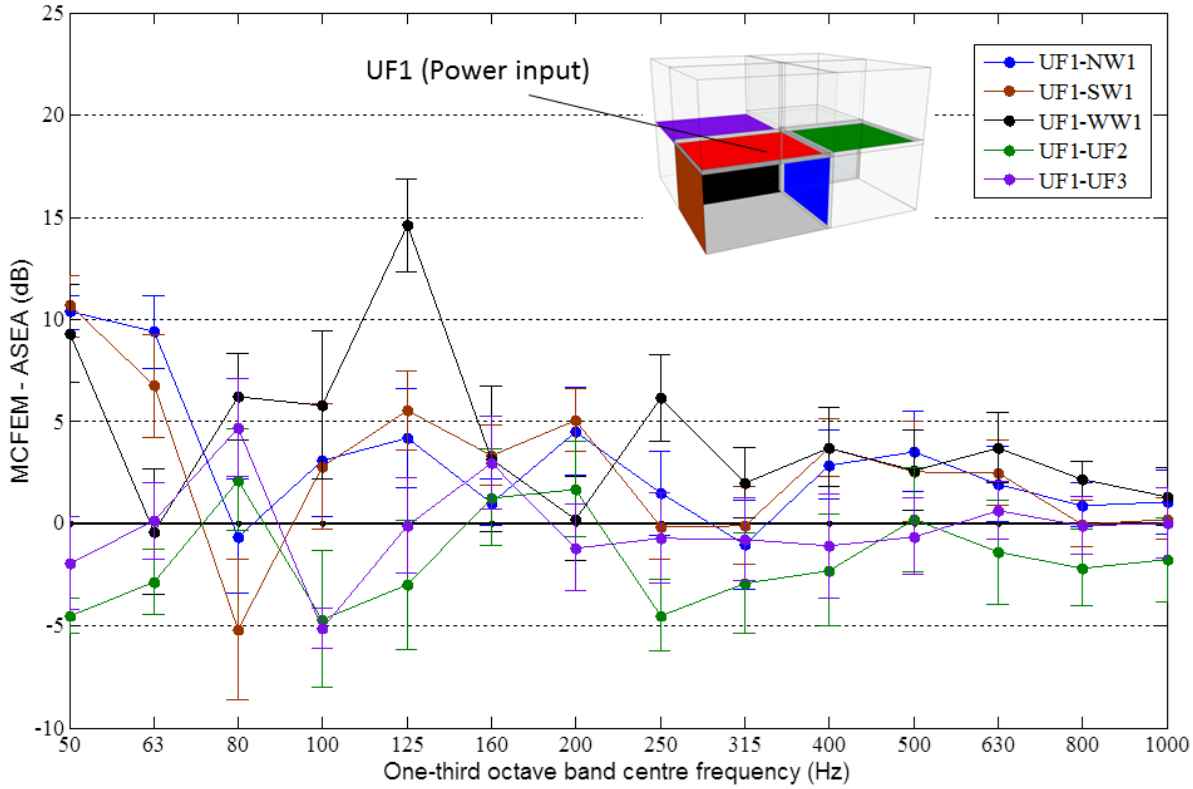

Figure.7.12. Difference between MCFEM ELD and ASEA ELDs for the case of the plates directly attached to the source plate, upper floor of room 1 in the 2_2_2 building. The zero line is shown in black. Curve corresponds to the ELD between the source plate and the receiving plate with the same colour.

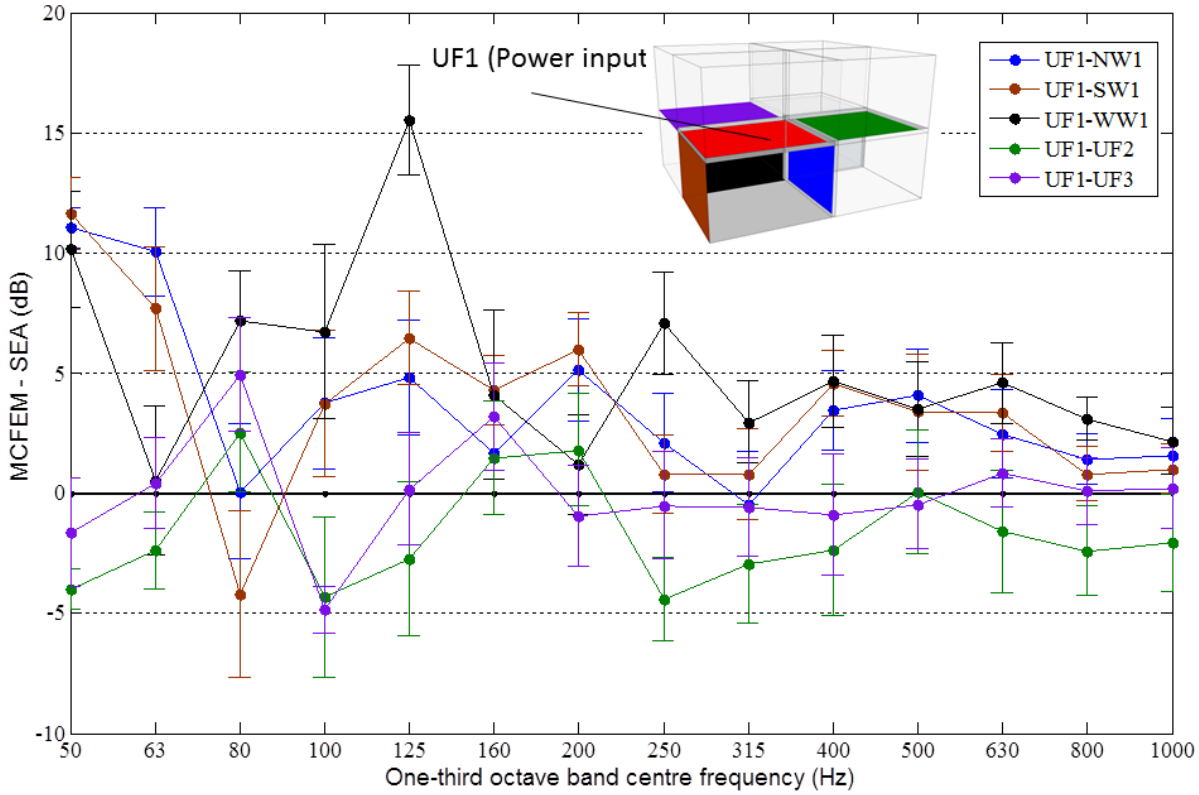

Figure7.13. Difference between MCFEM ELD and SEA ELDs for the case of the plates directly attached to the source plate, upper floor of room 1 in the 2_2_2 building. The zero line is shown in black. Curve corresponds to the ELD between the source plate and the receiving plate with the same colour.

This indicates that SEA is as accurate as ASEA for subsystems which are attached directly to the source subsystem. Referring back to the assessment of spatial filtering in Figure 7.4 it was shown that the power incident on the junction lines connecting the source to these plates was well described by the diffuse field assumption. Since SEA assumes the power in the plates to be diffuse it is expected that SEA would perform well for the case of plates directly attached to the source plate.

In this thesis a particular cases of interest is when the receiving subsystem is not situated in one of the rooms attached directly to the source room but diagonally adjacent to the source room. To try and improve prediction for this situation in Chapter 6 the global mode CLFs were incorporated into an SEA model of the 2_2_2 building. However, no improvement was found over SEA using CLFs from semi-infinite plate theory. In Figure 7.14 the ASEA ELDs from the source plate to the flanking walls in rooms 4 and 8 are directly compared against MCFEM. The ASEA ELDs are represented by lines with filled circular markers and the MCFEM results are represented by open circular markers. ASEA shows reasonable agreement with MCFEM in one-third octave bands above 200Hz with ASEA under-

predicting the ELD by up to 3dB. Referring back to Figure 5.26 it was seen that SEA underestimates the level difference to these subsystems by around 5dB in the frequency range 200 to 1000Hz. Below 200 Hz the ASEA results are generally with 10 to 15dB of the MCFEM results.

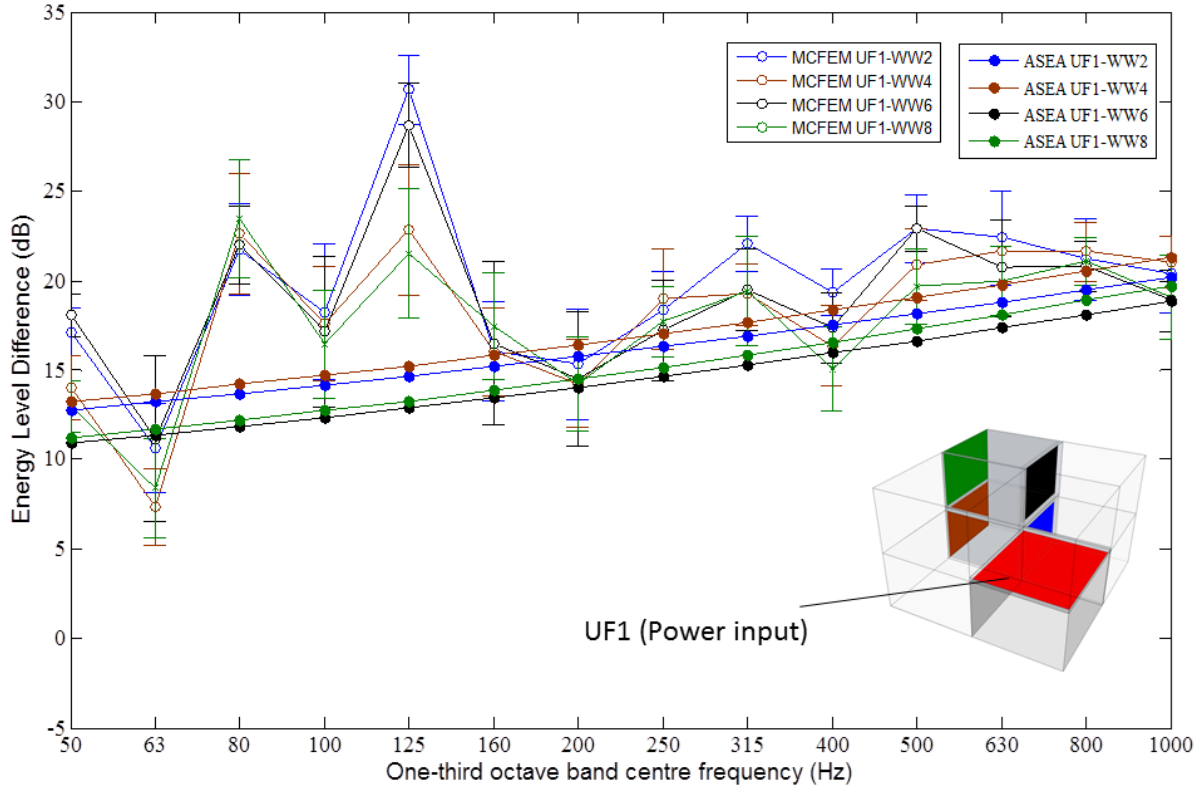

Figure.7.14. MCFEM and ASEA predictions for the ELD between the upper floor and room 1 and the flanking walls in room 4 and 8.

In Figure 7.15 the ASEA results are directly compared to MCFEM for the ELDs from the upper floor of room 1 to the thick separating walls connected to rooms 4 and 8. Close agreement is found between ASEA and MCFEM with most of the ASEA results lying within the 95% confidence limits of the MCFEM results. Above 200 Hz, most ASEA results are within 3dB of MCFEM. In Figure 5.25 the SEA results for the same case underpredicted the ELD by around 6dB in bands above 200 Hz. Below 200 Hz the ASEA results are within 10dB of MCFEM.

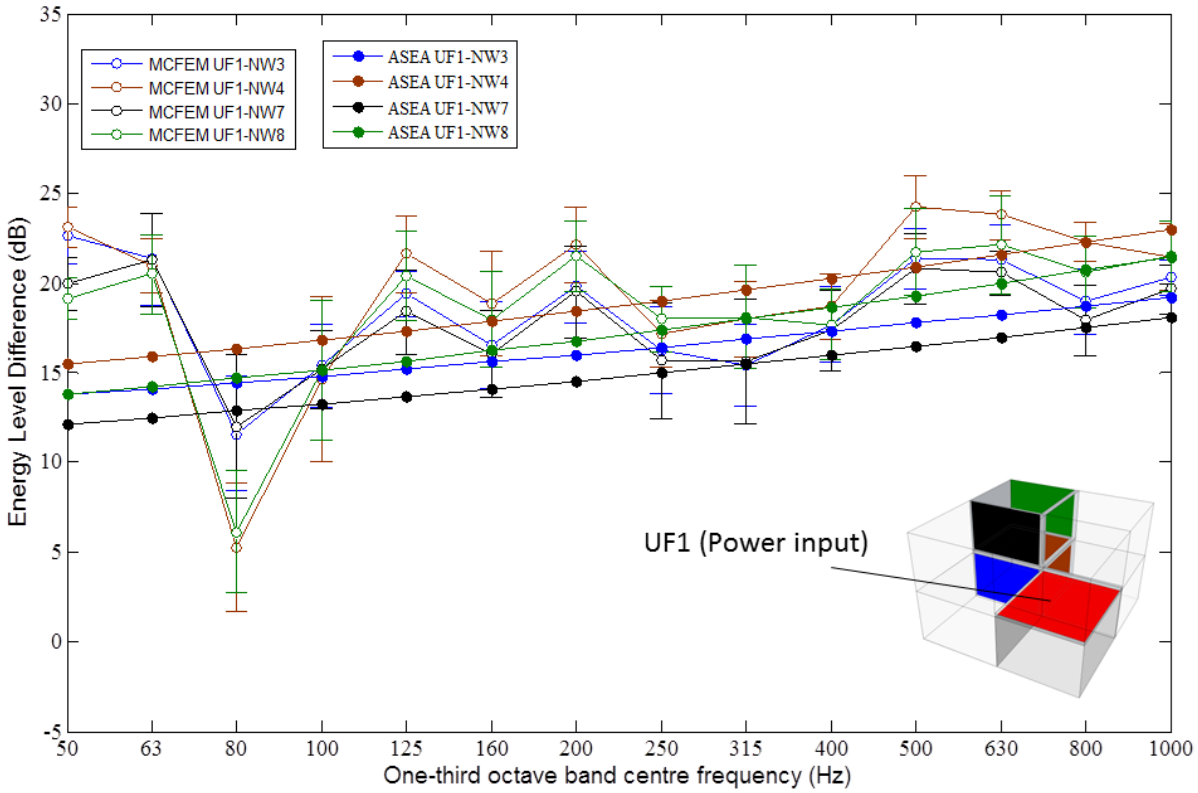

Figure.7.15. MCFEM and ASEA predictions for the ELD between the upper floor and room 1 and the separating walls between rooms 3 and room 4 and between rooms 7 and 8.

Figure 7.16 shows a comparison of the MCFEM and ASEA ELDs between the upper floor of room1 and the floors in room 4 and 5. The ASEA results are close to the MCFEM ELD between the upper floor of room 1 and the upper floor of room 8 and also between the upper floor of room 1 and the lower floor of room 4. The ASEA results are within the 95% confidence limits of MCFEM results in most one-third octave bands above 200 Hz. Compared to the SEA results for the same ELDs in Figure 5.24 ASEA shows a slight improvement over SEA for the case of these two floors. For the case of the ELD between the upper floor of room 1 and the upper floor of room 4 SEA shows closer agreement with MCFEM than ASEA. The strongest paths from the upper floor of room 1 to the upper floor of room 4 pass through the upper floors of room 3 and the upper floors of room 2 and it was shown in Figures 7.12 and 7.13 that SEA and ASEA give approximately the same result for these two subsystems. Other strong paths may pass through the west wall of rooms 2 or room 6 and for these subsystems the ASEA ELD is closer to the MCFEM ELD. Another possible strong path is through the north walls of room 1,3, 5 and 7 and again ASEA predicts an ELD which is closer to the MCFEM ELD for these subsystems. It therefore seems that SEA predicts the correct result due to incorrect assumptions.

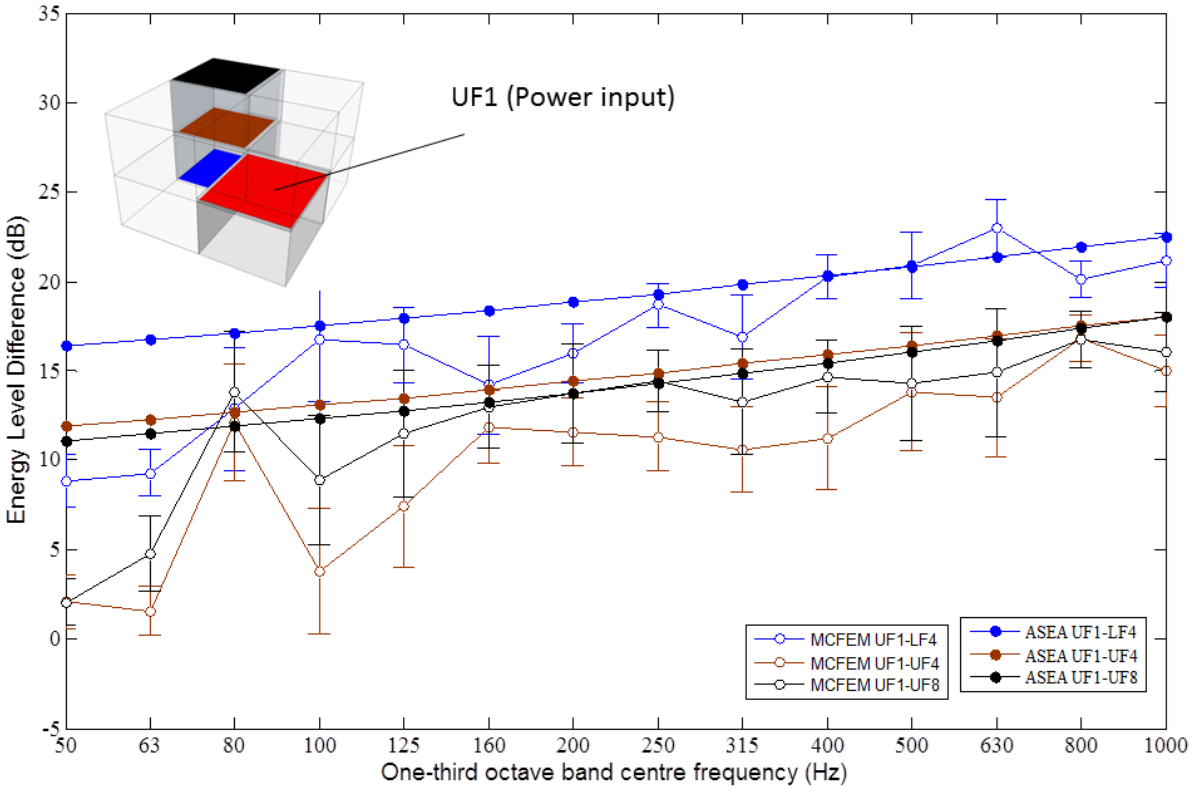

Figure.7.16. MCFEM and ASEA predictions for the ELD between the upper floor and room 1 and the floors in room 4 and 8.

Figures 7.17 to7.20 a direct comparison is made between the MCFEM and ASEA for the ELD between the upper floor of room1 and the remaining plates in the 5_1_1 building.

In Figure 7.17 the MCFEM and ASEA results are compared for the ELDs between the upper floor of room 1 and the flanking walls of the 5_1_1 building. (note that due to symmetry it is not nessesary to show the ELDs to the flanking walls on the other side of the building).

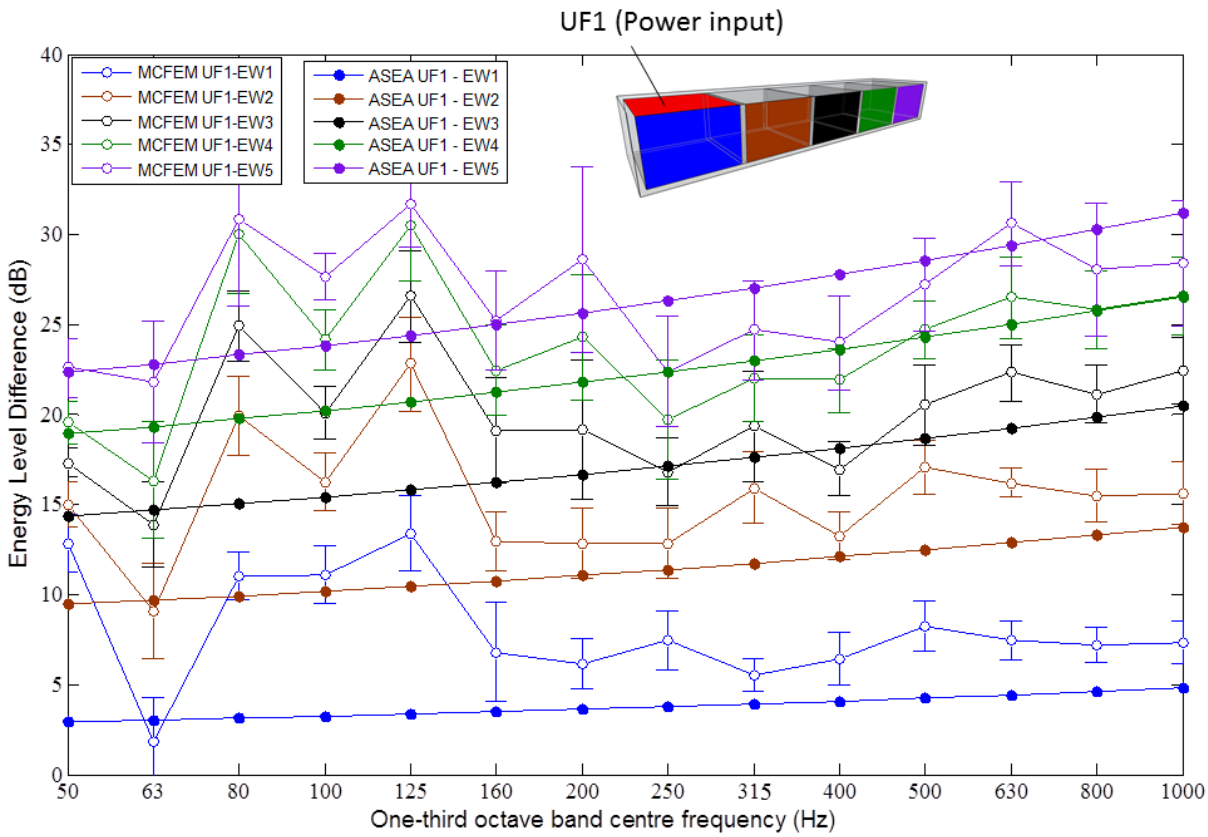

Figure.7.17. MCFEM and ASEA predictions for the ELD between the upper floor and room 1 and the flanking walls of the 5_1_1 building.

Above 200Hz the ASEA results are within 3dB of theMCFEM results. Good agreement is obtained for all the ELDs from the upper floor of room 1 to the flanking walls with most ASEA results being within 3 dB of MCFEM. ASEA is closest to MCFEM for the ELD from the upper floor in room 1 to the flanking walls in rooms 3, 4 and 5. However, ASEA underestimates the ELD of the flanking walls in room 1 and 2 hence this may be due to ASEA overpredicting the transmission from the upper floor of room 1 to the nearby flanking walls and underpredicting the strength of transmission paths to the more distant flanking walls via other plates.

Comparing ASEA with SEA (Figure 5.32) for the ELD between the upper floor of room 1 and the flanking wall of room 2 shows that SEA underestimates the ELD by ≈ 6 dB above 200Hz whereas ASEA underestimates by ≈ 3dB. This suggests that spatial filtering significantly reduces transmission to the flanking wall of the room that is adjacent to the room in which the source is placed. Below 200Hz ASEA underpredicts the ELD by ≈ 10 dB which is similar to SEA.

Figure 7.18 shows the ELD from the upper floor of room 1 to the remaining upper floors of the 5_1_1 building. ASEA gives closest agreement with MCFEM for the ELD from the upper floor of room 1 to the upper floor of room 2 and is within the 95% confidence limits in most one-third octave bands. The ASEA result for the upper floors of rooms 3 and 4 are generally within 5dB of the MCFEM results. The ASEA result for the upper floor of room 5 is within 7dB of the MCFEM result. This is a significant improvement over the SEA result (Figure 5.30) which overpredicts the ELD to the upper floor of room 5 by around 15dB from 50 to 1000Hz.

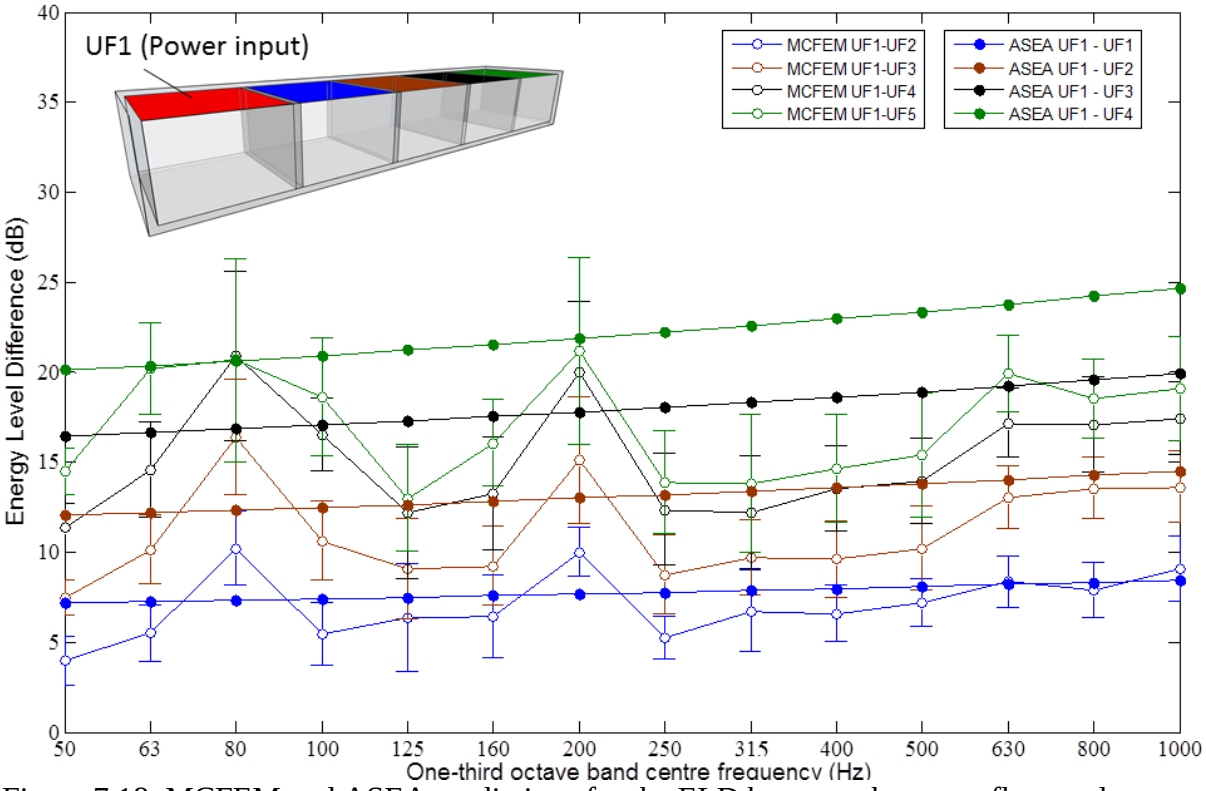

Figure.7.18. MCFEM and ASEA predictions for the ELD between the upper floor and room 1 and the remaining upper floors of the 5_1_1 building.

Figure 7.19 shows the ELDs between the upper floor of room 1 and the separating walls of the 5_1_1 building. Above 200 Hz there is good agreement between ASEA and MCFEM for ELDs between the upper floor of room 1 and the north wall of room 1 and 2 with most ASEA results lying within the 95% confidence limits. For the ELDs between the upper floor of room 1 and the north wall of room 1,2,3,4 and 5, above 400 Hz there is good agreement between the ASEA and MCFEM results with ASEA results within 3dB of the MCFEM results. However in the 250Hz and 315Hz bands there is very strong transmission from the upper floor of room 1 and the north walls of room 3,4 and 5 resulting in overlapping confidence

limits for MCFEM. ASEA cannot account for this feature and leads to ≈ 10dB overestimate of the ELD for the north walls of room 4 and 5 in these two bands.

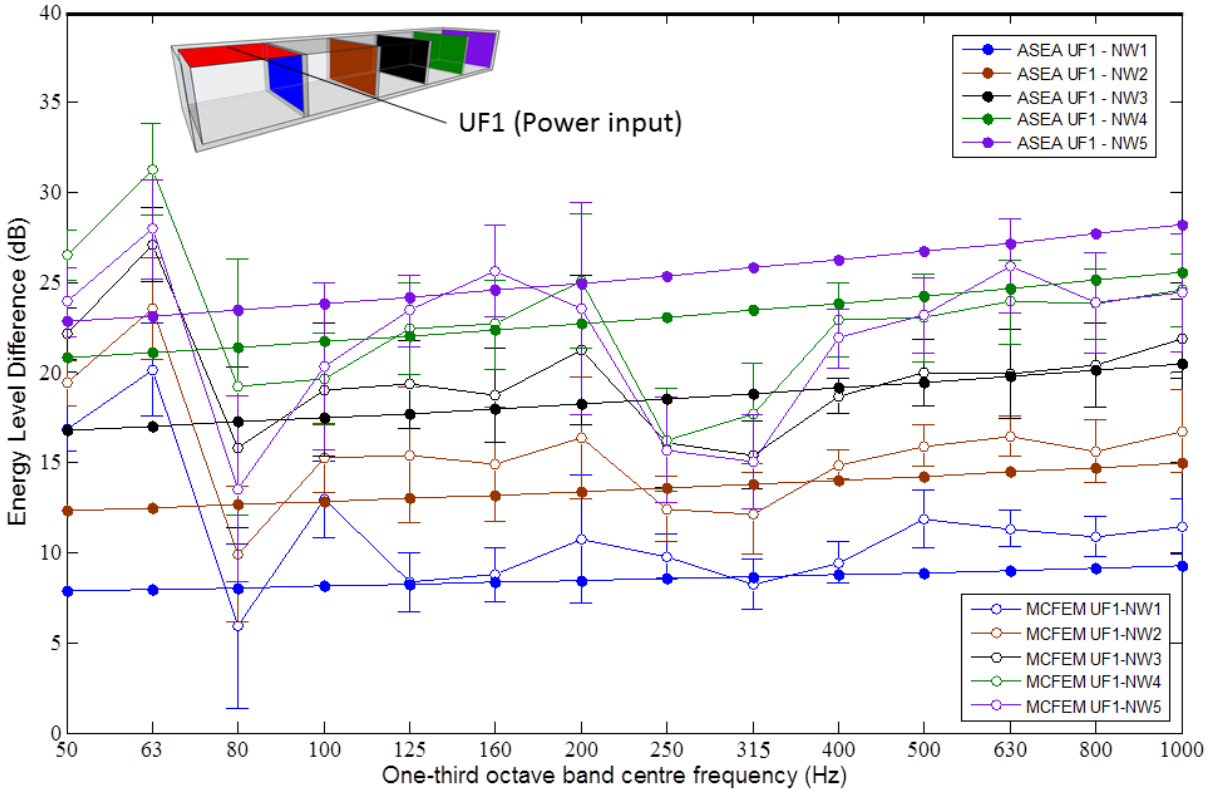

Figure.7.19. MCFEM and ASEA predictions for the ELD between the upper floor and room 1 and the separating walls of the 5_1_1 building.

Figure 7.20 shows the ELD between the upper floor of room 1 and the lower floors of the 5_1_1 building. For the ELD to the lower floors of room 1 and room 2 ASEA gives a good estimate of the MCFEM ELD with the ASEA result lying within the 95% confidence limits in most frequency bands. As the number of structural junctions between the source and receiver is increased the ASEA prediction becomes less accurate. For example, above 200Hz ASEA overestimates the ELD between the upper floor of room 1 and the lower floor of room 3 by ≈ 3dB and overestimates the ELD between the upper floor of room 1 and the lower floor of room 5 by ≈ 7dB.

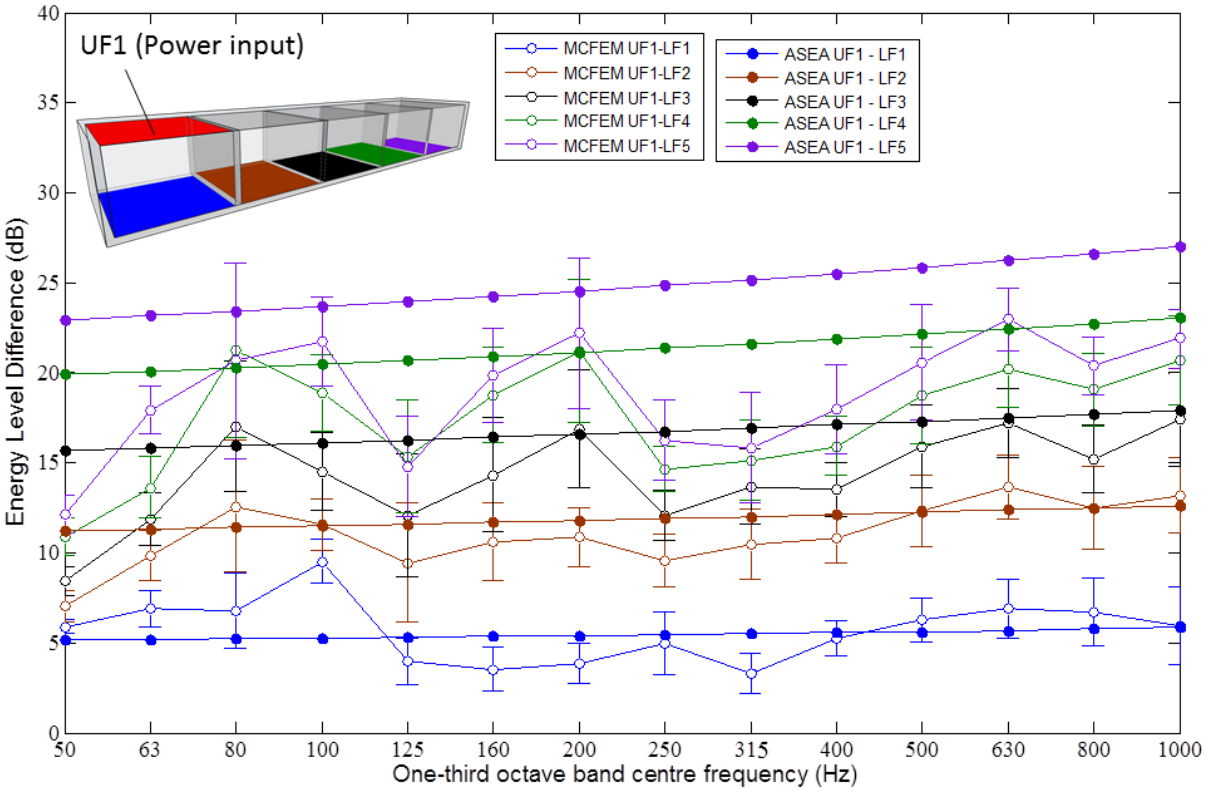

Figure.7.20. MCFEM and ASEA predictions for the ELD between the upper floor and room 1 and the lower floors of the 5_1_1 building.

7.4 Conclusions

In this chapter ASEA has been used to investigate the role of spatial filtering in building structures. The beam tracing method has been used to determine the angular distribution of power incident on the plate edges of the 5_1_1 building. On the source plate it was found that the power incident on the edges was similar to a diffuse field assumption. However in the receiver plates the angular distribution of power incident on the plate edges differed significantly from the diffuse field prediction with little or no power incident at normal incidence to the junction line.

In both the 5_1_1 and 2_2_2 buildings, ASEA predicted ELDs which were within ≈ 3dB of MCFEM for plates in the same room as the source plate or in the adjoining room for one-third octave bands between 200Hz and 1kHz whereas the error was ≈ 6dB for SEA. However for plates directly attached to the source plate, SEA results were similar to ASEA with both ASEA and SEA generally underestimating the ELD by 2 to 3dB. When using angular-average transmission coefficients from semi-infinite plate theory in ASEA and SEA the applied excitation evenly 'illuminates' the edges of the source plate at all angles of incidence. This assumption weights the transmitted power towards normal incidence. This assumption

weights the transmitted power towards normal incidence. However for both SEA and ASEA the source plates under investigation have low modal density and modal overlap factor over most of the frequency range of interest. Considering the principle of wave-mode duality, waves will only be incident on the plate boundaries at the equivalent angles of the modes excited in each one-third octave band. For this reason, ASEA and SEA generally underestimates the ELD to the plates that are directly connected to the source plate when compared against MCFEM. Equivalently, work carried out by Wester and Mace[19] has shown that the semi-infinite plate theory[20] overestimates the CLF between two finite rectangular plates. Since the angular-average transmission coefficient is directly related to the CLF, the semi-infinite plate transmission coefficients used in both ASEA and SEA overestimate the transmission between the plates and which incur some errors in the result.

The largest difference between ASEA and SEA was ≈3.5dB for the ELD from the upper floor of room 1 to the flanking walls of room 2. Therefore compared to ASEA, SEA underestimates the ELD by approximately the same amount as path analysis (see Section 5.3) overestimates the SEA ELD. Hence path analysis sometimes leads to the 'correct' result for the wrong reason.

For cases where a significant number of structural junctions lie between the source and receiver plates ASEA gave a significant improvement over the SEA prediction. For example, between 500 and 1000Hz the ASEA prediction for the ELD between the upper floor of room 1 and the upper floor of room 5 of the 5_1_1 building is within 6dB of MCFEM whereas SEA over-predicts by ≈ 15dB. The results from Section 5.2 indicate that spatial filtering of the wave-field by successive junctions weights the power incident towards normal incidence for the T-junctions that connect the upper floors. Therefore transmission across the T-junction becomes much greater than predicted by angular-average wave theory taken over all angles of incidence as is often used to calculate CLFs for SEA models.

Chapter 8 Conclusions and future work

8.1 Conclusions

This thesis investigated the prediction of structure-borne sound transmission across coupled plates affected by spatial filtering and non-diffuse vibration fields.

Chapter 2 introduced the framework of Statistical Energy Analysis and ASEA was introduced as a potential solution to deal with spatial filtering, non-diffuse vibration fields and propagation losses as waves travel across subsystems. An efficient ray tracing procedure was proposed to allow simulations of large buildings. An overview was given of Finite Element Methods and the Monte-Carlo approach used in this thesis as a form of numerical experiment for comparison with predictions using SEA and ASEA.

In Chapter 3 two different methods were described to calculate coupling loss factors between simply supported plates for bending wave transmission across the junction. For semi-infinite plates, wave theory was used to determine transmission coefficients which relate the amplitude of the outward propagating transmitted wave in each plate to the incident wave. For finite plates, the CLF can account for the fluctuations in the power flow between the coupled plates caused by interference. The global mode method was used to calculate CLFs with an ideal set of ROTR forces applied to the source plate.

Chapter 4 used measurements on a small heavyweight building structure to validate the FEM models and the MCFEM approach to account for uncertainty. Comparison of the driving-point mobility from FEM and the measurements showed good agreement in the region of the first modal peak. Although FEM overestimated the amplitude of this peak there was evidence that a global mode model (i.e. FEM) was necessary to predict the modal response because the local mode model consistently predicted a lower frequency for the first resonant peak than was observed experimentally. However FEM was unable to accurately predict the location of higher frequency peaks in the driving point mobility. For the ELDs, there was good agreement between MCFEM and the measurements above 250Hz. However below 250Hz there were discrepancies with up to 15dB difference between the measurements and MCFEM in some cases. This was attributed to the FEM model predicting eigenfrequencies for the first few global modes that were different to the actual eigenfrequencies. The results indicate that

a MCFEM approach can be used to accurately predict the structure-borne sound transmission in a simple single room heavyweight building structure in one-third octave bands at frequencies where the statistical mode count is greater than one. Consequently MCFEM was used to assess the accuracy of the approaches to predict structure borne sound transmission in large buildings in Chapters 5, 6 and 7.

Chapter 5 analysed results from SEA models using CLFs from semi-infinite plate theory for comparison with MCFEM for two large buildings (referred to as 5_1_1 and 2_2_2). Comparison of SEA models with and without air cavities representing the room subsystems indicated that the structure-borne sound transmission in heavyweight buildings can be modelled *in vacuo* without the need to include radiation coupling between the plates and the air cavities. Hence the focus was on the prediction of the vibration levels on plates without further consideration of the effect of the sound fields in the rooms.

Chapter 5 also investigated the effect of using a limited number of short transmission paths to predict energy levels of walls and floors in heavyweight buildings. For power input to the upper floor of room 1 in a 2_2_2 building, the approach used in EN12354 (first-order path analysis) underestimated the energy level in the source plate. For receiving subsystems which were attached directly to the source subsystem, EN12354 underestimates the energy levels by up to 7dB. When using path analysis, the effect of adding paths higher than first-order paths is to increase the receiving subsystem energy. When including energy contributions from paths which contain two or more CLFs than the direct path it was shown that the convergence to matrix SEA slows considerably. This is because most of the energy is transmitted to the receiver via a large number of paths. For example, in the 5_1_1 building with the source as the upper floor of room 1, the energy in the upper floor of room 5 predicted using only the direct path was 13dB lower than matrix SEA. In some cases it was shown to be necessary to include up to a million paths in order to converge on the matrix SEA result. Hence it is concluded that a path analysis approach such as EN12354 is not a feasible predictive method in heavyweight buildings for plates that are not directly attached to the source plate.

To assess the effect of low mode counts and low modal overlap factors when using one-third octave bands, matrix SEA was compared to MCFEM. ELDS were predicted between plates where the power was injected into the upper floor of room 1 of the 2_2_2 and 5_1_1 buildings. Between 80Hz and 200Hz the low statistical mode count leads to large fluctuations

in the plate responses and therefore SEA gave poor agreement with MCFEM with differences typically between -5dB and 15dB. In Chapter 6 the use of CLFs derived from finite plate theory will be used to investigate whether the matrix-SEA predictions can be improved in this low-frequency range. For the 2_2_2 building there was reasonable agreement between SEA and MCFEM above 200Hz where statistically there was more than one mode per band in all plates.

For the 2_2_2 building it was found that SEA under-predicted the ELD by between 3 and 5dB above 200Hz which is approximately the same amount that EN12354 underestimates the total energy calculated by matrix SEA in these receiving subsystems. Hence EN12354 gives the right answer for the wrong reason. ELDs from MCFEM and SEA were then compared for the case of walls and floors connected to rooms that were located diagonally opposite to room 1. In this case SEA results underestimated the ELDs by between 5 and 10dB between 500 and 1000Hz. It is hypothesised that this occurs due to the spatial filtering of the wave field in subsystems connected to the source across a minimum of two junctions.

The results from the 5_1_1 building were distinctly different from the 2_2_2 building. In some bands the ELD predicted by SEA was around 15dB higher than predicted by MCFEM for certain source and receiving subsystems indicating very strong transmission in some frequency bands.

Chapter 6 used finite plate theory CLFs to investigate whether the modal features can be predicted when CLFs from isolated plate junctions are incorporated into an SEA model rather than using CLFs from semi-infinite plate theory. This approach was used to try and improve the prediction compared to SEA models using CLFs calculated from semi-infinite plate theory. CLFs for isolated plate junctions were calculated using EICs from the global mode approach. When these CLFs were incorporated into SEA models this was referred to as the global mode SEA approach. EICs were used to calculate the ELDs for L-, X- and T-junctions which were compared against ELDs calculated using MCFEM. The close agreement between these two methods indicates that (a) ROTR is a good approximation to the ideal ROTR used in the global mode approach (b) that the global modes of the isolated junctions calculated analytically were in close agreement with the global modes calculated using FEM.

The CLFs from isolated junctions were incorporated into SEA models of the 2_2_2 and 5_1_1 buildings and the results compared against the ELDs calculated using MCFEM. Below 200Hz (where the statistical mode count in one-third octave bands is less than one) the global mode SEA approach was unable to predict the peaks and troughs in the ELDs in the building to one-third octave band accuracy. This is in contrast to the results for isolated junctions where good agreement was observed between MCFEM and global mode SEA. Above 200Hz (where the statistical mode count in one-third octave bands is greater than one), close agreement was observed between MCFEM and global mode SEA for plates directly connected to the source plate. However, for cases where the receiving subsystem is connected to the source across at least two junctions, there were significant errors in the global mode SEA approach. In some cases an offset of approximately 5dB was observed between MCFEM and global mode SEA. To investigate these errors further a five plate MCFEM model was generated on which ESEA could be applied. When indirect CLFs between subsystems were forced to zero an offset of around 5dB was found between the MCFEM results and the SEA results for subsystems which were not directly connected to the source subsystem. Hence it is concluded that indirect CLFs between subsystems which are not directly physically connected are essential for accurate prediction with SEA models. Comparison of the ESEA results with the global mode SEA approach indicates that the global mode SEA approach adequately predicts direct CLFs but unfortunately the method does not allow calculation of the indirect CLFs and hence is of limited use.

In Chapter 7 ASEA was applied to the 5_1_1 and 2_2_2 buildings to address the issue of the importance of indirect coupling that was identified in Chapter 6. The beam tracing method was used to determine the angular distribution of power incident on the plate edges of the 5_1_1 building. On the source plate it was found that the power incident on the edges was similar to a diffuse field assumption. However in the receiver plates the angular distribution of power incident on the plate edges differed significantly from the diffuse field prediction with little or no power incident at normal incidence to the junction line. In both the 5_1_1 and 2_2_2 buildings, ASEA predicted ELDs which were within ≈ 3dB of MCFEM for plates in the same room as the source plate or in the adjoining room for one-third octave bands between 200Hz and 1kHz whereas the error was ≈ 6dB for SEA. However for plates directly attached to the source plate, SEA results were similar to ASEA with both ASEA and SEA generally underestimating the ELD by 2 to 3dB. For cases where a significant number of

structural junctions lie between the source and receiver plates ASEA gave a significant improvement over the SEA prediction.

8.2 Future work

In this thesis the global mode approach was used to calculate CLFs between finite plates which were incorporated into SEA models of large buildings. It was shown that this method was unable to predict the peaks and troughs in the ELD between plates in large buildings. Alternative methods could therefore be developed to calculate CLFs which account for the finite width of the plates and the effects of strong coupling but do not contain the peaks and troughs associated with the global mode approach. A potential solution would be to extend the approach developed by Wester and Mace [19] to calculate the CLFs between X- and T-junctions for use in SEA models of building structures. This approach has been shown to work well for isolated L-junctions [22].

In one-third octave bands where the statistical mode count was greater than unity it was shown that ASEA provides a method for determining the mean energy levels of the plate subsystems in building structures to sufficient accuracy. However the method still assumes that a diffuse field is present on the source plate and assumes semi-infinite plate transmission coefficients between rectangular plate junctions. Both of these assumptions are questionable for plate subsystems with low mode count and modal overlap. Further work incorporating finite plate transmission coefficients [21,23] in ASEA could be investigated to address this issue. There is potential for this approach to improve the ASEA prediction in one-third octave bands where the statistical mode count is less than unity.

References

1. Craik, R.J.M., *The Noise-Reduction of Flanking Paths.* Applied Acoustics, 1987. **22**(3): p. 163-175.
2. Galbrun, L., *The prediction of airborne sound transmission between two rooms using first-order flanking paths.* Applied Acoustics, 2008. **69**(12): p. 1332-1342.
3. Hopkins, C., *Sound Insulation*. First ed2007, Oxford: Butterworth-Heinemann.
4. Lyon, R.H. and R.G. DeJong, *Theory and Application of Statistical Energy Analysis*. Second ed1995, Boston: Butterworth-Heinemann.
5. Gibbs, B.M. and C.L.S. Gilford, *Use of power flow methods for assessment of sound-transmission in building structures.* Journal of Sound and Vibration, 1976. **49**(2): p. 267-286.
6. Craik, R.J.M., *The prediction of sound transmission through buildings using statistical energy analysis.* Journal of Sound and Vibration, 1982. **82**(4): p. 505-516.
7. Craik, R.J.M., *Sound transmission through buildings using statistical energy analysis*. First ed1996, Cambridge: Gower.
8. Craik, R.J.M., *In-plane wave propagation in buildings.* Applied Acoustics, 1998. **53**(4): p. 273-289.
9. Craven, P.G. and B.M. Gibbs, *Sound-transmission and mode-coupling at junctions of thin plates, Part 1: Representation of the problem.* Journal of Sound and Vibration, 1981. **77**(3): p. 417-427.
10. Gibbs, B.M. and P.G. Craven, *Sound-transmission and mode-coupling at junctions of thin plates, Part 2: Parametric survey.* Journal of Sound and Vibration, 1981. **77**(3): p. 429-435.
11. Gibbs, B.M., *Mode-Coupling and Energy Partition of Sound in a System of Plate Junctions.* Journal of sound and vibration, 1986. **104**(1): p. 127-136.
12. Craik, R.J.M. and A. Thancanamootoo, *The importance of in-plane waves in sound transmission through buildings*, in *Applied Acoustics*1992. p. 85-109.
13. Hopkins, C., *Vibration transmission between coupled plates using finite element methods and statistical energy analysis. Part 1: Comparison of measured and predicted data for masonry walls with and without apertures.* Applied Acoustics, 2003. **64**(10): p. 955-973.
14. Hopkins, C., *Vibration transmission between coupled plates using finite element methods and statistical energy analysis. Part 2: The effect of window apertures in masonry flanking walls.* Applied Acoustics, 2003. **64**(10): p. 975-997.
15. Hopkins, C., *Experimental statistical energy analysis of coupled plates with wave conversion at the junction.* Journal of Sound and Vibration, 2009. **322**(1-2): p. 155-166.
16. Yap, F.F. and J. Woodhouse, *Investigation of damping effects on statistical energy analysis of coupled structures.* Journal of sound and vibration, 1996. **197**(3): p. 351-371.
17. Craik, R.J.M., J.A. Steel, and D.I. Evans, *Statistical Energy Analysis of Structure-Borne Sound-Transmission at Low-Frequencies.* Journal of sound and vibration, 1991. **144**(1): p. 95-107.
18. Boisson, C., et al., *Energy Transmission in Finite Coupled Plates .2. Application to an L-Shaped Structure.* Journal of sound and vibration, 1982. **81**(1): p. 93-105.
19. Wester, E.C.N. and B.R. Mace, *Statistical energy analysis of two edge-coupled rectangular plates: Ensemble averages.* Journal of sound and vibration, 1996. **193**(4): p. 793-822.
20. Cremer, L. and M. Heckl, *Structure-Borne Sound*. Third ed2005, Berlin: Springer-Verlag.

21. Park, W.S., D.J. Thompson, and N.S. Ferguson, *The influence of modal behaviour on the energy transmission between two coupled plates.* Journal of sound and vibration, 2004. **276**(3-5): p. 1019-1041.
22. Park, W.S., D.J. Thompson, and N.S. Ferguson, *Variability of the coupling loss factor between two coupled plates.* Journal of sound and vibration, 2005. **279**(3-5): p. 557-579.
23. Skeen, M.B.K., N.J., *An investigation of transmission coefficients for finite and semi-infinite coupled plate structures.* Journal of the Acoustical Society of America, 2007. **122**(2).
24. *EN 12354-2:2000 Building acoustics - Estimation of acoustic performance of buildings from the performance of elements - Part 2: Impact sound insulation between rooms*, 2000, European Committee for Standardization.
25. Gerretsen, E., *Calculation of the sound-transmission between dwellings by partitions and flanking structures.* Applied Acoustics, 1979. **12**(6): p. 413-433.
26. Magrans, F.X., *Definition and calculation of transmission paths within an SEA framework.* Journal of Sound and Vibration, 1993. **165**(2): p. 277-283.
27. Guasch, O.C., L., *Graph theory applied to noise and vibration control in statistical energy analysis models.* Journal of the Acoustical Society of America, 2009. **125**(6): p. .
28. Guasch, O. and A. Aragones, *Finding the dominant energy transmission paths in statistical energy analysis.* Journal of Sound and Vibration, 2011. **330**(10): p. 2325-2338.
29. Craik, R.J.M., *The contribution of long flanking paths to sound transmission in buildings.* Applied Acoustics, 2001. **62**(1): p. 29-46.
30. Zienkiwicz , O.C., *The Finite Element Method*1997, London: Magraw-Hill Company.
31. Simmons, C., *Structure-Borne Sound-Transmission through Plate Junctions and Estimates of Sea Coupling Loss Factors Using the Finite-Element Method.* Journal of sound and vibration, 1991. **144**(2): p. 215-227.
32. Steel, J.A. and R.J.M. Craik, *Statistical Energy Analysis of Structure-Borne Sound-Transmission by Finite-Element Methods.* Journal of sound and vibration, 1994. **178**(4): p. 553-561.
33. Hopkins, C., *Statistical energy analysis of coupled plate systems with low modal density and low modal overlap.* Journal of Sound and Vibration, 2002. **251**(2): p. 193-214.
34. Hopkins, C., *Structure-borne sound transmission between coupled plates*, in *Department of building engineering and surveying*2000, Herriot-Watt university.
35. Hopkins, C., *Measurement of the vibration reduction index, Kij on free standing masonry wall constructions.* Building Acoustics, 1999. **6**: p. 235-257.
36. Guyader, J.L., C. Boisson, and C. Lesueur, *Energy Transmission in Finite Coupled Plates .1. Theory.* Journal of sound and vibration, 1982. **81**(1): p. 81-92.
37. Fredo, C.R., *A SEA-like approach for the derivation of energy flow coefficients with a finite element model.* Journal of sound and vibration, 1997. **199**(4): p. 645-666.
38. Mace, B.R. and P.J. Shorter, *Energy flow models from finite element analysis.* Journal of sound and vibration, 2000. **233**(3): p. 369-389.
39. Mace, B.R., *Statistical energy analysis: coupling loss factors, indirect coupling and system modes*, in *Journal of Sound and Vibration*2005. p. 141-170.
40. Mace, B.R., *Statistical energy analysis, energy distribution models and system modes*, in *Journal of Sound and Vibration*2003. p. 391-409.

41. Langley, R.S. and A.W.M. Brown, *The ensemble statistics of the band-averaged energy of a random system.* Journal of sound and vibration, 2004. **275**(3-5): p. 847-857.
42. Langley, R.S. and A.W.M. Brown, *The ensemble statistics of the energy of a random system subjected to harmonic excitation.* Journal of sound and vibration, 2004. **275**(3-5): p. 823-846.
43. Langley, R.S.C.V., *Response variance prediction in the statistical energy analysis of built-up systems.* Journal of the Acoustical Society of America, 2004. **115**(2).
44. Contoni, V., R.S. Langley, and M.R.F. Kidner, *Numerical and experimental validation of variance prediction in the statistical energy analysis of built-up systems*, in *Journal of Sound and Vibration*2005. p. 701-728.
45. Langley, R.S., *A Wave Intensity Technique for the Analysis of High-Frequency Vibrations.* Journal of sound and vibration, 1992. **159**(3): p. 483-502.
46. Langley, R.S., *Wave Intensity Analysis of High Frequency Vibrations* Philisophical transactions of the Royal Society London. A, 1994. **346**: p. 489-499.
47. Bercin, A.N., *High frequency vibration analysis of plate structures*, 1993, Cranfield Institute of Technology.
48. Heron, K.H., *Advanced Statistical Energy Analysis.* Philisophical transactions of the Royal Society: Physical and Engineering Sciences, 1994. **346**: p. 501-510.
49. Yin, J.H., C., *Prediction of high frequency vibration transmission across coupled, periodic ribbed plates by incorporating tunneling mechanisms.* Journal of the Acoustical Society of America, 2013. **133**(4).
50. Yin, J., *Structure-borne sound transmission between isotropic, homogeneous plates and periodic ribbed plates*, in *School of Architecture*2012, University of Liverpool.
51. Fahy, F.J. and A.D. Mohammed, *A study of uncertainty in applications of SEA to coupled beam and plate systems. Part 1: Computational experiments.* Journal of Sound and Vibration, 1992. **158**(1): p. 45-67.
52. Lyon, R.H. and G. Maidanik, *Power flow between linerarly coupled oscillators.* Journal of the Acoustical Society of America, 1961. **34**(5): p. 623-639.
53. *EN 12354-5:2000 Building acoustics - Estimation of acoustic performance of buildings from the performance of elements - Part 5: Sound levels due to service equipment*, 2000, European Committee for Standardization.
54. Craik, R.J.M., *The contribution of long flanking paths to sound transmission in buildings*, in *Applied Acoustics*2001. p. 29-46.
55. Lyon, R.H., *Statistical Energy Analysis of Dynamical Systems: Theory and Applications*. First ed1975, Massachusetts: MIT Press.
56. Lalor, N., *Practical considerations for the measurement of internal and coupling loss factors on complex structures, ISVR Technical Report No. 182.* 1990.
57. Craig, R.R., *Structural Dynamics: An introduction to computational methods*1981, Canada: Joh Wiley and Sons Inc.
58. various, *Abaqus Theory Manual v6.9*.
59. various, *Abaqus Analysis Users Manual v6.9*.
60. Mindlin, R.D., *Influence of Rotatory Inertia and Shear on Flexural Motions of Isotropic, Elastic Plates.* Journal of Applied Mechanics-Transactions of the Asme, 1951. **18**(1): p. 31-38.
61. Bishop, R.E.D., *Mechanics of Vibration.*
62. Hyun Sil Kim, H.J.K., and Jae Seung Kim *Transmission of bending waves in inter-connected rectangular plates.* Journal of the Acoustical Society of America, 1994. **96**(3): p. 1557.

63. Steel, J.A., *Sound-Transmission between Plates in Framed Structures.* Journal of sound and vibration, 1994. **178**(3): p. 379-394.
64. Hecht , E., *Optics*. fourth ed2002: Addison Wesley.
65. Guyader, J., *Vibration in Continuous Media*, ed. S.F. d'Acoustique: ISTE.
66. Robinson, M., *Predicting sound and vibration response using Transient Statistical Energy Analysis*, in *School of Architecture*2012, University of Liverpool: Liverpool, UK.
67. *ISO 7626:1990 - Methods for experimental determination of mechanical mobility. Measurements using single-point translation excitation with an attached vibration exciter*, 1990, International Organization for Standardization.
68. Randall, R.B., *Frequency Analysis*. Third ed1987, Glostrup: Bruel & Kjaer.
69. Guyader, J.L., et al., *Sound-Transmission by Coupled Structures - Application to Flanking Transmission in Buildings.* Journal of sound and vibration, 1986. **106**(2): p. 289-310.
70. Craik, R.J.M., *Damping of Building Structures.* Applied Acoustics, 1981. **14**(5): p. 347-359.